Thin Film Bragg Deflection Gratings for Integrated Optics

Edwin Yue Bun Pun, B.Sc.

A thesis submitted to the University of Glasgow for the degree of Doctor of Philosophy in the Faculty of Engineering

June 1983

Contents

Summary

Two types of single mode thin film Bragg deflectors were investigated : periodic index waveguides (with the guiding layers posessing parallel boundaries) by diffusion through a metallic grating mask; and periodic thickness (corrugated) waveguides by forming photoresist gratings on top of the waveguides (four-layered devices), or with the relief patterns ion-beam etched (using argon ions) directly onto the surfaces of the guides (three-layered devices).

The periodic index waveguides were fabricated by silver-sodium ion exchange in glass substrates, and proton-exchange or titanium indiffusion in $LiNbO_3$ substrates. The metallic grating masks (periodicity = 3μm) on the surfaces of the guides prior to diffusion were formed by conventional photolithographic technique, followed by vacuum deposition of the metal and lift-off. Sputtered homogeneous 7059 glass waveguides on standard Fisher microscope slides were used in the manufacture of corrugated waveguides. Submicron gratings (periodicity = 0.3μm) were fabricated by holographic exposure of the photoresist-coated samples.

General waveguide theory of homogeneous and inhomogeneous dielectric slab waveguides is presented, using both geometrical (or ray) optics and electromagnetic theory. Properties of periodic waveguides are also described, and the Bragg deflectors fabricated are analysed using one-dimensional coupled mode formalism and two-dimensional coupled mode

formalism. The theory predicts two unique properties of oblique incidence not found in normal incidence : mode conversion (TE/TM) and variation of power across the width of the diffracted and transmitted beam.

The fabrication techniques for both types of deflectors, including the three diffusion processes and the interferometric technique for producing submicron gratings, are discussed in some details. The waveguide and grating parameters were measured using standard techniques, and the grating groove depths were deduced from diffraction efficiency measurements. The periodicity is determined from the measurement of the autocollimation angle of the first diffracted order.

The Bragg devices were tested using a visible HeNe laser. For periodic index waveguides, the experimental results are in good agreement with theoretical calculations using one-dimensional coupled mode formalism. However, mode conversion (TE-TM), a unique property in oblique incidence of guided wave onto a grating element, was not observed because of the long periodicity (small Bragg angle) of the devices. Furthermore, a two-step diffusion process, using the first diffusion to form the waveguide and a second diffusion to produce the grating structure, was also demonstrated. This gives further flexibility to the diffusion technique, and the parameters in the first and second diffusion steps can be chosen independently for optimised performance. For the corrugated waveguides, the experimental results agree better with calculations using the two-dimensional

coupled mode formalism. The two unique properties of oblique incidence : mode conversion (TE-TM) and non-uniform intensity distribution across the width of both the diffracted and transmitted beams, were observed. It is confirmed experimentally that for right angle deflection, the TE-TE coupling is zero. When the diffraction efficiency is high, the diffracted beam 'breaks up'.

The results from this investigation suggest that the periodic index waveguides fabricated have distinct advantages over the corrugated counterparts in terms of lower scattering loss, ease of fabrication and mechanical ruggedness. The two unique properties of oblique incidence may pose a problem in certain applications, such as beam expanders and multiplexer/demulplexer. 'Breaking up' of the beams and cross-talk introduced by mode conversion must be taken into account when designing these devices.

Acknowledgements

I am grateful to Professor J. Lamb for providing me with the opportunity to do research work in his group, and for provision of research facilities in the Department of Electronics and Electrical Engineering, and for his interest during the course of this research.

My special thanks to my supervisor Dr. P.J.R. Laybourn for his guidance, encouragement, and his helpful and constructive criticism of the draft of this thesis.

My thanks to Dr. A. Yi-Yan for the initial help in the fabrication of holographic gratings, Mr. R.H. Hutchins for looking after my personal well-being, and the technical staff for their excellent and skillful assistance. Thanks also to fellow research students, especially I. Andonovic, R. Urquhart and K.K. Wong, for making my stay at Glasgow a pleasant and enjoyable time.

The assistance of K.K. Wong in proof-reading the manuscript is appreciated.

My special thanks to my mother, brothers and sisters for their ceaseless encouragement, understanding, and support throughout my project.

A scholarship from the University of Glasgow is gratefully acknowledged.

Chapter 1

INTRODUCTION

1.1 General Introduction

Interest in optical guided wave technology (commonly called Integrated Optics) began about the same time (cira 1969) that the first fibres with losses low enough (∿20dB/km)for long distance telecommunications were produced in research laboratories[1.1-1.3]. These glass fibre cables are light weight and small, have high signal carrying capacity and low signal loss (at present ∿ 0.5 to 3 dB/km), and are immune to electromagnetic interference and noise[1.4].

A majority of optical fibre systems used today are multimode fibre systems, in which light propagates in mixtures of hundreds of electromagnetic modes. However, single mode fibre systems capable of higher transmission rate and longer transmission distance are receiving increasing interest. These systems are more compatible with integrated optical circuits and devices, which are mostly single mode structures.

The major goal in integrated optics is to develop sophisticated thin film optical circuits and devices, by combining thin film and integrated electronics technology, for optical fibre communication and data processing systems[1.5-1.7].

The effective use of thin-film integrated optical waveguide components that will perform most of the logic functions optically, such as switching, modulation, multiplexing, and so on, offers possible orders of magnitude improvement in

reliability, ruggedness, speed of operation, size, weight, electrical power requirements and costs.

Ideally, it would be most advantageous if several devices such as sources, modulators and detectors, could be fabricated on the same substrate material. This is known as monolithic integration. Group III and group V semiconductor compounds, such as alloys of indium phosphide and gallium arsenide, are promising materials. On the other hand, the performance of various devices on different materials can be optimised and then the devices may be connected together,known as hybrid integration. Lithium niobate (for active waveguiding functions) and low loss glass waveguides (for passive waveguiding functions) are the most widely used materials.

Although much of the initial research and development effort in fibre optics and guided-wave optics technologies has been directed towards communications applications, there are increasingly other important applications for these technologies, such as real time high speed signal processing[1.8], radio frequency spectrum analysis[1.9,1.10], logic operations[1.11], analogue to digital conversion[1.12,1.13], data bus interconnection of several high speed digital computers[1.14], and sensing of physical quantities[1.15].

1.2 Periodic Structures for Integrated Optics

The phenomenon of wave propagation in periodic structures recurs in many branches of physics. These structures

have special properties which made them unique and important:

(1) Although the individual interaction from each element in the periodic structure is small, the total phase synchronous effect can be large. This property is known as distributed feedback, or Bragg diffraction. As will be shown in a later chapter (chapter 3), the propagation wave vector can only be complex in certain frequency bands. This implies that a wave propagating in the periodic structure with a frequency in the stop band will encounter successive reflections; the propagating wave can only be supported in well specified propagation bands.

(2) There is an infinite number of space harmonics, with phase velocities varying from zero to infinity in the eigenmodes. This means the periodic structure has an inherent wave vector K ($K = 2\pi/\Lambda$, Λ being the period of the structure) that is adjustable by the designer, and can be used to conserve the momentum (or the vector) in the coupling between any two waves.

(3) Any small amount of random defects created in the fabrication process will not affect the characteristics of the devices significantly.

Thin film structures containing a periodic variation along the film play an important role in guided wave optics[1.16]. The periodic variation falls into one of the two categories (Fig. 1.1) :

(1) The guiding layer contains a homogeneous medium but its

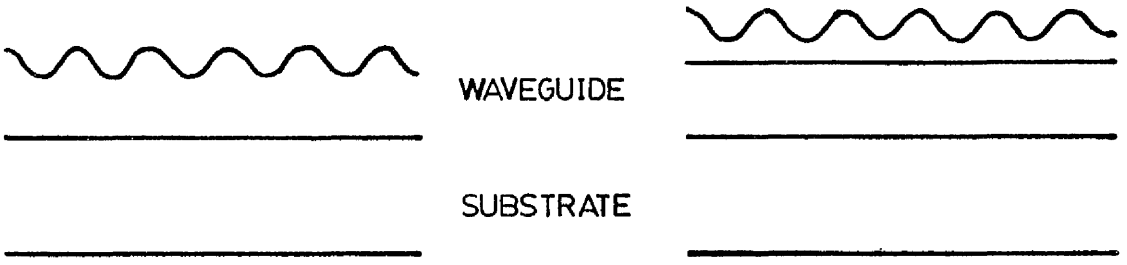

TYPE I

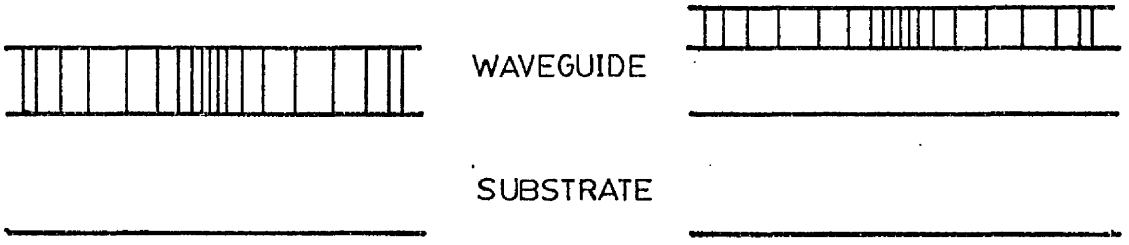

TYPE II

FIG 1.1 Basic types of periodic waveguides

upper boundary has a periodic variation, for example ion beam etched gratings achieving periodic changes in refractive index through their surface profile[1.17]; or

(2) The guiding layer possesses parallel planar boundaries and its periodicity is produced by a longitudinal modulation of its refractive index, for example a periodic change in refractive index can be achieved by the electro-optical effect using a modulating voltage applied to a periodic electrode[1.18] or by the acousto-optical effect using a surface acoustic wave at an appropriate frequency[1.19].

For monolithic integration purposes, it is desirable to have reflectors (like silvered mirrors in bulk optics) that are compatible with planar technology. They can be formed by cleaving or selective chemical etching in semiconductor materials, and polishing and coating the edges of a substrate with a reflecting surface in other materials such as glass or lithium niobate. These methods, however, are not compatible with planar technology, and cannot be used to form frequency selective devices. For example, it is difficult to integrate conventional semiconductor lasers (with cleaved mirrors) with other guided wave devices. The problem can be circumvented by the use of frequency selective grating structures, and appears to be the most promising and versatile planar technology.

Submicron-periodic grating structures are fabricated by means of a holographic technique, by recording the interference pattern of two beams from a laser onto photoresist, a light sensitive material. After development, the relief pattern can

be transferred onto the surface of the waveguide by chemical etching or ion beam etching. Alternatively, special material which changes its dielectric constant on exposure to light can be used as the waveguiding film, and then direct recording of the interference pattern is possible[1.20].

Guided wave optical devices that have been demonstrated using a grating structure include beam couplers[1.21-1.23], beam splitters[1.24], filters[1.25,1.26], mode convertors[1.27,1.28], modulators[1.29-1.31], directional couplers[1.32], distributed feedback and distributed Bragg reflector lasers[1.33-1.35], multiplexer-demultiplexer[1.36], waveguide lenses[1.37,1.38], second harmonic generators[1.39,1.40] and integrated optical signal processors[1.41,1.42].

1.3 Aims Of Research

In most of the grating devices mentioned previously, the incident and reflected waves are collinear, that is, the guided waves are perpendicular to the grating lines. This collinear geometry has become a textbook case, the most notable treatments being given by Yariv[1.43] and Marcuse[1.44], both using coupled-mode analysis. However, in devices such as multiplexer-demultiplexer, deflectors or grating lenses, the guided wave is incident obliquely on the grating. Such oblique propagation is very important in many aspect, with properties different from that of normal incidence, and advantages including good incident and deflected wave separation and accessibility, compactness,

considerable device versatility and design flexibility.

The holographic techniques for making submicron gratings are well established. However, the surface corrugations produced in this method are prone to environmental disturbance, and scattering losses due to the rough surfaces of the gratings occur.

The aims of this research were two-fold:

(1) To study beam deflection (or mode coupling) in corrugated waveguides when a guided wave is incident on the grating at an angle to the grating lines, and specifically giving a right angle deflection. We either used a photoresist grating on top of the waveguide, or the grating etched directly onto the surface of the guide by ion beam etching. Homogeneous sputtered Corning 7059 glass waveguides on Fisher microscope slides were used.

(2) To investigate a novel technique of fabricating periodic index waveguides with the guiding layers possessing parallel planar boundaries by diffusion through a grating mask. Beam deflectors were produced by silver-sodium ion exchange in glass substrates, and proton-exchange or titanium indiffusion in lithium niobate. The grating mask was delineated on top of the substrate by conventional photolithographic technique, followed by vacuum deposition and lift-off to obtain the fine pattern (periodicity $\sim$ 3μm).

1.4 Layout of Thesis

This thesis is divided into seven chapters. Following this introductory chapter, chapter 2 is on the general theories and properties of planar dielectric waveguides, for both homogeneous and inhomogeneous structures. Chapter 3 deals with the theoretical studies of the guided wave Bragg deflectors using coupled-mode analysis, while chapter 4 and chapter 5 are concerned with the fabrication techniques to produce the Bragg deflectors, by a novel technique of diffusion through a grating mask, and by holographic technique respectively. The experimental procedures, results and analysis are presented in chapter 6. Chapter 7, the last chapter, gives a conclusion of this work, with suggestions for future investigation.

References

1.1 K.C. Kao and G.A. Hockham
Proc. IEE, 113 p.1151 (1966)

1.2 S.E. Miller
Bell Syst. Tech. J., 48 p.2059 (1969)

1.3 F.P.Kapron, D.B. Keck and R.D. Maurer
Appl. Phys. Lett., 17 p.423 (1970)

1.4 S.E. Miller, E.A.J. Marcatilli and T. Li
Proc. IEEE, 61 p.1703 (1973)

1.5 H.F. Taylor and A. Yariv
Proc. IEEE, 62 p.1044 (1974)

1.6 H. Kogelnik
IEEE Trans. Micro. Theo. Tech., MTT-23 p.2 (1975)

1.7 T. Tamir, Ed.
'Integrated Optics' (Springer Press, Berlin, Germany)
(1975)

1.8 C.S. Tsai
IEEE Trans. Circ. & Syst., CAS-26 p.1072 (1979)

1.9 M.C. Hamilton, D.A. Wille and W.J. Miceli
Proc. Ultrasonics Symp., p.218 (1976)

1.10 D.B. Anderson, J.T. Boyd, M.C. Hamilton and R.R. August
IEEE J. Quant. Elect., QE-13 p.268 (1977)

1.11 H.F. Taylor
Appl. Opt., 17 p.1493 (1978)

1.12 H.F. Taylor
Proc. IEEE, 63 p.1525 (1975)

1.13 H.F. Taylor, M.J. Taylor and P.W. Bauer
Appl. Phys. Lett., 33 p.559 (1978)

1.14 E.G. Rawson and R.M. Metcaffe
IEEE Trans. Comm., Com-26 p.983 (1978)

1.15 T.G. Giallorenzi, J.A. Bucaro, A. Dandridge, G.H. Sigel Jr., J.H. Cole, S.C. Rashleigh and R.G. Priest
IEEE Trans. Micro. Theo. & Tech., MTT-30 p.472 (1982)

1.16 A. Yariv and M. Nakamura
IEEE J. Quant. Elect., QE-13 p.233 (1977)

1.17 H.L. Garvin, E. Gamire, S. Somekh, H. Stoll and A. Yariv
Appl. Opt., 12 p.455 (1973)

1.18 J.M. Hammer
Appl. Phys. Lett., 18 p.147 (1971)

1.19 L. Kuhn, M.L. Dakss, P.F. Heidrich and B.A. Scott
Appl. Phys. Lett., 17 p.265 (1970)

1.20 V.E. Wood, N.F. Hartman, C.M. Verber and R.P. Kenan
J. Appl. Phys, 46 p.1214 (1975)

1.21 M.L.Dakss, L. Kuhn, P.F. Heidrich and B.A. Scott
Appl. Phys. Lett., 16 p.523 (1970)

1.22 H. Kogelnik and T.P. Sosnowsky
Bell Syst. Tech. J., 49 p.1602 (1970)

1.23 D.G. Dalgoutte
Opt. Comm., 8 p.124 (1973)

1.24 K.S. Pennington and L. Kuhn
Opt. Comm., 3 p.357 (1971)

1.25 D.C. Flanders, H. Kogelnik, R.V. Schmidt and C.V. Shank
Appl. Phys. Lett., 24 p.194 (1974)

1.26 D.C. Flanders, C.V. Shank and R.D. Standley
Appl. Phys. Lett., 25 p.651 (1974)

1.27 L. Kuhn, D.F. Heidrich and E.G. Lean
Appl. Phys. Lett., 14 p.428 (1971)

1.28 H. Sasaki, J. Kushibiki and N. Chubachi
Appl. Phys. Lett., 25 p.476 (1974)

1.29 D.P. Gia Russo and J.H. Harris
Appl. Opt., 10 p.2786 (1971)

1.30 J.N. Polky and J.H. Harris
Appl. Phys. Lett., 21 p.307 (1972)

1.31 P.K. Tien and R.J. Martin, R. Wolfe, R.C. Lecrew and S.L. Blank
Appl. Phys. Lett., 8 p.394 (1972)

1.32 K.Ogawa, W.S.C. Chang, B. Sapori and F.J. Rosenbaum
J. Opt. Soc. Am., 63 p.478 (1973)

1.33 H. Kogelnik and C.V. Shank
Appl. Phys. Lett., 18 p.152 (1971)

1.34 C.V. Shank, J.E. Bjorkholm and H. Kogelnik
Appl. Phys. Lett., 18 p.395 (1971)

1.35 S. Wang
IEEE J. Quant. Elect., QE-10 p.413 (1974)

1.36 A.C. Lavanos, A. Katzir, A. Yariv and C.S. Hong
Appl. Phys. Lett., 30 p.519 (1977)

1.37 S.K. Yao and D.E. Thompson
Appl. Phys. Lett., 33 p.635 (1978)

1.38 P.R. Ashley and W.S.C. Chang
Appl. Phys. Lett., 33 p.490 (1978)

1.39 N. Bloemberger and A.J. Sievers
Appl. Phys. Lett., 17 p.483 (1970)

1.40 B.F. Levine, C.G. Bether and R.A. Logan
Appl. Phys. Lett., 26 p.375 (1974)

1.41 W.S.C.Chang, C.S. Tsai, R.A. Becker and S.W. Yao
IEEE J. Quant. Elect., QE-13 p.208 (1977)

1.42 D. Mergerian, E.C. Makarkey, R.P. Pautienus, J.C. Bradley, G.E. Marx, L.D. Hutcheson and A.L. Keilner
SPIE Proc., 239 p.121 (1980)

1.43 A. Yariv
IEEE J. Quant. Elect., QE-9 p.919 (1973)

1.44 D. Marcuse
'Theory of Dielectric Optical Waveguides' (Academic Press, New York, 1974)

Chapter 2

Theory of Dielectric Thin Film Waveguides

Dielectric waveguides are used in guided wave devices and integrated optical circuits to guide and confine light energy. The study of the simplest structures, dielectric slab waveguides, and their properties, is useful and necessary for the understanding of more complicated dielectric waveguides; like for example periodic structures in 'Integrated Optics'. In this chapter we will outline the fundamental theoretical properties of planar waveguides, using both geometrical (or ray) optics and electromagnetic theory. In the last section, we will also describe beam coupling to planar guides, and in particular the prism coupler, which is an efficient method of introducing optical energy from conventional lasers into these waveguides, and was used in our experimental work.

2.1 Propagation Of Waves In Homogeneous Asymmetric Slab Waveguides

A planar dielectric slab waveguide is shown schematically in Fig. 2.1, where a thin film of refractive index n_f is deposited on a substrate with refractive index n_s. The refractive index of the cover material is n_c, and we assume that

$$n_f > n_s \geq n_c \qquad (2.1.1)$$

Typical differences between n_f and n_s range from 0.001 to 0.1, and a typical film thickness T is 1 μm. The refractive index n_c

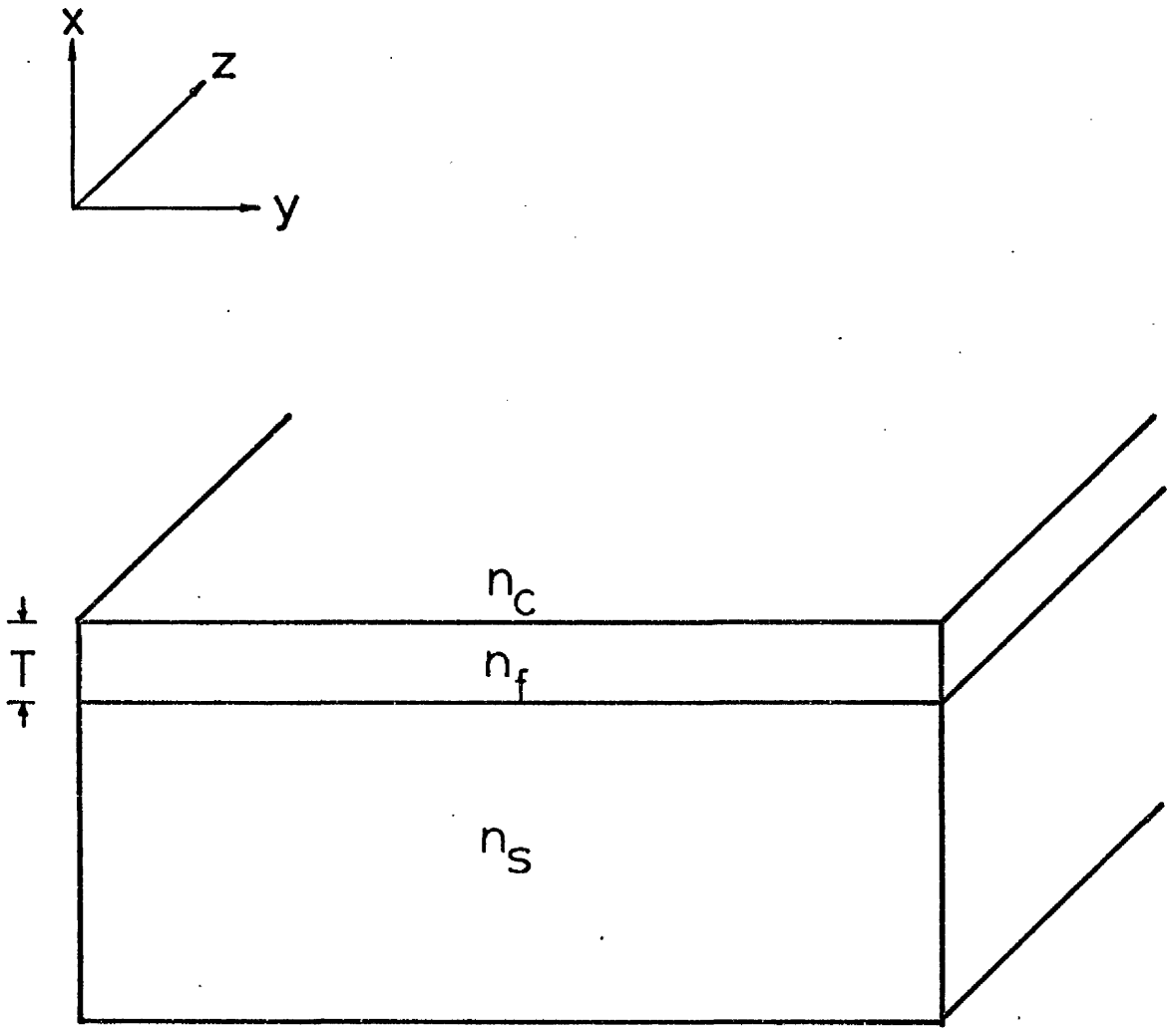

FIG 2.1 Schematic of a dielectric slab waveguide

is often unity when the cover material is air. If $n_c = n_s$, we have a symmetric slab waveguide, and there is no cut-off frequency of the lowest-order mode. This means a mode can propagate at arbitrarily low frequencies. By contrast, if $n_c \neq n_s$, we have an asymmetric slab waveguide, and all modes of the guide will have a cut-off frequency.

The asymmetric slab waveguide supports a finite number of guided modes and an infinite continuum of radiation modes. Both types of modes can be obtained as solutions of a wave equation from wave optics. However, the eigenvalue equation of the guided modes can also be intuitively derived from geometrical optics, which is supplemented by simple results of plane wave reflection and refraction at a plane dielectric interface. Hence we start with geometrical optics.

2.1.1 Geometrical Optics of Homogeneous Dielectric Slabs

Geometrical (or ray) optics approximates a narrow beam of light as light rays, which are the energy flow of the light, and are defined as the lines that are perpendicular to the surfaces of constant phase of the light field in a homogeneous, isotropic medium.

Consider the zig-zag ray pictures in Fig. 2.2. There is no confinement of light when $\Theta < \Theta_s$, Θ_c (known as 'radiation mode'), or $\Theta_c < \Theta < \Theta_s$ (known as 'substrate radiation mode'). Θ is the angle between the light ray and the normal to the

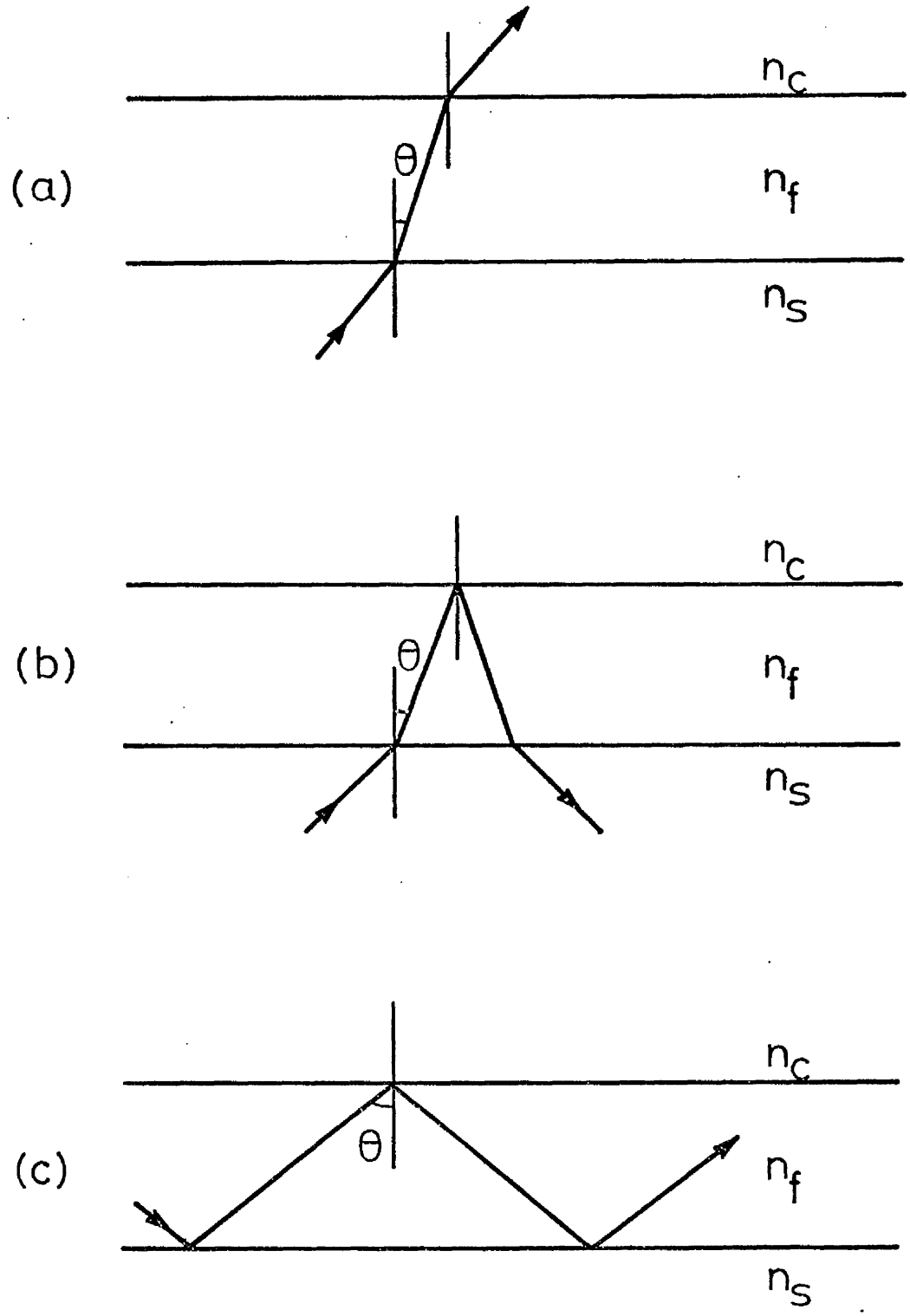

FIG 2.2 Zig-zag ray pictures for (a) the radiation modes, (b) the substrate modes, and (c) the guided modes

waveguide, θ_c and θ_s are the critical angle for the film-cover interface and film-substrate interface respectively. When θ_c, $\theta_s < \theta$, the light is trapped and confined in the film and propagates in a zig-zag manner with total internal reflection occurring at the two interfaces.

Under the conditions of total internal reflection, phase shifts will occur consistent with the flow of energy at the two interfaces, and are known as the Goos-Hanchen shifts[2.1,2.2]. From Fresnel formulas, the phase shifts ϕ_{TE} and ϕ_{TM} for the TE polarization (electric field vector parallel to the interface) and the TM polarization (magnetic field vector parallel to the interface) are[2.3]

$$\tan \phi_{TE} = \sqrt{(n_f^2 \sin^2\theta - n_{c,s}^2)}/n_f \cos\theta \qquad (2.1.2)$$

$$\tan \phi_{TM} = [\sqrt{(n_f^2 \sin^2\theta - n_{c,s}^2)}/n_f \cos\theta]\,(n_f^2/n_{c,s}^2) \qquad (2.1.3)$$

respectively for the two interfaces. The subscripts s, f and c refer to substrate, film and cover respectively. Fig. 2.3(a) shows the lateral shifts $2z_c$ and $2z_s$ of the ray associated with the phase shifts, and the ray penetration depths x_c and x_s in such a case, while Fig. 2.3(b) shows the refractive index profile for a homogeneous waveguide.

The two superimposed uniform plane waves with wavenormals following the zig-zag ray path propagate with a wavevector kn_f, where

$$k = 2\pi/\lambda_o = \omega/c \qquad (2.1.4)$$

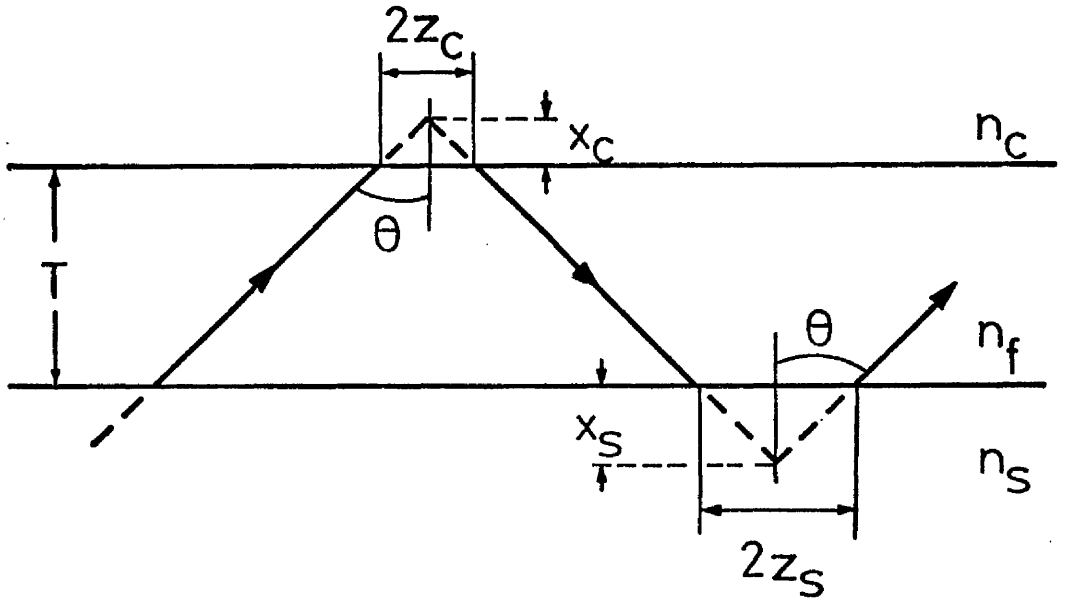

FIG 2.3a Ray picture showing the Goos-Hänchen shifts at the interfaces

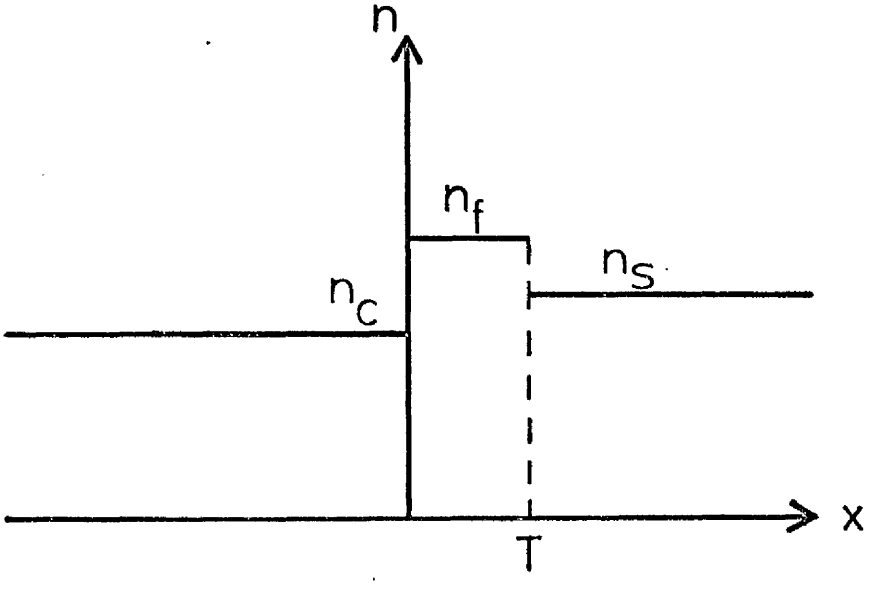

FIG 2.3b Refractive index profile of a slab waveguide

and λ_o is the free space wavelength, ω is the angular frequency, c is the velocity of light in vacuum. The guided mode of the slab waveguide has a propagation constant

$$\beta = k_z = kn_f \sin\theta = kN = \omega/v_p \qquad (2.1.5)$$

and is the z component of the wavevector kn_f. v_p is the phase velocity, and N is the effective index of the guide. Not all angles θ are allowed. The 'transverse resonance condition' requires the k_x components to interfere constructively, that is, the total phase shifts at the two interfaces together with that of the transverse passages must be a multiple of 2π. This condition can be expressed as

$$2kn_f T\cos\theta - 2\phi_s - 2\phi_c = 2m\pi \qquad (2.1.6)$$

where m is an integer (0,1,2 ...) corresponding to the mode number. Equation (2.1.6) is the dispersion equation of the guide and the value of the propagation constant can be predicted as a function of frequency ω and film thickness T, with the help of (2.1.2) to (2.1.5). Fig. 2.4 shows an $\omega-\beta$ diagram of the dispersion characteristics, while Fig. 2.5 shows the variation of the effective index of the guide as a function of film thickness.

Using (2.1.2), (2.1.3) and (2.1.5), the lateral shifts $z_{c,s}$ are

$$kz_{c,s} = (N^2-n^2_{c,s})^{-1/2}.\tan\theta \qquad (2.1.7)$$

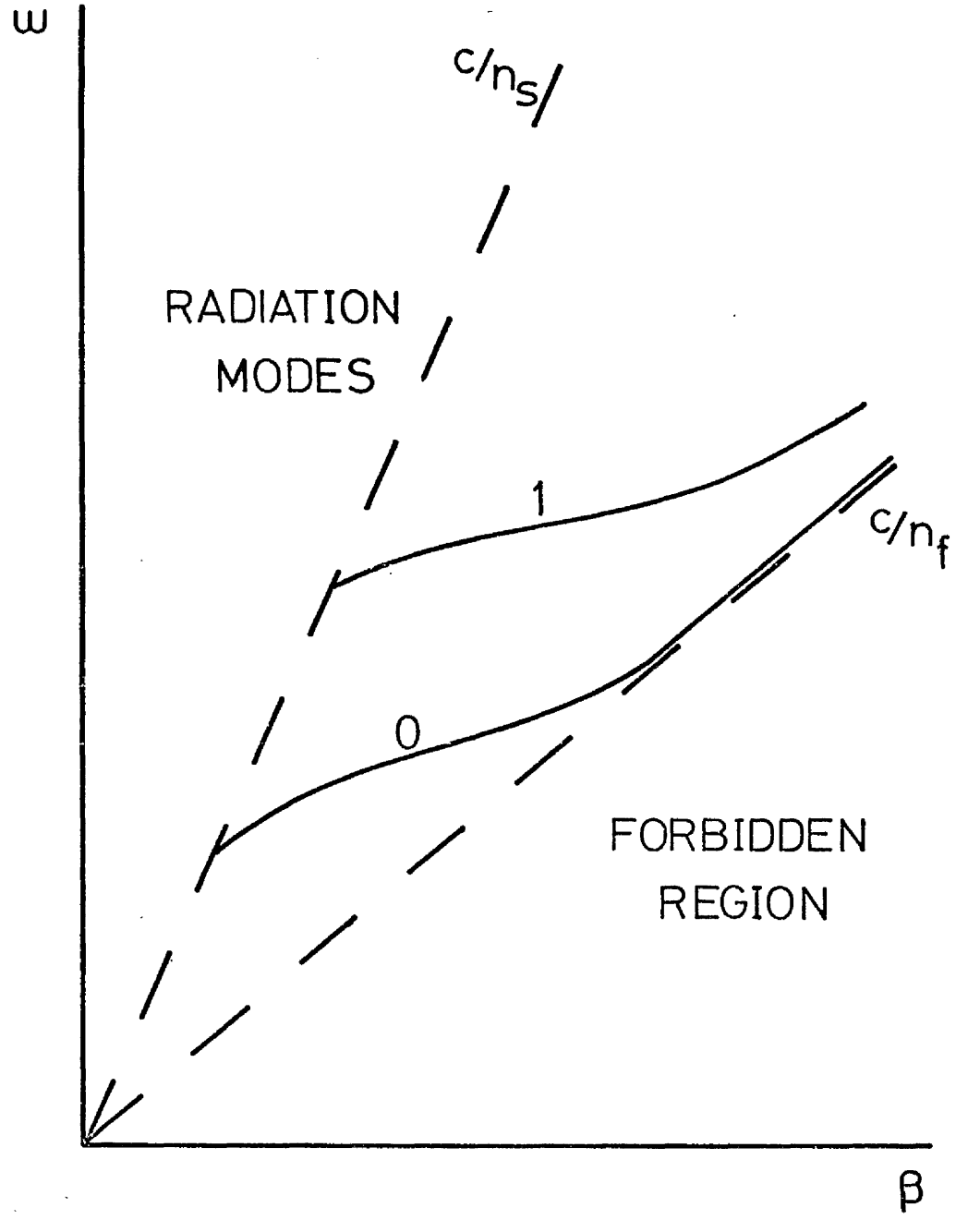

FIG 2.4 ω - β diagram of a dielectric waveguide

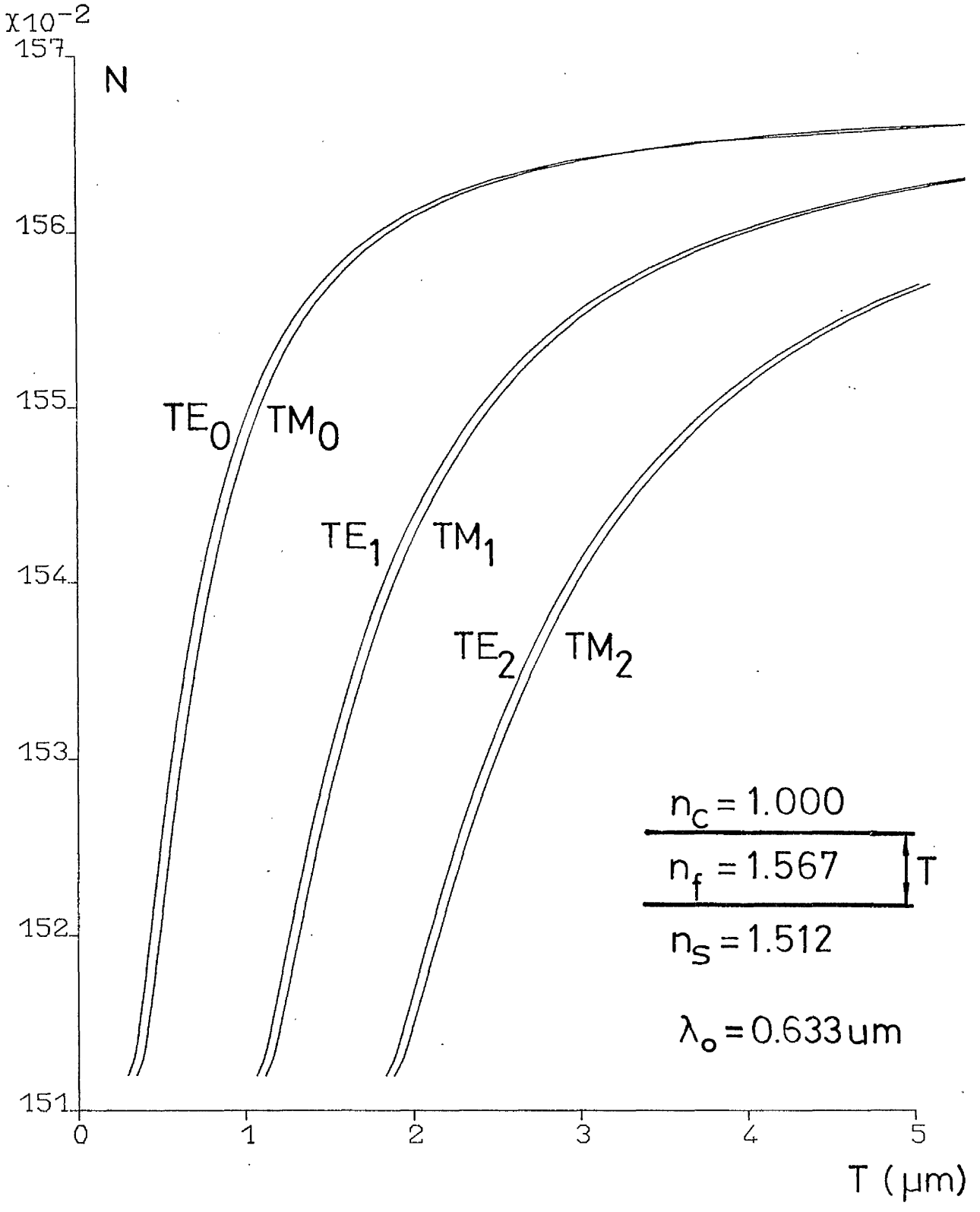

FIG 2.5 Effective guide index as a function of film thickness

for the TE modes, and

$$kz_{c,s} = (N^2 - n^2_{c,s})^{-1/2} \cdot \tan\Theta / (N^2/n^2_{c,s} + N^2/n_f^2 - 1) \qquad (2.1.8)$$

for the TM modes. The relation between the penetration depth $x_{c,s}$ and $z_{c,s}$ is

$$x_{c,s} = z_{c,s} \; / \; \tan\Theta \qquad (2.1.9)$$

These penetration depths $x_{c,s}$ are closely related to the decay constants of the evanescent fields in the cover and substrate (section 2.2, electromagnetic field solutions). The guided light spreads out into both the cover and the substrate and is essentially confined to an effective thickness T_{eff},

$$T_{eff} = T + x_s + x_c \qquad (2.1.10)$$

Although the conditions for mode propagation in slab waveguides can be intuitively obtained with the help of simple principles from ray optics and from the properties of plane waves, they are not complete. For example, the phase shifts at the two interfaces are negative in sign (equation (2.1.6)); this gives a mathematically correct result, but is physically difficult to interpret. In order to obtain a complete description of the mode propagation, electromagnetic theory has to be used.

2.1.2 Electromagnetic Theory of Homogeneous Dielectric Slabs

Maxwell's equations for isotropic, time dependent, source free fields are

$$\nabla \times E = -\mu (\partial H/\partial t) \tag{2.1.11}$$

$$\nabla \times H = \epsilon (\partial E/\partial t) \tag{2.1.12}$$

where ϵ and μ are the scalar permittivity and permeability of a lossless medium, t is the time, $\nabla = (\partial/\partial x, \partial/\partial y, \partial/\partial z)$ is the del operator, and E and H are the electric and magnetic field vectors.

We can further distinguish between the longitudinal field component E_z and H_z, and the transverse field components E_t and H_t,

$$E = E_t + E_z \quad , \quad H = H_t + H_z \tag{2.1.13}$$

and assuming a time dependence factor $e^{j\omega t}$ the Maxwell's equations can be rewritten in the form

$$\nabla_t \times E_t = -j\omega\mu H_z \tag{2.1.14}$$

$$\nabla_t \times H_t = j\omega\epsilon E_z \tag{2.1.15}$$

$$\nabla_t \times E_z + e_z \times \partial E_t/\partial z = -j\omega\mu H_t \tag{2.1.16}$$

$$\nabla_t \times H_z + e_z \times \partial H_t/\partial z = j\omega\epsilon E_t \tag{2.1.17}$$

where $\nabla_t = (\partial/\partial x, \partial/\partial y, 0)$ and e_z is a unit vector pointing

in the z - direction.

In a slab waveguide, the light is confined in one dimension only, and it is the x direction in our case (Fig. 2.1). There is no variation in the y direction, which means

$$\partial/\partial y = 0 \tag{2.1.18}$$

The normal time harmonic z dependent modes of the guide can be expressed in complex notation as

$$e^{j(\omega t - \beta z)} \tag{2.1.19}$$

and the time dependence factor $e^{j\omega t}$ is usually ignored.

There are two types of polarization of the waves, the transverse electric (TE) modes with no longitudinal electric field ($E_z = 0$) and transverse magnetic (TM) modes with no longitudinal magnetic field ($H_z = 0$). For TE modes, we get $H_y = 0$ from (2.1.15), $E_x = 0$ and

$$\beta E_y = -\omega\mu H_x \tag{2.1.20}$$

from (2.1.16). From (2.1.14)

$$\partial E_y/\partial x = -j\omega\mu H_z \tag{2.1.21}$$

and

$$\partial H_z/\partial x + j\beta H_x = -j\omega\epsilon E_y \tag{2.1.22}$$

from (2.1.17) and (2.1.19). Combining the last three equations

yields the wave equation

$$\partial^2 E_y/\partial x^2 = (\beta^2 - n^2k^2)E_y \qquad (2.1.23)$$

where

$$\varepsilon = n^2 \qquad (2.1.24)$$

$$k = \omega/\sqrt{\mu_0\varepsilon_0} = 2\pi/\lambda_0 \qquad (2.1.25)$$

The solutions for the wave equation (2.1.23) have been discussed by various people[2.2, 2.4-2.6]. We will first define the various propagation constants (k_i) and decay constants (γ_i) as

$$k_c^2 = n_c^2k^2 - \beta^2 = -\gamma_c^2 \qquad (2.1.26)$$

$$k_f^2 = n_f^2k^2 - \beta^2 \qquad (2.1.27)$$

$$k_s^2 = n_s^2k^2 - \beta^2 = -\gamma_s^2 \qquad (2.1.28)$$

For guided modes the solutions are

$$\begin{aligned} E_y &= E_c \exp[-\gamma_c(x-T)] && \text{for } T<x, \\ E_y &= E_f\cos(k_f x - \phi_s) && \text{for } 0<x<T, \\ E_y &= E_s \exp(\gamma_s x) && \text{for } x<0. \end{aligned} \qquad (2.1.29)$$

The boundary conditions require E_y (and H_x) and $\partial E_y/\partial x$ (and H_z) to be continuous across the film boundaries at $x = 0$ and $x = T$, hence we can obtain the expressions for the phase shifts

$$\tan \phi_{c,s} = \gamma_{c,s}/k_f \qquad (2.1.30)$$

and the dispersion relation

$$k_f T - \phi_s - \phi_c = m\pi \qquad (2.1.31)$$

which is identical to that obtained from a 'geometrical optics' approach. The relation between the peak fields E_f, E_s and E_c is

$$E_f^2(n_f^2-N^2) = E_s^2(n_f^2-n_s^2) = E_c^2(n_f^2-n_c^2) \qquad (2.1.32)$$

The modes are not normalised for power. We define the power P carried by a mode per unit guide width as

$$P = -2\int_{-\infty}^{\infty} dx E_y H_x = 2\beta/\omega\mu_o \int_{-\infty}^{\infty} dx E_y^2 = N\sqrt{\frac{\epsilon_o}{\mu_o}}\, E_f^2 T_E = E_f H_f T_E \qquad (2.1.33)$$

where $T_E = T + 1/\gamma_s + 1/\gamma_c$ is the effective TE mode thickness of the waveguide.

Similar procedures can be taken for the TM modes. By setting $E_y = 0$ we get $H_z = 0$, $H_x = 0$,

$$\beta H_y = \omega \epsilon E_x \quad , \qquad (2.1.34)$$

$$\partial H_y/\partial x = j\omega\epsilon E_z \quad , \qquad (2.1.35)$$

$$\partial E_z/\partial x + j\beta E_x = j\omega\mu H_y \quad , \qquad (2.1.36)$$

and the wave equation for H_y is

$$n^2(\partial/\partial x)(1/n^2\partial H_y/\partial x) = (\beta^2 - n^2k^2)H_y \ . \qquad (2.1.37)$$

For guided modes the solutions are

$$H_y = H_c \exp[-\gamma_c(x-T)] \qquad \text{for } T<x,$$

$$H_y = H_f \cos(k_f x - \phi_s) \qquad \text{for } 0<x<T, \qquad (2.1.38)$$

$$H_y = H_s \exp(\gamma_s x) \qquad \text{for } x<0.$$

The boundary conditions require the continuity of H_y (and ϵE_x) and of $1/n^2\partial H_y/\partial x$ (and E_z) across the two interfaces. Hence we obtain once again the phase shifts

$$\tan \phi_{c,s} = (n_f^2/n^2_{c,s})\gamma_{c,s}/k_f \qquad (2.1.39)$$

and the dispersion relation

$$k_f T - \phi_s - \phi_c = m\pi \qquad (2.1.40)$$

The relation between the peak fields is in the form

$$H_f^2(n_f^2-N^2)/n_f^2 = H_s^2(n_f^2-n_s^2)q_s/n_s^2 = H_c^2(n_f^2-n_c^2)q_c/n_c^2 \qquad (2.1.41)$$

where the reduction factors q_s and q_c are

$$q_s = (N/n_f)^2 + (N/n_s)^2 - 1 \ , \qquad (2.1.42)$$

$$q_c = (N/n_f)^2 + (N/n_c)^2 - 1 \ , \qquad (2.1.43)$$

as given in (2.1.8). The power P per unit guide width is

$$P = 2\int_{-\infty}^{\infty} dx E_x H_y = 2\beta/\omega\epsilon_o \int_{-\infty}^{\infty} dx H_y^2/n^2$$
$$= N\sqrt{\mu_o/\epsilon_o}\ H_f^2 T_M/n_f^2 = E_f H_f T_M \qquad (2.1.44)$$

where $T_M = T + 1/\gamma_c q_c + 1/\gamma_s q_s$ is the effective TM mode thickness of the waveguide.

2.2 Propagation of Waves in Inhomogeneous Asymmetric slab Waveguides

Several fabrication processes, like diffusion[2.7] and ion implantation[2.8], produce graded index dielectric waveguide layers with variation in the refractive index n(x) across the depth of the guides. In this section, we will discuss the analysis of such guides.

2.2.1 Geometrical Optics of Inhomogenous Dielectric Slabs

The zig-zag ray picture is shown in Fig. 2.6(a), and the refractive index distribution (a silver-sodium ion exchange waveguide in our case) in Fig. 2.6(b). The rays follow a curved trajectory rather than straight lines, in contrast to those of homogeneous waveguides. This is because the vertical component of the wavevector $k_x(x)$ depends on the depth of the guide. When the gradient of the ray path is zero, that is, when $n = N = \beta/k$, the point is known as the turning point x_t. Assuming that the

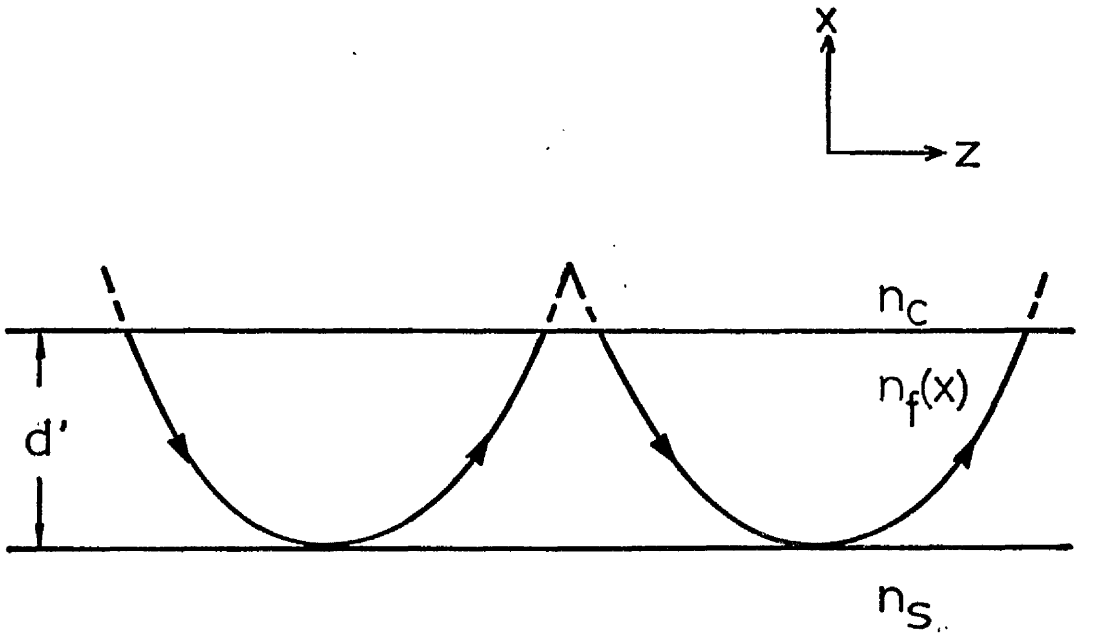

FIG 2.6a Ray picture of a guided wave in an inhomogeneous waveguide

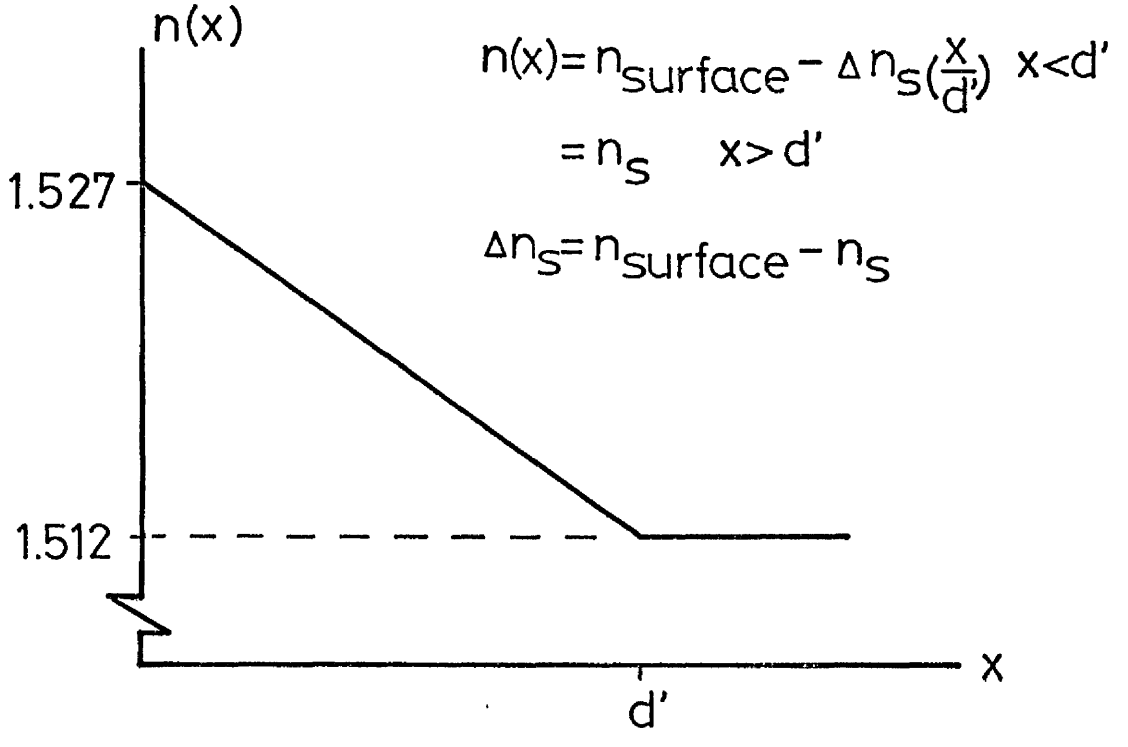

FIG 2.6b Refractive index profile of Ag-Na ion-exchanged waveguides in a 0.1% diluted melt

refractive index profile varies slowly in comparison with the wavelength, the 'transverse resonance condition' can be written as

$$2k\int_{-x_t}^{0}[n^2(x)-N^2]^{1/2}dx - 2\phi_c - \pi/2 = 2m\pi \qquad (2.2.1)$$

The phase change over the round passage is represented by the integral, while the phase reflection at the turning point is $\pi/2$. This method involves an initial trial value for N, and is commonly known as the WKB method[2.9]. It was first developed in the field of quantum mechanics[2.9], and has been applied to the analysis of dielectric waveguides[2.10]. The electric field expressions have also been given by Marcuse for TE modes[2.11]. The refractive index profile n(x) can be deduced from the WKB equation[2.7,2.12,2.13], with increased accuracy as the number of guided modes increases[2.14].

2.2.2 Electromagnetic Theory of Inhomogeneous Dielectric Slabs

Maxwell's equations in this case are

TE modes $$d^2E_y/dx^2 = [\beta^2-k^2n^2(x)]E_y \qquad (2.2.2)$$

TM modes $$d^2H_y/dx^2 = [\beta^2+1/n^2(x)\,(d\epsilon/dx)\,(d/dx)-k^2n^2(x)]H_y \qquad (2.2.3)$$

The wave equation (2.2.2) is similar to the Schrodinger equation of quantum mechanics, with N^2 $(=\beta^2/k^2)$ corresponding to the energy level and $n^2(x)$ to the potential energy well, and the same

solutions and analysis applied, hence exact solutions can exist for certain refractive index profiles[2.9]. If the gradient of n(x) is small, we can ignore the $d\epsilon/dx$ term in equation (2.2.3), and the same solution can also be used for the TM modes. However, the index profiles n(x) obtained in practice are such that the wave equations cannot be solved exactly, and approximate methods are used instead.

Marcuse[2.11] pointed out that the actual index profile can be approximated by straight line segments, and since an exact solution exists for a linear profile in terms of Bessel functions of the order $\pm$ 1/3, approximate solutions can be found by solving the resulting multilayer structures.

A similar method, developed by Vassell[2.15], subdivided the inhomogeneous waveguide into finite thin homogeneous sublayers. Each layer will have a constant refractive index corresponding to its relative position in the original waveguide, and determined by the refactive index profile. By applying the boundary conditions at the interfaces, the resulting simultaneous equations can be solved with the help of a computer, for both the effective index and the electric field distribution. This approach has been adopted in the analysis of inhomogeneous waveguides[2.16,2.17].

2.3 Beam Coupling to Planar Guides

Although the properties of the dielectric waveguides described in the last two sections are somewhat similar to those

of metallic guides at microwave frequencies, there are major differences. Firstly, the guide dimensions (1μm) at optical frequency are much smaller than at microwave frequency (λ_o ~1cm); secondly, dielectric guides are open waveguides (as opposed to closed metallic guides) with energy extending into the exterior space. These differences lead to different fabrication techniques, with different tolerances and capabilities. Consequently the methods used to produce the fields in optical guides are different from those used in closed metallic guides.

There are many methods of coupling a laser beam into a dielectric slab, such as end-fire coupling[2.18], holographic coupling[2.19], tapered film coupling[2.20], grating coupling[2.21] and prism coupling[2.22]. Although the grating coupler appears to offer the most satisfactory arrangement for integrated optics applications, the prism coupler is convenient to use, and is most suitable for laboratory purposes. We used prism couplers in our experiments, and hence include a brief description of the method.

2.3.1 The Prism Coupler

Prism couplers having high efficiency[2.23] can be built to couple light into and out of a thin film structure. Fig. 2.7 shows such an arrangement for an input coupler.

Coupling to a guided mode by means of a prism (with higher refractive index than that of the thin film) occurs when the phase velocity of the evanescent field in the gap region is

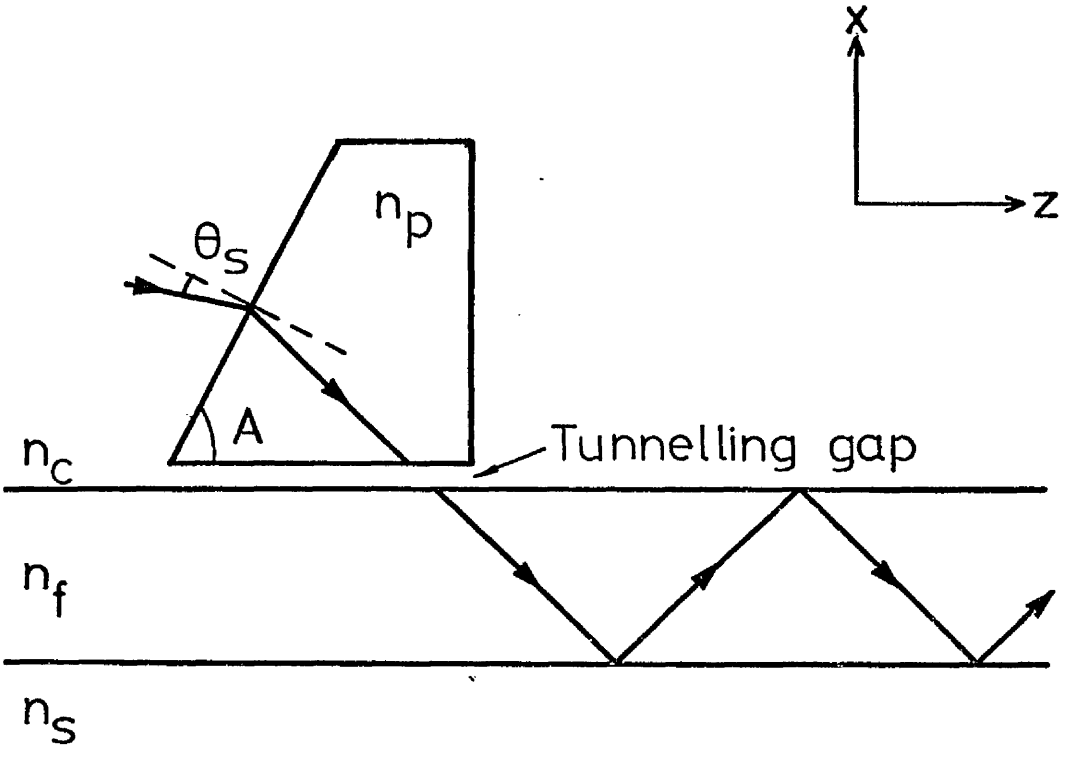

FIG 2.7 Prism coupler – the incident field couples to the surface wave via the evanescent field in the air gap

the same as that of the guided mode; the energy is transferred via a tunnelling effect, which is often known as optical tunnelling due to frustrated total reflection[2.2,2.24]. The corresponding angle is called the synchronous coupling angle, and is related to the effective index of the guide as

$$N = n_p \sin[\, A + \sin^{-1}(\sin\theta_s / n_p)\,] \qquad (2.3.1)$$

where θ_s is the synchronous coupling angle, n_p is the refractive index of the prism, and angle A is the angle between the base and the incident face of the prism. The angle θ_s is considered positive if the incident beam lies between the normal to the prism and its base.

By reciprocity, a surface wave incident from the right would couple energy into the prism and radiate out, hence achieving an output coupler. By observing the output m-line pattern, the effective index of the guide can be measured accurately. Measurement of more than one synchronous angle θ_s permits the film thickness and refractive index to be determined from the dispersion equation[2.2].

A disadvantage of the prism coupler is that the prism material must have a refractive index higher than that of the thin film. Although it presents no problem for material like glass ($n \sim 1.5$), it is not the case for a high refractive index material like Gallium Arsenide ($n \sim 3.6$). In addition care must be taken not to scratch the surface of the thin film when clamping on the prism.

2.4 Conclusions

In this chapter, we have outlined the general properties of and analytical methods for both homogeneous and inhomogeneous waveguides. Prism coupling, an efficient method of coupling laser light to thin film, has also been briefly discussed.

References

2.1 J.J. Burke
Opt. Sci. Newsletter, Univ. Arizona, 5 p.31 (1971)

2.2 P.K. Tien
Appl. Opt., 10 p.2395 (1971)

2.3 M. Born and E. Wolf
'Principle of Optics' (Pergamon Press, London)

2.4 J. Mckenna
Bell Sys. Tech. J., 46 p.1491 (1971)

2.5 N.N. Kapany and S.S. Burke
'Optical Waveguides' (Academic Press, New York)

2.6 D. Marcuse
'Theory of Dielectric Optical Waveguides' (Academic Press, New York)

2.7 T.G. Giallorenzi, E.J. West, R. Kirk, K. Ginter and R.A. Andrews
Appl. Opt., 12 p.1240 (1973)

2.8 D.T.Y. Wei, W.W. Lee and L.R. Bloom
Appl. Phys. Lett., 22 p.5 (1973)

2.9 L.D. Landau and E.M. Lifshitz
'Quantum Mechanics' (Pergamon Press, Oxford)

2.10 J.P. Gordon
Bell Sys. Tech. J., 45 p.321 (1966)

2.11 D. Marcuse
IEEE J. Quant. Elect., QE-9 p.1000 (1973)

2.12 G. Stwart, C.A. Miller, P.J.R. Laybourn, C.D.W. Wilkinson and R.M. De La Rue
IEEE J. Quant. Elect., QE-13 p.192 (1977)

2.13 J. Gallagher and R.M. De La Rue
Micro. Opt. & Acoust., 1 p.215 (1977)

2.14 A. Gedeon
Opt. Comm., 12 p.329 (1974)

2.15 M.D. Vassell
J. Opt. Soc. Am., 64 p.166 (1974)

2.16 A. Yi Yan
Ph.D. Thesis, Faculty of Engineering, University of Glasgow (1978)

2.17 A. McLachlan
Ph.D. Thesis, Faculty of Engineering, University of

Glasgow (1981)

2.18 D. Hall, A. Yariv, E. Gamire
Opt. Comm., 1 p.403 (1970)

2.19 E.A. Ash, E. Seaford, O. Soares and K.S. Pennington
Appl. Phys. Lett., 24 p.207 (1974)

2.20 P.K. Tien and R.J. Martin
Appl. Phys. Lett., 18 p.398 (1971)

2.21 M.L. Dakss, L. Kuhn, P.F. Heidrich and B.A. Scott
Appl. Phys. Lett., 16 p.523 (1970)

2.22 H. Osterberg, L.W. Smith
J. Opt. Soc. Am., 54 p.1078 (1964)

2.23 R. Ulrich
J. Opt. Soc. Am., 61 p.1467 (1971)

2.24 L.V. Iogansen and L. Bergstein
Appl. Opt., 6 p.2001 (1967)

Chapter 3

Theoretical Analysis of Thin Film Guided Wave Bragg Deflectors

Bragg waveguide deflectors have been fabricated by diffusion (silver-sodium ion exchange in glass, titanium indiffusion or proton-exchange in lithium niobate) through an aluminium grating mask, or by forming a thin phase photoresist grating on top of the waveguide, and ion-beam etching the pattern onto the surface of the waveguide.

The purpose of this chapter is to provide a theoretical background for the discussion on Bragg deflectors. In the following section, we discuss first the solution of the Hill's differential equations based on the Floquet theorem (for a TE mode, the wave equation is known as the Mathieu differential equation, which is a special case of the Hill's equation). We then proceed to show that the Coupled Mode Theory is adequate to analyse the Bragg deflectors made in this work. The attraction of this theory is its simplicity and versatility. Starting from Maxwell's equations we first derive a set of coupled wave equations for the incident and reflected beams, then a set of two-dimensional coupled wave equations for the profiles of the two beams (when the grating has finite dimensions). Finally the coupling constants for the interaction between TE-TE, TE-TM, and TM-TM guided modes are calculated.

3.1 Wave Propagation in Periodic Dielectric Slab Waveguide

Periodic waveguides can be classified into two types:

the periodicity is either a perturbation in the dielectric constant of the guiding film or its substrate (Type I), or a perturbation of the boundary (Type II). These structures can be analysed using perturbation techniques [3.1-3.4], or by a rigorous analytical method [3.5] and will now be considered in turn.

3.1.1 Perturbation in the dielectric constant

The source-free wave equations in a periodic medium with parallel boundary are :

$$\text{TE MODE } \nabla^2 E_y + k^2(z)E_y = 0,\ k^2(z) = k_o^2[\epsilon(z)/\epsilon_o] \qquad (3.1.1\ a)$$

$$\text{TM MODE } \nabla^2 H_y + k^2(z)H_y = 0,\ k^2(z) = \{k_o^2\ \epsilon(z)/\epsilon_o - [1/\epsilon(z).\partial\epsilon(z)/\partial z.\ \partial\ /\partial z]\} \qquad (3.1.1\ b)$$

where $k_o^2 = \mu_o\epsilon_o\omega^2$, ϵ_o and μ_o are the free space permittivity and permeability, $\epsilon(z)$ is the permitivity of the inhomogeneous medium, and ω is the angular (radian) frequency.

To solve these equations, the function $k^2(z)$ can be expressed in a Fourier expansion series, then the fields inside the perturbation region are found, and finally the boundary conditions are applied to determine the field amplitudes and propagation constants for the whole structure. A closed form solution exists for TE modes, and it is in the form of a Floquet infinite series of space harmonics (see Appendix 3A). A closed form solution may also exist for TM modes, depending on the form

of the function $k^2(z)$ [3.6]. Rigorous solutions for both TE and TM modes have also been formulated [3.5].

The dispersion relation can be represented graphically by the Brillouin diagram (Fig 3.1). The space harmonics (in this case restricted to $\pm K$, the grating vector) appear because of the periodic perturbation. Coupling occurs at the phase-matching points, that is, intersection points where two space harmonics have the same wave vector, or phase velocity. As the two coupled harmonics are contradirectional (group velocities having opposite signs) a stopband appears. The waves in the stop bands are exponentially increasing or decreasing functions. In the passbands, the propagation constant β is real when the medium is passive, and the normal modes of the wave equation are periodic functions since they represent the free-running waves in the periodic waveguide. In the stopbands β is complex, as shown in Fig. 3.1. The phenomenon is equivalent to the well known Bragg diffraction of X-rays in crystal lattices, given by $\beta = mK/2$ for the m-th order interaction, m being any positive integer, and K being the grating vector.

Although the Floquet formulation is relatively simple, the numerical calculations are involved. In a large number of cases, however, the periodic perturbation is relatively small and only few space harmonics have to be taken into account in the neighbourhood of a stopband for sufficient accuracy. This means that the Hill determinant (see Appendix 3A) can be truncated. For low order Bragg coupling, an accuracy better than 1 per cent can be obtained with a matrix of size $(2m+3) \times (2m+3)$ [3.7].

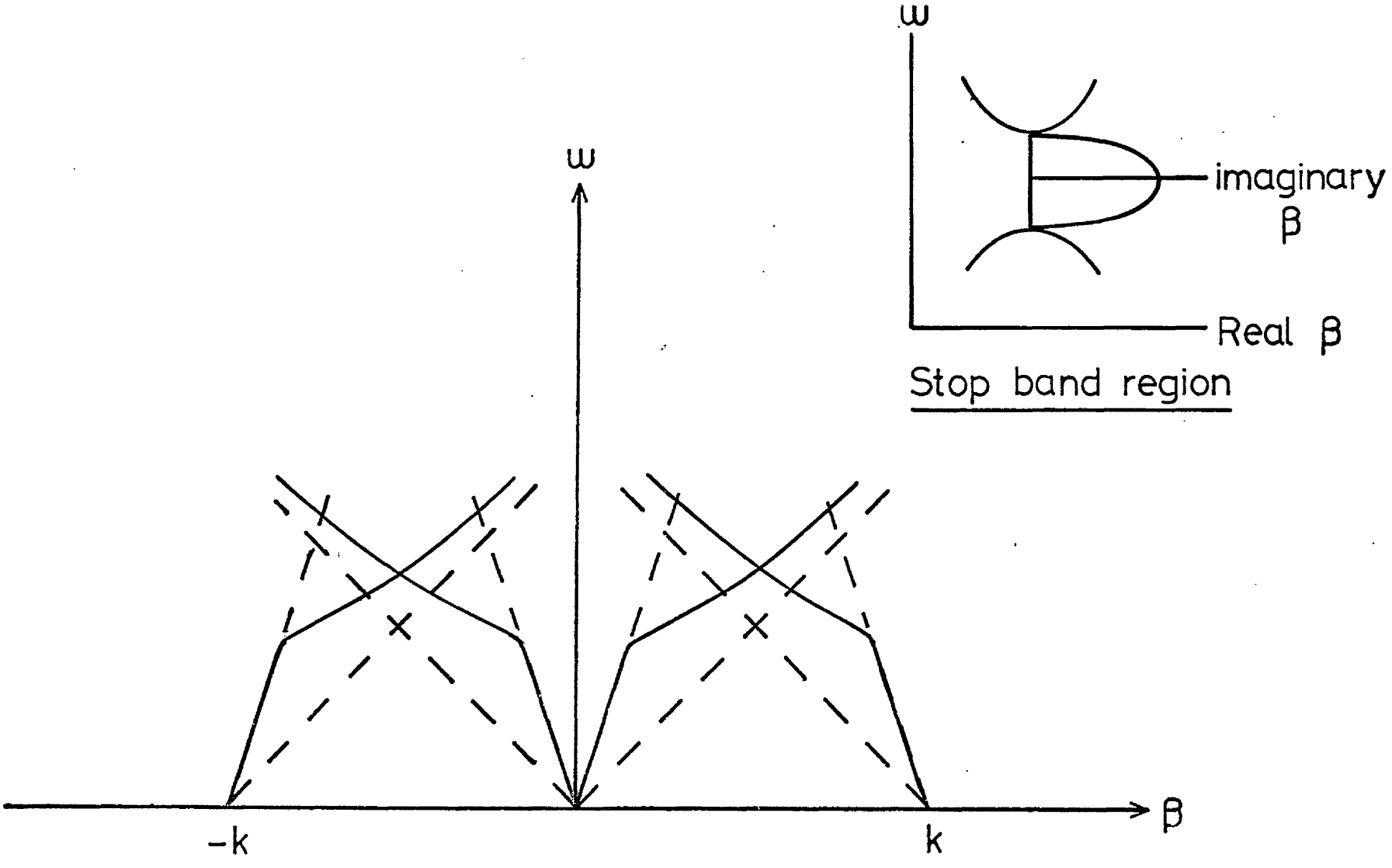

FIG 3.1 Brillouin (dispersion) diagram for a periodic slab waveguide

Alternatively, since the eigensolutions of the unperturbed smooth waveguide are known, the wave solutions of the perturbed waveguide can be constructed from these eigensolutions. This type of perturbation theory is called coupled mode theory and is only applicable if the coupling coefficient, or perturbation, is small. In the case of sinusoidal periodicity $\{\epsilon(z) = \epsilon_o \epsilon_r [1+D \cos(Kz)]\}$, where D is the modulation coefficient, and $\Lambda = 2\pi/K$ is the periodicity), however, numerical calcuations show that the coupled mode theory gives good results even for D up to a value of 1 [3.8]. The theory predicts closely the correct value for the imaginary part of the wave vector, but does not predict well the position of the stopband.

This is because β, the propagation wave vector, is assumed to be that of the unperturbed waveguide, whereas in the Floquet-Bloch formalism, β is determined from the Hill determinant. However, corrections to the unperturbed β can be obtained by evaluating the average change in β over one period [3.8].

The above discussion is concernly mainly with first order Bragg coupling. For high order Bragg coupling, similar coupled mode equations can be derived [3.9]. The main change is in the coupling coefficient χ. For the first-order Bragg coupling, χ is proportional to the perturbation D. For the m^{th} order Bragg coupling, $\chi \sim (m/2^m m!)^2 D^m$.

3.1.2 Boundary Periodicity

The wave equations in this case are :

TE MODE $\nabla^2 E_y + k^2(x,z)E_y = 0, \quad k^2(x,z) = k_o^2[\epsilon(x,z)/\epsilon_o]$ (3.1.2a)

TM MODE $\nabla^2 H_y + k^2(x,z)H_y = 0, \quad k^2(x,z) = \{k_o^2[\epsilon(x,z)/\epsilon_o]$

$\cdot [\nabla\epsilon(x,z)/\epsilon(x,z)]\nabla H_y$ (3.1.2b)

The solution is more complicated because of the functional form $k^2(x,z)$ (both x and z coordinates are present) and the boundary conditions (at the curved profile of the surface corrugation). Only rigorous solutions exist for both TE and TM modes (3.10, 3.11).

If the grating has a rectangular profile, approximations can be made, and by replacing the grating by a layer of constant thickness but modulated dielectric constant (3.12), the problem reduces to the case discussed in subsection 3.1.1 . For a more general form of grating, three methods can be used:

1) By subdividing the grating into many fine layers and approximating each one of these profiles by a rectangular profile;

2) By employing an exact numerical integration;

3) By averaging the permittivity over x for every value of z inside the grating layer of thickness T, i.e. for a profile of the form $x = h(z) = h(z+\Lambda)$, $0<x<T$, the average permittivity becomes $\epsilon(z) = \epsilon_2+(\epsilon_2-\epsilon_1)h(z)/T$. The problem is then reduced to that of a layer with uniform thickness, but varying $\epsilon(r)$.

Wang [3.13] and De Wames [3.14] have also studied rectangular gratings in terms of a periodic changes in the waveguide thickness. The three-dimensional electromagnetic field problem in this case is represented by a one-dimensional wave equation which assumes that the mode index of the waveguide varies periodically in space. The approximate solution of 3.1.1a can be used if the grating height is less than T/(m+1), where T is the waveguide thickness, and m is the mode number. This condition is usually satisfied in most devices. Furthermore, in the expansion of $k^2(z)$, the higher-order Fourier components of a nearly sinusoidal grating are much smaller than those of a rectangular grating. Consequently fewer terms in the Floquet infinite series are required to calculate relevant parameters for the same accuracy.

In the case where the surface perturbation is small, again the coupled mode theory can be used. Yariv and Gover [3.15] showed that the coupled mode and the Floquet-Bloch formalism in periodic optical waveguide are equivalent, with the Hill matrix in the Floquet calculation truncated.

The same Brillouin diagram described in section 3.1.1 also applies here. The stopband of the corrugated waveguides can be predicted more accurately by either redefining the thickness of the waveguide [3.16] or by transforming the structure into a Type I waveguide [3.17].

3.2 Coupled Wave Solution

Before embarking on the detailed analysis we shall

consider the common features of the coupled mode theory.

In a large number of interactions, only two guided modes are considered to have sufficient phase synchronism for power exchange. All other modes are neglected, and simple coupled wave differential equations are obtained to describe the interaction. There are two types of interactions, co-directional interactions and contra-directional interactions. Co-directional coupling occurs between a forward and backward mode.

For co-directional interaction, the changes in the amplitudes of two coupled waves A and B can be described by the differential equations of the form

$$A' = -j\kappa B e^{-2j\delta z} \quad , \qquad (3.2.1)$$

$$B' = -j\kappa A e^{2j\delta z} \quad , \qquad (3.2.2)$$

where κ is the coupling constant which is real and uniform in this simple case. The coupling constant is determined by the physical situation under consideration, and will be derived explicitly in section 3.4. δ is a measure of the deviation from synchronism (δ =0 for synchronism). By means of the simple substitution

$$A = Re^{-j\delta z}, \quad B = Se^{j\delta z} \quad , \qquad (3.2.3)$$

the coupled wave equations take the form

$$R' - j\delta R = -j\kappa S \quad , \qquad (3.2.4)$$

$$S' + j\delta S = -j\kappa R \quad . \qquad (3.2.5)$$

If the boundary conditions are such that R(0)=1, S(0)=0 the solutions are

$$S(z) = -j\kappa \sin(\sqrt{\kappa^2+\delta^2}.z)/\sqrt{\kappa^2+\delta^2} \quad , \qquad (3.2.6)$$

$$R(z) = \cos(\sqrt{\kappa^2+\delta^2}.z)+j\delta \sin(\sqrt{\kappa^2+\delta^2}.z)/\sqrt{\kappa^2+\delta^2} \quad . \qquad (3.2.7)$$

At synchronism (δ =0), there is a sinusoidal interchange of energy between R and S,

$$S(z) = -j\sin(\kappa z), \quad R(z) = \cos(\kappa z) \qquad (3.2.8)$$

A plot of the intensities $|R^2|$ and $|S^2|$ is shown in Fig. 3.2. The solutions are periodic functions and are in the passband. For large phase mismatch $\delta >> |\kappa|$ there is negligible power exchange.

The diffraction efficiency η for a waveguide deflector (transmission type) is

$$\eta = \sin^2(\phi^2+\delta^2)^{1/2}/[1+(\delta^2/\phi^2)] \quad , \qquad (3.2.9)$$

where $\phi = \kappa L$, $\delta = (1/2)KL\Delta\Theta$ and L is the grating length, K is the grating vector, and $\Delta\Theta$ is the angular deviation from the Bragg condition at fixed wavelength. We can approximate ϕ as independent of $\Delta\Theta$ for significant deviation, without causing an appreciable change in the prediction of (3.2.9), since ϕ and δ are of comparable magnitude. The curves for the angular sensitivies

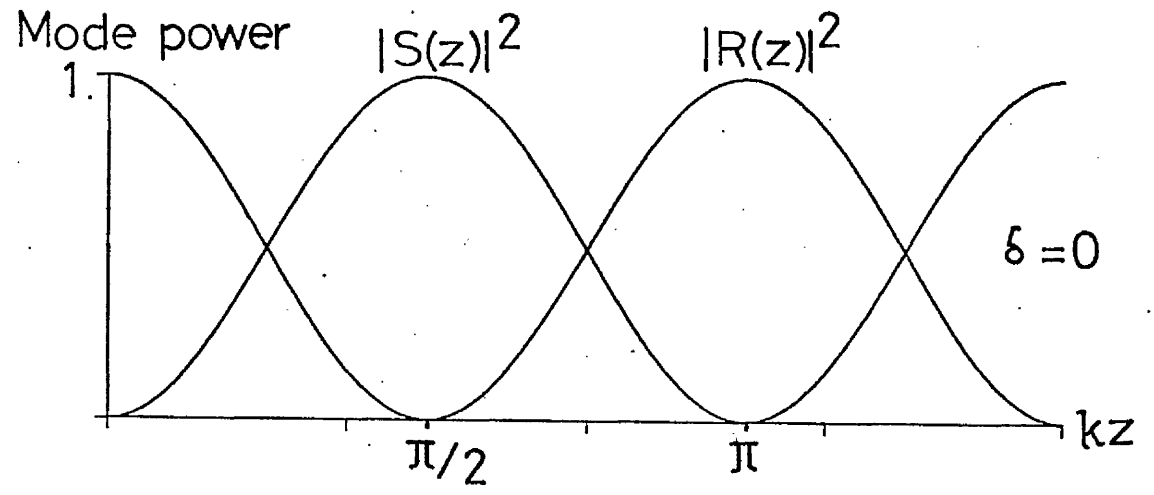

(a)

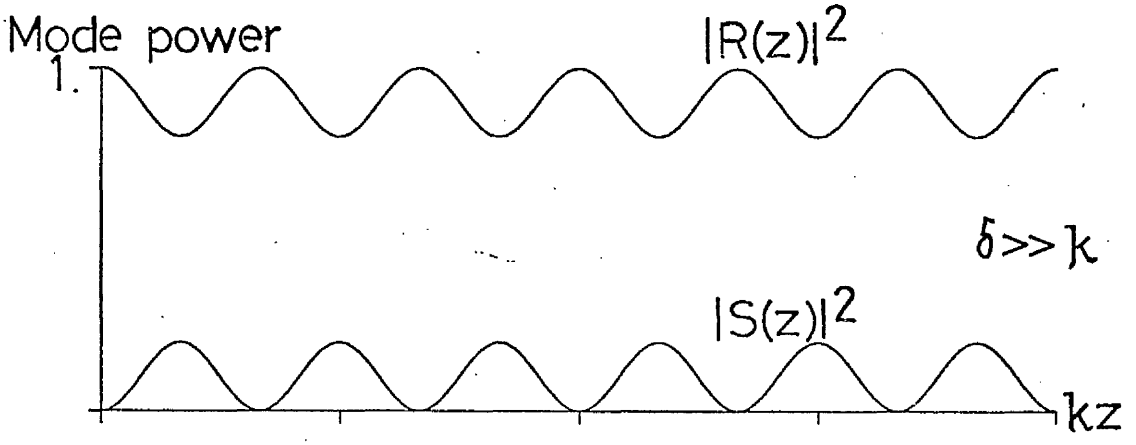

(b)

FIG 3.2 Power exchange between two coupled modes : (a) phase-matched condition, (b) phase-mismatched condition; for co-directional interaction

are shown in Fig. 3.3, where the normalised efficiencies are plotted as a function of δ for three values of ϕ. The curve for $\phi = \pi/2$ corresponds to a peak efficiency of 1, and those for $\phi = \pi/4,\ 3\pi/4$ to a peak value of 0.5. There is some narrowing in the sensitivity curves for increasing values of ϕ, and a marked increase in the side lobe intensity.

For contra-directional interactions, the differential equations are of the form

$$A' = -j\kappa B\, e^{2j\delta z} \quad , \qquad (3.2.10)$$

$$B' = j\kappa A\, e^{-2j\delta z} \quad , \qquad (3.2.11)$$

and the substitutions

$$A = Re^{j\delta z}, \qquad B = Se^{-j\delta z} \quad , \qquad (3.2.12)$$

transform these into the coupled-wave equations

$$R' + j\delta R = -j\kappa S \quad , \qquad (3.2.13)$$

$$S' - j\delta S = j\kappa R \quad . \qquad (3.2.14)$$

If the boundary conditions are such that $R(0) = 1$, $S(L) = 0$ at the end of the perturbation $z = L$, the solutions are

$$S(0) = -j\kappa/[\sqrt{\kappa^2 - \delta^2}\coth(\sqrt{\kappa^2 - \delta^2}.L) + j\delta] \quad , \qquad (3.2.15)$$

$$R(L) = \sqrt{\kappa^2 - \delta^2}/[\sqrt{\kappa^2 - \delta^2}\cosh(\sqrt{\kappa^2 - \delta^2}.L) + j\delta\sinh(\sqrt{\kappa^2 - \delta^2}.L)] . \qquad (3.2.16)$$

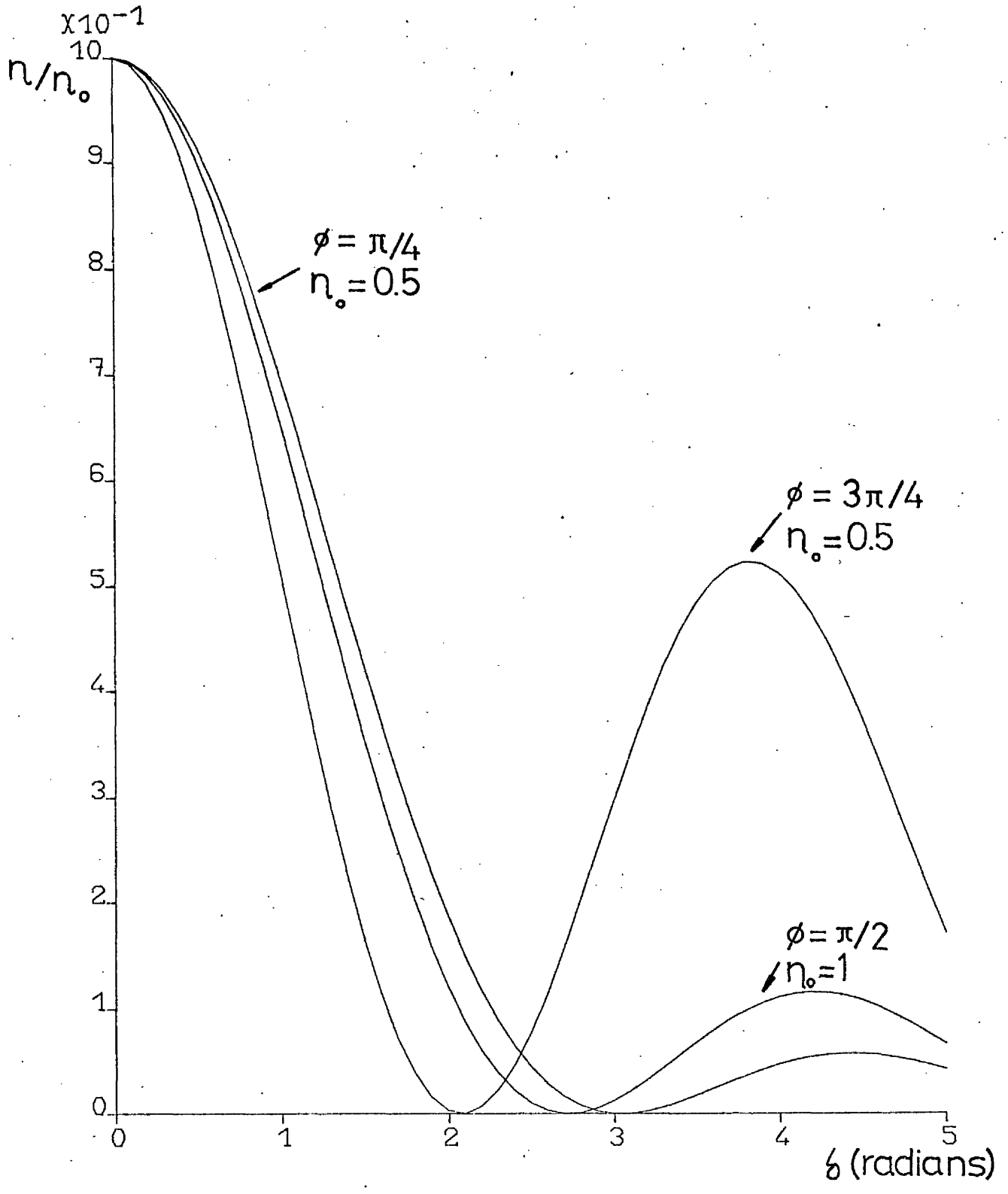

FIG 3.3 Angular sensitivities for co-directional interaction: normalised efficiency as a function of the off-Bragg parameter δ

At synchronism,

$$S(0) = -j\tanh(\kappa L), \qquad R(L) = 1/\cosh(\kappa L) \ . \qquad (3.2.17)$$

A plot of the mode powers $|R^2(z)|$ and $|S^2(z)|$ is shown in Fig. 3.4. For sufficiently large arguments of the cosh and sinh functions in (3.2.17), the incident mode power decays exponentially, due to reflection of the power, and not absorption. This exponential decay behaviour corresponds to the stopband region of a periodic medium discussed in subsection 3.1.1.

The diffraction efficiency η (for reflection-type) is

$$\eta = \{1 + (1-\delta^2/\phi^2)/[\sinh^2(\phi^2-\delta^2)]^{1/2}\}^{-1} \ , \qquad (3.2.18)$$

where ϕ and δ have the same definition as that for a transmission-type, and the angular sensitivity curves calculated are illustrated in Fig. 3.5. The peak efficiencies are 43%, 84% and 96% for $\phi = \pi/4$, $\pi/2$ and $3\pi/4$, respectively. The discontinuity at $\phi = \delta$ occurs when the argument of the hyperbolic function in (3.2.18) becomes imaginary, and the efficiency is falling rapidly for $\delta > \phi$.

3.3 Coupled Wave Formalism

The scattering of light that occurs in periodic waveguides having a deformation $\epsilon(x,y,z)$ (periodic in the z-direction) is a physical process. It can be viewed and analysed

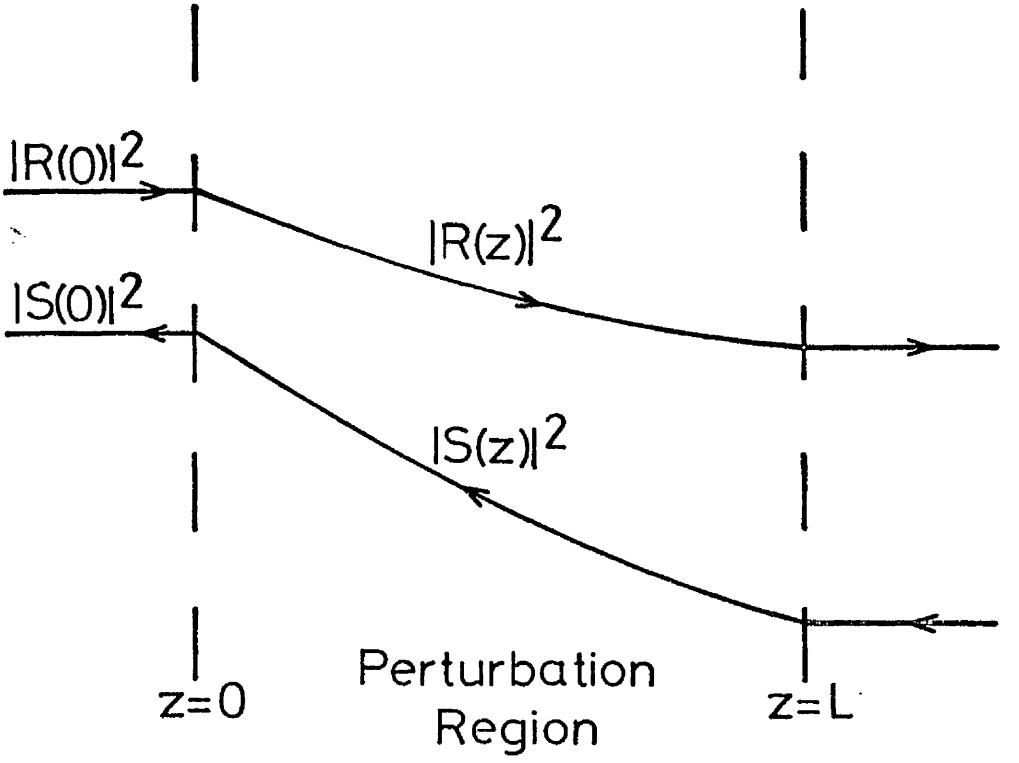

FIG 3.4 Power exchange between two coupled modes under phase-matched condition for contra-directional interaction

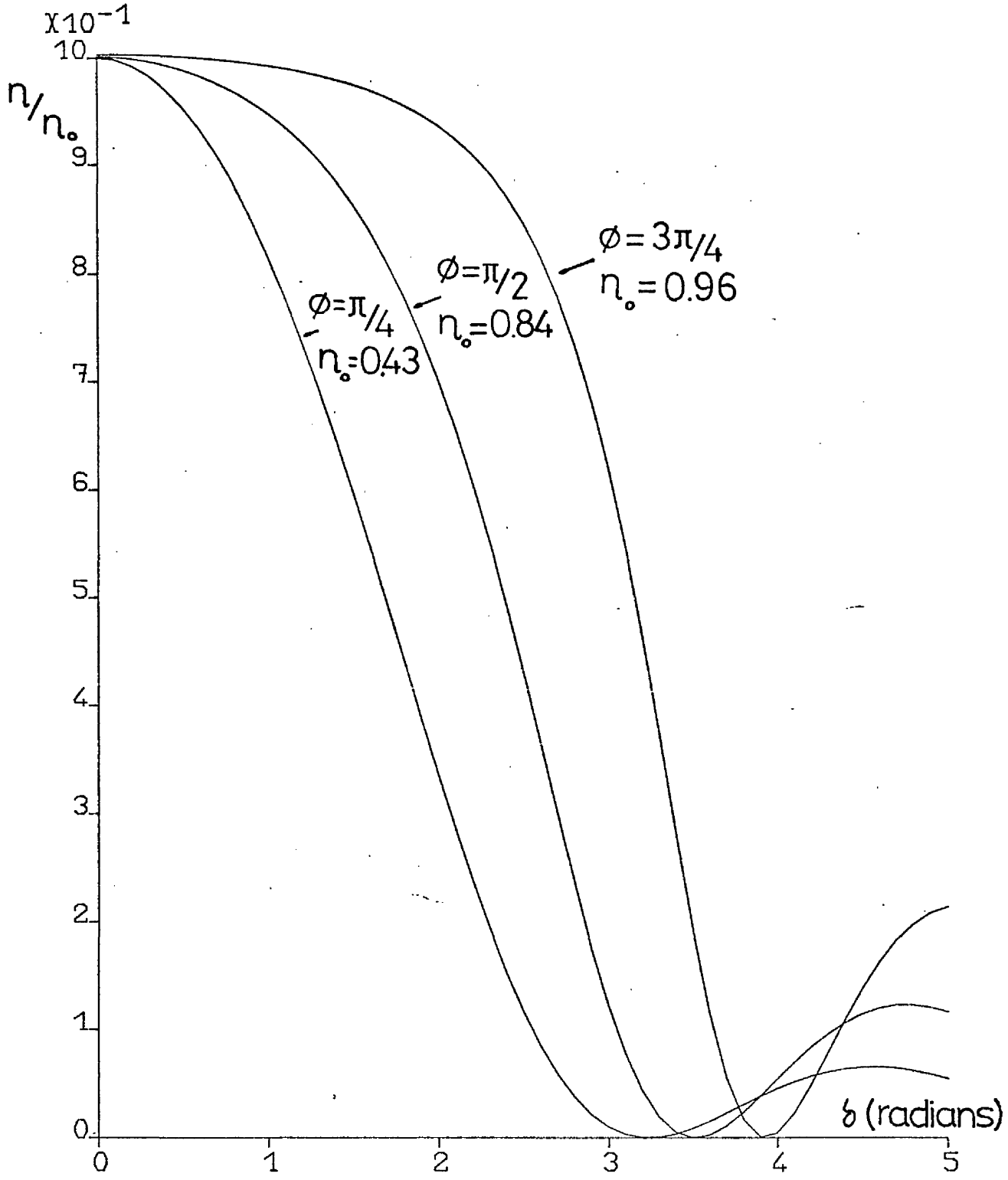

FIG 3.5 Angular sensitivities for contra-directional interaction : normalised efficiency as a function of the off-Bragg parameter δ

as a coupled-mode process. First, only two modes, being approximately synchronous for a given frequency, are identified, and then the coupled-wave solutions given in section 3.2 can be applied.

We start with Maxwell's equations having the form

$$\nabla \times E = -j\omega\mu H \quad , \qquad (3.3.1)$$

$$\nabla \times H = j\omega\epsilon E + j\omega P \quad , \qquad (3.3.2)$$

where the complex amplitude $P(x,y,z)$ represents a distribution of sources exciting various waveguide modes. Using the vector identity $\nabla.(axb) = b.(\nabla xa)-a.(\nabla xb)$, the fields caused by two different induced polarizations P_1 and P_2 are

$$\nabla (E_1 x H_2^* + E_2^* x H_1) = -j\omega P_1 E_2^* + j\omega P_2^* E_1 \quad . \qquad (3.3.3)$$

If we set $P_2 = 0$ and identify the field 2 with a mode of the waveguide, and as in Appendix 3B, integrate over a cross section of the waveguide (z = constant), and apply the divergence theorem, we get

$$\iint_{-\infty}^{\infty} dxdy\,(\partial/\partial z)\,(E_1 x H_2^* + E_2^* x H_1)_z = j\omega \iint_{-\infty}^{\infty} dxdy\; P_1 E_2^* \qquad (3.3.4)$$

The orthogonality of the modes (Appendix 3B) allows us to express the transverse components of the field distribution as a superposition of confined modes,

$$E_{1t} = \sum (a_v+b_v) E_{tv} \quad , \quad H_{1t} = \sum (a_v-b_v) H_{tv} \quad , \qquad (3.3.5)$$

where $a_\nu(z)$ and $b_\nu(z)$ are the coefficients of the forward and backward modes respectively, and are functions of z only. If we choose field 2 as a forward mode (travelling in the +z direction):

$$E_2 = E_\mu e^{-j\beta_\mu z} \quad , \quad H_2 = H_\mu e^{-j\beta_\mu z} \quad . \tag{3.3.6}$$

By substituting (3.3.5) and (3.3.6) into (3.3.4) and applying the orthogonality relation, the b_ν coefficients disappear and we obtain

$$(\partial/\partial z)\ [a_\mu(z)] = -j\omega \iint_{-\infty}^{\infty} dxdy\ P.E_\mu^* \quad . \tag{3.3.7}$$

Similarly, if field 2 is a backward mode,

$$E_2 = E_{-\mu} e^{j\beta_\mu z} \quad , \quad H_2 = H_{-\mu} e^{j\beta_\mu z} \quad , \tag{3.3.8}$$

and we get

$$(\partial/\partial z)\ [b_\mu(z)] = j\omega \iint_{-\infty}^{\infty} dxdy\ P.E_{-\mu}^* \quad . \tag{3.3.9}$$

The above equations are valid only for propagation modes. If we define the amplitudes $A_\mu(z)$ and $B_\mu(z)$ of the forward and backward modes as

$$a_\mu(z) = A_\mu(z) e^{(-j\beta_\mu z)} \quad , \quad b_\mu(z) = B_\mu(z) e^{(j\beta_\mu z)} \quad , \tag{3.3.10}$$

the presence of a polarization source will induce changes to

these amplitudes given by

$$A'_\mu = -j\omega \iint_{-\infty}^{\infty} dxdy\ P.E_\mu^*\, e^{(+j\beta_\mu z)} \quad , \qquad (3.3.11)$$

$$B'_\mu = j\omega \iint_{-\infty}^{\infty} dxdy\ P.E_{-\mu}^*\, e^{(-j\beta_\mu z)} \quad , \qquad (3.3.12)$$

where the prime indicates differentiation with respect to z.

A scalar deformation of the waveguide can be represented by the difference $\Delta\epsilon(x,y,z)$ in the dielectric constant and an induced polarization source of the form

$$P = \Delta\epsilon E \quad . \qquad (3.3.13)$$

Combining (3.3.5) and (3.3.13),

$$P_t = \Delta\epsilon\, E_t = \Delta\epsilon \sum (a_v+b_v) E_{tv} \quad . \qquad (3.3.14)$$

For the E_z component we obtain from (3.3.2)

$$j\omega(\epsilon+\Delta\epsilon)E_z = \nabla_t \times H_t \quad , \qquad (3.3.15)$$

and the expression for P_z is, using (3.3.5), (3.3.15) and (2.1.15)

$$\begin{aligned} P_z = \Delta\epsilon E_z &= [\Delta\epsilon/(\epsilon+\Delta\epsilon)]\,(1/j\omega)\,(\nabla_t \times H_t) \\ &= [\Delta\epsilon/(\epsilon+\Delta\epsilon)]\,(1/j\omega) \sum (a_v-b_v) \nabla_t \times H_{tv} \qquad (3.3.16) \\ &= [\Delta\epsilon.\epsilon/(\epsilon+\Delta\epsilon)] \sum (a_v-b_v) E_{zv} \end{aligned}$$

Hence (3.3.11) and (3.3.12) become

$$A'_\mu = -j\omega\iint_{-\infty}^{\infty} dxdy \sum \{(a_v + b_v)\Delta\epsilon E_{tv}.E_{t\mu}^* + (a_v - b_v)[\Delta\epsilon.\epsilon/(\epsilon+\Delta\epsilon)]\ E_{zv}.E_{z\mu}^*\} e^{j\beta_\mu z}, \quad (3.3.17)$$

$$B'_\mu = j\omega\iint_{-\infty}^{\infty} dxdy \sum \{(a_v + b_v)\Delta\epsilon E_{tv}.E_{tu}^* - (a_v - b_v)[\Delta\epsilon.\epsilon/(\epsilon+\Delta\epsilon)]\ E_{zv}.E_{z\mu}^*\} e^{-j\beta_\mu z}, \quad (3.3.18)$$

Using the symmetry relations ($E_{t2}(z)=E_{t1}(-z)$), $E_{z2}(z)=-E_{z1}(z)$). To simplify further, we introduce tangential and longitudinal coupling coefficients $\chi^t{}_v$ (z) and $\chi^z{}_v$ (z) defined by

$$\chi^t{}_{v\mu} = \omega\iint_{-\infty}^{\infty} dxdy\,\Delta\epsilon E_{tv}.E_{t\mu}^* \quad (3.3.19)$$

$$\chi^z{}_{v\mu} = \omega\iint_{-\infty}^{\infty} dxdy[\Delta\epsilon.\epsilon/(\epsilon+\Delta\epsilon)]\ E_{zv}.E_{z\mu}^* \quad (3.3.20)$$

Using the two coupling coefficients and (3.3.10), (3.3.17) and (3.3.18) become

$$A'_\mu = -j\sum \{A_v(\chi^t{}_{v\mu} + \chi^z{}_{v\mu})e^{-j(\beta_v-\beta_\mu)z} + B_v(\chi^t{}_{v\mu} - \chi^z{}_{v\mu})e^{j(\beta_v+\beta_\mu)z}\} \quad (3.3.21)$$

$$B'_\mu = j\sum \{A_v(\chi^t{}_{v\mu} - \chi^z{}_{v\mu})e^{-j(\beta_v+\beta_\mu)z} + B_v(\chi^t{}_{v\mu} + \chi^z{}_{v\mu})e^{j(\beta_v-\beta_\mu)z}\} \quad (3.3.22)$$

These two expressions are the coupled wave equations for the case of waveguide deformation. For co-directional coupling, by substituting A = A_μ and B = A_v, (3.2.1) and (3.2.2) can be obtained from (3.3.21). Similarly, by substituting A = A_μ and B = B_μ in (3.3.21) and (3.3.22), (3.2.10) and (3.2.11) can be obtained for contra-directional coupling. (3.3.21) and (3.3.22)

indicate the change in the amplitude of each mode (μ) as a function of the deformation $\Delta\epsilon$, the modal field distribution, and of the amplitudes of all other modes present in the guides. Note that the coupling coefficient is expressed in vector form, and is valid for both TE and TM modes.

At this stage, one can make some simplifying assumptions. We assume that only two guided modes are important and that all other modes can be ignored. This leads to the coupled wave interactions described in section 3.2. Another common assumption is that $\Delta\epsilon(x,y,z)$ is only a small perturbation of the dielectric constant $\epsilon(x,y)$ of the waveguide.

3.3.1 Oblique Incidence in Thin Film Periodic Waveguide

Consider a guided TE mode incident obliquely at an angle θ onto a periodic region of a dielectric slab waveguide. The grating vector K is defined as $2\pi/\Lambda$, where Λ is the periodicity of the grating (Fig. 3.6). The interaction between the grating and the incident wave generates another guided TE or TM wave, which moves away from the grating at an angle θ_v. Their propagation constants β_μ, β_v satisfy the well-known grating equation

$$\beta_\mu \cos\theta_\mu + \beta_v \cos\theta_v = K \qquad (3.3.23)$$

$$\beta_\mu \sin\theta_\mu = \beta_v \sin\theta_v \qquad (3.3.24)$$

Using (3.3.21) and (3.3.22), the coupled wave equations for such

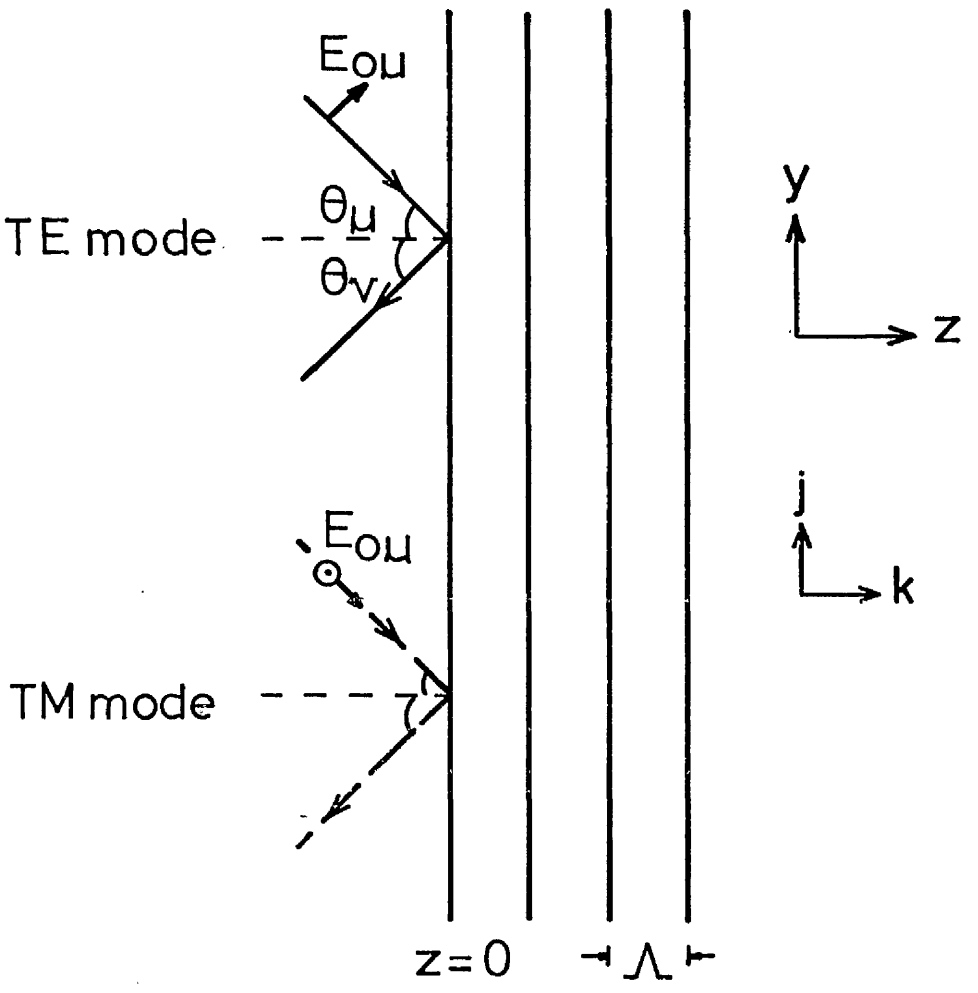

FIG 3.6 Schematic diagram of a wave incident obliquely onto a grating region

a non-collinear case are

$$da_\mu^+/dz + j\beta_\mu \cos\theta \cdot a_\mu^+ = \kappa_{\mu\nu}^{+-} \cdot a_\nu^- \qquad (3.3.25)$$

$$da_\nu^-/dz - j\beta_\nu \cos\theta \cdot a_\nu^- = \kappa_{\mu\nu}^{-+} \cdot a_\mu^+ \qquad (3.3.26)$$

where a_μ^+ ($=A_\mu$) and a_ν^- ($=B_\nu$) are the mode amplitudes ofthe incident and reflected waves respectively, and κ is the coupling constant. These equations have the same form as that described in section 3.2, and the same solutions applied here. The most important parameter, κ, the coupling constant, and its relation to the coupling coefficient, χ, will be described in section 3.4.

3.3.2 Two Dimensional Coupled Wave Formalism

The above coupled wave theory for oblique incidence has also been derived separately by Stegeman et al.[3.18], and Wagatsuma et al.[3.19]. In all of these derivations, the grating (or perturbation) is assumed to extend infinitely in two dimensions so that the field components are dependent only on the single remaining coordinate along which the grating is finite (z-direction in our case). Generally good agreement with experiments has been obtained using this one-dimensional theory, for both diffraction efficiency and angular/wavelength selectivity. However, there is no assessment of the beam quality. To do this, a two-dimensional coupled wave theory[3.20] is used instead (Fig. 3.7).

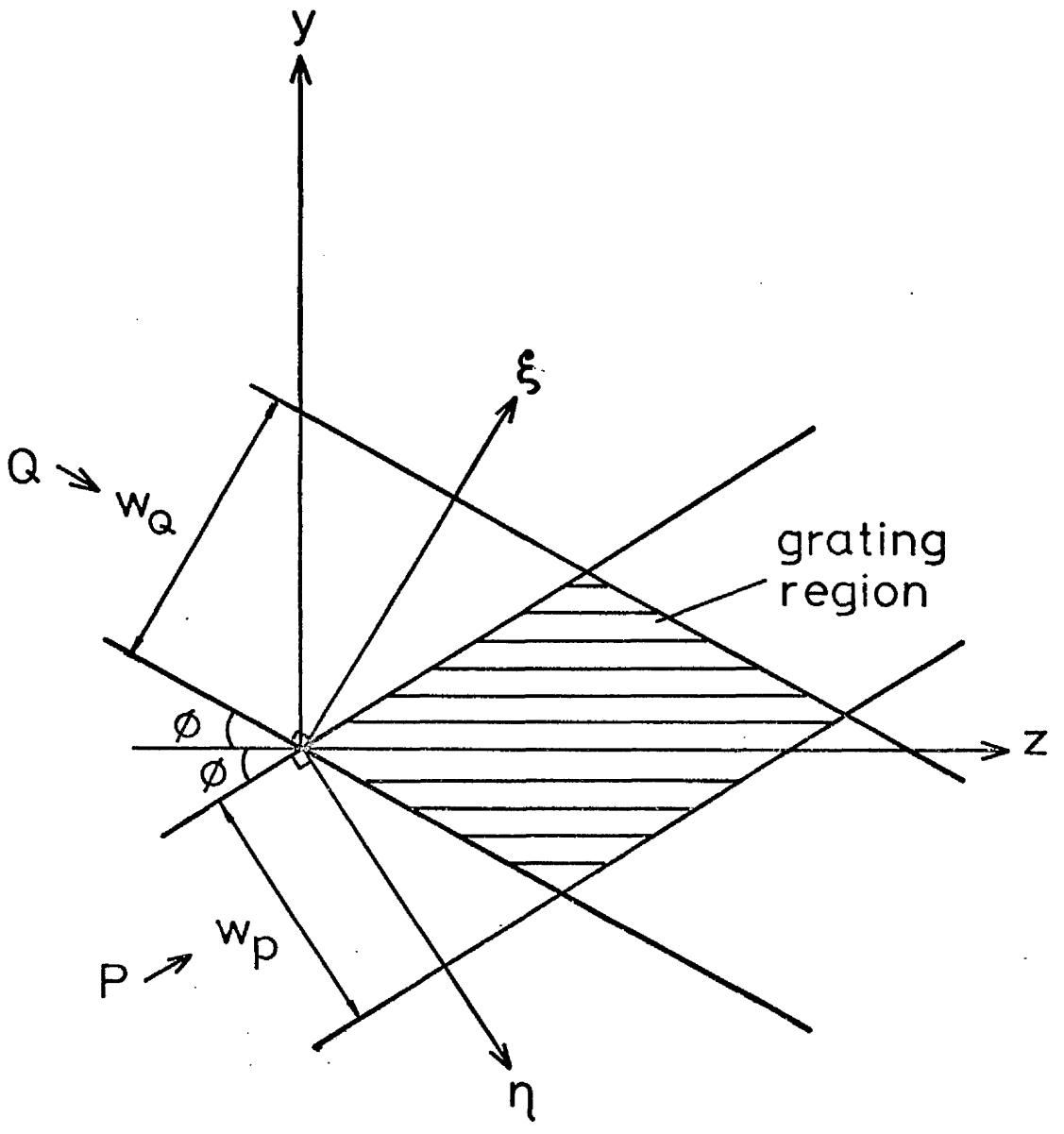

FIG 3.7 The geometry of a grating with finite dimensions

At Bragg incidence, neglecting the phase curvature of the beams (it is common to assume two quasi-plane waves), the total electric field in the grating region can be written as :

$$E(y,z) = P(y,z)e^{-jK_+r} + Q(y,z)e^{jK_-r} \qquad (3.3.27)$$

where $P(y,z)$ and $Q(y,z)$ are the complex amplitudes of the transmitted and diffracted waves, and $r = (x,y,z)$. Here $K_{\pm}r = \beta(\pm y \sin\phi + z\cos\phi)$, β is the propagation wave vector, and ϕ is the Bragg angle. By substituting (3.3.27) into the wave equation

$$\nabla^2 E + k_o^2 n^2(y,z)E = 0 \quad , \qquad (3.3.28)$$

neglecting $\nabla^2 P$ and $\nabla^2 Q$ (assuming energy interchange between P and Q to be slow) and all other waves generated in directions other than K_+ and K_-, together with all other higher diffraction orders, leads to the coupled wave equations (comparing terms with equal exponentials)

$$\cos\phi\,(\partial P/\partial z) + \sin\phi\,(\partial P/\partial y) + j\kappa Q = 0 \qquad (3.3.29)$$

$$\cos\phi\,(\partial Q/\partial z) - \sin\phi\,(\partial Q/\partial y) + j\kappa P = 0 \qquad (3.3.30)$$

where κ is the coupling constant.

To solve (3.3.29) and (3.3.30), we introduce new coordinates ξ, orthogonal to K_-, and η, orthogonal to K_+ (see Fig. 3.7), such that

$$\xi = y\cos\phi + z\sin\phi \qquad (3.3.31)$$

$$\eta = -y\cos\phi + z\sin\phi \quad , \qquad (3.3.32)$$

resulting in a simplified version of the coupled wave equations, with $P(y,z)$ and $Q(y,z)$ being transformed to $P(\xi,\eta)$ and $Q(\xi,\eta)$. The amplitude distribution across the beams are dependent on ξ and η only.

The new equations are :

$$\partial P/\partial\xi + j\chi' Q = 0 \qquad (3.3.33)$$

$$\partial Q/\partial\eta + j\chi' P = 0 \qquad (3.3.34)$$

where $\chi' = \chi/\sin 2\phi$. (3.3.33) and (3.3.34) can be simplified further by one more transformation :

$$u = \chi'\int_0^{\xi} d\xi' \qquad (3.3.35)$$

$$v = \chi'\int_0^{\eta} d\eta' \qquad (3.3.36)$$

and we arrive at the final form of the coupled wave equations :

$$\partial P/\partial u + jQ = 0 \qquad (3.3.37)$$

$$\partial Q/\partial v + jP = 0 \qquad (3.3.38)$$

The equations can be solved once the boundary conditions are specified. The boundary conditions then imply that the function is given on one line and its derivatives on another.

These lines are characteristic of differential equations, in which case Riemann's technique[3.21] is applicable. However, Laplace transformation is used in what follows, and the same results can also be obtained from Solymar's solution[3.21] by properly accounting for the boundary and performing the resulting integration.

The grating boundaries are coordianate lines in the (ξ, η) coordinate system, and we specify the boundary conditons as

$$P(0,\eta) = 1 \quad \text{(a plane wave)} \tag{3.3.39}$$

$$Q(\xi,0) = 0 \tag{3.3.40}$$

Performing the Laplace transform with respect to u,

$$s\hat{P}(s,v) + j\hat{Q} = 1 \tag{3.3.41}$$

$$\partial\hat{Q}(s,v)/\partial v + j\hat{P} = 0 \tag{3.3.42}$$

where s is the transform variable, and tildes indicate the transforms of P and Q. The solution is

$$P(u,v) = J_o(2\sqrt{uv}) \tag{3.4.43}$$

$$Q(u,v) = j\sqrt{v/u}\, J_1(2\sqrt{uv}) \tag{3.4.44}$$

The intensity profiles for the transmitted and diffracted beams for various values of w_o $(=2\lambda'\sqrt{W_P W_Q})$ are plotted in Figs. 3.8 and 3.9 respectively. The intensity distribution

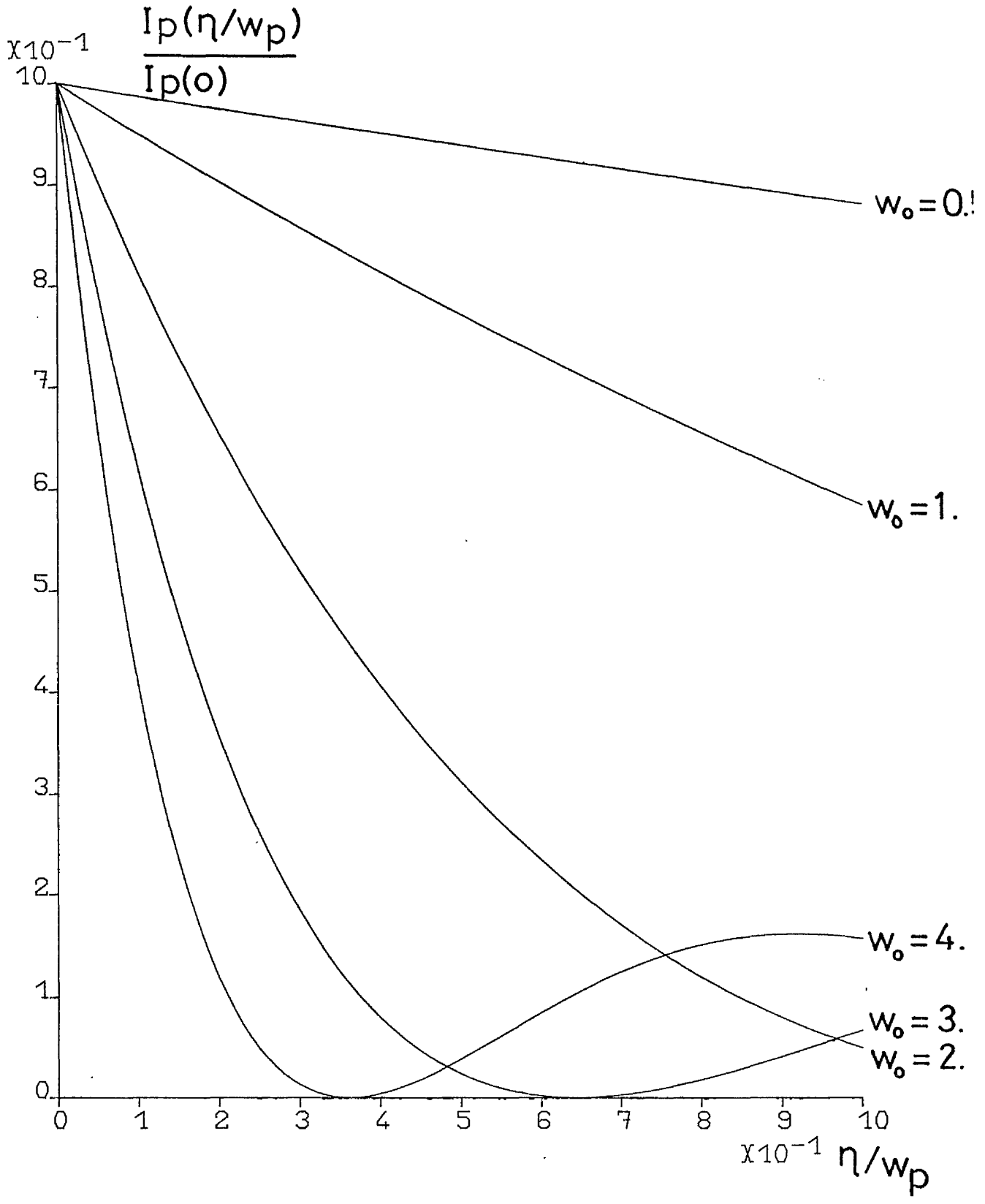

FIG 3.8 Normalised intensity profiles for the transmitted beam for various values of w_o

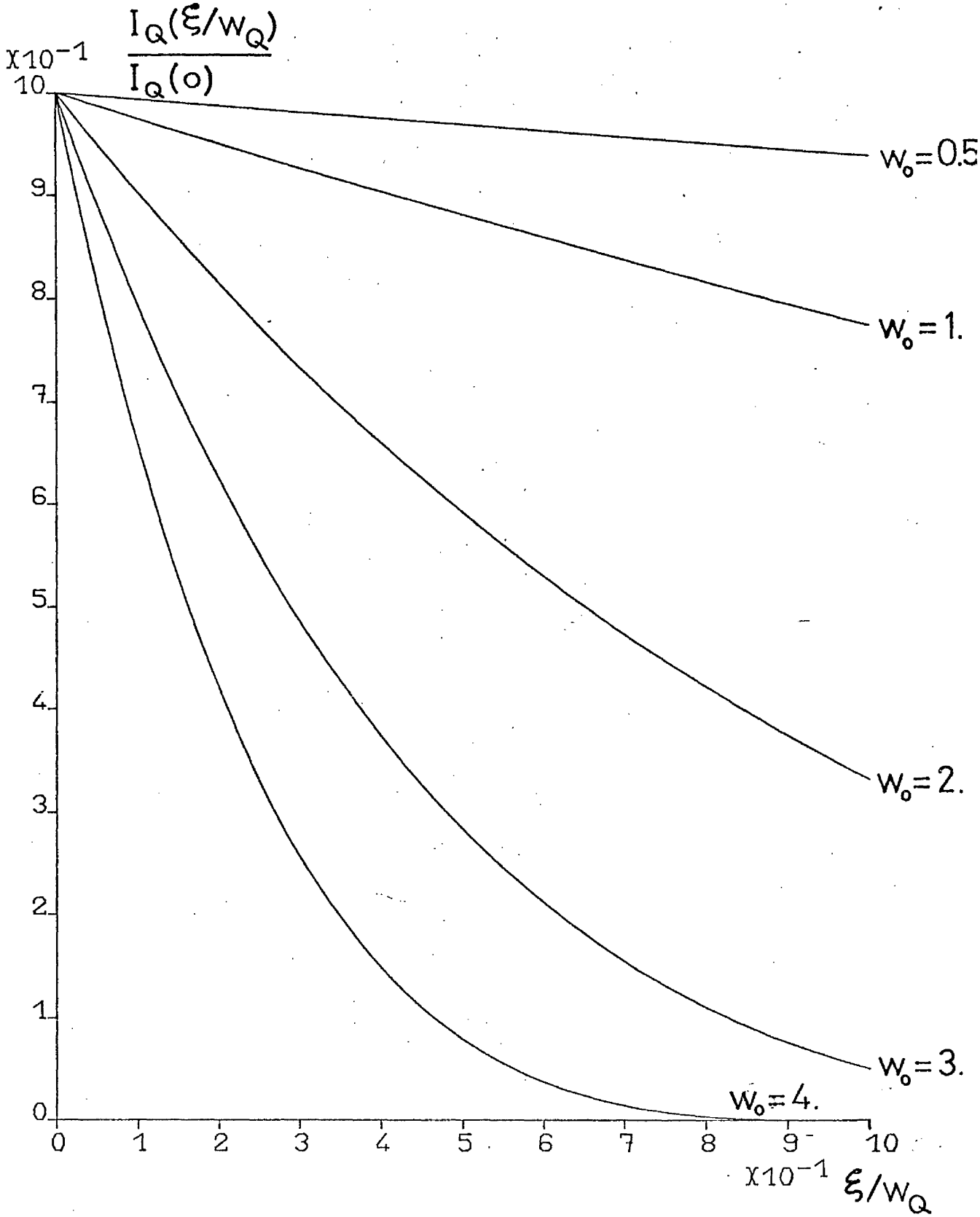

FIG 3.9 Normalised intensity profiles for the diffracted beam for various values of w_o

is uniform (resembling the original beam) at first, but, as the coupling increases, there is variation across the beam, for both the diffracted and transmitted beams.

The powers in the input and output beams are

$$P^P_{in} = \int_{\xi=0} d\xi = W_P \tag{3.3.45}$$

$$P^P_{out} = \int_0^{\omega_P} J_o^2(2\chi'\sqrt{uW_Q})\,du = W_P[J_o^2(w_o)+J_1^2(w_o)] \tag{3.3.46}$$

$$P^Q_{out} = \int_0^{\omega_Q} (W_P/v)J_1^2(2\chi'\sqrt{W_P v})\,dv = W_P[1-J_o^2(w_o)-J_1^2(w_o)] \tag{3.3.47}$$

It can be seen that power is conserved. The diffraction efficiency $E(w_o)$ is

$$E(w_o) = 1 - J_o^2(w_o) - J_1^2(w_o) \tag{3.3.48}$$

The right hand side of $E(w_o)$ is a non-decreasing function of w_o having horizontal tangents at the zeros of $J_1(w_o)$, Figs. 3.10 and 3.11. It therefore has a character in between Kogelnik's reflection holograms, whose efficiency is an increasing function, having no horizontal tangents, and transmission holograms, which have oscillating efficiency functions, with periodic horizontal tangents. One hundred per cent efficiency is not possible, since the diffracted beam breaks up.

Also note that the same efficiency will be obtained if the coupling constant and the product $W_P W_Q$ are the same (Fig. 3.12). This seems odd at first. The reason is because of the

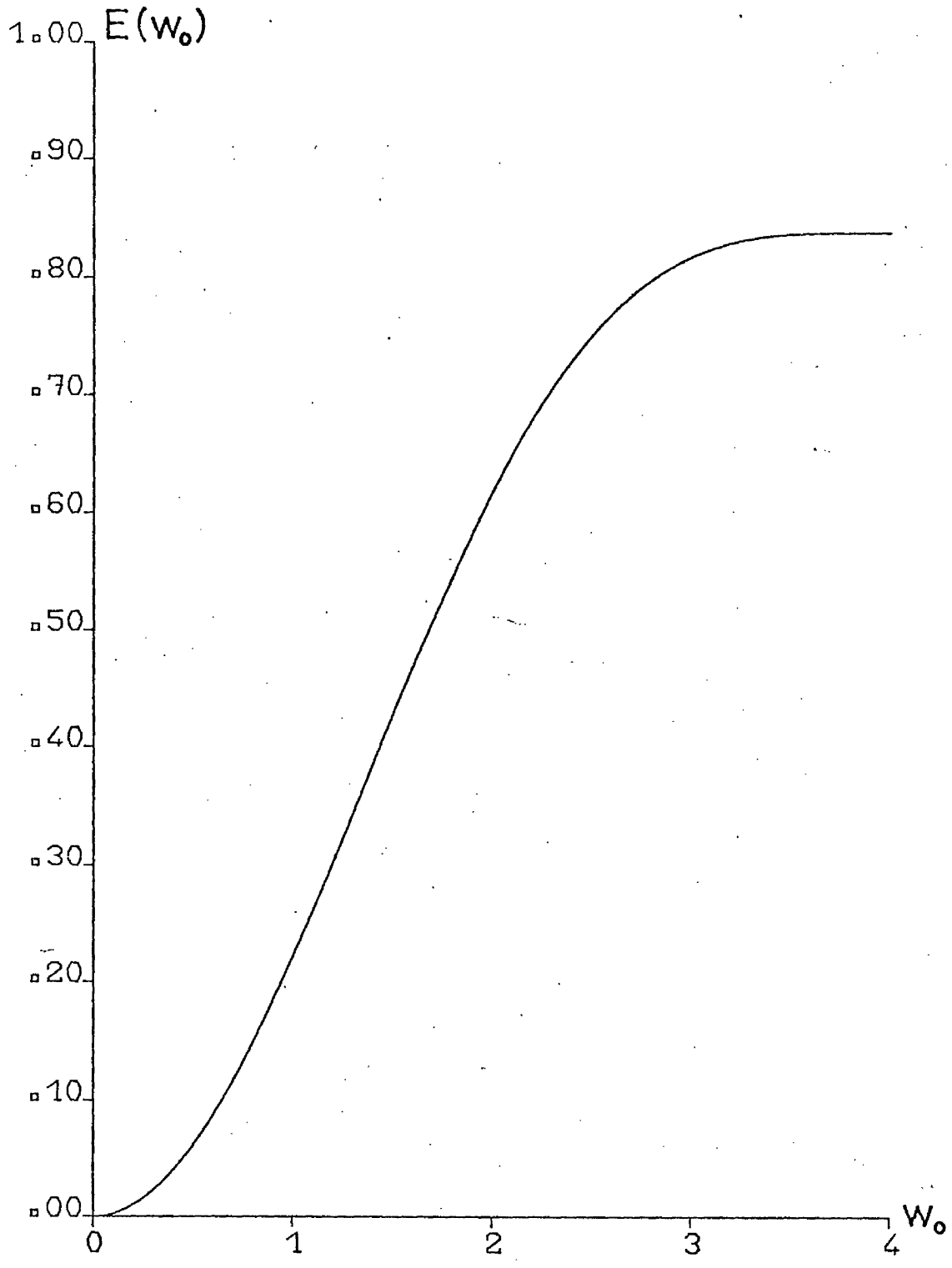

FIG 3.10 The diffraction efficiency $E(w_o)$ for $0 \leq w_o \leq 4$

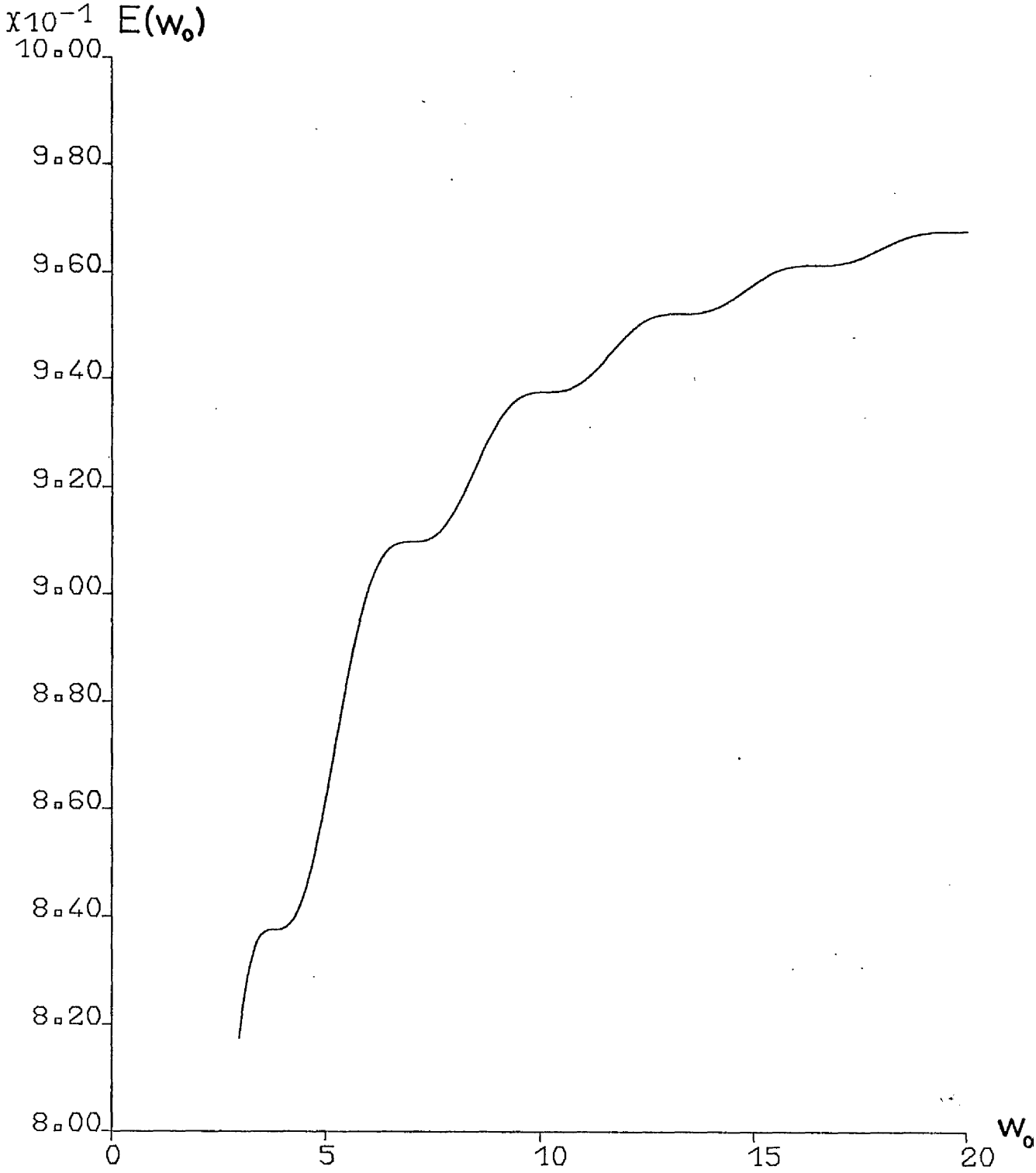

FIG 3.11 The diffraction efficiency $E(w_0)$ for $3 \leq w_0 \leq 20$. The appearance of a horizontal tangent signals the appearance of a "hole" in the diffracted beam

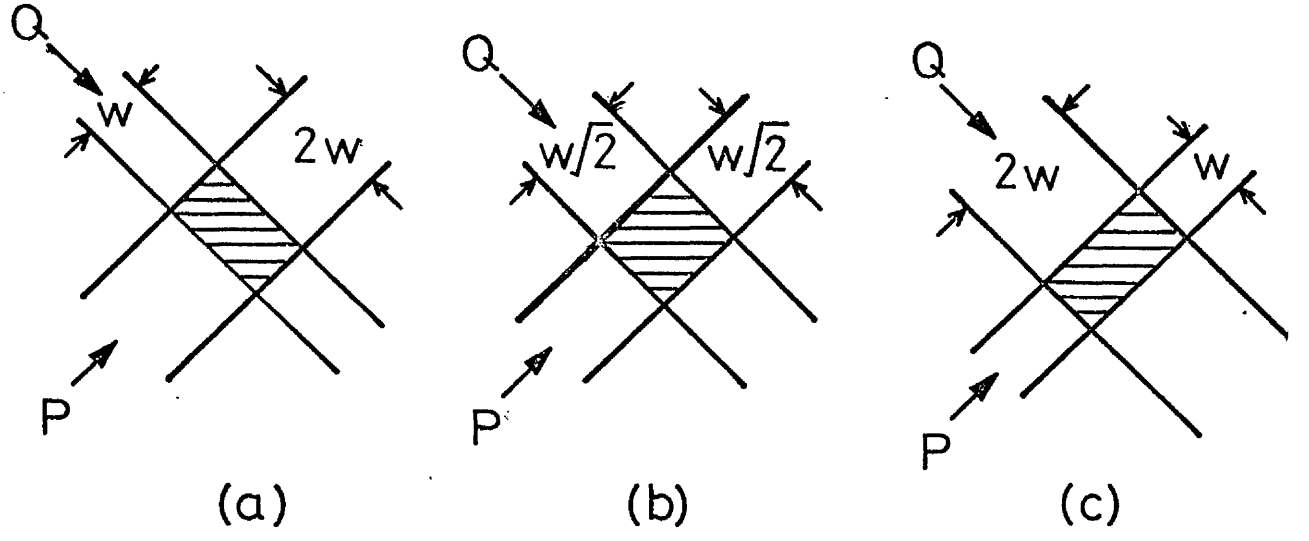

FIG 3.12 Diffracted and transmitted beams having different widths : (a) $w_p = w_Q 2$ (b) $w_p = w_Q$ (c) $w_p 2 = w_Q$. If the coupling coefficient is the same for all three cases, the diffraction efficiency will be the same

phase shift $\pi/2$ imparted to the diffracted beam by the grating. The diffracted beam produced by the first scattering would be scattered out into the original direction in a second scattering event (the grating will scatter light in both directions, Fig. 3.13). However, this second scattering produces a beam which is out of phase with the straight through beam, and reduces the total output amplitude. Hence the efficiency in Fig. 3.12(a) is not higher than that in Fig. 3.12(b) or 3.12(c).

3.4 Coupling Coefficient

In this section, the coupling coefficient (and constant) will be evaluated explicitely, with the help of (3.3.19) to (3.3.22).

3.4.1 Coupling Constants of Corrugated Waveguides

We first discuss the case of a corrugated planar slab waveguide. The periodically varying film thickness can be represented by (Fig. 3.14)

$$h(z) = T + \Delta h \cos(Kz) \quad , \qquad (3.4.1)$$

where K ($= 2\pi/\Lambda$) is the grating vector, Λ is the period, and T is the film thickness without the corrugation. Combining (3.3.19) and (3.3.20), the coupling coefficient per unit width along the y-direction can be written as

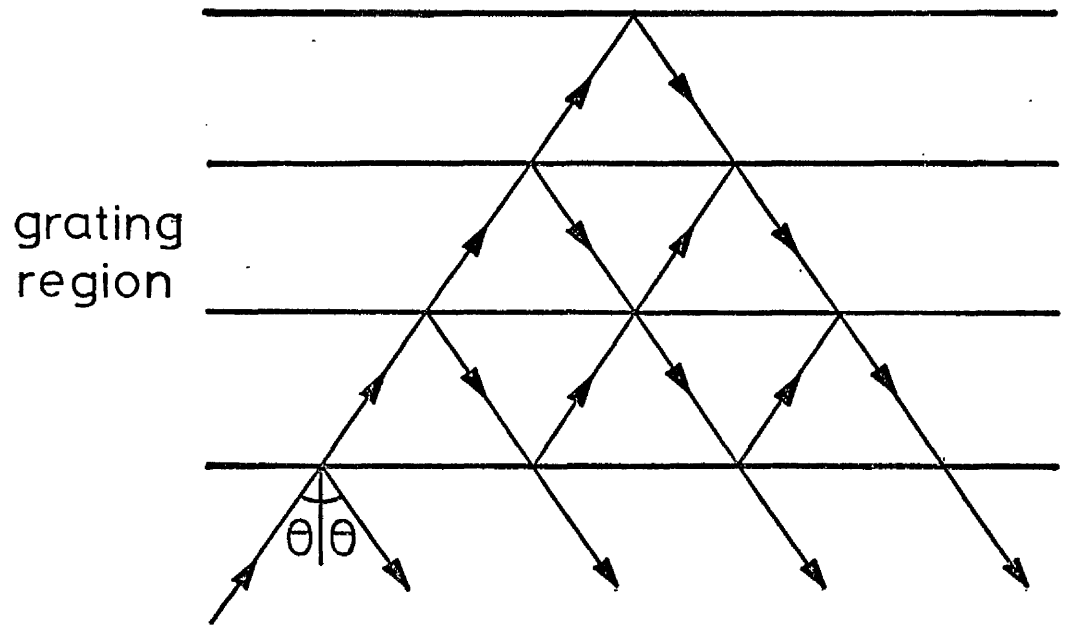

FIG 3.13 Oblique incidence of a wave onto a grating region showing Bragg scattering (multiple reflections) inside the region

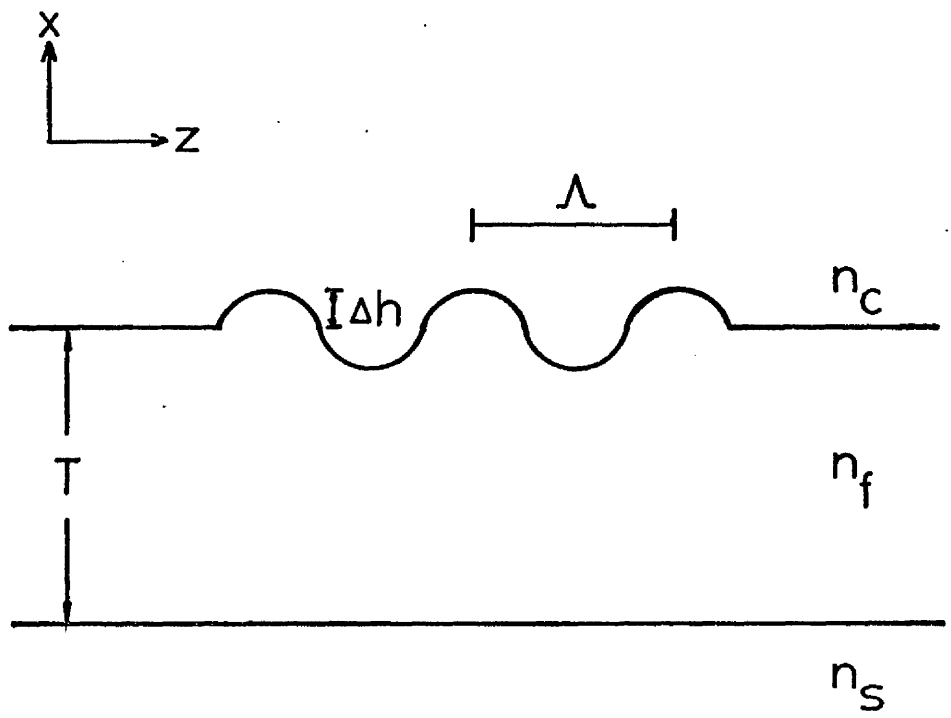

FIG 3.14 Cross section of a corrugated slab waveguide. T is the film thickness, Δh is the amplitude of the corrugation, and Λ is the period

$$\chi_{\mu\nu} = \omega \int dx\, \Delta\epsilon [E_{tv} E_{t\mu}^{*} + (\epsilon/[\epsilon+\Delta\epsilon]) E_{zv} E_{z\mu}^{*}] \quad . \qquad (3.4.2)$$

By expressing $\Delta\epsilon$ in terms of the refractive indices n(x) and $n_o(x)$ of the perturbed and unperturbed waveguide, and integrating only in the x-direction, (because in planar guides the light is confined in one dimension only, and the corresponding modal fields are functions of this coordinate only), $\chi_{\mu\nu}$ becomes

$$\chi_{\mu\nu} = \epsilon_o \omega \int \{ (n^2 - n_o^2) [E_{tv} E_{t\mu}^{*} + (n_o^2/n^2) E_{zv} E_{z\mu}^{*}] \} dx \quad . \qquad (3.4.3)$$

The relation of $\chi_{\mu\nu}(z)$ to the coupling constant χ of the coupled wave equations is

$$\begin{aligned} \chi_{\mu\nu} &= \omega\epsilon_o \int \{ (n^2 - n_o^2) [E_{tv} E_{t\mu}^{*} + (n_o^2/n^2) E_{zv} E_{z\mu}^{*}] \} dx . \Delta h \cos(Kz) \\ &= \chi [e^{(jKz)} + e^{(-jKz)}] \quad . \qquad (3.4.4) \end{aligned}$$

Hence the normalised coupling constant $\overline{\chi_{uv}}$ (= $\chi_{\mu\nu}$/ P, P is the power per unit length along the y-direction) is, using (3.4.3), (3.4.4) and (2.1.33),

$$\overline{\chi_{\mu\nu}} = \omega^2 \epsilon_o \mu_o / 2\beta \cdot \{ \int (n^2 - n_o^2) [E_{tv} E_{t\mu}^{*} + (n_o^2/n^2) E_{zv} E_{z\mu}^{*}] dx / \int E_y^2 dx \} \quad .... (3.4.5)$$

The difference $n^2 - n_o^2$ is non-zero only in the region $-\Delta h < x < \Delta h$. When the grating surface bulges outward from the mean surface (x=0), $n^2 - n_o^2 = n_f^2 - n_c^2$ and $n_o^2/n^2 = n_c^2/n_f^2$; when the grating surface bulges inward, $n^2 - n_o^2 = n_c^2 - n_f^2$ and $n_o^2/n^2 = n_f^2/n_c^2$. It is apparent that the doubled-valued ratio n_o^2/n^2 will cause a

problem in (3.4.5). In our analysis we follow Marcuse's work[3.22] and approximate n_o^2/n^2 by the geometric mean (which is unity in this case) of its two values.

For collinear incidence, the direction of propagation is parallel to the grating vector, and the E field of the TE mode is perpendicular to the E fields of the TM mode, and there is no mode conversion.

For oblique incidence, by defining the unit vectors $\vec{i}$, $\vec{j}$, $\vec{k}$ along the coordinate axes x, y and z, the electric fields are (Fig. 3.6)

TE mode
$$E_{t\mu} = \vec{j}\, E_{o\mu}\cos\Theta_\mu\, e^{(-j\beta_\mu Y \sin\Theta_\mu)} \quad , \qquad (3.4.6)$$

$$E_{z\mu} = -\vec{k}\, E_{o\mu}\sin\Theta_\mu\, e^{(-j\beta_\mu Y \sin\Theta_\mu)} \quad , \qquad (3.4.7)$$

TM mode
$$E_{t\mu} = [(\vec{i}\beta_\mu/\omega\epsilon_o n_o^2)H_{o\mu} + (\vec{j}/j\omega\epsilon_o n_o^2)(\partial H_{o\mu}/\partial x)\sin\Theta_\mu] \cdot e^{(-j\beta_\mu Y \sin\Theta_u)} \quad , \qquad (3.4.8)$$

$$E_{z\mu} = [\vec{k}/j\omega\epsilon_o n_o^2 (\partial H_{o\mu}/\partial x)\cos\Theta_\mu] e^{(-j\beta_\mu Y \sin\Theta_\mu)} \quad . \qquad (3.4.9)$$

By substituting the appropriate E vector components into (3.4.5), the normalised coupling constants for the cases TE-TE, TE-TM and TM-TM are :

$$\overline{\kappa}_{\mu\nu}(\text{TE-TE}) = \frac{k_o^2 \cos(\Theta_\mu + \Theta_\nu) \int_{-\infty}^{\infty} \Delta n^2 E_{o\mu} E_{ov}^* dx}{2j(\beta_\mu\cos\Theta_\mu \cdot \beta_\nu\cos\Theta_\nu)\left[\int_{-\infty}^{\infty} E_{ov}^2 dx \int_{-\infty}^{\infty} E_{o\mu}^2 dx\right]^{1/2}} \quad .... \quad (3.4.10)$$

$$\overline{\kappa_{\mu\nu}(\text{TE-TM})} = \frac{-k_o\left(\frac{\beta_\mu}{\beta_\nu}\right)^{1/2}\sin(\theta_\mu+\theta_\nu)}{2(\cos\theta_\mu\cos\theta_\nu)} \frac{\int_{-\infty}^{\infty}\Delta n^2 E_{o\nu}{}^{*}\left(\frac{1}{\beta_\mu}\frac{1}{n_o^2}\frac{\partial H_{o\mu}}{\partial x}\right)dx}{\left[\int_{-\infty}^{\infty}E_{o\nu}{}^2dx\int_{-\infty}^{\infty}H_{o\mu}{}^2/n_o{}^2dx\right]^{1/2}} \quad \ldots\ldots (3.4.11)$$

$$\overline{\kappa_{uv}(\text{TM-TM})} = \frac{(\beta_\mu\beta_\nu)^{1/2}\int_{-\infty}^{\infty}\Delta n^2\left[\left(\frac{H_{o\mu}}{n_o^2}\right)\left(\frac{H_{o\nu}^{*}}{n_o^2}\right)-\cos(\theta_\mu+\theta_\nu)\frac{1}{\beta_\mu}\frac{1}{\beta_\nu}\left(\frac{1}{n_o^2}\frac{\partial H_{o\mu}}{\partial x}\right)\left(\frac{1}{n_o^2}\frac{\partial H_{o\nu}}{\partial x}\right)\right]}{2j(\cos\theta_\mu\cos\theta_\nu)^{1/2}\left[\int_{-\infty}^{\infty}\frac{H_{o\mu}^2}{n_o^2}dx.\int_{-\infty}^{\infty}\frac{H_{o\nu}^2}{n_o^2}dx\right]^{1/2}} \quad \ldots\ldots (3.4.12)$$

where $\Delta n^2=n^2-n_o{}^2$, $k_o=2\pi/\lambda_o$, λ_o is the free space wavelength. The coupling constants above can be evaluated by inserting the field expressions derived in chapter 2 (Appendix 3C).

In Figs. 3.15 and 3.16, we plot the normalised coupling constant as a function of film thickness and incidence angle respectively. Waveguide parameters such as film index and substrate index ~~and corrugation depth $2\Delta h$~~ are listed in the figures. As expected, the coupling constant becomes zero for TE-TE coupling at 45^o. The TM-TM coupling can also be zero, depending on the waveguide parameters. By examining these curves, the influence of different parameters can be explored so as to allow optimised design of the grating devices.

3.4.2 Coupling Constants of Periodic Index Waveguides

Assuming that the tranverse distribution of the refractive index along the z-coordinate normal to the lines of the grating (along the grating vector) is a function of f(z), then

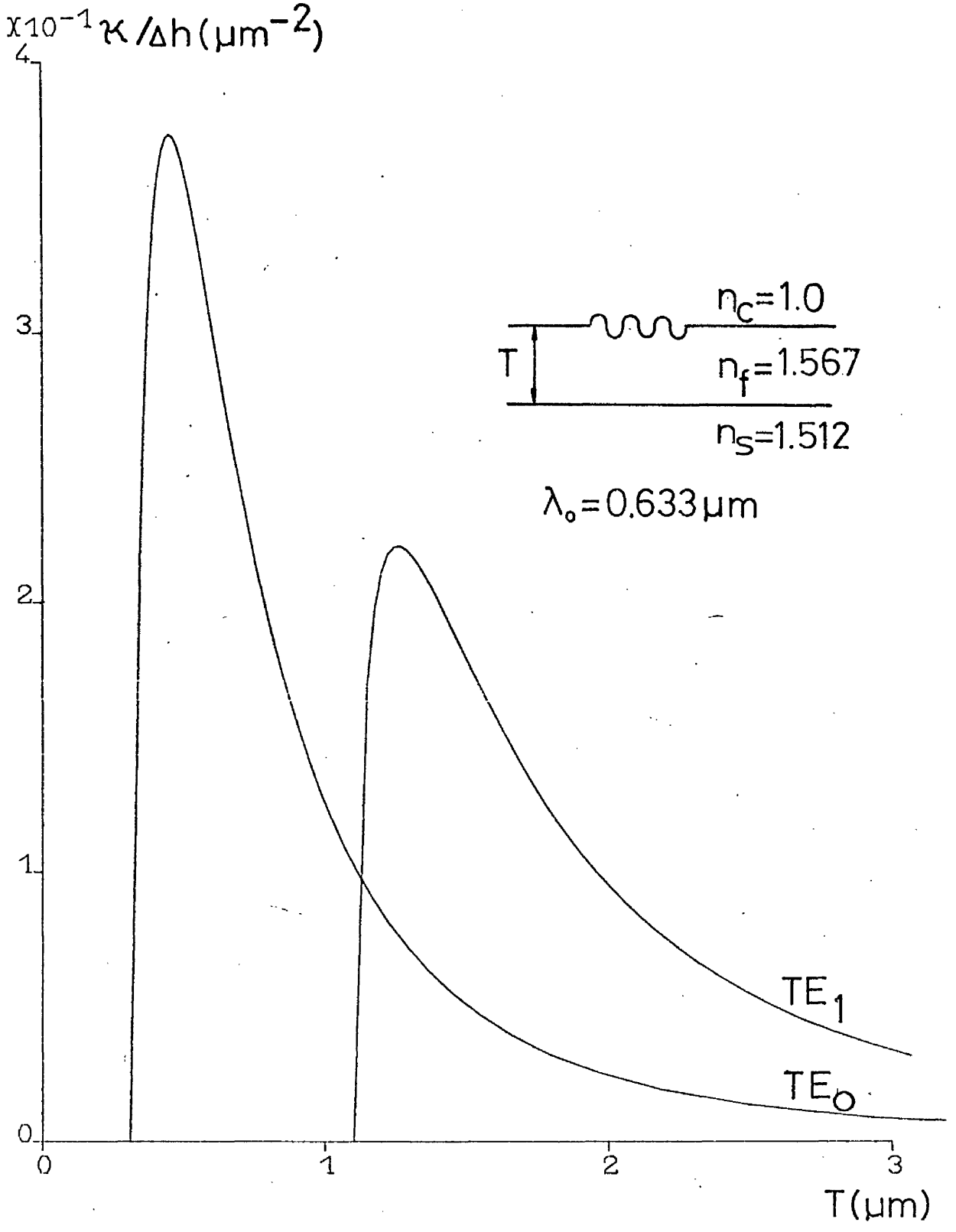

FIG 3.15 Coupling coefficient as a function of waveguide thickness for the two lowest order modes ($\theta = 0^\circ$)

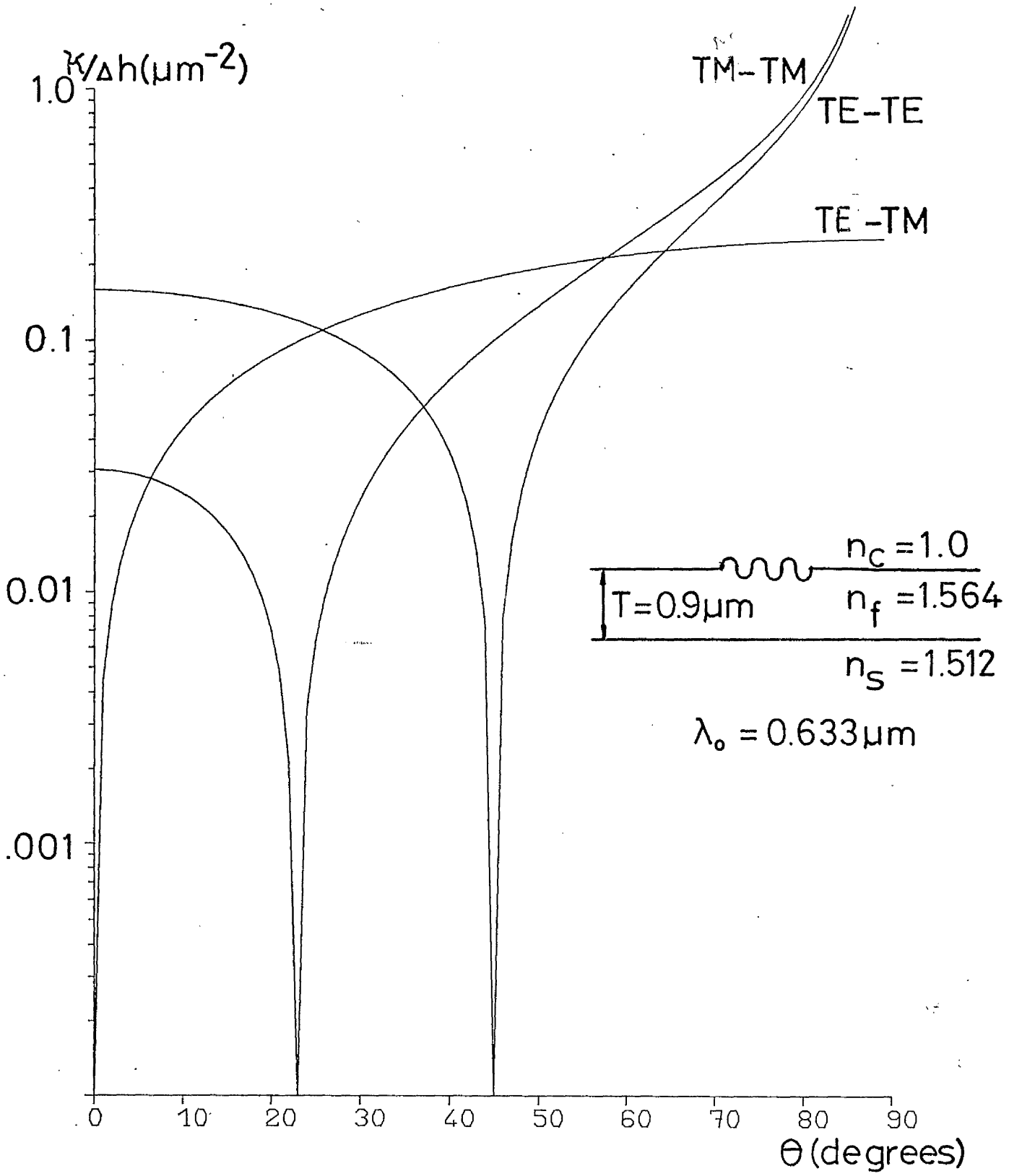

FIG 3.16 Coupling coefficient of a three-layered corrugated waveguide as a function of incidence angle θ

$$n(x,z) = n_{substrate} + [\Delta n\ f(z)]v(x) \qquad (3.4.13)$$

where Δn is the amplitude of the spatial modulation. $v(x)$ takes into account the variation of the refractive index change normal to the plane of the waveguide (for an inhomogeneous waveguide).

$n(x,z)$ can be expanded in a Fourier series as

$$n(x,z) = n_{substrate} + \Delta n_o + v(x) \sum_{m=1}^{\infty} n_m \cos[2\pi/(\Lambda/m)]z \qquad (3.4.14)$$

where n_m is the m^{th} Fourier component of the grating. Since only the fundamental Fourier component is instrumental in the firsr order Bragg diffraction, we can neglect all higher harmonics terms, and (3.4.14) can be written as

$$n(x,z) = (n_{substrate} + \Delta n_o) + v(x)\overline{\Delta n} \cos(2\pi/\Lambda)z \quad . \qquad (3.4.15)$$

We are concerned with TE modes only, and the normalised coupling constant can be obtained by substituting (3.4.15) into (3.4.10),

$$\overline{\kappa_{uv}} = \frac{\pi}{\lambda_o} \frac{n_{average}}{N} \frac{\cos 2\theta\, \overline{\Delta n} \int_{-T}^{0} v(x) E_y^2 dx}{\cos\theta \int_{-\infty}^{\infty} E_y^2 dx}$$

$$= \frac{\pi}{\lambda_o} \frac{n_{average}}{N} \frac{\cos 2\theta \overline{\Delta n}\, c}{\cos\theta} = \frac{\cos 2\theta \overline{\Delta n}\, k\, \pi}{\cos\theta\ \lambda_o} \qquad (3.4.16)$$

where N is the effective index, $n_{average} = n_o + \Delta n_o$ as defined in (3.4.14), c is defined as the overlap integral constant (a

measure of the overlap between the TE fields across the refractive index variation) and has a value between zero and one, and $k = (n_{average}/N)c$.

A similar expression has also been derived by Kenan[3.23]. For a well guided mode in a uniform slab waveguide ($v(x) = 1$, $n_{average} = n_f$)

$$\overline{\chi_{\mu\nu}} = \frac{\pi \overline{\Delta n}\, N_f \cos 2\theta}{\lambda_0\, N \cos\theta} \tag{3.4.17}$$

3.5 Conclusions

In this chapter we have discussed in detail the coupled wave formalism used in the analysis of the Bragg deflectors fabricated in our experiments. Both one-dimensional and two-dimensional coupled wave equations have been derived, and their solutions presented.

Appendix 3A

The wave equation in a symmetrically periodic medium is of the form.

$$d^2\psi/dz^2 + f(z)\psi = 0 \tag{1}$$

$$f(z) = f(z+2\pi/K) = \sum_{n=0}^{\infty} a_n \cos(nKz) \tag{2}$$

where a_n are related to the Fourier coefficients of the periodicity function and to the wavenumber $k_o = 2\pi/\lambda_o$, λ_o is the free space wavelength and $\Lambda = 2\pi/K$ is the period of the medium. a_o is also related to the transverse wave vector whenever it exists. The solution of (1) are the Hill functions of which Mathieu's functions are a special case (when $a_n = 0$ for $n \neq 0, 1$). The Hill equation also applies for f(z) odd. The general solution is in a Floquet form

$$\psi = A(z)\, e^{j\beta z} \tag{3}$$

where A(z) is a periodic function, and β, which is single-valued function of the a_n's, is the propagation wave vector. The periodic function A(z) can be expanded in a Fourier series, and the solution then is

$$\psi = \sum_{n=-\infty}^{n=+\infty} A_n\, e^{j(\beta+nK)z} \tag{4}$$

The different components of ψ are called the space harmonics of the propagation wave. The space harmonics do not

exist independently. They are part of a total solution.

Substituting (4) into (1), one obtains

$$\sum_n [-(\beta+nK)^2 A_n + 1/2 \sum_m a_m (A_{n-m}+A_{n+m})] . e^{[j(\beta+nK)z]} = 0 \qquad (5)$$

Since the above relation must hold for any value of z, (5) reduces to an infinite set of homogeneous equations

$$-2(\beta+nK)^2 A_n + \sum_m a_m (A_{n-m}+A_{n+m}) = 0 \quad , \; n = 0, +1 \; .. \qquad (6)$$

which can be written in a matrix form

$$\left| M \right| \cdot \left| A \right| = 0 \qquad (7)$$

The solution will be non-trival if the determinant of the Hill's matrix is zero, i.e.,

$$\det \left| \left| M \right| \right| = 0 \qquad (8)$$

This is the dispersion relation which gives the value of β as a function of the a_n's. The solution of (7) would then give the relative values of the space harmonics, that is, A_n/A_o. The value of A_o is determined from the boundary condition.

Appendix 3B

For a lossless, source-free scalar medium, (3.3.3) becomes

$$\nabla \cdot (E_1 \times H_2^* + E_2^* \times H_1) = 0 \qquad (1)$$

If we separate E and H into longitudinal fields components and transverse field components relative to the direction of the waveguide axis (z-axis in this case), (1) becomes

$$\nabla_t \cdot (E_1 \times H_2^* + E_2^* \times H_1)_t + \nabla_z \cdot (E_1 \times H_2^* + E_2^* \times H_1)_z = 0 \quad , \qquad (2)$$

where $\nabla_t = (\partial/\partial x, \partial/\partial y, 0)$ is the transverse del operator, and $\nabla_z = (0, 0, \partial/\partial z)$ is the longitudinal del operator.

The next step is to integrate over a cross section of the waveguide (z=constant), and applying the divergence theorem to the first term we get

$$\iint_{-\infty}^{\infty} dxdy \nabla_t \cdot (E_1 \times H_2^* + E_2^* \times H_1)_t = \oint_C ds (E_1 \times H_2^* + E_2^* \times H_1)_t \cdot e_t \quad , \qquad (3)$$

where e_t is the unit vector perpendicular to the curve enclosing the waveguide (the line integral). If one of the two modes is a guided mode with field decaying exponentially towards infinity, the line integral becomes zero. Hence after integration the remaining terms are

$$\iint_{-\infty}^{\infty} dxdy (\partial/\partial z) (E_{t1} \times H_{t2}^* + E_{t2}^* \times H_{t1}) = 0 \quad . \qquad (4)$$

If we assume further that the two forward modes have different propagation constants, that is, $\beta_1 \neq \beta_2$, then we can drop $\partial/\partial z$, and (4) becomes

$$\iint_{-\infty}^{\infty} dxdy\,(E_{t1} \times H_{t2}^{*} + E_{t2}^{*} \times H_{t1}) = 0 \quad , \beta_1 \neq \beta_2 \quad . \qquad (5)$$

Using the z-reversal symmetry, the fields of the backward travelling modes are

$$E(-z) = E(z) \quad , \quad H(-z) = H(z) \qquad (6)$$

and (4) becomes

$$\iint_{-\infty}^{\infty} dxdy\,(E_{t1} \times H_{t2}^{*} - E_{t2}^{*} \times H_{t1}) = 0 \quad , \beta_1 \neq \beta_2 \quad . \qquad (7)$$

Adding (4) and (7) we obtain the simple orthogonality relation

$$\iint_{-\infty}^{\infty} dxdy\,(E_{t1} \times H_{t2}^{*}) = 0 \quad , \beta_1 \neq \beta_2 \quad . \qquad (8)$$

Appendix 3C

TE-TE Coupling

As shown in Fig. 3.14, $\Delta\epsilon = \begin{cases} \epsilon_o(n_f^2 - n_c^2) & , \quad h(z) > T. \\ -\epsilon_o(n_f^2 - n_c^2) & , \quad h(z) < T. \end{cases}$ (1)

Inserting (1) into (3.4.10), assuming Δh is small so that we can replace $E_y(x)$ by the constant field E_c at the film-cladding interface,

$$\overline{\chi_{\mu\nu}} = \frac{\pi \Delta h \cos 2\theta \, (n_f^2 - n_c^2) E_c^2}{\lambda_o \cos\theta \, N_e \int_{-\infty}^{\infty} E_y^2 dx} \tag{2}$$

From (2.1.32) and (2.1.33) we get the normalised value of E_c, and

$$\overline{\chi_{\mu\nu}} = \frac{\pi \Delta h \cos 2\theta \, (n_f^2 - n_c^2) E_c^2}{\lambda_o \cos\theta \, N_e \, E_f^2 T_e} \tag{3}$$

$$= \frac{\pi \Delta h \cos 2\theta \, (n_f^2 - N_e^2) E_f^2}{\lambda_o \cos\theta \, N_e \, E_f^2 T_e} \tag{4}$$

$$= \frac{\pi \Delta h \, (n_f^2 - N_e^2) \cos 2\theta}{\lambda_o \, N_e \, T_e \, \cos\theta} \tag{5}$$

TE-TM Coupling

$\partial H/\partial x$ (which is E_z) is continuous across the film-cladding boundary, and we can use the same procedure as above, by replacing $\partial H/\partial x$ with a constant value H_c. Using (2.1.5) and (2.1.37),

$$\frac{\partial H}{\beta \, n_o^2 \, \partial x} = \frac{H_c (N_m^2 - n_c^2)^{1/2}}{N_m \, n_c^2} \tag{6}$$

$$\overline{\chi_{\mu\nu}} = \frac{H_f (n_f^2 - N_m^2)^{1/2} (N_m^2 - n_c^2)^{1/2}}{(n_f^2 - n_c^2)^{1/2} (q_c)^{1/2} \; n_c \; N_m} \qquad (7)$$

Hence combining (5),(7) and (2.1.44), we get, after some algebra

$$\overline{\chi_{\mu\nu}} = \frac{\pi \Delta h \; \sin 2\theta \, (N_m)^{1/2} (n_f^2 - N_m^2)^{1/2} \; (n_f^2 - N_e^2)^{1/2} \; (N_m^2 - n_c^2)^{1/2}}{\lambda_o \; \cos\theta \, (N_e)^{1/2} \qquad (q_c T_e T_m)^{1/2} \; n_c N_m} \qquad (8)$$

TM-TM Coupling

The $H_{o\mu}/n_o^2$ (E_x) component is discontinuous across the film-cover boundary, which leads to the appearance of higher harmonics in $\overline{\chi_{\mu\nu}}$. We neglect them by defining $\overline{\chi_{\mu\nu}}$ as the fundamental amplitude. Again we assume Δh is small, and using the relation $n_c^2 E_x(\text{outside}) = n_f^2 E_x(\text{inside})$, and the results derived for the TE-TM case, we get

$$\overline{\chi_{uv}} = \frac{\pi \Delta h \; (n_f^2 - N_m^2) \; \left\{ (N_m/n_f)^2 - \cos 2\theta \, [(N_m/n_c)^2 - 1] \right\}}{\lambda_o \; T_m \; N_m \qquad \cos\theta \, [(N_m/n_f)^2 + (N_m/n_c)^2 - 1]} \qquad (9)$$

In this calculation, the field is assumed to be that for a flat slab waveguide of thickness T. This approach is termed "local normal modes", developed by Marcuse[3.22]. Our result agrees with that of Stegeman et al.[3.18], who use a perturbation field theory.

References

3.1 C. Elachi and C. Yeh
J. Appl. Phys., 44 p.3146 (1973)

3.2 C. Elachi, G. Evans and C. Yeh
J. Opt. Soc. Am., 65 p.404 (1975)

3.3 A. Yariv
IEEE J. Quant. Elect., QE-9 p.919 (1973)

3.4 D. Marcuse
'Light Transmission Optics' (Van Nostrand Press, New York)

3.5 S.T. Peng, T. Tamir and H.L. Bertoni
IEEE Trans. Micro. Theo. Tech., MTT-23 p.123 (1975)

3.6 L.R. Lewis and A. Hessel
IEEE Trans. Micro. Theo. Tech., MTT-19 p.276 (1971)

3.7 T. Tamir, H.C. Wang and A.A. Oliner
IEEE Trans. Micro. Theo. Tech., MTT-12 p.324 (1964)

3.8 D.L. Jaggard and C. Elachi
J. Opt. Soc. Am., 66 p.674 (1976)

3.9 R.S. Chu and T. Tamir
IEEE Trans. Micro. Theo. Tech., MTT-17 p.486 (1970)

3.10 M. Neviere, R. Petit and M. Cadilhac
Opt. Comm., 8 p.113 (1973)

3.11 M. Neviere, P. Vincent, R. Petit and M. Cadilhac
Opt. Comm., 9 p.48 (1974)

3.12 S.T. Peng and T. Tamir
'Proc. Symp. Optical and Acoustical Micro-Electronics'
(Polytechnic Press, New York 1974)

3.13 S. Wang
J. Appl. Phys., 44 p.787 (1973)

3.14 R.E. De Wames and W.F. Hall
Appl. Phys. Lett., 23 p.28 (1973)

3.15 A. Yariv and A. Gover
Appl. Phys. Lett., 26 p.537 (1975)

3.16 W. Streifer, D.R. Scifres and R.D. Burnham
IEEE J. Quant. Elect., QE-11 p.867 (1975)

3.17 K. Handa, S.T. Peng and T. Tamir
Appl. Phys., 5 p.325 (1975)

3.18 G.I. Stegeman, D. Sarid, J.J. Burke and D.G. Hall
J. Opt. Soc. Am., 71 p.1497 (1981)

3.19 K. Wagatsuma, H. Sasaki and S. Saito
IEEE J. Quant. Elect., QE-15 p.632 (1979)

3.20 J. Van Roey and P.E. Lagasse
Appl. Opt., 20 p.423 (1981)

3.21 L. Solymer and M.P. Jordon
Micro., Opt. and Acous., 1 p.89 (1977)

3.22 D. Marcuse
'Theory of Dielectric Optical Waveguides' (Academic Press, New York)

3.23 R.P. Kenan
J. Appl. Phys., 46 p.4545 (1976)

Chapter 4

Fabrication of Thin Film Bragg Deflectors by Diffusion Processes

Optical waveguides formed by various types of diffusion processes[4.1-4.6] are widely used in integrated optics. These techniques are based on a modification of the composition in a superficial layer of a dielectric substrate. Active devices such as switches and modulations are formed in electro-optic or acousto-optic materials like lithium niobate and lithium tantalate, while passive devices such as lenses or power splitters are formed in glass substrates.

In this chapter we describe novel techniques to produce periodic index waveguides by diffusion processes. The planar geometry of the periodic waveguides produced in this work have distinct advantages over waveguides with periodic surfaces (Chapter 5) in terms of lower scattering losses and ease of fabrication. Passive Bragg deflectors have been demonstrated using an ion-exchange process in glass, and a proton-exchange* or titanium indiffusion** process in lithium niobate. We will first outline briefly the basic mechanism of the three processes, and then the manufacturing steps of the Bragg deflectors.

* Done in collaboration with I. Andonovic and K.K. Wong

** Done in collaboration with I. Andonovic, B. Bjortorp and A.Yi-Yan

4.1 Ion Exchanged Glass Optical Waveguides

The method of producing passive optical waveguides by ion exchange is well established[4.1,4.7,4.8]. Its advantages over more complicated fabrication technologies[4.9,4.10] include ease of fabrication, low optical loss and low material cost.

The chemical ionic exchange between a glass substrate and a molten bath of a suitable electrolyte has been known for a long time. It improves the surface mechanical properties of glass, and is a simple and effective technique of producing a gradient index layer in a glass substrate. A soda lime glass can be described as an erratic lattice of chemically bonded silicon and oxygen atoms (SiO_{2+x}). Na^+ ions remain in the vicinity of monobonded oxygen atoms inside the lattice. When a piece of glass is immersed into a molten melt of a A^-B^+ salt, Na^+ ions in the glass thermally outdiffuse and are replaced by indiffused B^+ metallic ions from the melt. This exchange-diffusion process penetrates below the surface of the glass substrates to a depth of several microns depending on the melt temperature and length of immersion time, can be spontaneously or electrically assisted, and the waveguides formed can be made compatible, in both geometry and refractive index, with glass optical fibres.

Not all types of glasses are suitable for the ion-exchange process. The glass should possess mobile cations, since it is these loosely bound mobile cations that diffuse readily through the essentially immobile silicate structure and exchange with ions in a melt at the glass surface. The new ions

will then diffuse through the silicate structure (ion exchange may therefore be viewed as an "interdiffusion" of two or more ionic species).

It has been shown experimentally that the presence of CaO inhibits the exchange process[4.11], because the Ca^{2+} decreases the mobility of sodium ions in silica glass. However, the presence of other oxides like Na_2O, K_2O or Li_2O will modify the silicate structure and made available mobile cations. Possible exchangeable ions are Li^+ [4.12], K^+ [4.1], Tl^+ [4.3], Ag^+ [4.8], Cs^+ [4.13].

In our work, silver/sodium ion exchange is chosen because detailed studies of planar optical waveguides fabricated by this technique have been carried out in our department[4.7,4.8,4.14], using both pure and diluted (with sodium nitrate) melts of silver nitrate. By evaporating a thin film of aluminium on the glass surface and delineating stripe windows in the aluminium film prior to the exchange process, stripe optical waveguides have also been formed using silver/sodium ion-exchange in a pure melt[4.15] (the aluminium film inhibits the ion-exchange process, except in the opening, or window region) and have been analysed.

The larger mass and higher polarisability of the silver ions, compared to those of the sodium ions, increase the refractive index of the glass. With pure silver nitrate melt, a large change in the refractive index, typically 0.09 at the glass surface, is produced[4.8]. However, the high silver concentration present in the glass is a problem, because the

silver atoms may turn into colloidal crystals, and these inhomogeneities (yellow staining of the glass) lead to large angle scattering, increasing the propagation losses of the waveguide[4.16]. Furthermore, the repeatability of the mode indices is poor, unless the temperature of the melt is controlled to within $0.1^{o}C$ [4.17].

To circumvent the problem, melts of silver nitrate diluted with sodium nitrate are used instead. The peak surface index difference can be varied from its maximum value (0.09) to 0, depending on the degree of dilution (Fig. 4.1). In our work, a very dilute melt (0.1% $AgNO_3/NaNO_3$ by weight) was used[4.14].

4.1.1 Interdiffusion Theory

The silver concentration at the glass surface depends on the equilibrium state between the melt phase and the glass phase[4.11,4.18]. In the glass the indiffusing Ag^+ ions will have a lower mobility compare to that of the outdiffusing Na^+ ions. Hence a net electric charge (negative in the glass) and electric field will initially build up as the interdiffusion proceeds. However, the electric field set up will speed up the slower moving Ag^+ ions and slow down the faster moving Na^+ ions, and electrical neutrality is preserved by this electric potential (or diffusion potential). Under this condition, if we assume that the depletion of the Ag ions from the melt can be ignored[4.19], and that the self diffusion coefficients of the Ag and Na ions in glass are independent of concentration, the

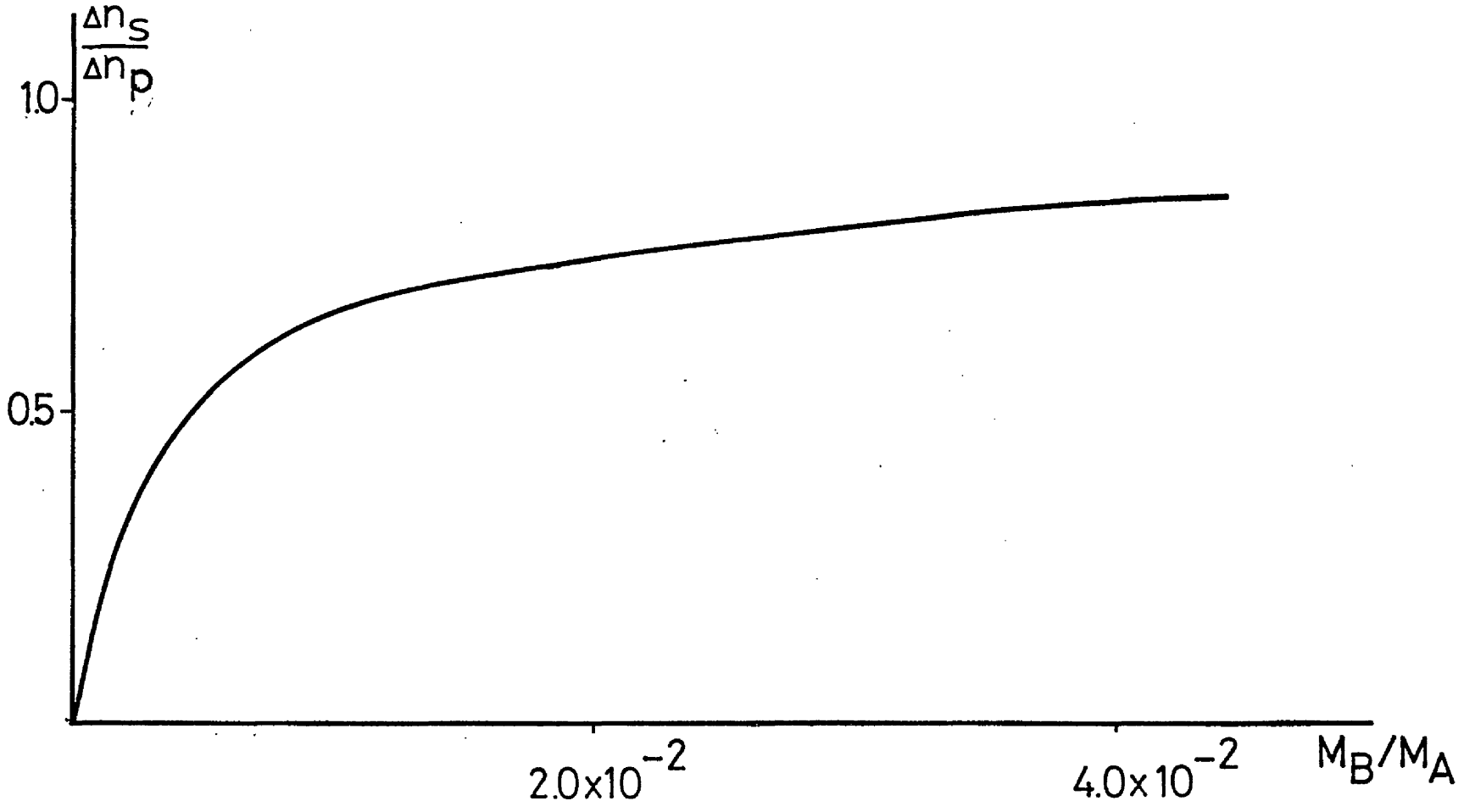

FIG 4.1 Relationship between surface refractive index and melt composition (after ref. 4.14)

exchange process can be represented by the equation

$$Na^+(glass) + Ag^+(melt) = Ag^+(glass) + Na^+(melt) \qquad (4.1.1)$$

The equilibrium condition (equation 4.1.1) will be determined by a equilibrium constant k_{ab}, and may be written as (4.20)

$$\ln(w_s/1-w_s) = 1/\ [\ln(M_{Ag}/M_{Na}) - (E_m/RT).(1-2M_{Na})+\ln(k_{ab})\ ] \qquad (4.1.2)$$

where w_s is the fraction of Na ions replaced by Ag ions at the surface, and M_{Ag}, M_{Na} are the mole fractions of Ag and Na ions in the melt, respectively. E_m is the net interaction energy of the ions ($E_m = 3.5 \times 10^3$ J.mole^{-1} of $AgNO_3/NaNO_3$ melt) and γ is a constant ($\gamma > 1$). Stewart et al.(4.8) found that $k_{ab} = 131$, and $\gamma = 1.32$. From equation (4.1.2), it can be seen that by changing the melt composition the surface concentration of Ag ions, and hence the surface index change, can be any desired value, ranging from its maximum value for a pure melt to zero.

4.1.2 Diffusion Profile Without A Mask

If the refractive index is assumed to vary linearly with the silver concentration, the concentration profile C can be expressed theoretically by the diffusion equation(4.19)

$$\partial C/\partial t = \partial/\partial x \quad [D_{AB}(\partial C/\partial x)] \qquad (4.1.3)$$

where D_{AB} is the interdiffusion coefficient. (4.1.3) can be

rewritten in the form

$$D_{AB} = D_B/[1-\alpha(C_S/C_o)(C_B/C_o)] = D_B/[1-\alpha(\Delta n_s/\Delta n_p)C] \qquad (4.1.4)$$

where $\alpha = (D_A-D_B)/D_A$: D_A, D_B are the sodium and silver self-diffusion coefficients. $C = C_B/C_S$, where C_B is the silver concentration and C_S is the surface concentration of silver. C_o is the sodium concentration in the unexchanged glass, and Δn_p and Δn_s are the surface index changes with a pure and dilute melt respectively. From (4.1.4), the profile depth and profile form changes with dilution of the melt. For a very dilute melt (as in our case), $\alpha(\Delta n_s/\Delta n_p) \sim 0$, $D_{AB} = D_B$ and the solution of (4.1.2) is [4.21]

$$C = \text{erfc}\ (x/2\sqrt{D_B t}) \qquad (4.1.5)$$

The value of the diffusion coefficient D_B can be calculated using the Arrhenius equation[4.19]

$$D_B = D_0\ e^{(-\Delta H/RT)} \qquad (4.1.6)$$

where ΔH is the activation energy, R is the Universal Gas Constant, and T is the absolute temperature.

Stewart[4.16] found that the refractive index profile of a waveguide fabricated from a pure melt has the form

$$n(x) = n_s - \Delta n_p\ [(x/d)+b(x/d)^2] \qquad (4.1.7)$$

where $$d = 1.19\times10^{4}\ t^{1/2} \exp(-1.02\times10^{4}/2T)\ \text{um} \qquad (4.1.8)$$

b = 0.64, t is the diffusion time in minutes, and T is the temperature of the melt in Kelvin. For a very dilute melt ($\Delta n_s/\Delta n_p < 0.3$), a linear profile can be assumed by putting b = 0 and replacing the depth parameter d by d' in (4.1.7)

$$d'/d = 0.26+0.74(\Delta n_s/\Delta n_p) \qquad (4.1.9)$$

4.1.3 Diffusion Profile Through A Mask

The concentration profile in this case becomes a two dimensional problem, and can be expressed theoretically as[4.22]

$$\partial C/\partial t = (\partial/\partial x)[D_{AB}(\partial C/\partial x)] + (\partial/\partial y)[D_{AB}(\partial C/\partial y)] \qquad (4.1.10)$$

where D_{AB} has the same definition as in (4.1.3).

The use of aluminium as a diffusion mask means there is an electrically conducting diffusion barrier, and unfortunately it is impractical to derive an exact solution of the differential equation with a conducting boundary. Walker[4.15] found that for stripe waveguides made using a metallic mask there was 'silver reduction' along the inner boundary of the aluminium windows, where the aluminium film and the diffused region overlapped. Nitric acid had no effect on this deposition, indicating that it was more than a surface deposition. Waveguides made using an anodised mask were free from this 'silver reduction'. No such 'silver reduction' was

also observed for metallic mask when two stripe waveguides converge to within 8um of each other, or when a piece of the mask is electrically isolated from the bulk (e.g. the centre portion of a ring resonator). This indicates that under these conditions the metallic mask, despite its electrochemical field, will act like a non-conducting mask, and will have little effect upon the quantity of silver ions diffused in through the window, and the final diffusion profile. From a thermodynamic point of view, the diffusion rate will depend on the free energy of the system, and will be affected only by some external energy source. In this case the only external energy source will be the electrochemical potential, which appears to be negligible. By replacing the metallic mask with a non-conducting mask, numerical techniques can be carried out to solve the differential equation, subject to the boundary conditions of an insulating mask[4.23].

We use an aluminium grating mask in our work, the aluminium lines being close to one another (1.5μm spacing between two lines), hence the model of the non-conducting mask is used for the diffusion profile, and our experimental results (Chapter 6) confirm this assumption.

By substituting $z = \log(1 - \alpha C)$ in (4.1.10), α having the same definition as in (4.1.4), we obtain

$$\partial z/\partial t = D_B e^{-z}(\partial^2 z/\partial x^2 + \partial^2 z/\partial y^2) \qquad (4.1.12)$$

This non-linear ion-exchange equation in two dimensions can be solved by a finite-difference technique[4.24-4.27]. A typical

contour plot of the concentration of silver ions underneath the grating mask is shown in Fig. 4.2(a)*. The mask is assumed to be non-conducting, but opaque to silver ions. In figure 4.2(b), a contour plot is also shown for the same conditions as in figure 4.2(a), except that the mask is now conductive, and the silver ion concentration is zero at the mask-glass interface.

4.2 Proton Exchanged $LiNbO_3$ Optical Waveguides

Ion-exchange has also been used to produce high index changes ($\Delta n \sim 0.12$) in $LiNbO_3$, using melts of $AgNO_3$[4.28] and $TlNO_3$[4.29]. Unfortunately the results are not consistently repeatable[4.30], and it was found that the index change is not due to exchange of ions, but rather a proton exchange process, with water impurities in the melt acting as the source of hydrogen[4.31].

Jackel et al.[4.32,4.33] have recently shown that proton exchange will take place when a $LiNbO_3$ crystal is immersed in hot acid, or in certain hydrate melts. Lithium ions will be lost from the crystal, and replaced by H^+. There is complete exchange in strong acids like HNO_3 or H_2SO_4, and a new stoichiometric hydrogen perovskite compound will form, which precludes the formation of a surface layer. In less acidic

* The computer program, called DIF, was first developed by Prof. C.D.W.Wilkinson. The assistance of Mr. Tom Cullen in running the program is acknowledged.

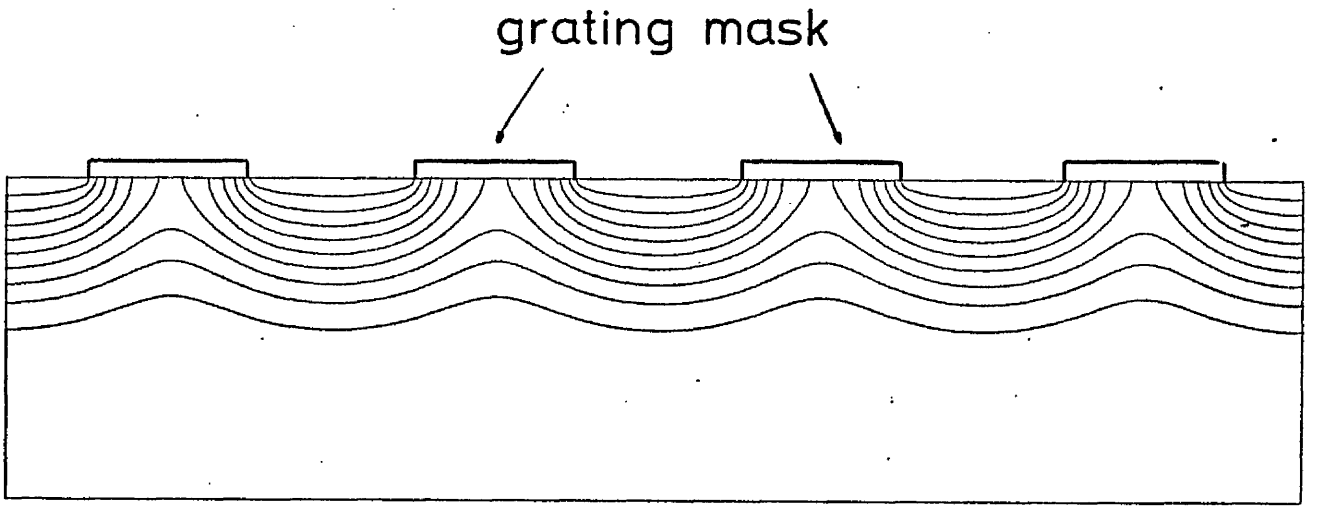

(a)

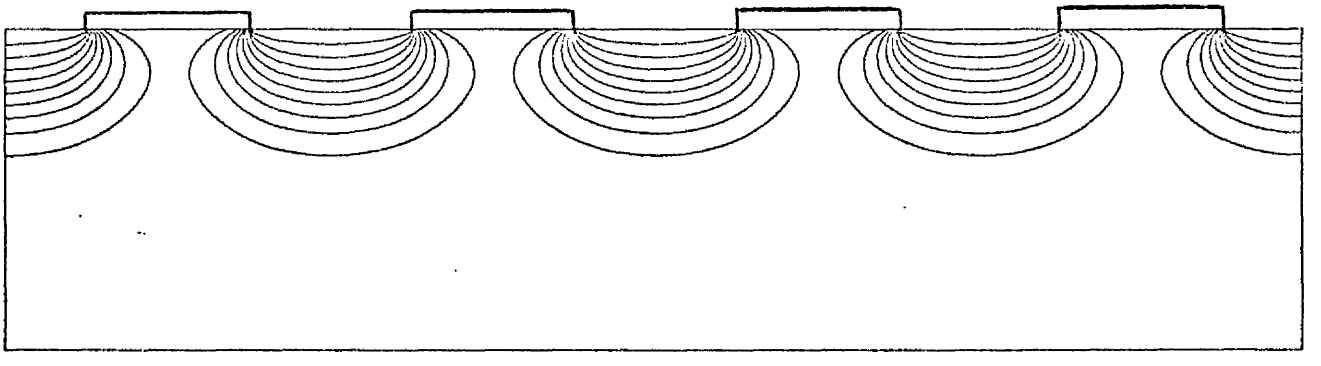

(b)

FIG 4.2 Contour plot of the diffused silver-ions concentration underneath the grating mask : (a) non-conducting mask and (b) conducting mask

melt, like $Mg(NO_3)_2.6H_2O$ or benzoic acid (C_6H_5COOH)[4.34], incomplete exchange occurs, and no major structural change takes place even if 50% of the lithium is replaced by hydrogen. However, the reactive ion-etching rate for the new compound will increase (almost 70% in this case), due to lower lithium content in the crystal.

Lowloss slab waveguides ($\sim$1dB/cm) can be made in both x-cut and z-cut crystals, but not y-cut crystals, as the proton source will etch these faces. Only the extraordinary refractive index is increased ($\Delta n \sim 0.12$ at 0.633um wavelength), but not the ordinary refractive index. M. De Micheli et al.[4.35] found that the ordinary refractive index actually decreases, making imbedded TM guides a possibility. They have also shown that by combining titanium indiffusion and the proton exchange process, the optical waveguide characteristics can be optimised for specific application, such as non-linear interactions.

The refractive index profile for proton exchange waveguide in x-cut $LiNbO_3$ is a nearly step-index profile, and the diffusion depth d can be expressed as

$$d = 2\sqrt{D(T)t} \qquad (4.2.1)$$

where D(T) is the diffusion coefficient, and t is the diffusion time in hours. The diffusion coefficient can be obtained by measuring the diffusion depths at a given temperature. Using a standard curve fitting technique (Fig. 4.3) the diffusion coefficient D(T) may be expressed as:

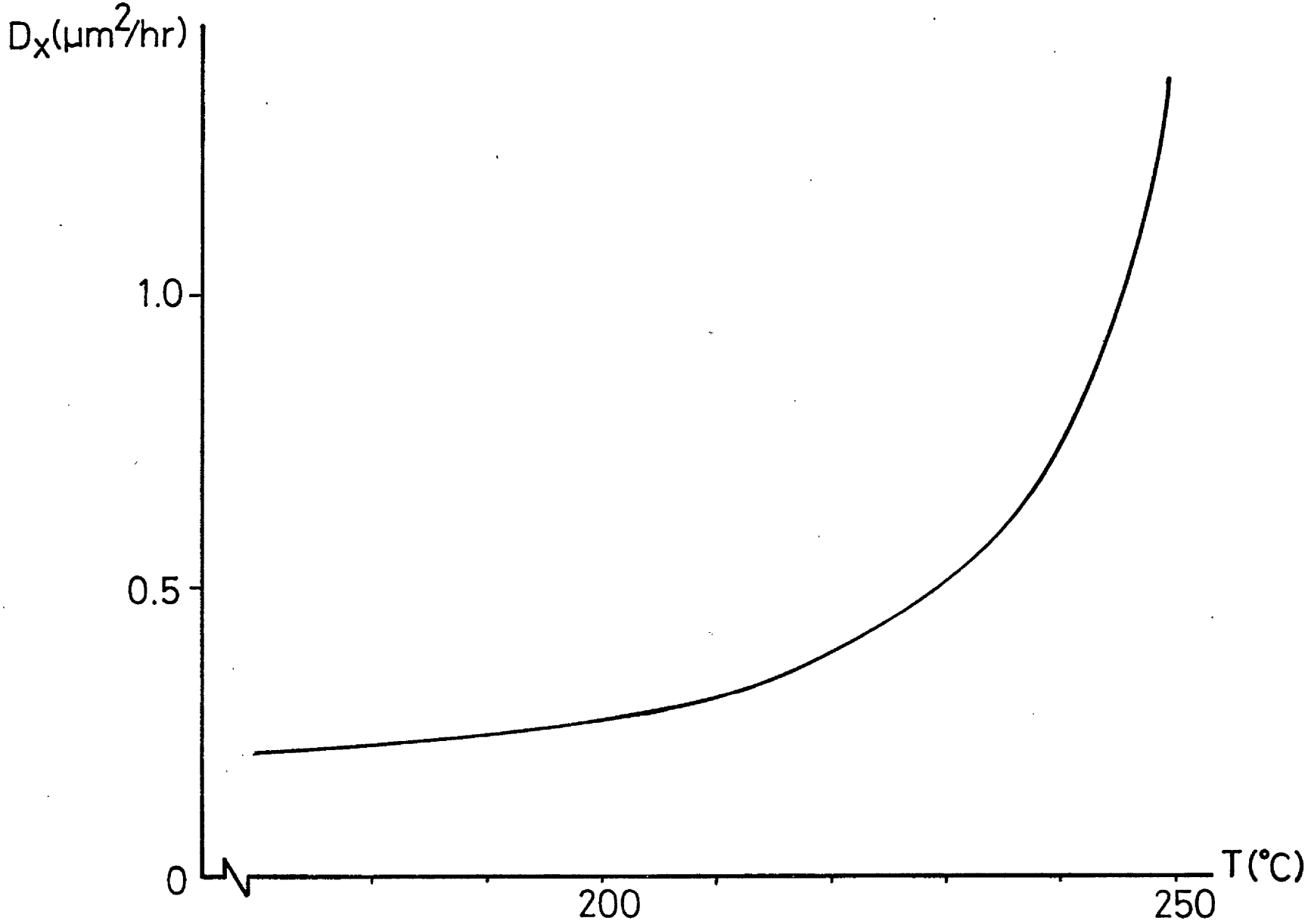

FIG 4.3 Diffusion coefficient as a function of temperature

$$D(T) = 1.604\times10^{9}\exp[(-1.09\times10^{-4})/T]\ \mu m^2 hr^{-1} \quad (4.2.2)$$

and hence $$d = 1.03\times10^{4}\exp(-1.09\times10^{-4}/2T)\sqrt{t'}\ \mu m \quad (4.2.3)$$

where T is the diffusion temperature in Kelvin, and t' is the diffusion time in minutes.

Since most metals are not attacked by benzoic acid, aluminium grating masks were again used to make high efficiency gratings. In our work, x-cut $LiNbO_3$ was used, and the temperature chosen was 170°C.

4.3 Ti indiffused $LiNbO_3$ Optical waveguides

Titanium diffusion[4.36-4.38] is a standard technique for fabricating optical waveguides in $LiNbO_3$. The diffused waveguide is electro-optically active, diffusion temperatures are below the Curie temperature, and tight optical confinement is possible with low transmission loss.

Although the optical properties of Ti:$LiNbO_3$ diffused layers have been reported by various workers, many aspects of Ti indiffusion are still not well understood. Sugii et al.[4.39] studied the diffusion mechanism and suggested that the Ti ions enter at the Nb sites of the $LiNbO_3$ lattice, and the change in refractive index is due to the Ti ions, whose ionic radius and polarisability are different from those of the Nb ions. Esdaile[4.41] suggested further that another possibility could be a crystal structure rearrangement involving a rotation of the

oxygen octahedra to accomodate the diffusing ions[4.41,4.42].

The initial steps of Ti diffusion were studied recently by Armenise et al.[4.43], who found that the Ti metal oxidised first (TiO_x) at intermediate temperatures (300°C to 500°C), followed by epitaxial frowth of a $(Ti_xNb_{1-x})O_2$ phase, x having a value of 0.6 ± 0.05 in their studies. This compound acts as a source for Ti diffusion at high temperatures (of the order of 950°C).

4.3.1 Diffusion Profiles of Ti:$LiNbO_3$ Slab Waveguides

For long diffusion times when all the metal film enters the crystal, and assuming that it is a limited source simple diffusion case, the concentration profile may be assumed to be a Gaussian function[4.44]

$$C(x) = C_o \exp[-(x/d_x)]^2 \qquad (4.3.1)$$

where x is the depth below the surface, $C_o = \alpha\tau/d_x$, α is a constant, τ is the initial Ti film thickness, $d_x = 2\,[D_x(t)t]^{1/2}$ = diffusion depth, $D_x(t)$ = diffusion coefficient, of the form $D_o e^{-(T_o/T)}$, and t is the diffusion time.

For short diffusion times, when the metal is not completely diffused into the crystal, there is a thin layer of high index change at the surface (about 2.7 at the beginning of the diffusion), and the concentration profile is a complementary error function[4.44]. For diffusion times comparable to the

time required for all the metal to enter the crystal, the Ti film will change slowly to TiO_2, and the concentration profile will be intermediate between the Gaussian and erfc profiles.

The concentration profile can be measured using electron microprobe, secondary ion mass spectroscopy (SIMS), or Rutherford α- particle backscattering. Experimental results[4.36,4.39-4.42] showed that a Gaussian profile is a good enough approximation to the refractive index profile, and the discrepancies increase due to factors such as LiO_2 outdiffusion. This is in agreement with the electron microprobe observation (depth resolution $\sim$ lum).

Burns et al.[4.36], using the SIMS method which has a depth resolution of $\sim$100Å, observed that the Gaussian depth diffusion has an additional peak, having a diffusion depth of about 0.3μm directly below the crystal surface. They postulate that this may be due to the formation of an multiphase polycrystalline layer prior to diffusion, which results in a thermodynamically preferred $LiTiO_3$ state. Johnson and Pitt[4.45], using the Rutherford α- particle backscattering method (depth resolution $\sim$100Å), found a concentration profile intermediate between that of an erfc function and a Gaussian function.

In our work, we use the result of McLachlan[4.46]. The refractive index profile is given by :

$$n(x) = n_{substrate} + \Delta n(0)\{ \exp[-(x/d_x)^2]\} \qquad (4.3.2)$$

where $\Delta n(0) = A.\tau/d_x$, $A = 6.2\times10^{-5}$, $d_x = 3.2(t/18)^{1/2}$ μm, is the initial titanium thickness in Å, t is the diffusion time.

For complete diffusion of the Ti metal, the minimum time is

$$t_{min} = 0.015\tau \text{ hr} \qquad (4.3.3)$$

and the variation of Δn_{eff} with diffusion time is shown in Fig. 4.4. It can be seen that the effective index as well as its rate of change decreases with time. Hence to improve repeatability of the guides a long diffusion time (1.5 to 2 times the minimum diffusion time) is usually chosen. However, this means that Δn and the diffraction efficiency will be small. To circumvent this problem, a two-step diffusion or double diffusion is employed. The first diffusion (time = t_1) forms the waveguide and a second diffusion (time = t_2) forms the grating structure[4.47]. This process is more flexible, because t_1 and t_2 can be optimised independently for the waveguide structure and the diffraction efficiency. The thickness of the initial Ti layer can also be chosen independently.

4.3.2 Diffusion Profiles of Ti:$LiNbO_3$ Stripe Waveguides

For y-cut $LiNbO_3$ crystal, both Fakuma et al.[4.48] and Minakata et al.[4.49,4.50] found that there is enhanced lateral

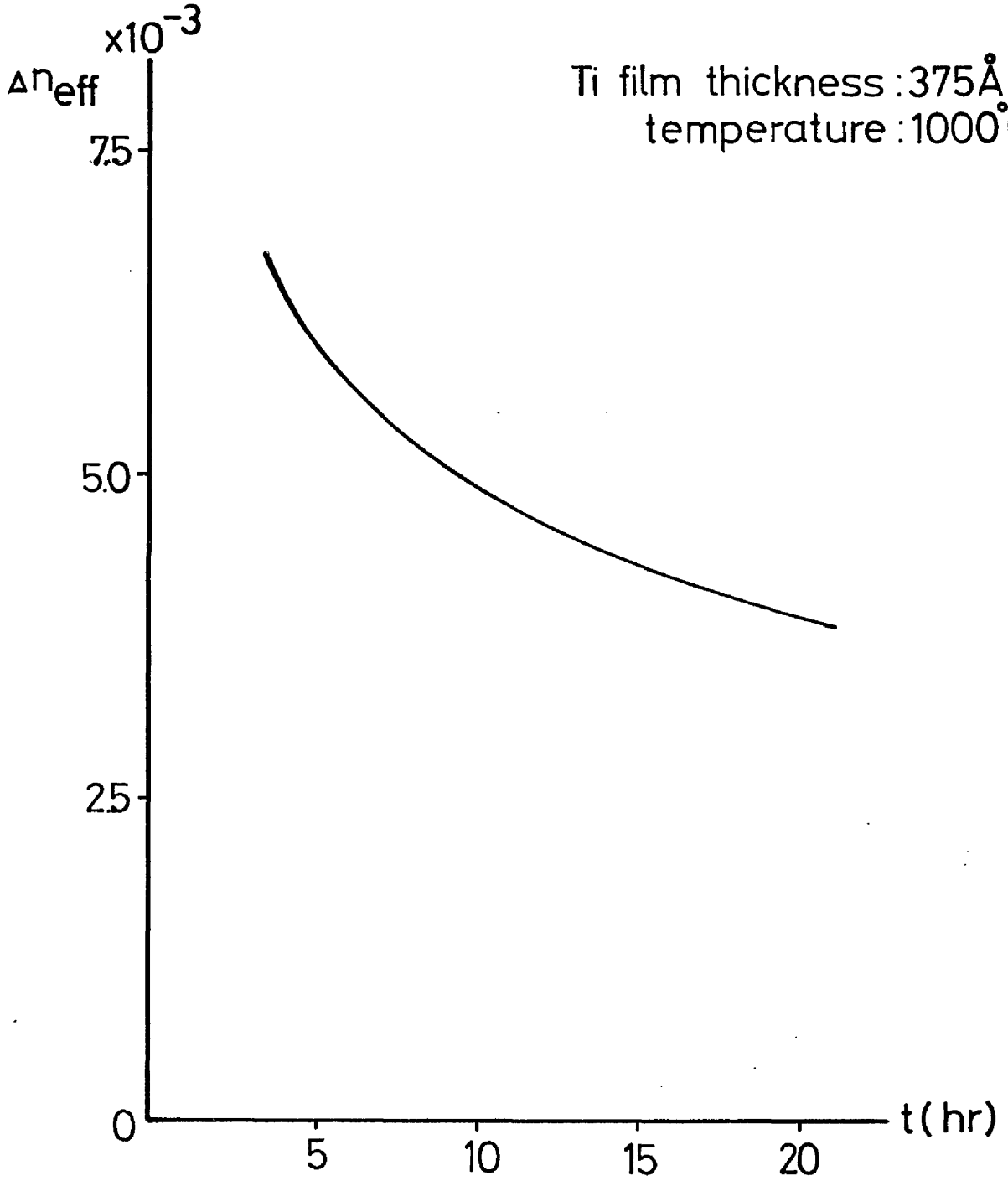

FIG 4.4 Theoretical slab waveguide dispersion curve as a function of diffusion time (after ref. 4.36)

diffusion. Similar effects have also been observed by Burns et al.[4.36]. This lateral diffusion is much less for a z-cut crystal.

If the diffusion axes coincide with the crystal axes (for $LiNbO_3$ crystal, being uniaxial, $d_x = d_z \neq d_y$) the theoretical profile can be calculated by assuming separation of variables in the diffusion problem[4.20], and a complete expression for the refractive index profile of a stripe waveguide, of width w, is of the form[4.37]

$$n(x,y) = n_{substrate} + \Delta n(0)\{\exp[-(x/d_x)^2] \cdot (1/2)[\operatorname{erfc}(w+2y)/2d_y + \operatorname{erfc}(w-2y)/2d_y]\} \quad (4.3.4)$$

where $\Delta n(0)$ and d_x will have the same meaning as that of (4.3.3), and $d_y \sim 1.2 d_x$. Fig. 4.5 shows the concentration profile of titanium indiffused stripes in y-cut $LiNbO_3$ crystal. The profiles are similar to that of ion-exchange in glass with a non-conducting mask (Fig. 4.2a).

4.4 Production of Bragg Deflectors

A two dimensional, or planar fabrication technique is used to fabricate the grating devices. The basic principles of the planar fabricaiton techniques are illustrated in Fig. 4.6. A radiation sensitive polymer film is deposited on a substrate surface and exposed to radiation in some desired pattern. Following exposure, either the exposed or unexposed polymer is

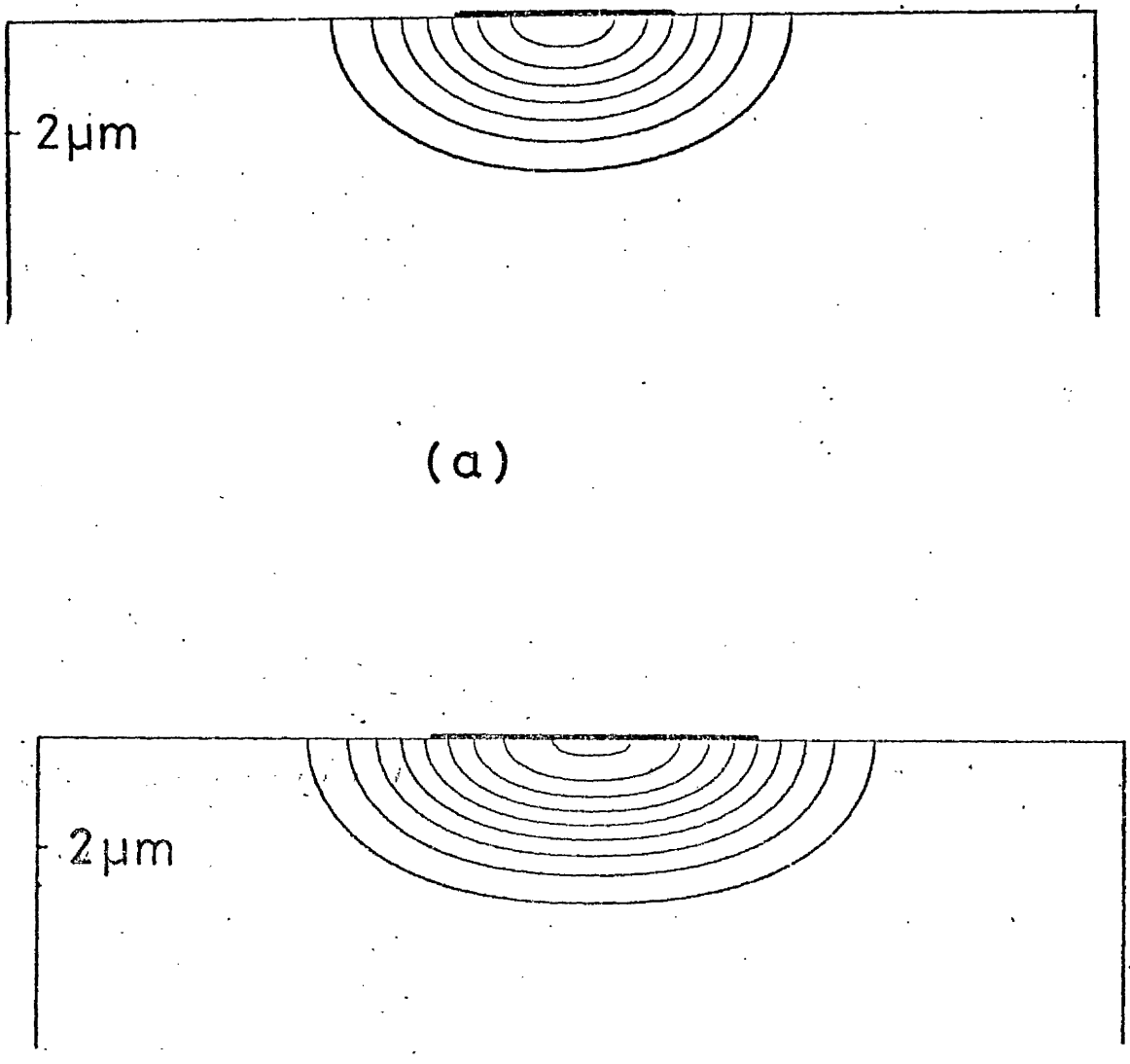

FIG 4.5 Concentration profile of $Ti:LiNbO_3$ stripe waveguide. Width = (a) 4 μm and (b) 6 μm. Diffusion time = 8 hrs at 1000°C (after ref. 4.46)

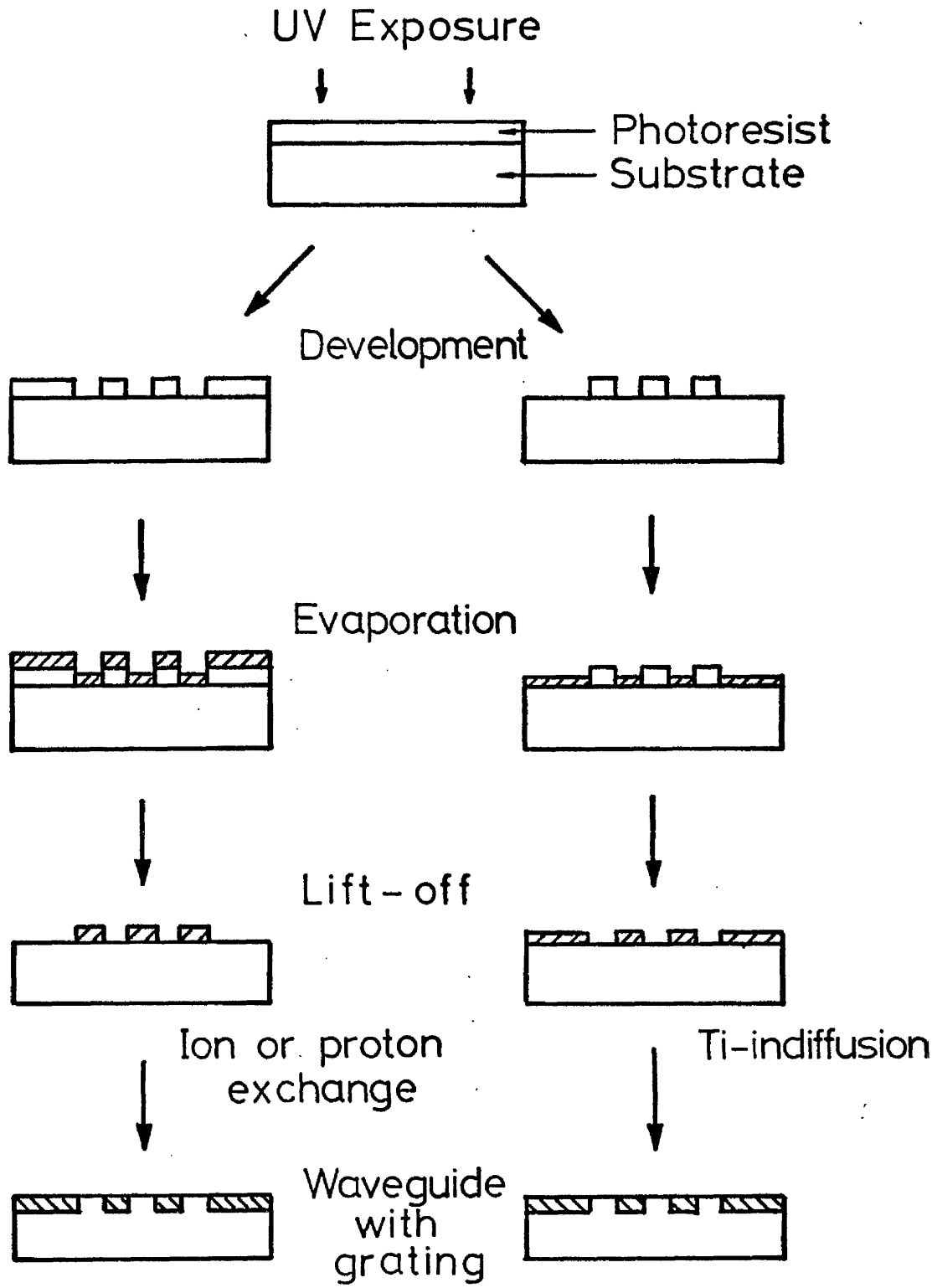

FIG 4.6 Illustration of the basic principles of the planar fabrication techniques

removed by a development step, and the pattern in relief is left on the substrate surface. Many processing steps are then available to convert the pattern into three dimensional device structures. A relief structure can be etched in the substrate itself, the pattern areas can be chemically doped, or a material can be deposited into the interstices of the polymer relief pattern. The etching can be done by either ion-bombardment or chemical means. Both ion implanatation and thermal diffusion can be used for chemical doping, and an oxide or metal pattern (formed either by etching or the lift-off technique) is usually used as the mask rather than a polymer. The latter approach, thermal diffusion and the lift-off technique, was chosen for the device fabrication.

4.4.1 Substrate and Polymer Film Preparation

4.4.4.1 Substrate Cleaning

Fisher brand precleaned microscope glass slides (containing 14% in weight of Na_2, and with refractive index = 1.512 at 0.633μm wavelength) were used as substrates for the ion-exchange process because of their better surface quality and homogenity compared with other brands. SAW grade y-cut $LiNbO_3$ crystal was used for Ti indiffusion, and x-cut crystal for proton exchange.

The major contaminants are usually waxes, greases, fingerprints, lints, and dust particles. The principles of

substrate cleaning have been discussed extensively in the literature[4.51,4.52]. The cleaning procedure consists of ultrasonic agitation in hot detergent bath, followed by rinsing in organic solvent and distilled water. For example, the procedure used for cleaning glass substrates is as follows:

(1) Immerse in trichlorethylene, 10 minutes.

(2) Immerse in methanol, 5 minutes.

(3) Immerse in diluted Decon detergent bath at 65°C with ultrasonic agitation, 10 minutes.

(4) Rinse off detergent in distilled water.

(5) Immerse in acetone with ultrasonic agitation, 10 minutes.

(6) Immerse in methanol with ultrasonic agitation, 10 minutes.

(7) Blow dry with jet of dry nitrogen.

This cleaning procedures was carried out in a class 100 cleanroom, and is an important first step in device fabrication, irrespective of the subsequent processing procedure. Failure in metal film adhesion will result if the substrate is not clean. The optical wave propagation will also be affected by the surface contamination.

Since the lift-off technique was chosen, the substrates were immediately coated with a radiation sensitive polymer after cleaning.

4.4.1.2 Polymer Film Preparation

The radiation sensitive polymer films are called photoresists. They respond to short visible wavelengths and ultraviolet light exposure, and the exposed regions undergo

reactions leading to selective solubility, either by undergoing cross linking (negative photoresist) or chain scission (positive photoresist). The Shipley positive photoresist AZ1350J has high resolution capability (better than 100A) and vertical sidewalls can be produced[4.53]. Consequently we used such a photoresist throughout our experiments.

The AZ1350J photoresist contains a base resin plus diazide compounds (also known as the "inhibitors"). The latter strongly absorb the ultraviolet light, and undergo photochemical decomposition, leading to enhanced solubility of the resist in aqueous alkaline solutions. The characteristics of the resist will be discussed in more detail in the next chapter (section 5.2.1).

The usual method of coating a substrate consisted of flooding the surface with filtered photoresist liquid (0.2um millipores, type FGLP filter) from a syringe, and then spinning the substrate on a high acceleration whirler (Headway EC10). Films of uniform thickness (1.8μm$\pm$200Å, as measured with a Talystep surfometer after baking) were readily obtained with a speed of 4000 rpm and a time of 20 seconds.

After the coating step, the resist films were baked in accordance with the manufacturer's instructions. A temperature of 90°C was used, and the baking time was 30 minutes. It was found that coated samples stored in light-tight containers for periods of up to a month suffered no adverse effects on exposure sensitivity.

4.4.2 Photolithography

A grating pattern of periodicity 12μm was generated by electron beam writing (this mask was made in Bell Laboratories, Holmdel, New Jersey). It was further reduced to a periodicity of approximately 3um by photoreduction with a high quality lens (x4 micro Tropel 495-G lens which is operated as a projection printer onto a Balzers low reflectivity chrome plate, previously spin-coated with photoresist). The line to space ratio of the grating is 1:1, and the overall dimensions are approximately 2mmx0.75mm.

The photomask (grating pattern in thin film chromium on a glass plate) was held in closed proximity to, or contact with, a resist-coated substrate, and the pattern was printed onto the resist by passing collimated ultraviolet light (quartz halogen lamp) through the photomask, followed by development of the resist in an alkaline based developer (AZ developer, diluted with filtered water in a ratio 1:1). This replication technique, called shadow printing, or contact printing, is simple and convenient. A linewidth of 1μm is more or less a limit because of diffraction effects, but this problem can be circumvented by using a conformable photomask[4.54].

4.4.3 Lift-off Technique

The lift-off technique used consists of evaporating a

thin layer of metal (either aluminium 500Å thick or titanium 200Å thick) over a photoresist pattern on a substrate in a vacuum chamber, and then dissolving the resist in acetone. A pattern in the metal material is then left behind on the substrate. To ensure successful lift-off for metal films as thick as 2/3 of the resist the sidewalls of the resist must be vertical or slightly undercut, and the deposited material must arrive at the substrate at near normal incidence (4.55).

A grating pattern in aluminium of periodicity 3μm on the surface of a glass substrate is shown in Fig. 4.7a and 4.7b. An unsuccessful lift-off is also shown in Fig. 4.7c. The smoothness of the edges of the lines indicates the high resolution and faithful reproduction to a dimensional tolerance of at least a few hundred angstroms of the lift-off method.

4.4.4 Diffusion Processes

4.4.4.1 Silver-Sodium Ion Exchange

Ion-exchanged waveguides, with periodic aluminium grating lines on top of the glass surface, were manufactured by immersing theprepared substrates in a 0.1% diluted melt of $AgNO_3/NaNO_3$. Melt temperatures ranging from 315°C to 330°C and diffusion times from 20 minutes to 1.5 hours were used. The melt was contained in a stainless steel container controlled to ± 1°C, and the glass slide was supported by two steel arms projecting from a rod, and inserted into the melt by angular

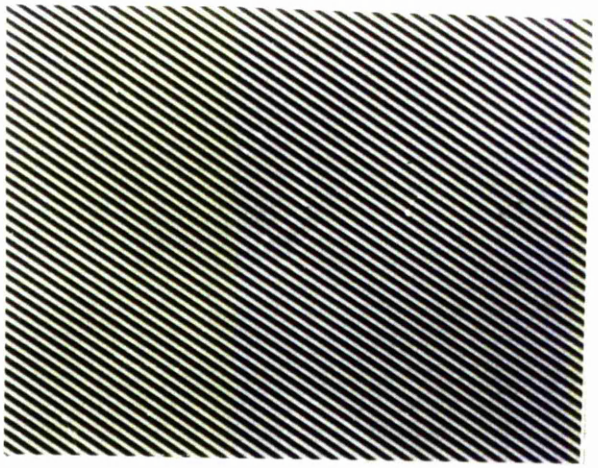

(a) Low magnification

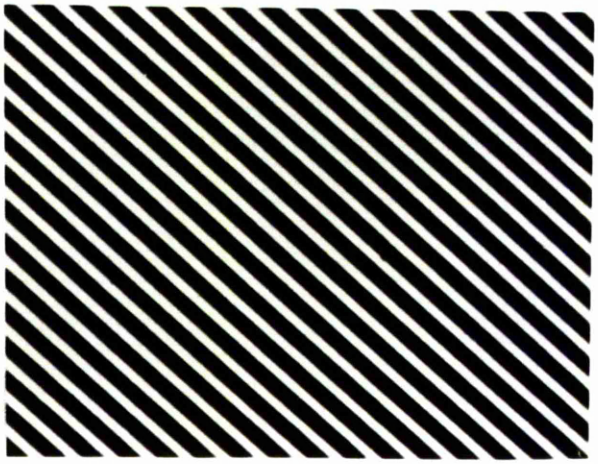

(b) High magnificatior

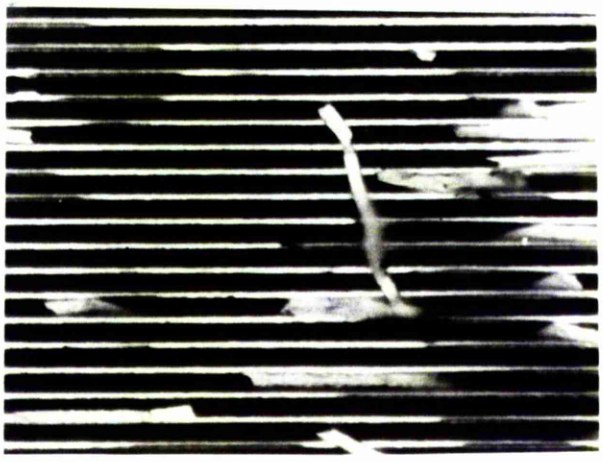

(c) Unsuccessful lift-off

FIG 4.7 Photographs of the aluminium grating masks(periodicity = 3μm)

rotation (Fig. 4.8).

As the aluminium strips have the effect of partially inhibiting the ion-exchange process, a waveguide and a grating are formed simultaneously on the same substrate.

The waveguides obtained exhibited low losses (<0.5 dB/cm), and the variation in N, the effective index, from a batch of similar substrates was typically of the order of $\pm$ 0.001.

A final step was carried out to remove the aluminium gratings from the surfaces of the guides using a chemical solvent.

4.4.4.2 Proton Exchange in Benzoic Acid

Single mode slab waveguides incorporating gratings were fabricated by immersing x-cut $LiNbO_3$ substrates (with aluminium grating lines utilised as masks on the surfaces) in molten benzoic acid for 90 minutes at a temperature of 170°C.

The benzoic acid was melted in a stainless steel beaker using a heating mantle inside a ventilated chamber (benzoic acid is toxic), and the temperature was controlled to within $\pm$ 10°C (Fig. 4.9). The substrates were preheated before immersion, and after removal from the melt, any excess benzoic acid (a solid at room temperature) was dissolved in chloroform. The aluminium gratings were also dissolved away using a chemical solvent.

The experimental set up was simple, but for our

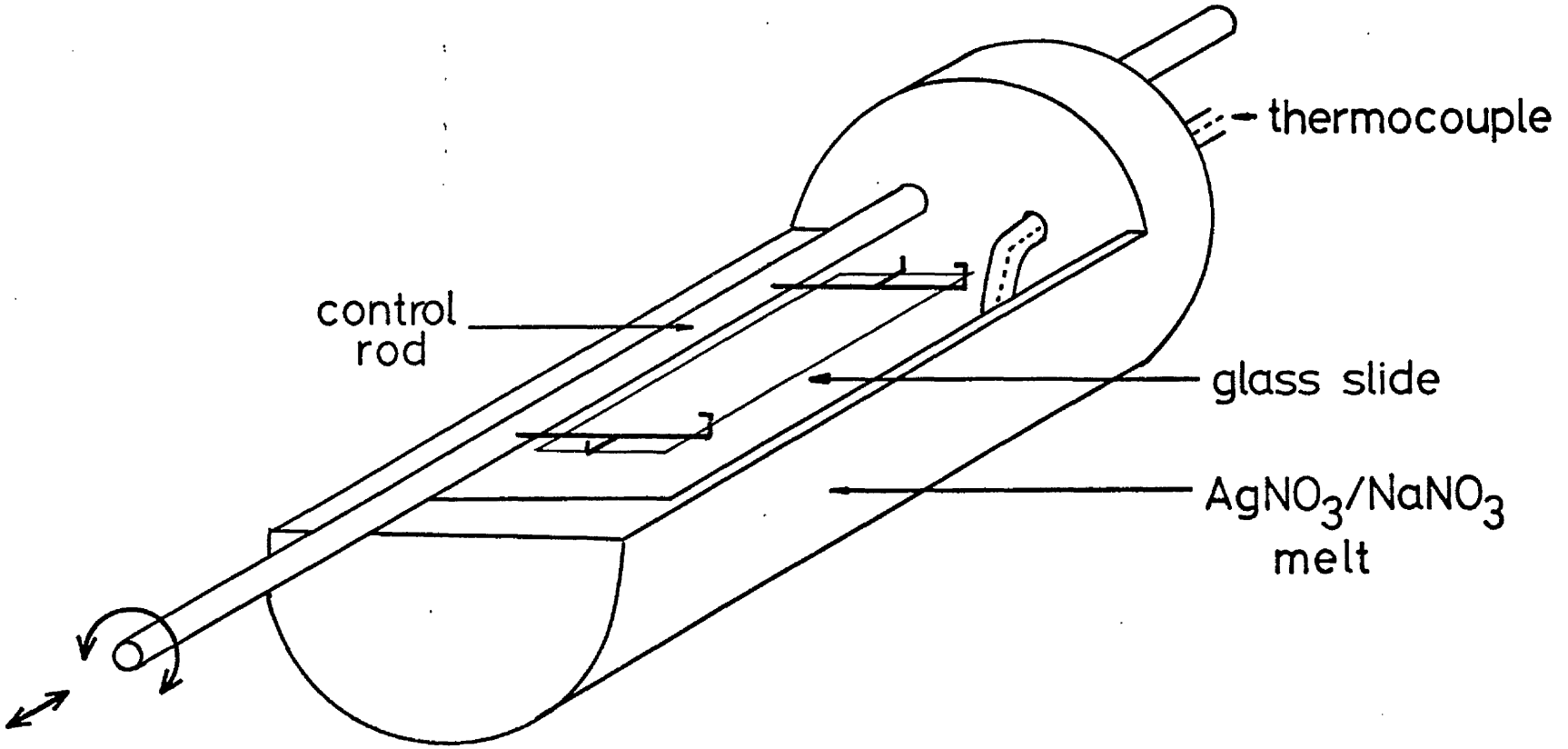

FIG 4.8 Schematic diagram of the ion-exchange apparatus

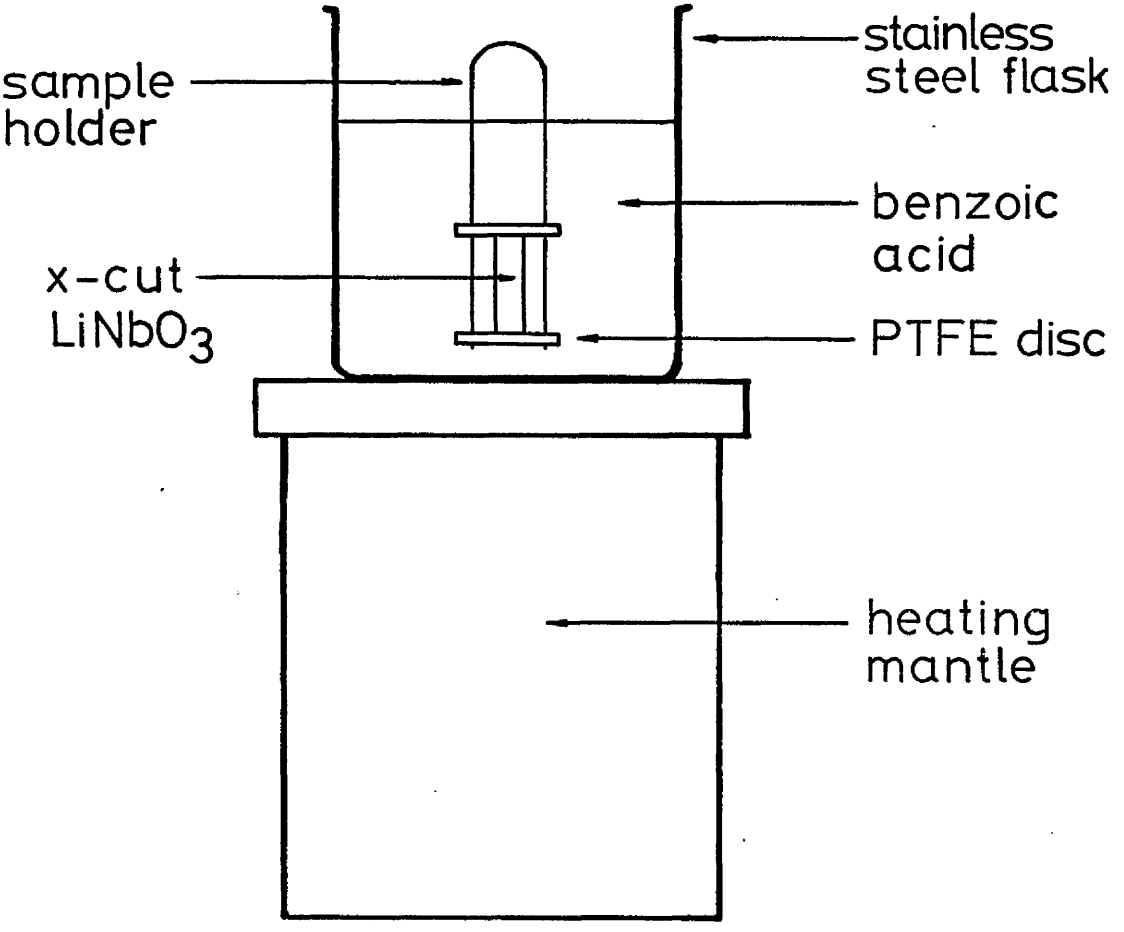

FIG 4.9 Experimental set-up for proton-exchange process

purposes was considered adequate, since we were not concerned with the precise control of the waveguide parameters at the time.

4.4.4.3 Titanium indiffusion

Single mode periodic index waveguides ($\sim$1 dB/cm), with Ti grating strips on the surface prior to diffusion, were fabricated using y-cut SAW grade $LiNbO_3$. The film thickness was monitored by an optical system[4.56], and is typically 200Å. To avoid out-diffusion of LiO_2, the substrates were diffused at 1000°C in a closed tube system[4.57] (Fig. 4.10). The vapour pressure of LiO_2 was maintained at the equilibrium value by the presence of a small amount of congruent composition $LiNbO_3$ powder in the inner aluminium tube. The temperature was controlled to $\pm$ 1°C, and diffusion times (excluding warm up period) ranging from 3 hours to 10 hours were used.

For the two-step diffusion process, a single mode waveguide was initially formed by a first diffusion, t_1 ranging from 5 hrs. to 8 hrs., and the grating region was formed by a second diffusion, t_2 ranging from 3 hrs. to 6 hrs.

4.5 Conclusions

We have developed a novel technique to fabricate periodic waveguides by diffusion processes, resulting in periodic variation of local refractive index in the waveguides. This planar technology has distinct advantages over the holographic corrugated grating technique in terms of ease of

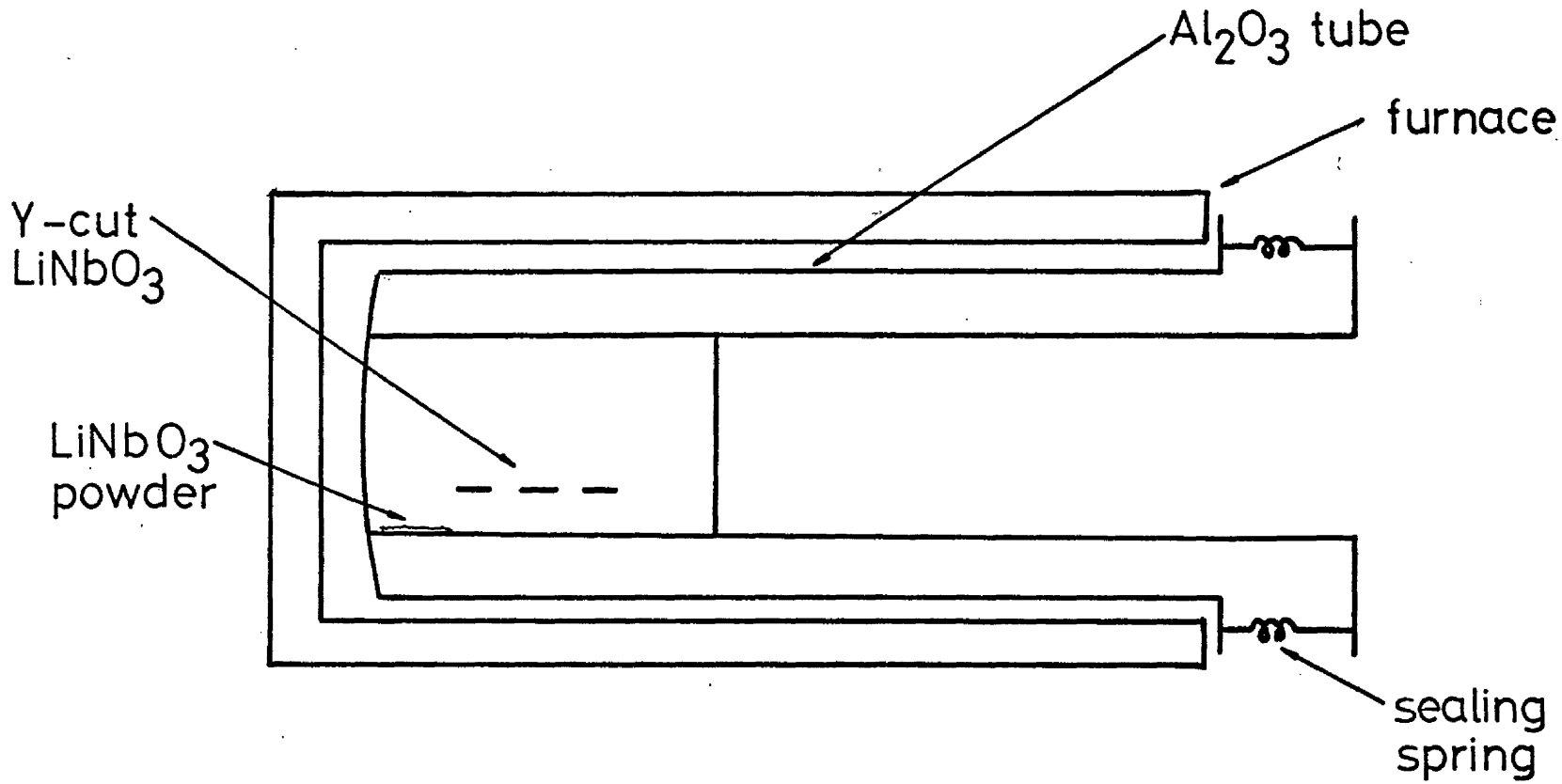

FIG 4.10 Closed tube system for Ti:indiffusion in $LiNbO_3$

fabrication and low scattering loss in the periodic region.

References

4.1 T.G. Giallorenzi, E.J. West, R.Kirk and R.A. Andrews
Appl. Opt., 12 p.1240 (1973)

4.2 H.F. Taylor, W.E. Martin, D.B. Hall and V.N. Smiley
Appl. Phys. Lett., 21 p.95 (1972)

4.3 T. Izawa and H. Nakagome
Appl. Phys. Lett., 21 p.584 (1972)

4.4 I.P. Kaminow and J.R. Carruthers
Appl. Phys. Lett., 22 p.326 (1973)

4.5 R.V. Schmidt and I.P. Kaminow
Appl. Phys. Lett., 25 p.458 (1974)

4.6 R.D. Stanley and V. Ramaswamy
Appl. Phys. Lett., 25 p.711 (1974)

4.7 J.G. Gallagher and R.M. De La Rue
Electron. Lett., 12 p.397 (1976)

4.8 G. Stewart, C.A. Miller, P.J.R. Laybourn, C.D.W. Wilkinson and R.M. De La Rue
IEEE J. Quant. Elect., QE-13 p.192 (1977)

4.9 S. Valltte, G. Labruine, J.C. Deutech and J. Lizet
Appl. Opt., 16 p.1289 (1977)

4.10 L.I. Maissel and M.H. Francombe
'An introduction to Thin Films' (Gordon and Breach, New York)

4.11 J.A. Marinsky
'Ion Exchange:a series of Advances' (Dekker, New York)

4.12 G.H. Chartier, P. Jaussaud, A.D. de Oliveria and O. Parriaux
Electron. Lett., 13 p.763 (1977)

4.13 V. Neuman, O. Parriaux and L.M. Walpita
Electron. Lett., 15 p.704 (1979)

4.14 G. Stewart and P.J.R. Laybourn
IEEE J. Quant. Elect., QE-14 p.930 (1978)

4.15 R. Walker
Ph.D. Thesis, Faculty of Engineering, University of Glasgow (1980)

4.16 G. Stewart
Ph.D. Thesis, Faculty of Engineering, University of Glasgow (1979)

4.17 C.A. Miller and R.H. Hutchins
J. Phys. D, 11 p.1567 (1978)

4.18 Garfinkel H.
'Membranes:A series of Advances' vol.1 (Dekker, New York)

4.19 R.H. Doremus
J. Phys. Chem., 68 p.2212 (1964)

4.20 R.W. Laity
J. Amer. Chem. Soc., 79 p.1849 (1957)

4.21 J. Crank
'The Mathematics of Diffusion' (Clarendon Press, Oxford)

4.22 F. Helffeich and M. Plesset
J. Chem. Phys., 128 p.418 (1978)

4.23 C.D.W. Wilkinson and R. Walker
Electron. Lett., 14 p.599 (1978)

4.24 W.F. Ames
'Numerical Methods for Partial Differential Equations'
(Academic Press, London)

4.25 D.U. Von Rosenberg
'Methods for the numerical solutions of Partial Differential Equations' (Elsevier Press, New York)

4.26 A.R. Mitchel
'Computational Methods in Partial Differential Equations'
(Wiley Press, London)

4.27 G.F. Carrier and C.E. Pearson
'Partial Differential Equations-Theory and Techniques'
(Academic Press, London)

4.28 L.S. Manhu
Appl. Phys. Lett., 20 p.652 (1975)

4.29 J.L. Jackel
Appl. Phys. Lett., 37 p.739 (1980)

4.30 Y.X. Chen, W.S.C. Chang, S.S. Lau, L. Weilunski and R.L. Holman
Appl. Phys. Lett., 40 p.10 (1982)

4.31 J.L. Jackel and C.E. Rice
Appl. Phys. Lett., 41 p.508 (1982)

4.32 J.L. Jackel and C.E. Rice
Ferroelectrics, 38 p.801 (1981)

4.33 C.E. Rice and J.L. Jackel
J. Solid State Chem., 41 p.308 (1982)

4.34 J.L. Jackel, C.E. Rice and J.J. Veselka
Appl. Phys. Lett., 41 p.607 (1982)

4.35 M.De. Micheli, J. Botineaum, P. Sibillot, D.B. Ostrowsky and M. Papuchon
Opt. Comm., 42 p.101 (1982)

4.36 W.K. Burns, P.H. Klein, E.J. West and L.E. Plew
J. Appl. Phys., 50 p.6175 (1979)

4.37 L.W. Stultz
Appl. Opt., 18 p.2041 (1979)

4.38 M.K. Barnoski, B.U. Chen, T.S. Joseph, Y.Y.M. Lee and O.G. Ramer
IEEE Trans. Circ. Syst., CAS-26 p.1113 (1979)

4.39 K. Sugii, M. Fukuma and H. Iwasaski
J. Mat. Sci., 13 p.523 (1978)

4.40 R.J. Esdaile
Ph.D. Thesis, Faculty of Engineering, University of Glasgow (1979)

4.41 D.P. Kaindach, W.S. Maiorow and L.B. Meisner
Sov. Phys. Solid State, 18 p.1756 (1976)

4.42 H.D. Megaw
Acta Cryst., 24 p.583 (1968)

4.43 M.N. Armenise, C. Canali, M.De. Sario, A. Carnera, P. Mazzoldi and G. Glotti
IEEE Trans. Comp., Hybr. & Manufac. Tech., CHM-15 p.212 (1982)

4.44 P.G. Shewmon
'Diffusion in Solids' (McGraw Hill, New York)

4.45 M. Johnson and C.W. Pitt
Opt. Comm., 23 p.121 (1977)

4.46 A. McLachlan
Ph.D Thesis, Faculty of Engineering, University of Glasgow (1981)

4.47 B. Bjortorp
Ph.D. Thesis, Faculty of Engineering, University of Glasgow (to be submitted)

4.48 M. Fukuma and J. Noda
Appl. Opt., 19 p.591 (1980)

4.49 M. Minakata, S. Saito, M. Shibata and S. Miyazawa
J. Appl. Phys., 49 p.4677 (1978)

4.50 M. Minakata, S, Saito, M. Shibata and S. Miyazawa
J. Appl. Phys., 50 p.3962 (1979)

4.51 R.W. Berry, D.M. Hall and M.T. Harris
'Thin Film Technology' (Princeton, New Jersey)

4.52 L.I. Maissel and R.Glang
'Handbook of Thin Film Technology' (McGraw Hill, New York)

4.53 A.R. Neureuther and F.H. Hill
Proc. Micro. Research Institute Symposium XXlll (1974)

4.54 H.I. Smith, E. Efremow and P.L. Kelly
J. Electrochem. Soc., 121 p.1503 (1975)

4.55 J. Melngailis, H.I. Smith, N. Efremow
IEEE Trans. Elect. Dev., ED-22 p.496 (1975)

4.56 R.T. Kempworth
Rev. Sci. Intro., 43 p.740 (1972)

4.57 R.J. Esdaile
Appl. Phys. Lett., 33 p.733 (1978)

Chapter 5

Fabrication of Thin Film Bragg Deflectors by Holographic Technique

Holographic diffraction gratings, because of their accurate periodicity over long distances, have been used extensively in the fabrication of corrugated waveguide devices for integrated optics. In this chapter we will describe the various fabrication steps involved in the construction of corrugated thin film deflectors using submicron gratings. The production of thin film waveguides by sputtering is discussed first, followed by the technique used to produce the submicron holographic gratings, and finally the ion-beam milling step used to transfer the pattern onto the surfaces of the waveguides.

5.1 Sputtered Thin Film Glass Waveguides

Although there is a lot of interest in the preparation and use of single crystal films for active devices in integrated optics, thin amorphous dielectric films have potential for use in the fabrication of passive devices as well as for use in the connection of active devices.

Good low loss optical films have been deposited by sputtering, and many materials were successfully used as amorphous films in the fabrication of waveguiding structures [5.1-5.5]. Indeed, sputtering has emerged in recent years as one of the most versatile techniques in thin film technology.

5.1.1 Basic Mechanism

Sputtering is a process which involves the transport of material from a source, called a target, to a substrate of almost any other material. The ejection of the source material is accomplished by the bombardment of the surface of the target with energetic gas ions accelerated by a high voltage. Particles are ejected from the target as a result of momentum transfer between the incident ions and the target. These ejected particles traverse the vacuum chamber and are subsequently deposited on a substrate as a thin film.

Some of the impact energy in sputtering, however, results in heat rather than ejection of a target atom. This heat is undesirable, and is removed by water cooling the back surface of the target.

The early process was DC (direct current) sputtering, and is only useful in laying down a metallic film (with an insulating target the charge delivered by the arriving ions cannot leak away and builds up, eventually repelling any further ions and preventing sputtering). RF (radio frequency) sputtering, proposed by Wehner[5.6] and demonstrated by Anderson et al.[5.7], expands the uses of sputtering to dielectric materials. By applying a high frequency potential across the plasma by two disc electrodes, one of which is usually a metal backing bonded to the dielectric target, the positive charge accumulated by the dielectric surface in one half cycle is neutralised by electron bombardment during the other half cycle, because no net current can flow to the dielectric surface.

However, because the mobility of electrons is about 10^5 times greater than the ion mobility, the neutralization and negative charging of the surface takes place in only a fraction of the half period during which the backing electrode is positive. The average target potential is therefore negative and positive ion bombardment occurs during most of the cycle, provided that the frequency is suitably chosen. This r.f. sputtering, or glow discharge, gives the added advantage of allowing work to be done under low pressure conditions (typically $1x10^{-3}$ - $5x10^{-3}$ Torr).

5.1.2 Sputtering Apparatus

The sputtering apparatus consists essentially of four components : a vacuum system to evacuate the chamber, a target, a power supply and the sputtering chamber.

A sputtering system, using a standard Edwards 6" diffusion pump incorporating a liquid nitrogen trap (pumping speed 400 litres/sec. at the sputtering pressure of $1.5x10^{-3}$ Torr), had been constructed in our department[5.8]. The system has a twin-headed arrangement (known as Hydra), and both chambers are identical in construction, consisting of an aluminium water cooled baseplate and substrate table, surmounted by a 30cm diameter pyrex cylinder (Fig. 5.1). The electrode assembly, being made of aluminium and water cooled as well, forms an integral part of the chamber top plate. Three standard microscope slides can be put into the chamber at one time, and the target to substrate distance is 3-4 cm. A toroidal

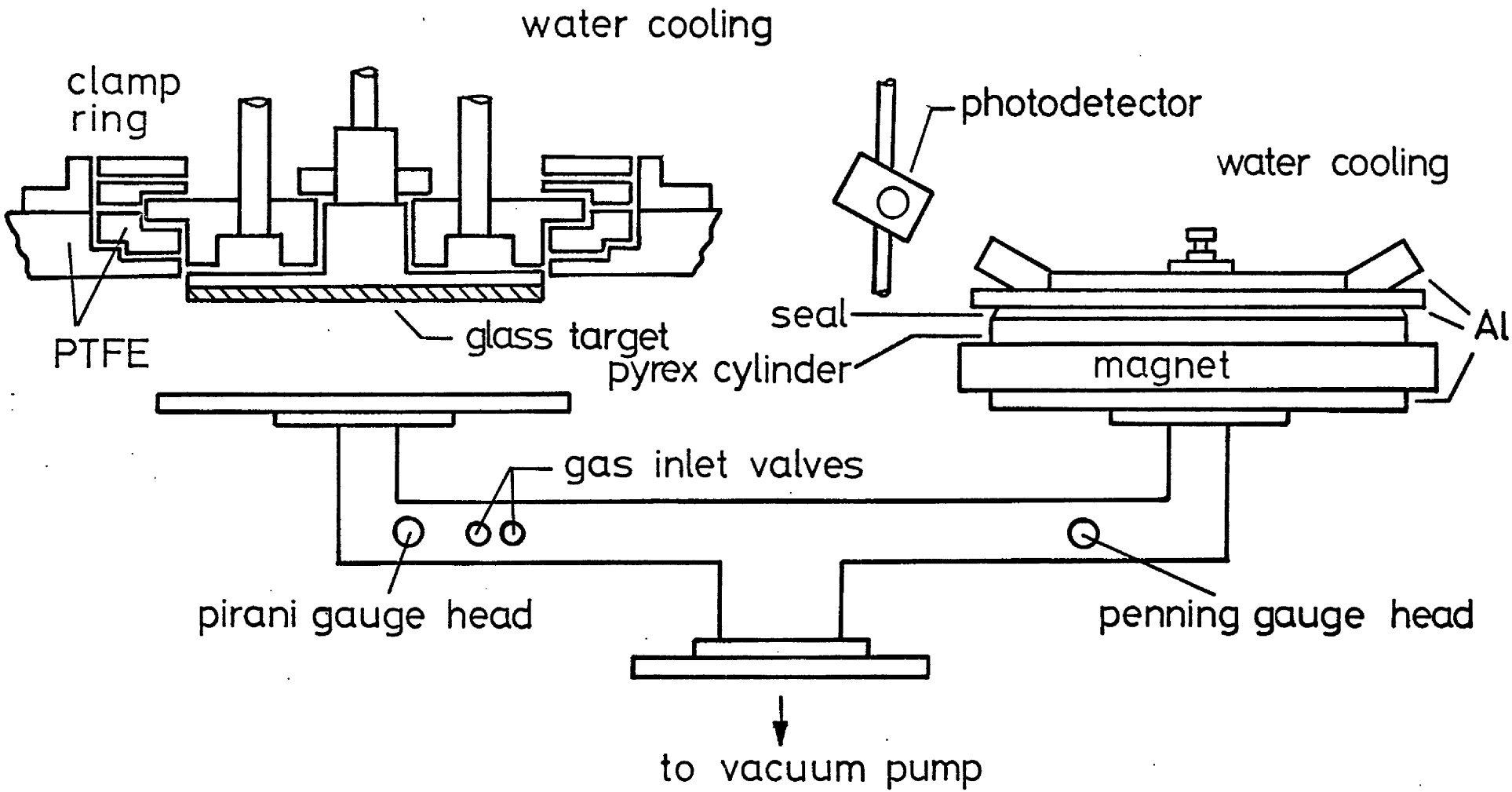

FIG 5.1 Schematic diagram of the sputtering apparatus

electromagnet surrounding the pyrex cylinder helps to confine the plasma.

A crystal controlled r.f. generator (working frequency 13.56 MHz, peak to peak voltage up to 6 KV, and power up to 1.5 KW) feeds power via a 50 ohms coaxial cable and a π-type matching network. The r.f. current to each electrode is measured by thermocouple meters, and the forward and reflected powers are measured by standing wave ratio detectors.

The film deposition thickness is measured by means of an optical monitor (as used in the titanium deposition unit, subsection 4.4.4.3), with an accuracy of better than 10%, as checked by a Hobson Talystep instrument.

5.1.3 Sputtered Corning 7059 Glass Waveguides

In our department the sputtering work has been concentrated on sputtering Corning 7059 glass (composition : 50.2% SiO_2, 25.1% BaO, 13% B_2O_3, 10.7% Al_2O_3 and 0.4% As_2O_3) onto soda-lime microscope slide. The constant input gas composition of 80% Argon:20% Oxygen is a compromise as the optical loss of the film increases with decreasing O_2 content in the plasma, while the deposition rate increases with the percentage of argon in the plasma. With a gas of pressure 2×10^{-3} Torr, and constant r.f. power (head current reading of 6 Amperes), the deposition rate ($\sim$ 0.4 μm/hr) and refractive index (1.567 at 0.633μm wavelength) of the sputtered film are found to be extremely consistent from run to run. Hence films of well defined thickness can be produced by sputtering for a pre-

determined period.

Experimental observation indicates that the sputtered film does not have the same composition as the target material, the sputtered layer having a higher index than the bulk material. Nishimura et al.[5.9] found that the sputtered films have a different barium content than the bulk. This can be attributed to the fact that the different atoms from the cathode may not all find a suitable bonding site within a given time period, and are re-emitted. Therefore some types of atoms stick to the surface better than others, resulting in a changed composition.

The losses of the single mode waveguides produced were measured to be less than 0.5 dB/cm, and the film thickness was uniform over an area of 25mm diameter. The quality of the waveguide can in principle be further improved by laser annealing with a CO_2 lasser[5.10], but that was not necessary in our work.

5.2 Holographic Diffraction Gratings

The fabrication of gratings by holographic interference as opposed to electron beam methods[5.11] was first proposed by Denisyuk[5.12] with a view to spectrographic applications, and had been carried out in this department since 1969[5.13].

Submicron photoresist gratings are fabricated by holographically exposing a thin film of resist to the interference pattern of two plane waves of blue argon laser light at an appropriate angle, followed by development of the resist,

hence the term 'exposure and development', or ED method. Precise periodicity control is possible[5.14], and curved[5.15] and chirped[5.16] gratings have been demonstrated using spherical wavefronts instead of plane wavefronts.

Another method, called Simultaneous Exposure and Development (SED) [5.17], involves exposure of the sample inside a container filled with developer so that the resist is removed as it is exposed, thus reducing the effect of absorption on exposure parameters. This SED method is superior to the ED method because gratings with grooves cut down to the substrates are readily obtainable; it is difficult for the ED method to produce such gratings because exposure parameters are difficult to control. A SED cell was constructed from aluminium and had two rectangular shaped quartz windows optically flat to $\lambda/20$ (to preserve good quality wavefronts). The inner wall of the cell was specially coated to prevent chemical reaction betweeen the cell and the developer. Unfortunately some reactions did occur, and the windows were contaminated. Organic solvents had no effect on such contamination, and it was expensive to repolish the windows. Since it was not necessary to have gratings with grooves cut down to the substrates for ion-beam milling, the ED method was adopted for fabrication of grating patterns.

In the following subsections, we will discuss the properties of the photoresist used, the interferometer set-up, and the experimental photoresist gratings produced.

5.2.1 Characteristics of AZ 1350J Photoresist

The general properties of the Shipley AZ positive photoresist were mentioned briefly in subsection 4.4.1.2. Neureuther and Dill[5.18] discussed in detail the AZ1350J photoresist, and showed that the resist exposure response is nonlinear, and can be expressed mathematically as follows:

$$\partial I(x,t)/\partial x = -I(x,t)\ [A.M(x,t) + B] \qquad (5.2.1)$$

$$\partial M/\partial t = -I(x,t).M(x,t).C \qquad (5.2.2)$$

where the coordinate x is normal to the resist film, t is the time, I(x,t) is the light intensity, and M(x,t) is the fractional concentration of the diazide compound. When M is unity, the resist dissolution rate is negligible. When M is reduced, the rate rapidly increases. The constants A, B and C can be evaluated empirically from a plot of the optical transmission of the resist film as a function of time. The dissolution rate R in a 1:1 mixture of water and AZ developer can also be modelled by the following equation:

$$R = \exp\ (E_1 + E_2M + E_3M^2) \qquad (5.2.3)$$

where E_1, E_2 and E_3 are constants, M is the fractional concentration of inhibitor, and R is in Å/sec.

On this basis, one can calculate numerically the relief structure in a resist film, given the light intensity distribution, the exposure time, and the development time. Dill

et al.[5.19,5.20] have further extended their work, and examined the effects of temperature on the resist. Various other workers[5.21-5.24] have also tried to characterize AZ series positive photoresist.

The behaviour of photoresist depends strongly on parameters such as exposure, development, temperature, humidity and so on, and there is no fixed precise processing method. Because of this, we base our work on data previously obtained in this department[5.25].

Because standing waves occur in the resist film normal to the glass substrate during exposure, the optimum thickness of the resist is about one-half of the grating period[5.22]. In our work, a grating period of approximately 0.3μm was used (appropriate for right angle deflection of guided light), which requires a resist thickness of about 0.15μm.

The thickness of resist films depends on the spin speed, duration of spinning, and ratio of resist to AZ thinner, and follows the relation[5.26]

$$t = k\, D^2/\sqrt{S} \qquad (5.2.4)$$

where k is a constant, D is the percentage of solid in the resist, and S is the spinning speed. Fig. 5.2 shows the thickness of diluted resist (1 part resist:3 parts AZ thinner) at various spinning times and speeds. The thickness (at the centre of the substrate) was measured using an ellipsometer, and checked with a Talystep surfometer. For resist films spun on

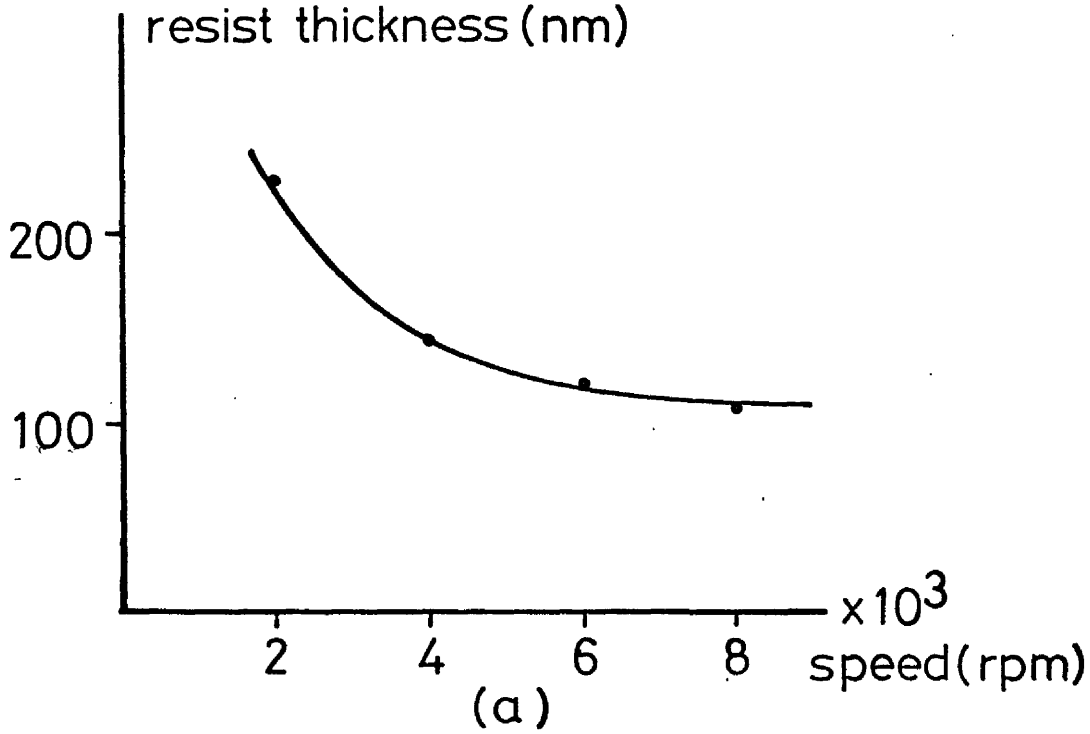

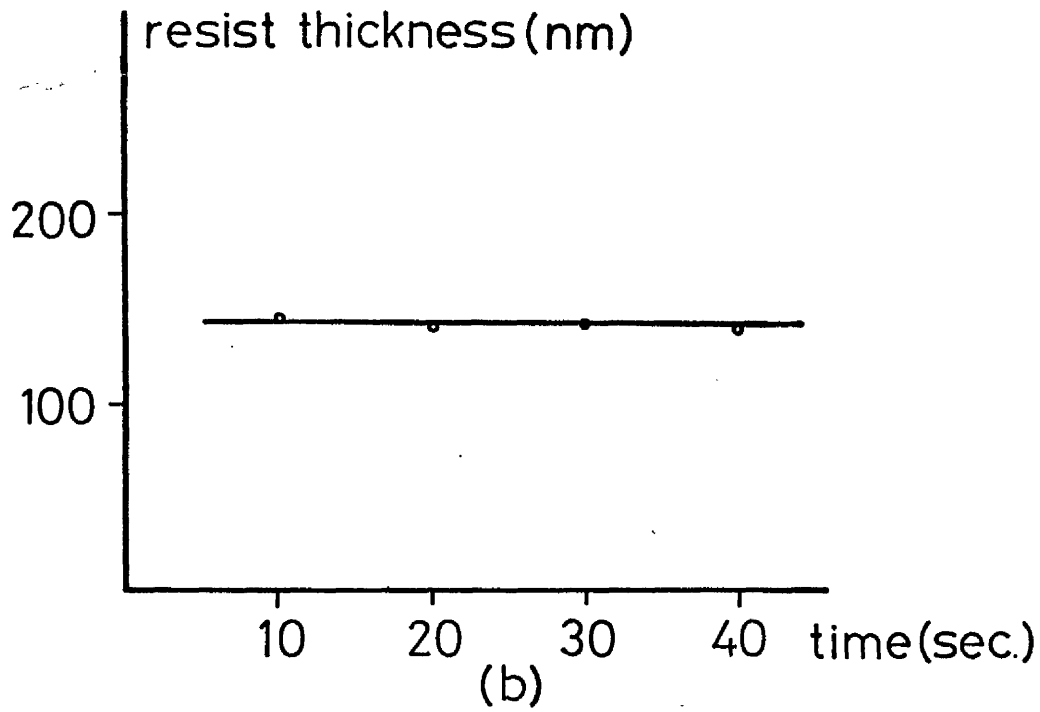

FIG 5.2 Thickness of diluted (1 part resist : 3 parts thinner) resist at various (a) spinning speeds and (b) times

large substrate, the thickness decreases with distance from the axis (Fig. 5.3). Throughout our work, a dilution of 1:3 (25% resist), a spinning speed of 4000rpm for 20 seconds, and pre-expose baking at 75°C for 30 minutes on an open hot plate was used. The average film thickness was 0.14μm, and the standard deviation from batch to batch was 10%.

The exposure and development characteristics of AZ1350J photoresist to the 457.9nm argon ion laser line are shown in Fig. 5.4(a) and 5.4(b). A contact mask was used to protect half the sample during exposure, so that a step was produced on development for thickness measurements. The incident exposure power was measured using an UDT Model 122 power meter, calibrated at 457.9nm. After development the samples were rinsed in filtered (1μm) water, and blown dry with nitrogen gas. In the manufacture of gratings, we fixed the development time, and varied the exposure time to compensate for any variation in the parameters for consistent results.

5.2.2 Interferometer Arrangement

The interferometer set-up for exposing the resist is shown in Fig. 5.5. The 457.9nm line of a Spectra Physics Model 165 argon ion laser, after going through a spatial filter (a combination of microscope objective and 20μm pinhole) was collimated using a plano-convex lens in 'best form' arrangement to minimise aberrations, and checked for phase accuracy with a shearing interferometer[5.27]. This gave a 20mm diameter beam

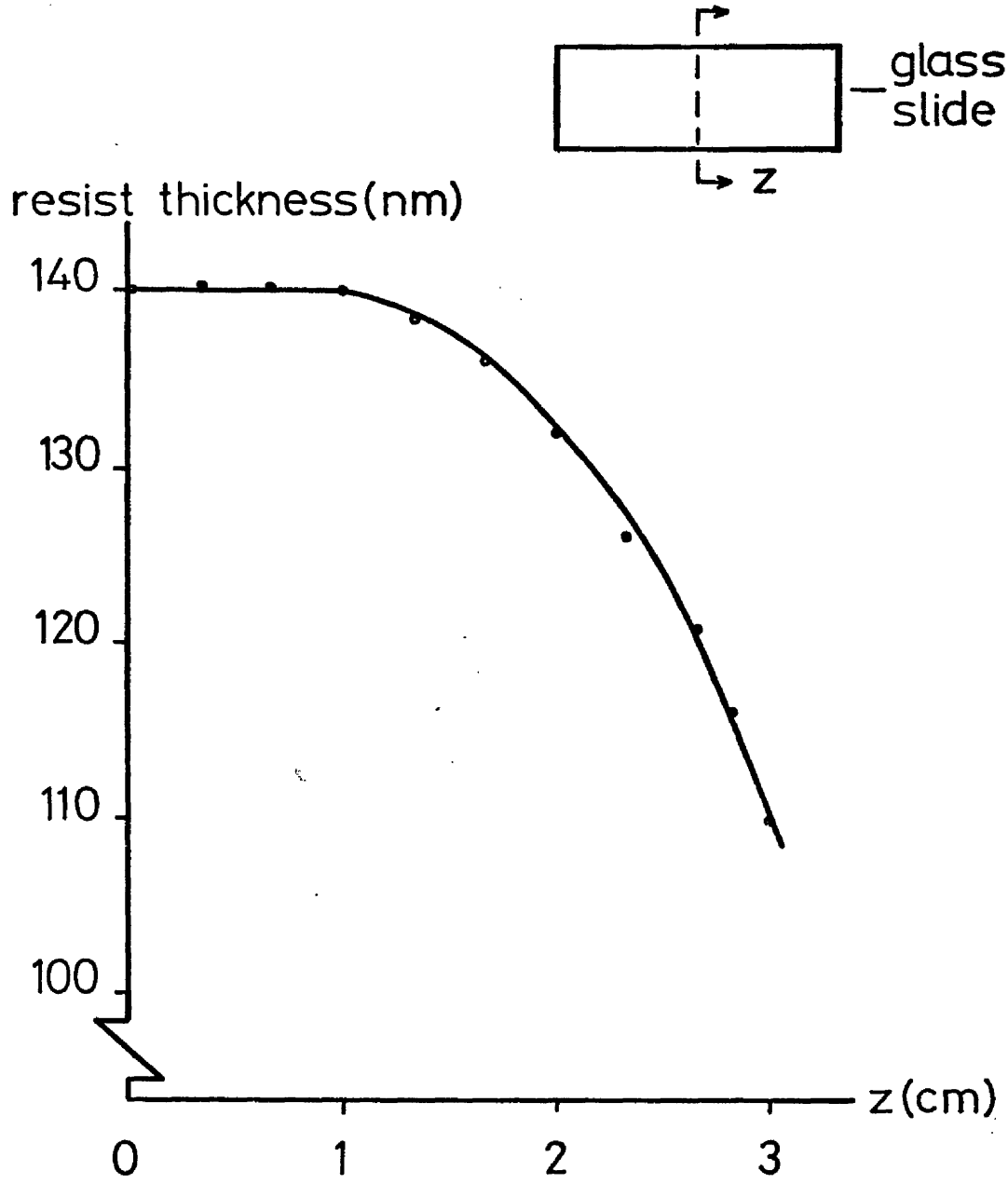

FIG 5.3 Resist thickness along the length of a glass slide (diluted 1:3 in thinner, ω = 4000 rpm, t = 20 sec)

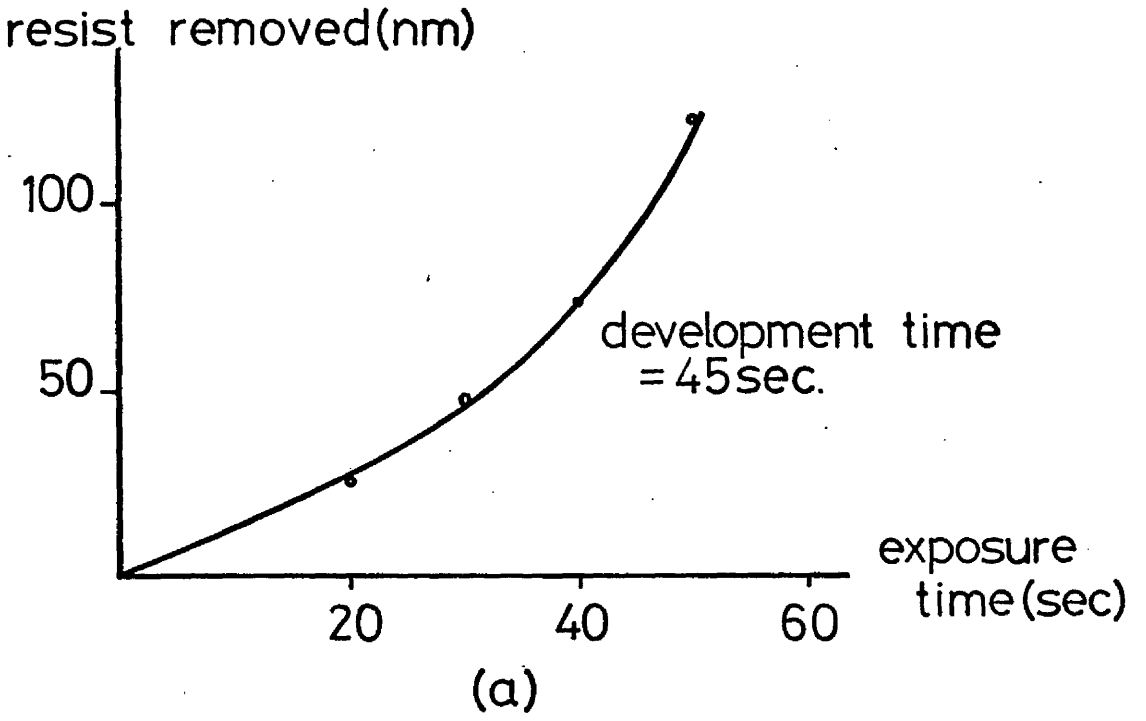

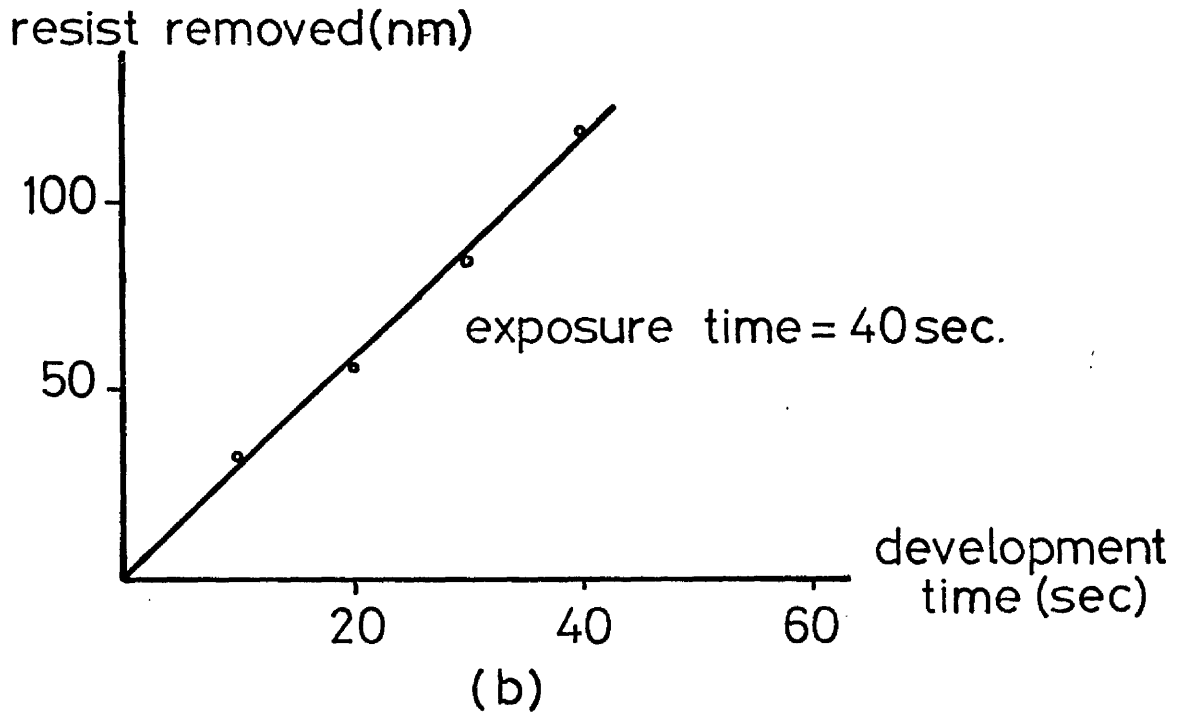

FIG 5.4 Exposure (a) and development (b) characteristics of AZ 1350J resist (λ=457.9nm, 30mW/cm^2)

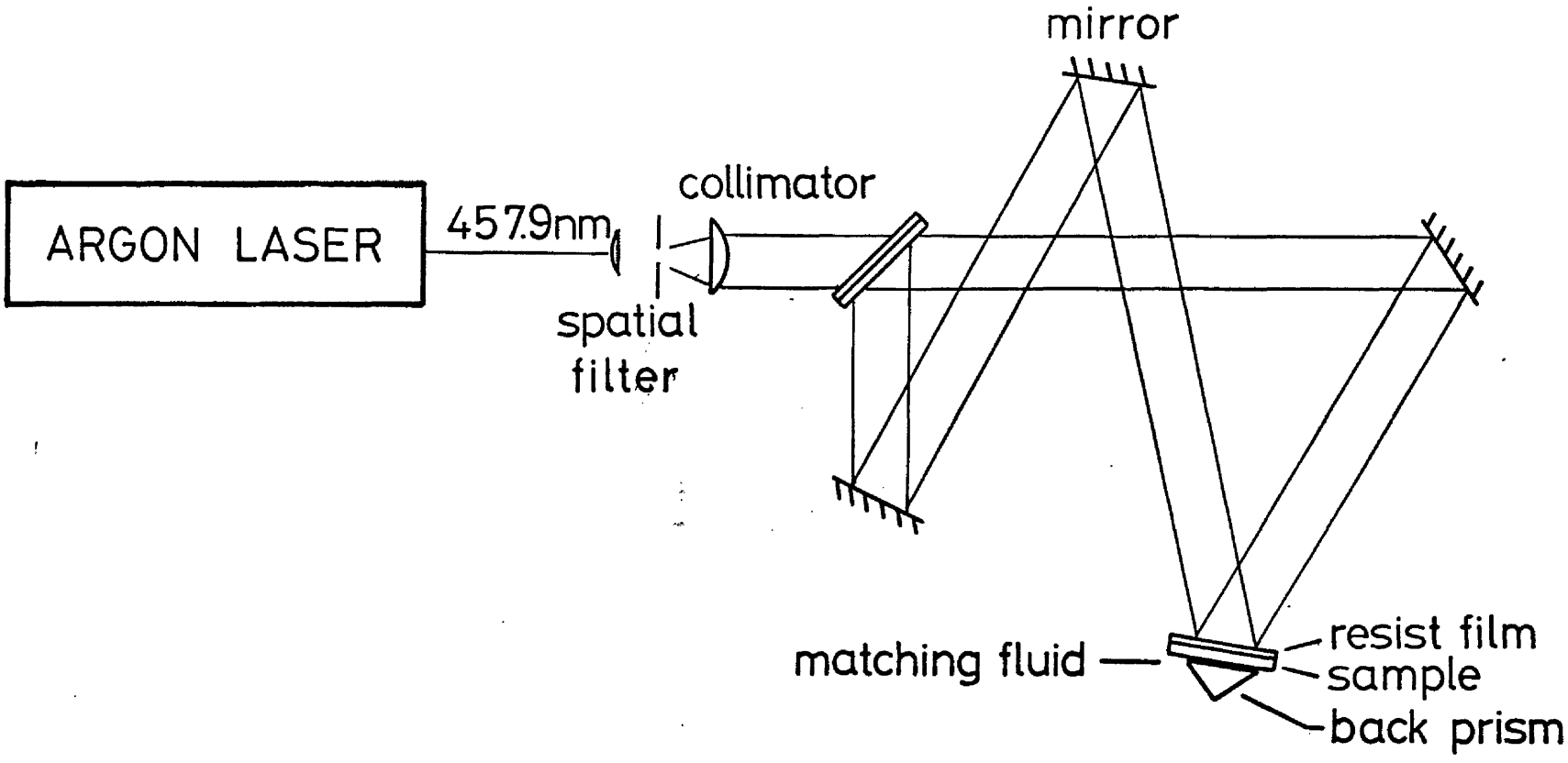

FIG 5.5 The three-mirror interferometer arrangement

and single TEM_{oo} mode operation (by adjustment of the intra-activity aperture of the laser). The stabilised output power was ~70mW, and the effective beam diameter ($1/e^2$ points) was about 11mm. The beam was then split into two by means of a dielectric-coated beam splitter (the surfaces were optically flat to $\lambda/20$ and were slightly wedged to reduce secondary reflections), and recombined via the three mirrors on the sample supported by a goniometer stage at an angle Θ with respect to the normal of the sample. The three-mirror system prevents lateral inversion of the superimposed beams and ensures equal path lengths to the sample. The period of the grating in this case is given by

$$\Lambda = \lambda_o / 2 \sin \Theta \qquad (5.2.5)$$

where λ_o is the free space wavelength of the laser light, and 2Θ is the angle between the two beams.

A good optical table top (from Ealing) enables accurate alignment of the components of the interferometer to a horizontal plane. Another important alignment would be the adjustment of the intensities of two interfering beams. Ideally, the two beams would have equal intensities. However, experimental and theoretical results[5.22] indicate that slight variations in the intensities are tolerable. Considering the fringe visibility F for two interfering beams of intensities I_1 and I_2[5.28]

$$F = (I_{max}-I_{min})/(I_{max}+I_{min}) = 2\sqrt{I_1 I_2}/(I_1+I_2) \qquad (5.2.6)$$

where I_{max} and I_{min} are the maximum and minimum intensities in the fringe pattern. For a 10% difference in beam intensities, the fringe visibility decreases by only 0.14%.

An alternative arrangement, composed of two spatial filters and two mirrors (Fig. 5.6), was also tested. It was found that the quality of the gratings, as examined under a scanning electron microscope, did not improve drastically[5.22], and since this system was more troublesome to use (every time a new angle was chosen, the spatial filters and collimators had to be re-adjusted), the three mirror system was adopted.

A similar arrangement, using UV radiation at 351.1nm, was also set up (Fig. 5.7). An anti-reflection coated prism was used to separate the two lines (351.1nm and 363.8nm) emittted from the argon ion laser, and a 10μm pinhole was used in the spatial filter. With this set-up, gratings with periodicity down to 0.2μm were produced without the need for the front prism technique[5.29]. Because the argon laser was not designed to lase in the UV, mode hopping was observed. The quality of the gratings as similar to that obtained using the 457.9nm set-up, and since the UV laser arrangement was primarily intended for another project, most of our work was done using the 457.9nm set-up.

Attempts were made to remove the resist remaining between grating lines by oxygen plasma ashing[5.30]. The etching reactor includes a vacuum chamber and vacuum pump, a power supply to energize the discharge, and a valve to control the flow of gas to the chamber. The samples were placed

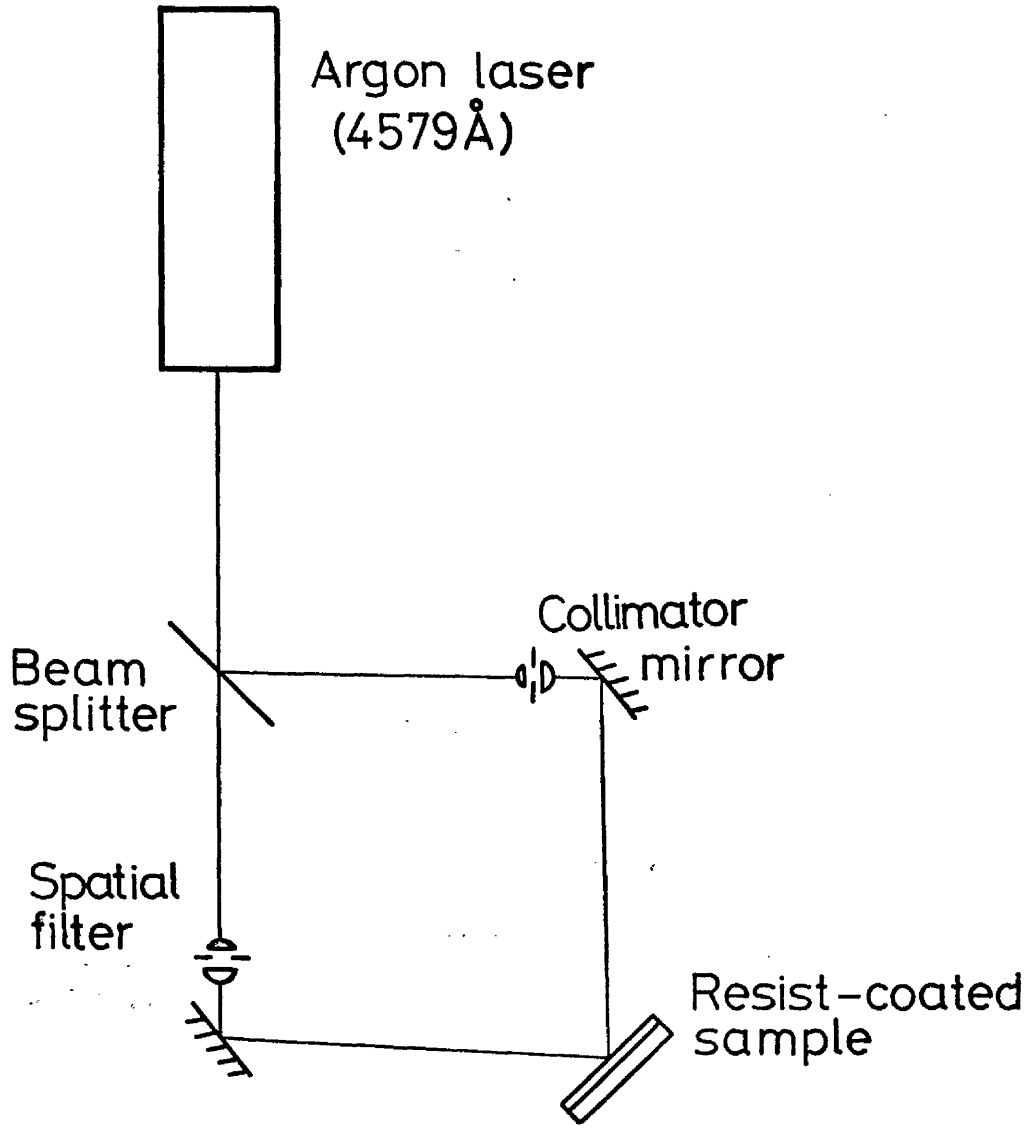

FIG 5.6 The two-mirror interferometer arrangement

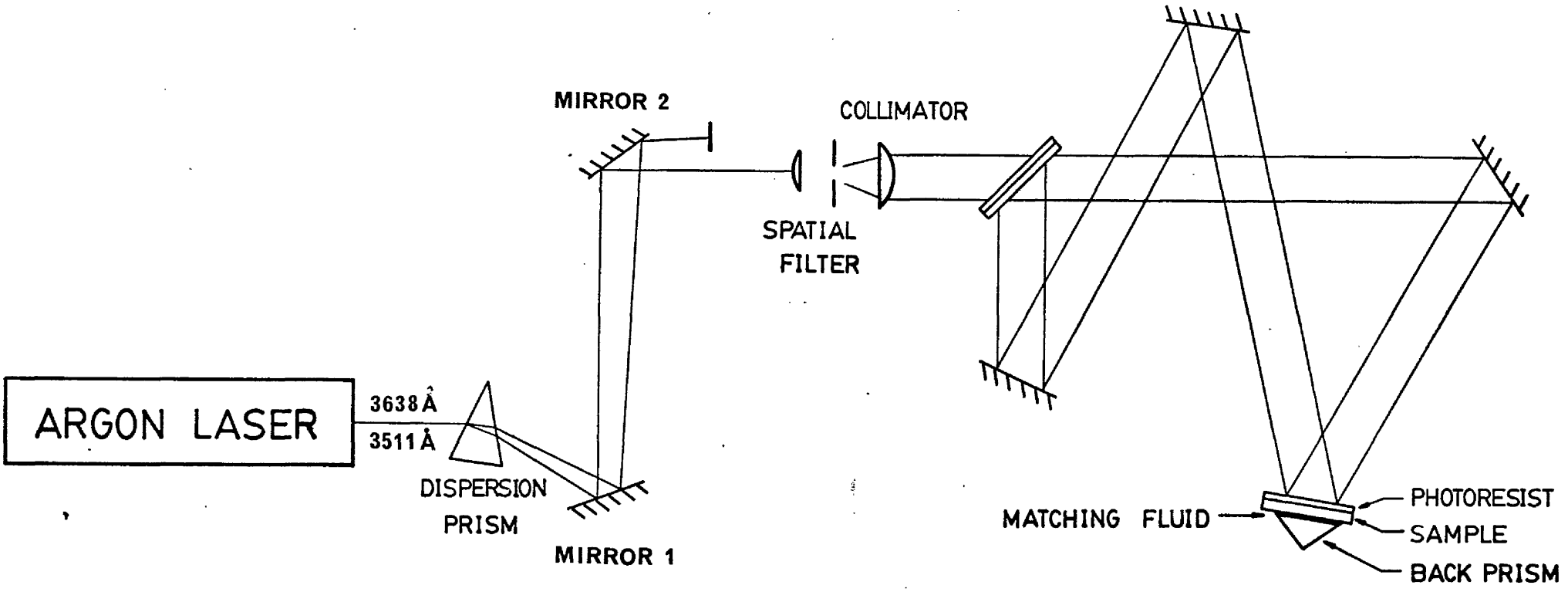

FIG 5.7 Basic interferometer arrangement for producing holographic diffraction grating

horizontally in the cylindrical-shaped chamber, and r.f. power was applied to a coil wound round the chamber. Fig. 5.8 shows typical plots of variation in grating height with respect to etching time. The heights were calculated from diffraction efficiency measurements[5.31-5.33]. Unfortunately no conclusive results could be drawn from these experiments, although L. D. Westbrook et al.[5.34] reported having successfully used this method to obtain resist gratings cut down to the substrates.

5.2.3 Quality of Photoresist Gratings

Good quality resist gratings with periodicity 0.3μm were successfully manufactured using the three-mirror arrangement. Fig. 5.9 shows SEM pictures of a typical photoresist grating, at both high and low magnification. As can be seen in these pictures, spurious modulations from unwanted multiple reflections in the interferometer set-up were minimised. Diffraction efficiency measurements (obtained by scanning the grating pattern with a HeCd laser beam, λ_o= 325nm, spot size $\sim$ 50μm) showed that the gratings were uniform in height over an area of $\sim$7mm diameter (Fig. 5.10). The ripple effect is due to the absorption of the incident light by the resist. No such effect was observed for an ion-beam etched grating (Fig. 5.10).

Fig. 5.11 shows SEM pictures of a short period (Λ0.2μm) grating, using the UV interferometer. Again high quality gratings were possible.

Grating patches of desirable dimensions were

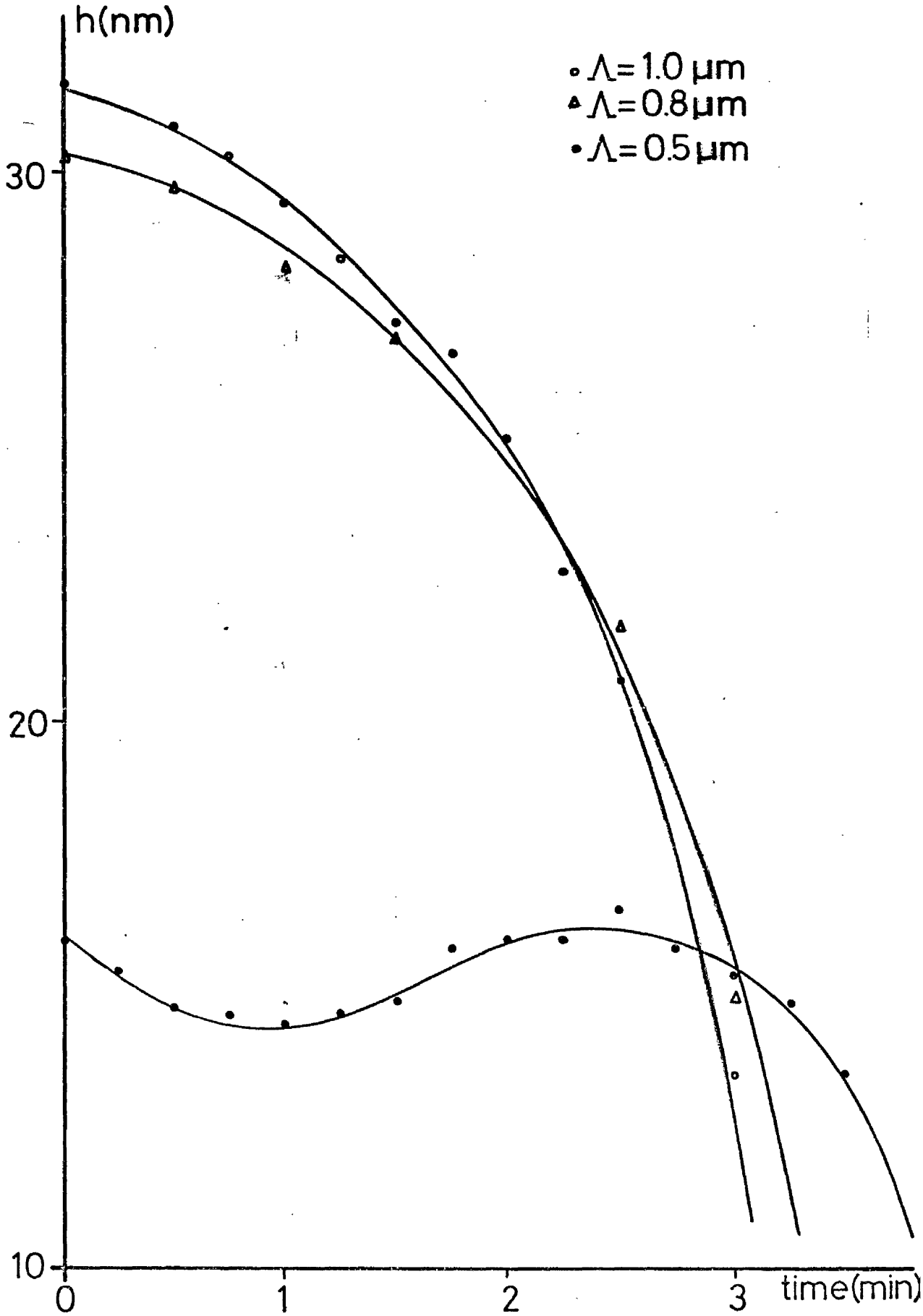

FIG 5.8 Removal rate of AZ1350J resist gratings by plasma ashing

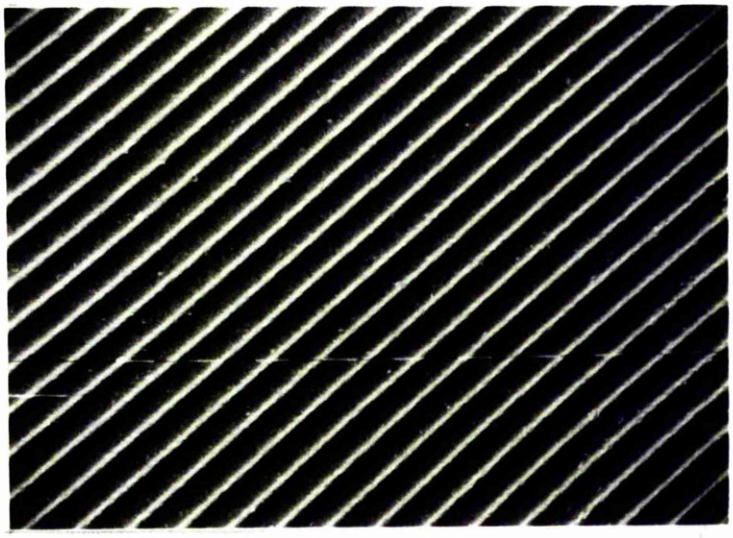

(a) High magnification

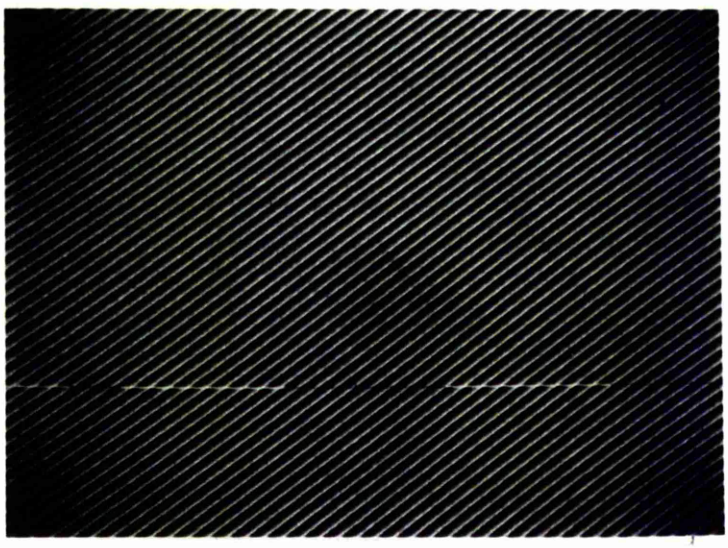

(b) Low magnification

FIG 5.9 SEM photographs of a photoresist grating (Λ= 0.3μm)

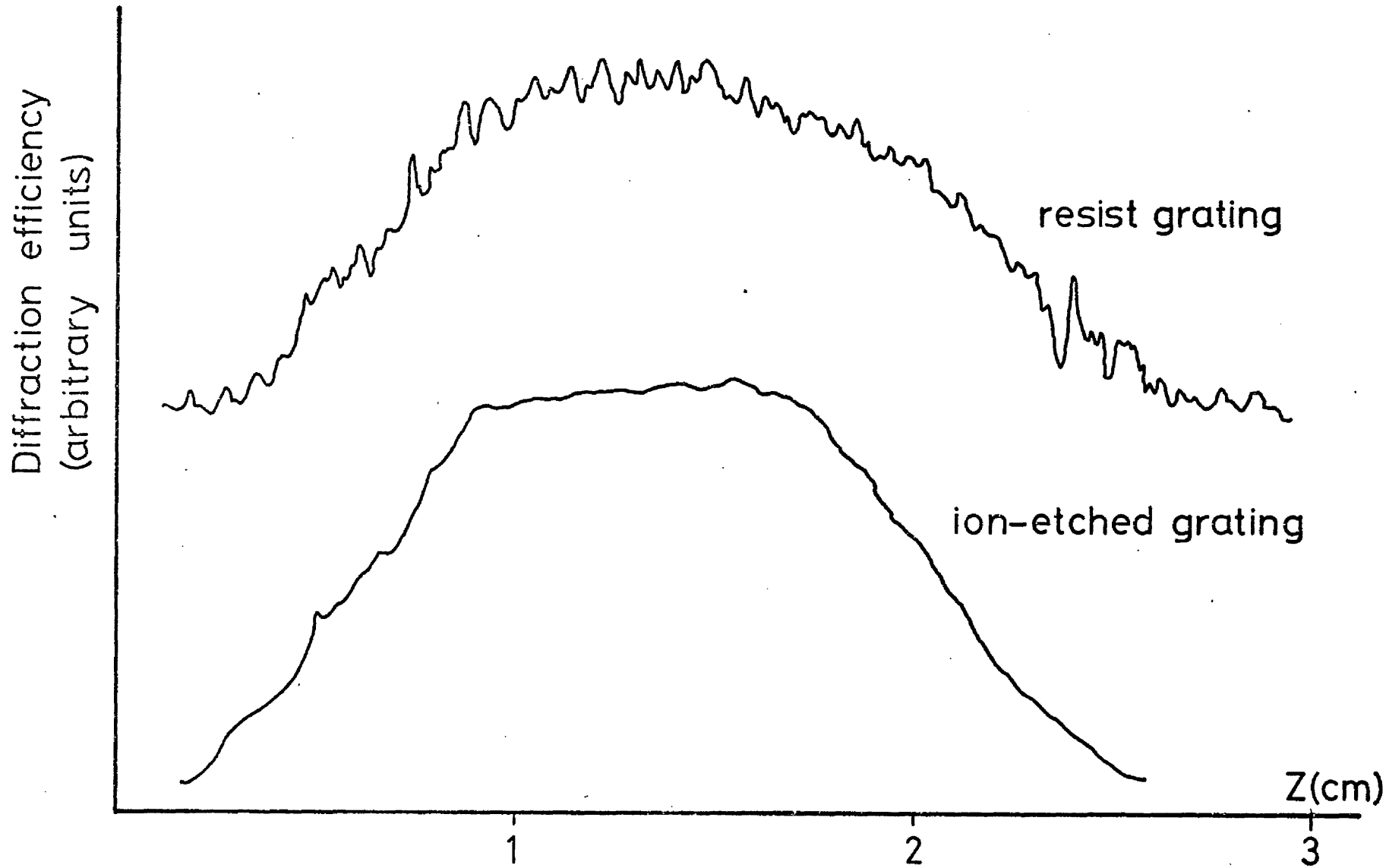

FIG 5.10 Diffraction efficiency measurements showing uniformity in height of gratings fabricated

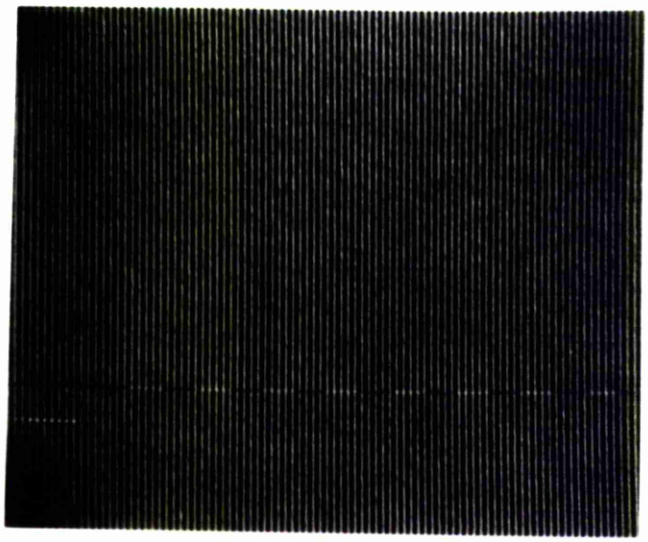

(a) High magnification

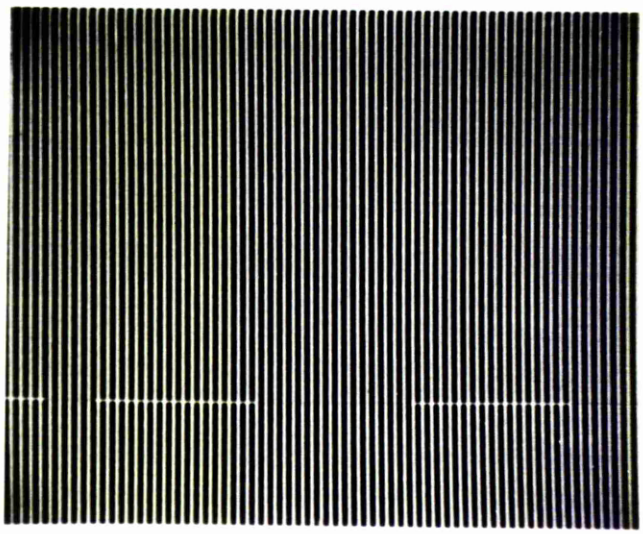

(b) Low magnification

FIG 5.11 SEM pictures of a resist grating ($\Lambda = 0.2\,\mu m$)

subsequently cut out of the recorded pattern by photolithographic technique, using a photographic emulsion mask and a mercury lamp. Care was taken to align the mask within the area defined by the half-power points of the Gaussian beam used to record the grating, in order to minimise variation in the grating groove depth. After rinsing and drying, the samples were ready for one further process, ion-beam milling.

5.3 Ion Beam Milling

Ion beam milling (or etching) using inert gas ions is widely used in transferring a mask pattern (either metal or photoresist) onto a substrate material[5.35-5.40]. The main advantages are : control of the direction of ions, allowing some control over step edge profiles; lower gas pressure, minimizing back scattering contamination; ion current density and energy can be controlled independently, allowing quantitative evaluation of etch rates. Recently, reactive gases have also been used, combining some of the advantages of ion beam milling with the anisotropic etching and selectivity of reactive ion etching[5.41].

5.3.1 Basic Mechanism

In ion milling, ions are extracted from a gaseous plasma (generated far away from the substrates) and accelerated by a dc

potential towards the substrates where the surface erosion is caused by momentum transfer.

The rate of ion milling is related to the impinging ion flux density and the sputtering yield (defined as the number of atoms ejected from the substrate per incident ion). The former factor is related to the ion source design, while the sputter yield depends on the compositions of the substrate and of the ion beam, the ion aceleration voltage, and the angle of incidence of the beam onto the substrate. Theoretical analysis of the processes have been give by several workers[5.42,5.43], in particular Ducommum et al.[5.44] and Johnson[5.45]. Both use the faceting phenomenon of ion beam milling to determine erosion profiles of grating relief patterns on the surfaces of substrates.

This faceting effect is shown schematically in Fig. 5.12. The rounded portion (due to exposure and development conditions) at the top edge of a photoresist feature will be subjected to bombardment at various angles of incidence, ranging from perpendicular at the top ($\Theta = 0^{o}$) to grazing at the walls ($\Theta = 90^{o}$). Because the milling rate of photoresist is fastest at some angle Θ between 45^{o} and 90^{o}, a facet will form at this corner. This effect will continue until it reaches the film-resist interface, at which point the line width will start to decrease and a new facet will be milled into the thin film being etched.

In general, ion beam etching with inert gas ions is capable of producing very high resolution patterns[5.46,5.47],

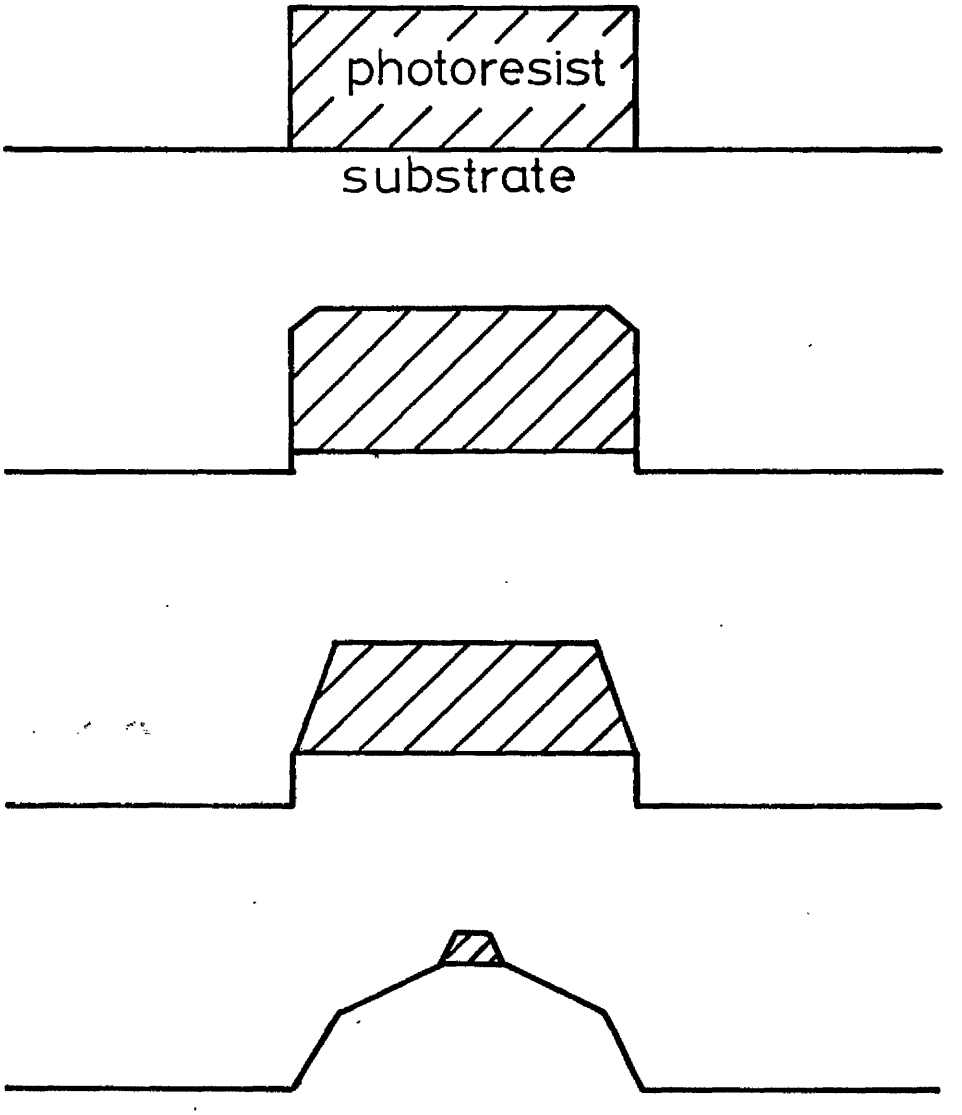

FIG 5.12 Facet formation in photoresist due to ion bombardment

with aspect ratio (ratio of depth to width of an etched feature) less than or equal to unity. For aspect ratios greater than unity, wall shapes become difficult to control, and reactive gas ions are necessary.

5.3.2 Ion Beam Etcher

A GV planar Model IB7 ion beam etching equipment was available. The system consists of a diffusion pumped vacuum chamber, a water-cooled tungsten filament wire coated with lanthanum hexaboride, power supplies for the filament, the acceleration of the ion beam and the generation of the ion plasma, and a 10cm diameter water-cooled specimen holder plate (turret) rotating at 1 rpm (Fig. 5.13). The microscope slides are thermally contacted to the plate by a paint made up of a mixture of Indium (10% by weight) and Gallium (84%).

Several modifications were made on the equipment[5.25] to improve its performance. Unfortunately no major alterations were possible because of the construction of the chamber and design of the power supplies. Nevertheless, the source-sample distance was reduced, and the gas pressure was lowered to increase the mean free path of the ions.

Experimental results indicated reasonable uniformity around the periphery of the turret, and the etch rate was a bell-shaped curve along the diameter of the turret. The pressure of the pure argon gas in the chamber was 2μm (of Hg), the beam current was set at 200 $\mu A/cm^2$, and the accelerating potential was

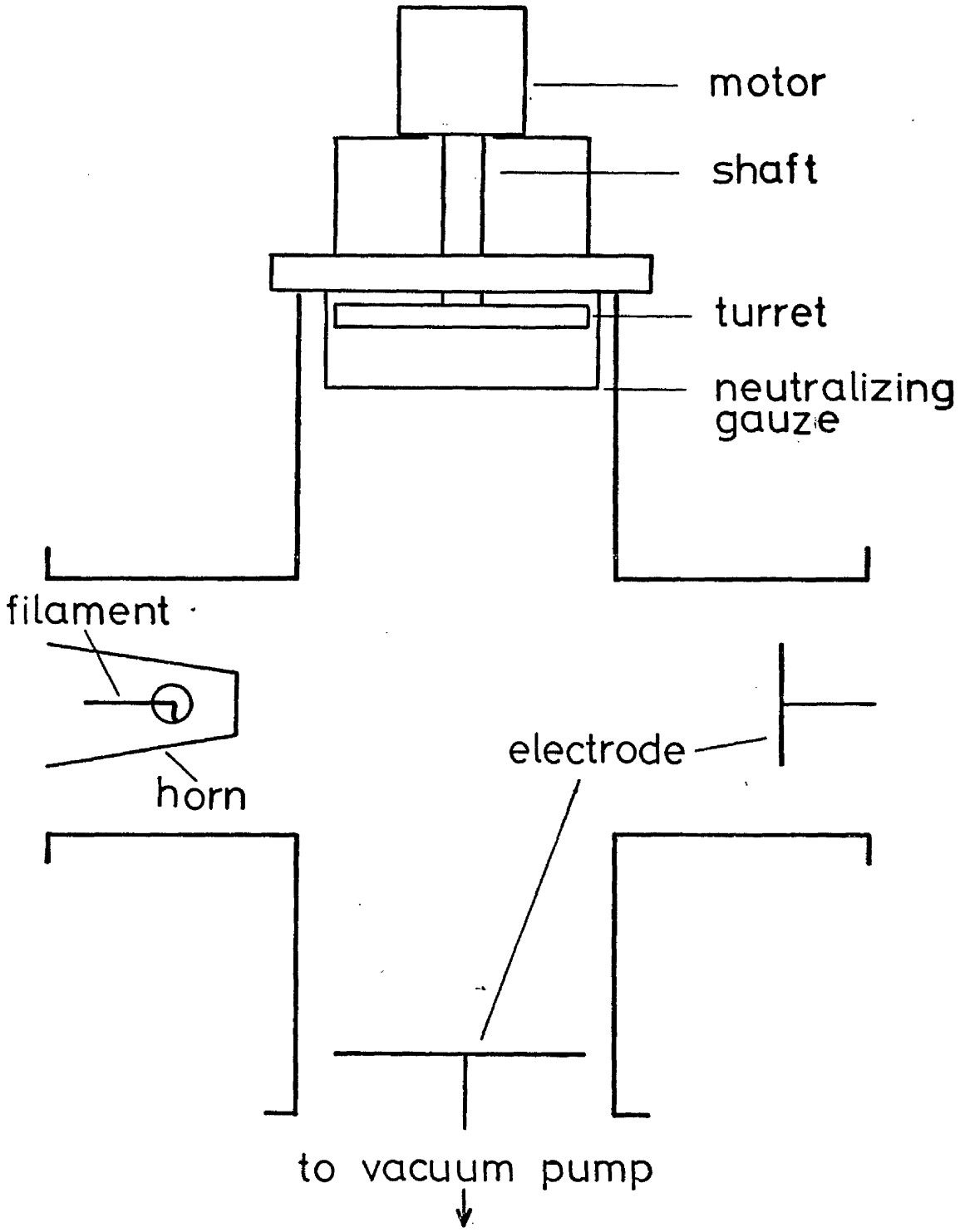

FIG 5.13 Schematic diagram of the ion beam etcher

5kV (built up at a rate of 0.5 kV/min).

There were a lot of problems with the equipment, partly because of its age (over ten years), and partly because of etching materials other than glass, for example lithium niobate through a carbon mask with butane/argon gases, or germanium. Contamination resulted from these experiments, and an oxygen run had to be carried out to clean the system.

Attempts were made to use other ion-beam etchers, and the SERC equipment at Rutherford Laboratory was used. The resolution of the machine was found to be better than 0.2μm, but due to surface contamination of the waveguides[5.48] its use was discontinued. The loss measurement of an etched silver-sodium ion exchange waveguide is shown in Fig. 5.14. Traces of chromium, aluminium and some unidentified organic residue were found on the surface. The metals may come from remains of etched chrome plate (primarily the function of this equipment) and from the substrate holder (made of aluminium).

5.3.3 Ion-etched Gratings on Glass

Because of the many problems encountered, the yield from our departmental equipment was low, less than 10%. Postbaking of the photoresist gratings was not possible because of the short periodicity, and a blistering effect of the resist sometimes occurred (Fig. 5.15). Nonetheless, occasional good results were possible, and Fig. 5.16 shows a SEM picture of a successful grating etched on sputtered 7059 glass. The sample

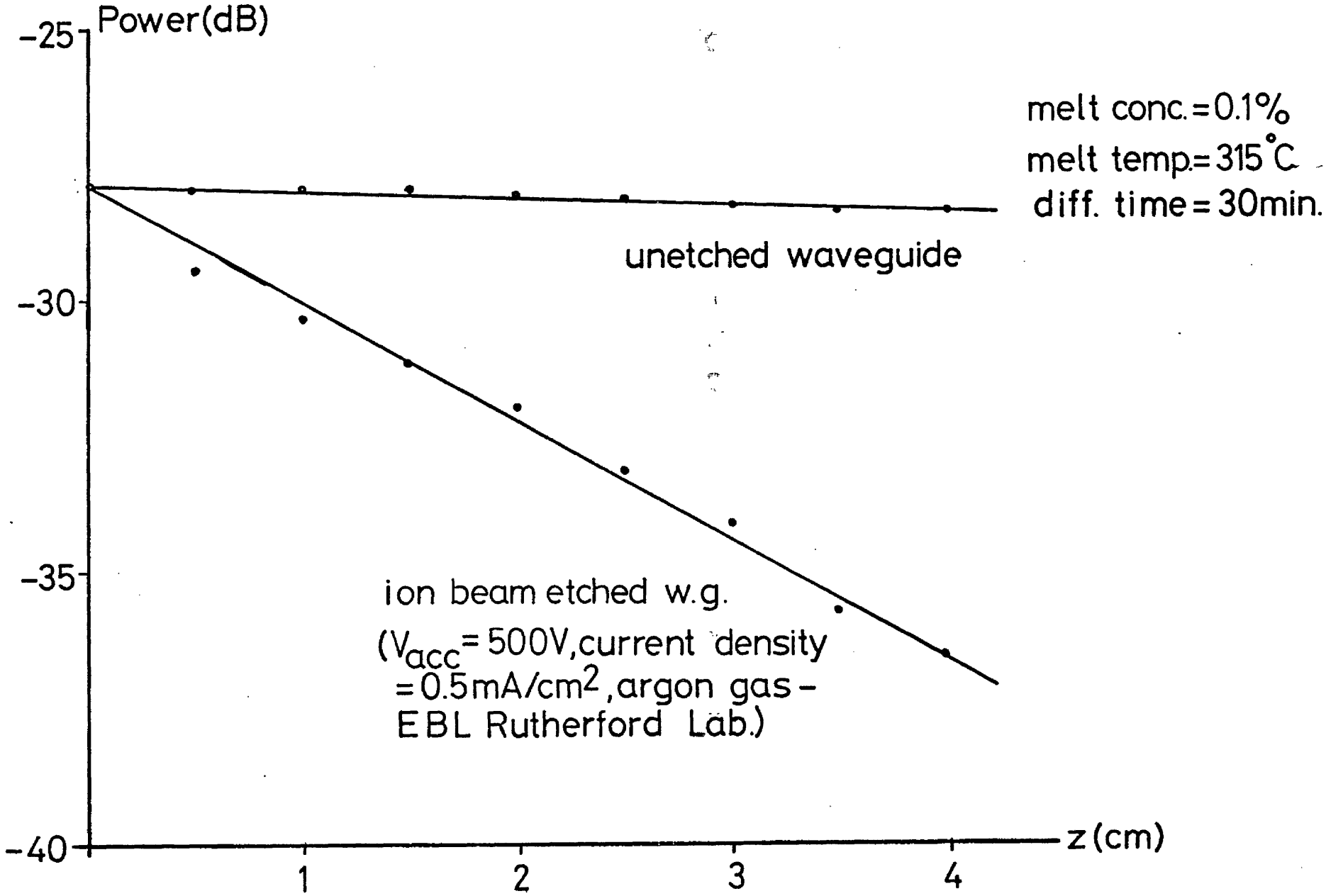

FIG 5.14 Loss measurement in diluted $AgNO_3$ ion exchanged waveguide

FIG 5.15 Blistering of the resist inside the ion beam etcher

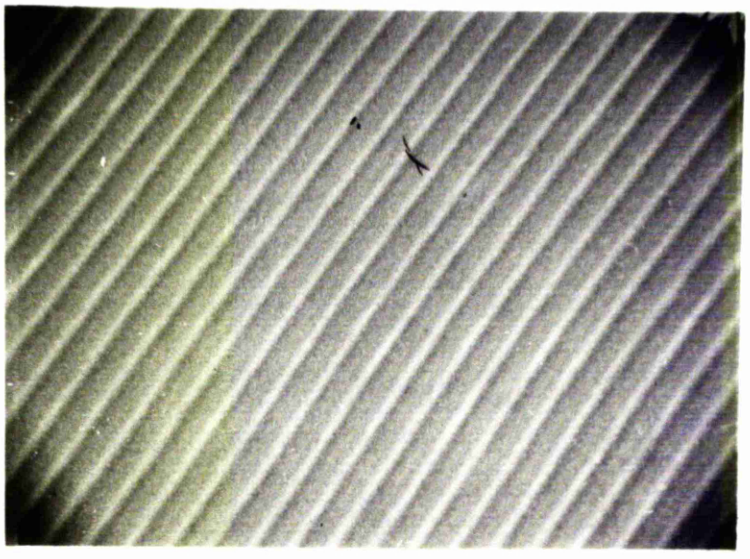

FIG 5.16 Grating etched on sputtered 7059 glass

was placed along the periphery of the turret, and the etching time was typically 25 minutes. The etch rate of the waveguide was about 230 Å/min, and of the resist about 180 Å/min. After etching, the remaining resist was normally removed by oxygen plasma ashing. Sometimes it was extremely difficult to remove the burnt resist completely, and dipping in a mixture of 7 parts concentrated H_2SO_4 and 2 parts H_2O_2 for a few minutes was necesary. Some degrading of the waveguide (increase in scattering loss) was observed.

5.4 Conclusions

We have described various fabrication steps in the manufacture of periodic waveguides with surface corrugations. The homogeneous thin-film waveguide was formed by sputtering Corning 7059 glass on Fisher brand microscope slide. The grating was made by holographic exposure (by laser light) of the photoresist film on top of the waveguide, and finally the grating relief pattern was transferred onto the surface of the waveguide by ion-beam milling. A summary of the various steps is given in Appendix 5A.

Appendix 5A

Data for the fabrication of Holographic Gratings

Resist	: Shipley AZ1350J (Europe)*
Dilution ratio	: 1 part resist to 3 parts AZ thinner
Spin speed	: 4000rpm
Spin time	: 20 seconds
Pre-bake temperature	: 75°C using open hot plate
Pre-bake time	: 30 minutes
Average thickness	: 0.14 micron
Thickness variation	: 10% from batch to batch

Humidity affects exposure parameters; it should not exceed 60% during spin-coating and baking processes.

* Shipley UK informed us that the base resin of 1350J supplied in Europe differs from that supplied in the USA.

Exposure wavelength	: 457.9 nm (351.1 nm)
Exposure power	: 25 mW (10 mW)
Exposure time	: 25 seconds (8 seconds)
Developer	: AZ developer, 1:1 dilution with water
Development time	: 1 minute
Ion milling equipment	: GV Planar (Kauffman gun with tetrode arrangement
Beam Current	: 15 mA
Acceleration potential	: 5 kV
Gas	: High purity argon
Gas pressure	: 2 microns of Hg
Etch rate	: 200 Å/min (average) for glass
Etch ratio	: unbaked AZ1350J mask/glass ~1
Mask removal	: by oxygen plasma oxidation

References

5.1 J.E. Goell and R.D. Stanley
Bell Syst. Tech. J., 48 p.3445 (1969)

5.2 C.W. Pitt
Electron. Lett., 9 p.401 (1973)

5.3 R.H. Peitch, E.J. West, T.G. Giallorenzi and J.F. Weller
Appl. Opt., 13 p.712 (1974)

5.4 W.J. Coleman
Appl. Opt., 13 p.946 (1974)

5.5 C.W. Pitt, F.R. Gfeller and R.J. Stevens
Thin Film Solids, 26 p.725 (1975)

5.6 G.K. Wehner
'Advances in Electronics and Electron Physics',vol V11 p.239 (Academic Press, New York)

5.7 G.S. Anderson, W.N. Mayer and G.K. Wehner
J. Appl. Phys., 33 p2991 (1962)

5.8 R.H. Hutchins and C.R. Stanley
Technical Memorandum of the Dept. of Elect. and Elect. Eng., University of Glasgow (1973)

5.9 T. Nishimura, Y. Murayama, K. Dota and H. Matsumaru
Digest fo the Third Symposiuim on the deposition of thin films by sputtering, p.96 (Bendix Corp. 1969)

5.10 S. Dutta, H.E. Jackon and J.T. Boyd
Appl. Phys. Lett., 37 p.512 (1980)

5.11 J.J. Turner, B. Chen, L. Yang, J.M. Ballantyne and C.L. Tang
Appl. Phys. Lett., 23 p.333 (1973)

5.12 Y. Denysiuk
Dokl. Akad. Nauk SSSR, pl44 (1962)

5.13 D.G. Dalgoutte
Ph.D. Thesis, Faculty of Engineering, University of Glasgow (1971)

5.14 S.T. Zhou, Z.Q. Lin and W.S.C. Chang
Appl. Opt., 20 p.1270 (1981)

5.15 P.K. Tien
Opt. Lett., 1 p.64 (1977)

5.16 A.C. Livanos, A. Katzir and A. Yariv
Opt. Comm., 20 p.179 (1979)

5.17 W.T. Tsang and S. Wang
Appl. Phys. Lett., 24 p.196 (1974)

5.18 A.R. Neureuther and F.H. Dill
Proc. Microwave Research Institute Symposium XXIII (1974)

5.19 F.H. Dill and J.M. Shaw
IBM J. Res. Develop., 21 p.210 (1977)

5.20 J.M. Shaw, M.A. Frisch and F.H. Dill
IBM J. Res. Develop., 21 p.219 (1977)

5.21 S. Austin and F.T. Stone
Appl. Opt., 15 p.1071 (1976)

5.22 F. Johnson, G.W. Kammlott and K.A. Inzersoll
Appl. Opt., 17 p.1165 (1978)

5.23 R.A. Bartolini
Appl. Opt., 13 p.129 (1974)

5.24 F. Iwata and J. Tsujiuchi
Appl. Opt., 13 p.1327 (1974)

5.25 A. Yi Yan
Ph.D. Thesis, Faculty of Engineering, University of Glasgow (1979)

5.26 L.F. Thompson and R.E. Kerwin
Ann. Rev. Mat. Sci., 6 p.267 (1976)

5.27 M.V.R.K. Murty
Appl. Opt., 3 p.531 (1964)

5.28 M. Born and E. Wolf
'Principles of Optics' (Pergamon Press, Oxford)

5.29 C.V. Shank and R.V. Schmidt
Appl. Phys. Lett., 23 p.154 (1973)

5.30 S.M. Irving
Electrochem. Soc. Extend. Abstr., 60 p.460 (1967)

5.31 H. Kogelnik
Proc. Sym. Modern Optics (Polytechnics Press, Brooklyn, New York)

5.32 D. Marcuse
Bell Syst. Tech. J., 51 p.1801 (1972)

5.33 W.J. Tomlinson and H.P. Weber
J. Opt. Soc. Am., 63 p.685 (1973)

5.34 L.D. Westbrook, A.J.N. Houghton and M.W. Austin
Colloquium on 'Integrated Optics' IEE Savoy Place (1980)

5.35 E.G. Spencer and P.H. Schmidt
J. Vac. Sci. Tech., 8 p.252 (1971)

5.36 H.C. Hughes and M.J. Rand eds.
'Etching for Pattern Definition' p.113 (Electrochem. Soc., Princeton, New Jersey 1976)

5.37 P.G. Gloersen
J. Vac. Sci. Tech., 12 p.28 (1975)

5.38 H. Dimigen and H. Luthji
Philips Tech. Rev., 35 p.199 (1975)

5.39 D.T. Hawkins
J. Vac. Sci. Tech., 12 p.1389 (1975)

5.40 C.M. Melliar-Smith
J. Vac. Sci. Tech., 13 p.1008 (1976)

5.41 J.W. Coburn and H.F. Winters
J. Vac. Sci. Tech., 19 p.391 (1979)

5.42 P. Sigmund
Phys. REv., 184 p.383 (1969)

5.43 R.J. MacDonald
Adv. Phys., 19, p.457 (1970)

5.44 J.P. Ducommum, M. Cantugrel and M. Marchal
J. Mater. Sci., 9 p.725 (1974)

5.45 L.F. Johnson
Appl. Opt., 18 p.2559 (1979)

5.46 H. Garvin, E. Garmire, S. Somekh, H. Stoll and A. Yariv
Appl. Opt., 16 p.126 (1977)

5.47 S. Somekh and H.C. Casey Jr.
Appl. Opt., 16 p.126 (1977)

5.48 Y. Kerr
M.Sc. Thesis, Faculty of Engineering, University of Glasgow (1982)

Chapter 6

Experimental Procedures and Results

We have outlined the fabrication of two types of passive Bragg waveguide deflectors (periodic index variation and periodic thickness variation) in chapters 4 and 5. In this chapter we will describe the measurement procedures and the experimental results, and compare the results with theoretical calculations given in chapter 3.

6.1 Measurement of Device Parameters

In this section we will give a brief description of the techniques used to measure the various parameters (such as optical constants, geometry and so on) of our devices.

6.1.1 Refractive Index Measurements

For bulk solids (e.g. glass substrates) we used a Bellingham and Stanley type 60/ED Abbe refractometer. The instrument is calibrated at sodium D-line(.5896μm), and at the wavelength used (0.6328μm) the accuracy is $\pm$ 0.0001.

For thin films (e.g. sputtered 7059 glass) we used the synchronous angle measurement technique[6.1]. The input beam was not focussed, and weak coupling was maintained to minimise disturbance to the waveguide. An accuracy of $\pm$ 0.0001 is possible[6.1,6.12] using the prism coupling method, especially

for multimode waveguides. In single mode waveguides the film index and the thickness can be calculated from the synchronous angle measurements of the TE and TM mode, with the help of the dispersion equation[6.1].

6.1.2 Waveguide Attenuation Measurements

An output prism coupler was firstly placed at the end of the guide, and then moved towards the input prism, measurements being taken at equal spacing along the guide. The light coupled out was measured, together with a reference beam (the laser light was split into two initially), using two UDTPIN 10 photodiodes. The input beam was mechanically chopped at a frequency of 1KHz, and the relative power measurements of the signal beam to the reference beam are accurate to $\pm$ 0.2dB.

6.1.3 Grating Parameters

The beam angle Θ for the first order free space Bragg diffraction of a sinusoidal grating of period Λ is given by

$$\Theta = \sin^{-1}(\lambda_o/2\Lambda) \qquad (6.1.1)$$

where Θ is measured from the normal of the grating face as shown in Fig. 6.1. By measuring this autocollimation angle (to $\pm$ 2' of an arc), the periodicity is accurate to $\pm$ 0.1nm.

For a periodic index grating the refractive index change

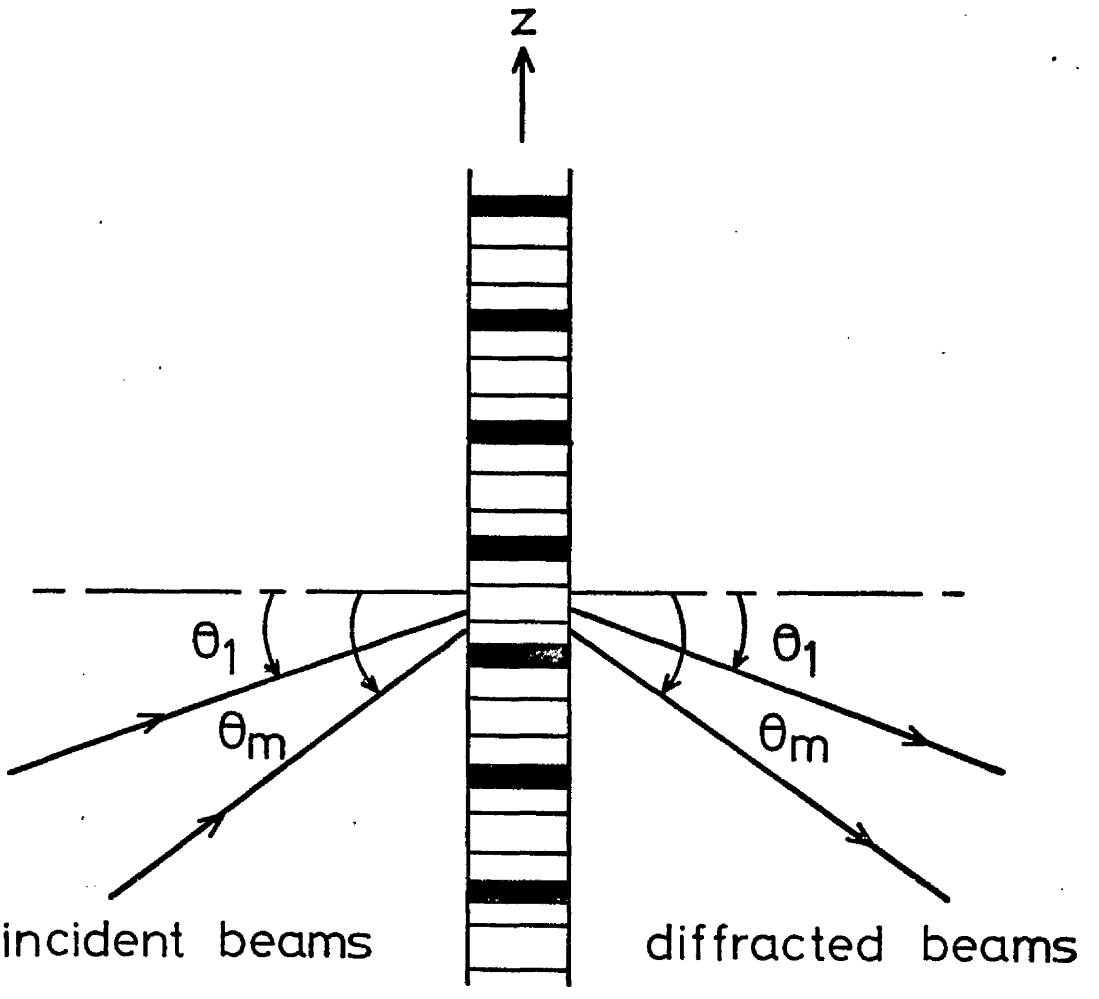

FIG 6.1 Bragg diffraction of a sinusoidal grating

Δn was estimated from the measurement of the diffraction efficiency η_d (ratio of the diffracted beam intensity to the incident beam intensity), when a light beam was incident from the air onto the film surface. η_d is given by[6.2]

$$\eta_d = \sin^2(\pi \Delta n d/\lambda_o) \qquad (6.1.2)$$

where d is the film thickness, and λ_o is the free space wavelength of light used.

Fora surface corrugation grating,the grating depth h was also calculated from the diffraction efficiency measurement. For long period gratings, the diffraction efficiency η_d is[6.2]

$$\eta_d = \{ J_1[(2\pi/\lambda_o)\Delta h(n-1)]\}^2 \qquad (6.1.3)$$

where n is the refractive index of the grating, and J_1 is the Bessel function of the first order. For short period gratings, the approximate theory by Tomlinson et al.[6.3] was used, and a computer program (based on the exact solutions by Marcuse[6.4]) was available* to calculate Δh. An accuracy of $\pm$ 2.5nm was estimated.

The grating length L was measured using a Union Microscope shearing eyepiece, with an accuracy of $\pm$ 1%.

* Program written by Dr. J.A.H. Wilkinson

6.2 Experimental Set-up and Procedures

The experimental arrangement is shown schematically in Fig. 6.2. A quarter-wave plate was placed in front of a NEC 3mW HeNe visible laser, together with a polarizer for mode selectivity. The beam was then chopped mechanically at a frequency of 1 KHz (to minimise ambient noise), and split into two. The undeflected beam was directed towards the goniometer stage, and a focussing lens was used to focus the undeflected beam (focussed spot-size $\sim$ 250μm $\pm$ 25μm, beam divergence $< 0.1^{o}$) onto the coupling spot of the prism coupler. The deflected beam acted as a reference beam.

A MICRO CONTROLE Goniometer (Fig. 6.3) was used in our experiments. It has a rotation stage (about a vertical axis, angular accuracy $\pm$ 5') and an XYZ translational stage. Rotation in the vertical plane was provided by a goniometer cradle (angular accuracy $\pm$ 1'). One arm of a U-shaped clamp was used to hold the input prism coupler (Schott SF15 glass prism for glass waveguide, rutile prism for $LiNbO_3$ waveguide), while the other arm housed a nylon screw (perpendicular to the base of the input prism). The waveguide was clamped down by mechanically contacting the surface of the guide to the base of the prism, and adjusting the screw against the back of the substrate to form a coupling spot (area $\sim$1mm diameter, distance of separation $\sim$0.2μm).

A pair of United Detector Technology PIN10 photodiodes, which were connected to a Hewlett-Peckard gain-phase meter model 3575A, were used to measure the relative powers of the amplitudes

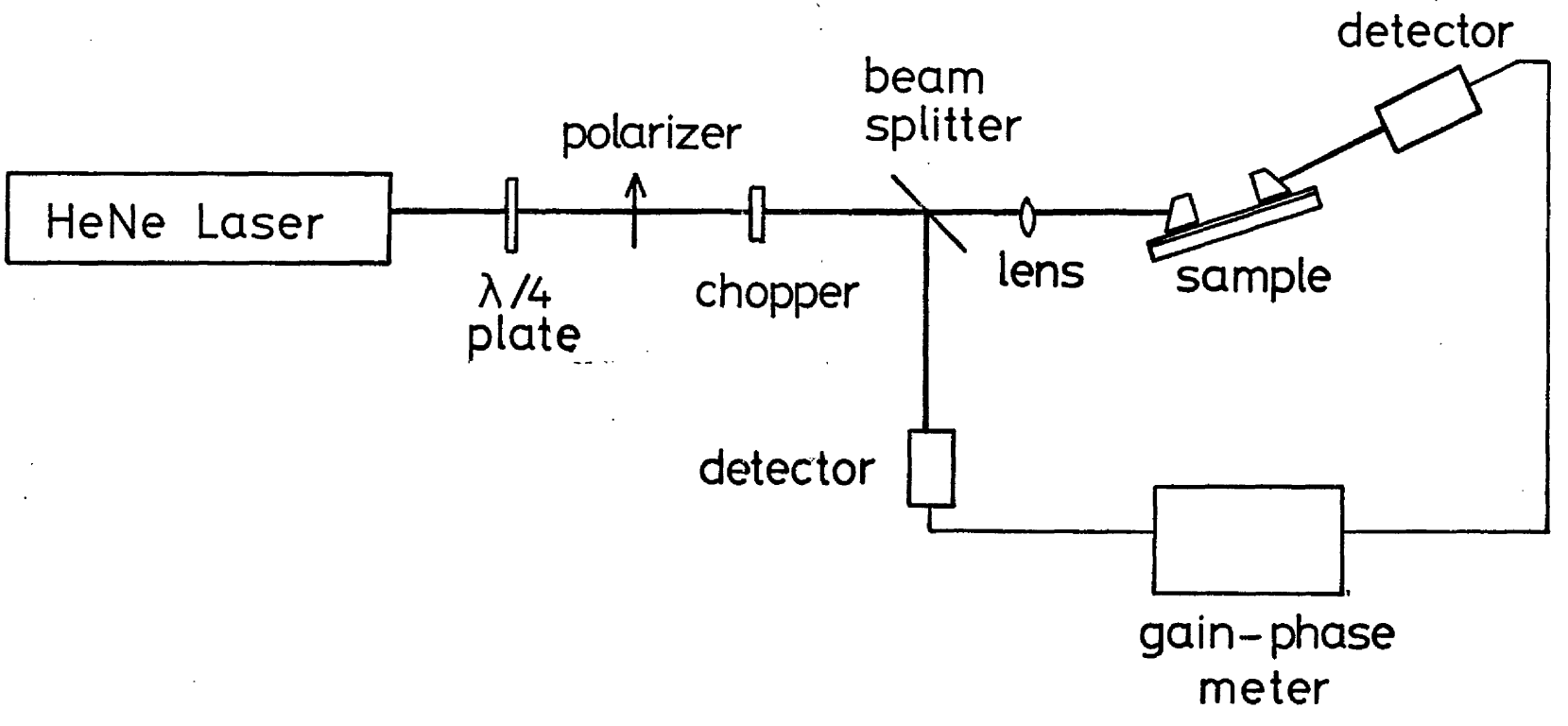

FIG 6.2 Schematic diagram of the experimental equipment

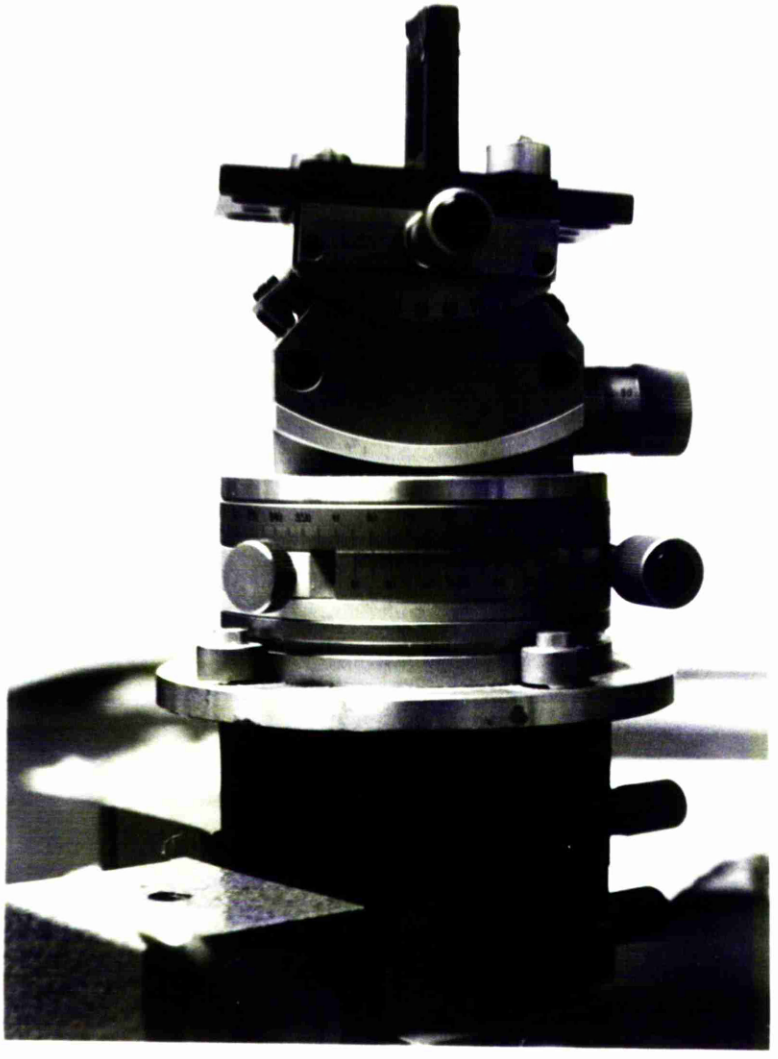

FIG 6.3 Photograph of the goniometer used

of the reference beam and the coupled beam . The meter has an analogue output and digital display of the ratio of the two input signals in dBV. The analogue output from the meter was connected to a Hewlett-Peckard X-Y-T plotter (model 7045A).

A Photodyne optical power meter (model 44xL), which has a range from 1.999 to 1999 μW, was also used in the power measurement. The deviation between the two systems is $\pm$ 2%.

Light from the HeNe laser (λ_o = 0.6328μm) was launched into the waveguide using a prism coupler. By tilting the substrate with respect to the incoming beam, the angle of incidence Θ of the guided TE_o onto the grating element was adjusted to satisfy the Bragg condition. The diffracted and transmitted beams were coupled out (Fig. 6.4), and by monitoring the intensities of the output m-lines, the diffraction efficiency (defined as $P_D/(P_D+P_T)$, where P_D is the diffracted beam intensity and P_T is the transmitted beam intensity) was obtained. As for the bandwidth, we measured the angular selectivity of the grating by rotating the goniometer cradle, and adjusting the incident angle Θ.

For surface corrugation gratings, an additional prism coupler was used to monitor the incident power just before the grating region (to minimise error due to random scattering in the region), and a polarizer was used to separate the diffracted TE and TM modes. The exact determination of Θ_B was made difficult by the large width of the diffracted beam, as compared to the coupling spot. Index matching liquid was used in an attempt to increase the coupling region, but was abandoned because of the

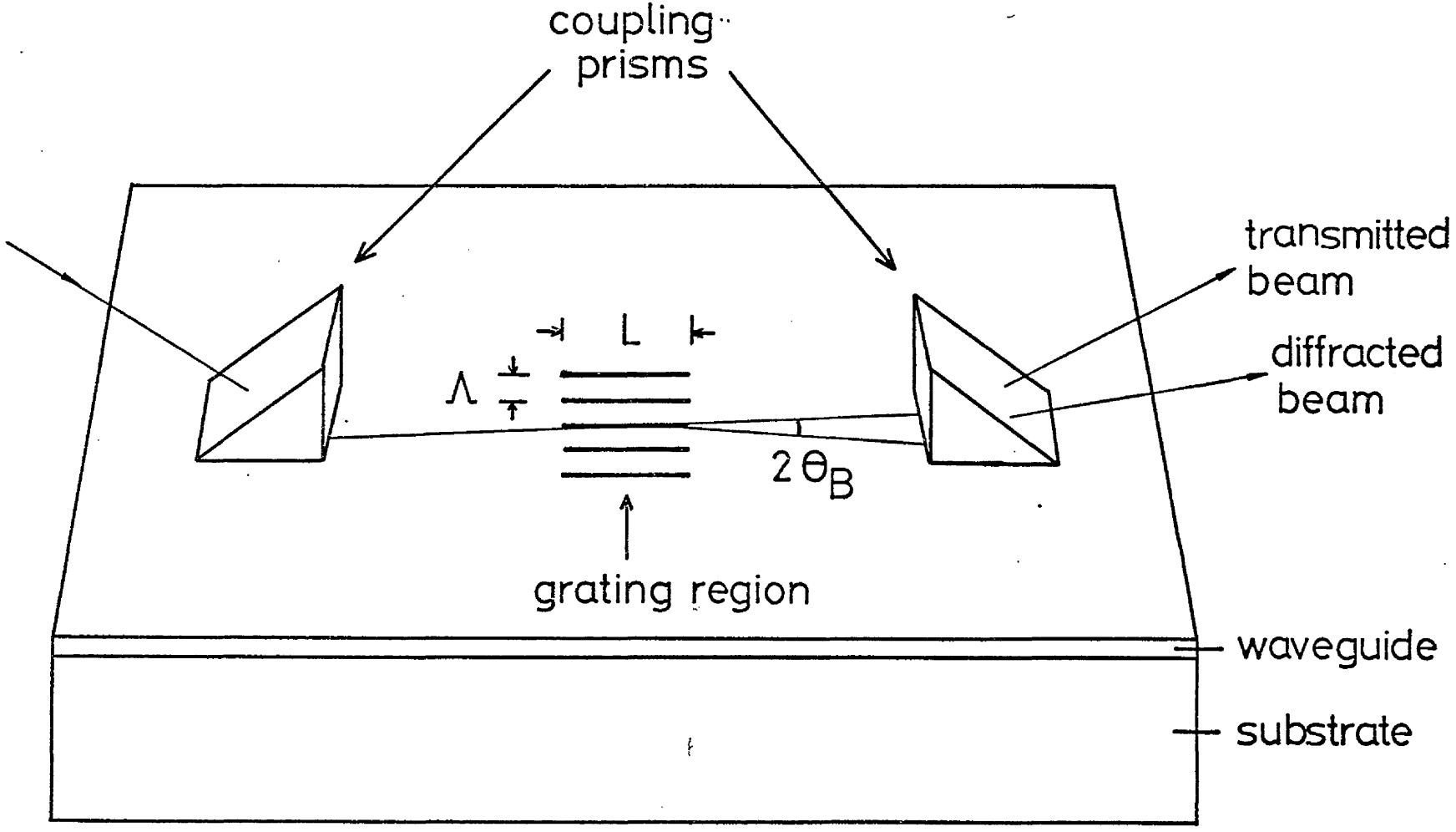

FIG 6.4 Experimental arrangement for power measurement

scattering introduced, which made measurement difficult, especially in the beam profile experiment. Hence the interaction length L of the grating region was restricted to < 1mm. The beam profile of the diffracted beam was monitored by a scanning photodetector with an aperture of $\sim 50\mu$m.

6.3 Results

6.3.1 Periodic Index Waveguides by Ion Exchange in Glass

A number of single mode ion-exchanged Bragg deflectors were fabricated as described in chapter 4, and their measured and calculated performances and parameters are summarised in Table 6.1. Photographs of the beam splitter using first order diffraction are shown in Fig. 6.5. There is negligible random scattering of light at the grating region, and the Bragg angle θ_B ($\sim 4^o$) was determined from the photograph, with an accuracy of $\pm$ 1^o. The photographs were taken from a Hamamatsu C1000 vidicon monitor, which incorporates a vertical line scan to give a quantitive measurement of the intensities of the two beams.

Higher order Bragg diffraction was also observed, the diffraction efficiencies being lower than that of the fundamental ($\sim$15% for the second order, and $\sim$1% for the third order).

The normalised diffraction efficiency as a function of interaction length L is plotted in Fig. 6.6. The diffraction efficiency follows closely a $\sin^2(\kappa L)$ dependence, where κ is the coupling constant. The maximum intensity for the first

TABLE 6.1 EXPERIMENTALLY MEASURED DIFFRACTION EFFICIENCY

Device	Interaction Length L(μm)	Diffraction Efficiency η_d% (+5%)	Normalized Diffraction Efficiency η_d/η_o(%)	Half Bandwidth Δθ in air (′)	Half Bandwidth Δθ in waveguide (′)	η_d cal. (%)	Δθ cal. (′)
Fb1	101	5	6.5	46	30	6	45
Fb4	205	20.6	26.3	40	26	23	22
Fb6	309	38.3	50.4	27	18	48	14
Fb8	404	54.1	71.2	17	11	71	11
Fb10	515	71	93	12	8	91	8.5
Fb12	620	76	100	10	7	99	7
Fb17	750	73	88.1	10	7	91	6

0.1% diluted $AgNO_3/NaNO_3$ melt

Diffusion time = 30 minutes

Temperature = 315°C

Effective index N = 1.5172

$$\eta_d = \sin^2\left(k\frac{\pi\overline{\Delta n}}{\lambda_o} L\right)$$

$$k\,\overline{\Delta n} \approx 5\times10^{-4}$$

(a)

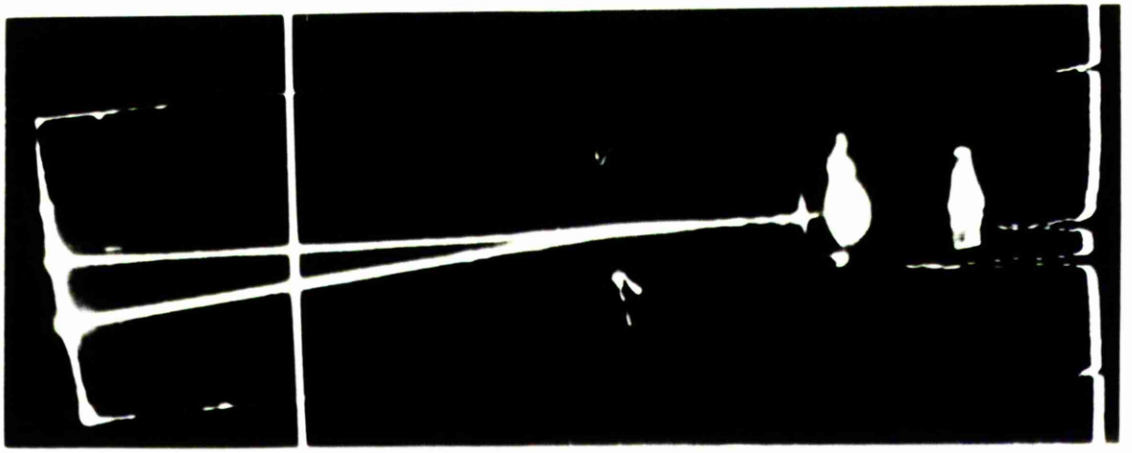

(b)

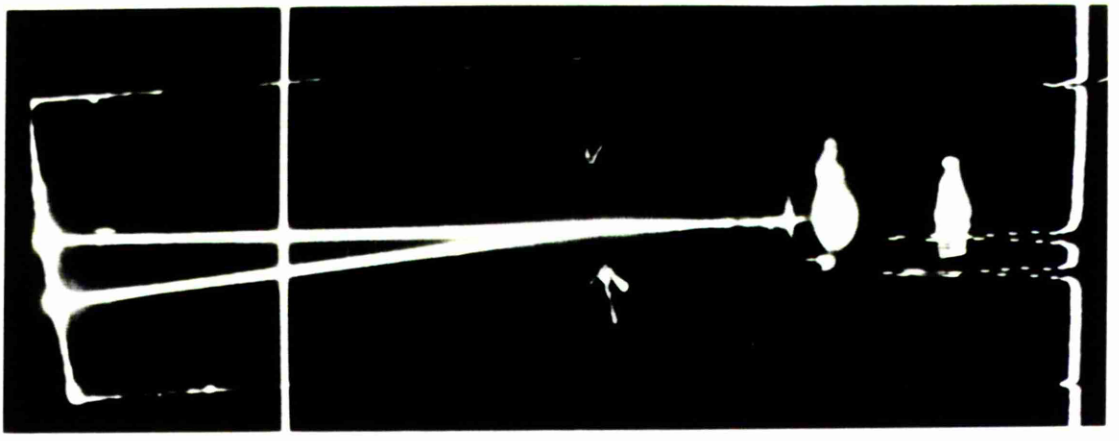

(c)

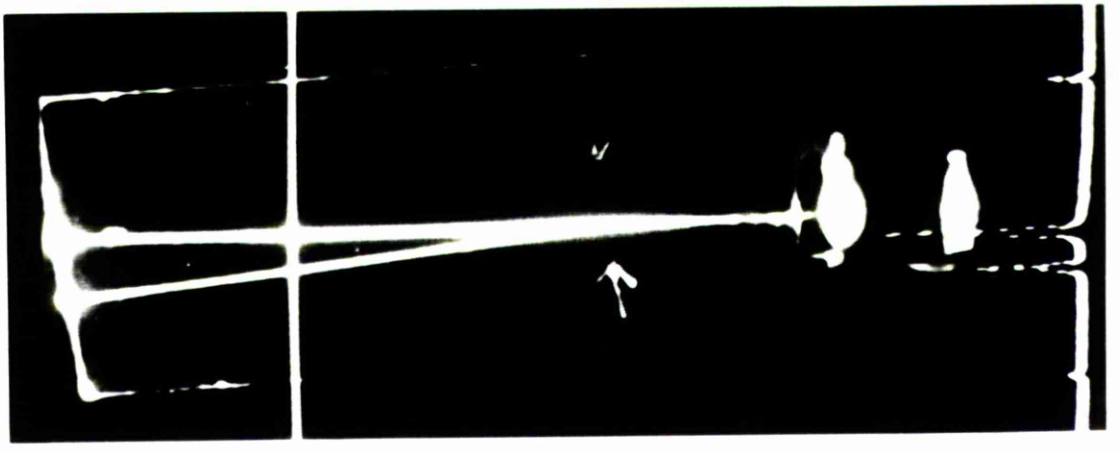

FIG 6.5 Photographs of the beam splitter (Fb 17) showing variation of diffracted power as a function of θ. (a) $\eta \simeq 70\%$, (b) $\eta \simeq 50\%$, (c) $\eta \simeq 30\%$. Tuning range for (a)-(c) : $\Delta\theta \simeq 0.3°$

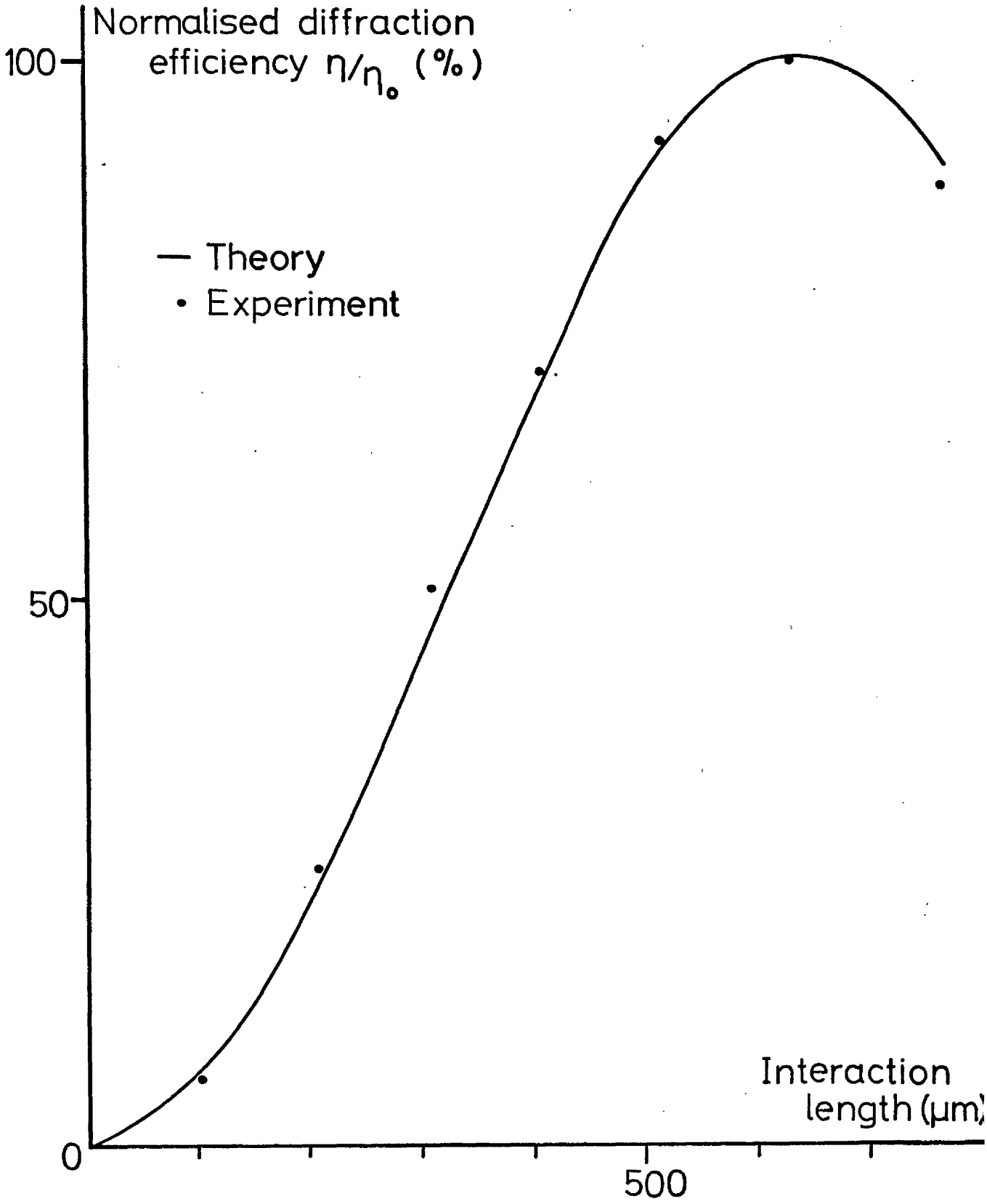

FIG 6.6 Normalised diffraction efficiency as a function of interaction length

order diffracted beam was measured to be only 76%. This is because a finite Gaussian beam was used in our experiments, whereas an 'infinite plane wave' theoretical model was used. Also the grating strength ($\propto \overline{\Delta n}$) is not uniform throughout the film, nor is it optimised for the overlap integral constant k. The curve is plotted after the overlap integral k is adjusted to fit the experimental data. Excellent agreement between calculated and measured values was obtained, for both the diffraction efficiency and the bandwidth.

The side diffusion of silver ions underneath the aluminium strips is of paramount importance in this fabrication technique. The complete absence of silver ions in these regions would cause the guided mode to be coupled into the substrate. To investigate this side diffusion mechanism, several multimode Bragg deflectors were fabricated, and their results are summarised in Table 6.2.

A micrograph of the grating region of a three-moded waveguide is shown in Fig. 6.7. The mark-space ratio observed in the picture clearly indicates the extent of silver diffusion underneath the aluminium mask, and justifies the assumption that the metallic mask used acted like a non-conducting mask. Scanning microprobe analysis* on the surface shows a 4% relative difference in the concentration of silver ions between the regions of clear and dark fringes, and there is no silver in a gap of 0.1μm width. With a 0.1% diluted melt the difference

* By Professor P.C. Jaussaud, ENSIEG Grenoble, France

TABLE 6.2 EXPERIMENTALLY MEASURED CONVERSION EFFICIENCY

(a) Three moded waveguide

input \ output	TE_o	TE_1	TE_2
TE_o	46%	32%	20%
TE_1	34%	25%	17%
TE_2	20%	17%	13%

Percentage error: +5%

(b) Two moded waveguide

input \ output	TE_o	TE_1
TE_o	67%	20%
TE_1	19%	7.8%

Percentage error: +5%

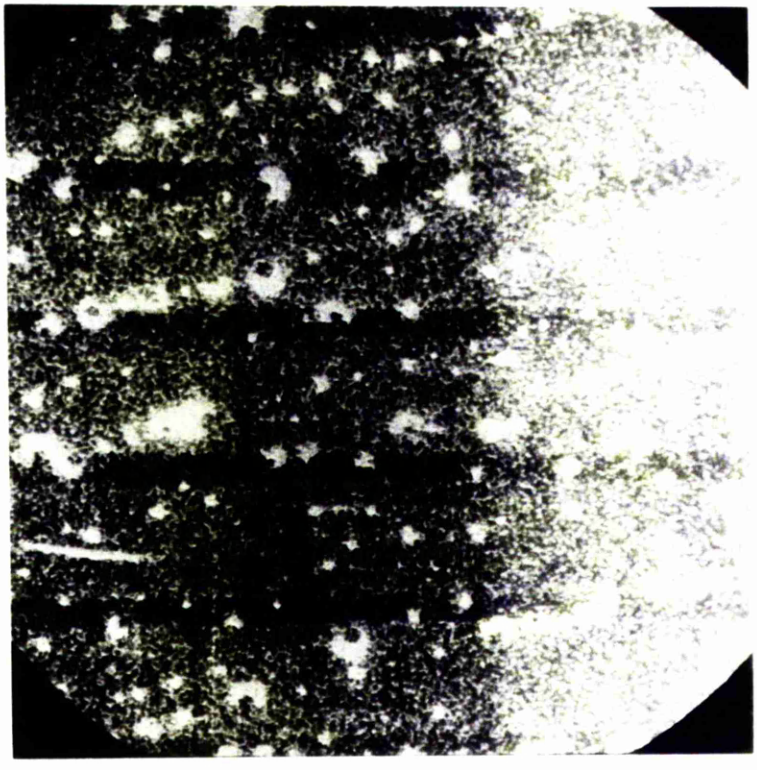

FIG 6.7 SEM micrograph of an ion-exchanged grating (immersion time of 90 minutes in a 0.1% dilute melt of $AgNO_3/NaNO_3$

between the surface and the substrate indices is 1.5×10^{-2}, thus the maximum index difference in the grating at the surface is 6×10^{-4}. Thecalculated value of $k\overline{\Delta n}$ (for η_d = 40%) is 2×10^{-4}. This is not unreasonable, since the waveguides have a graded index profile, and the gratings do not have a sinusoidal variation.

The measured $k\overline{\Delta n}$ (from free space diffraction) and the corresponding calculated function (from guided wave diffraction) are plotted in Fig. 6.8 as a function of time. The discrepancies resulted from the fact that as side diffusion increases, $\overline{\Delta n}$ decreases, although the overlap field integral c approaches unity as diffusion time increases. Using a standard curve fitting technique, the change in $k\overline{\Delta n}$ can be expressed as

$$k\overline{\Delta n} = 1.19\times10^{-4} \quad e^{(46.9/t)} \qquad (6.3.1)$$

where t is the diffusion time in minutes.

For the non-collinear TE_m to TE_n mode conversion experiments, the angle of incidence Θ_m of the input TE_m mode was adjusted so as to satisfy the phase matching condition (Fig. 6.9). Θ_m is given by

$$\sin\Theta_m = (\lambda_o/2N_m\Lambda)\ [1+(\Lambda^2/\lambda_o^2)(N_m^2-N_n^2)] \qquad (6.3.2)$$

where N_m and N_n are the effective indices of the intervening modes. Sample photographs of the output m-lines of a three-moded waveguide are shown in Fig. 6.10. High conversion

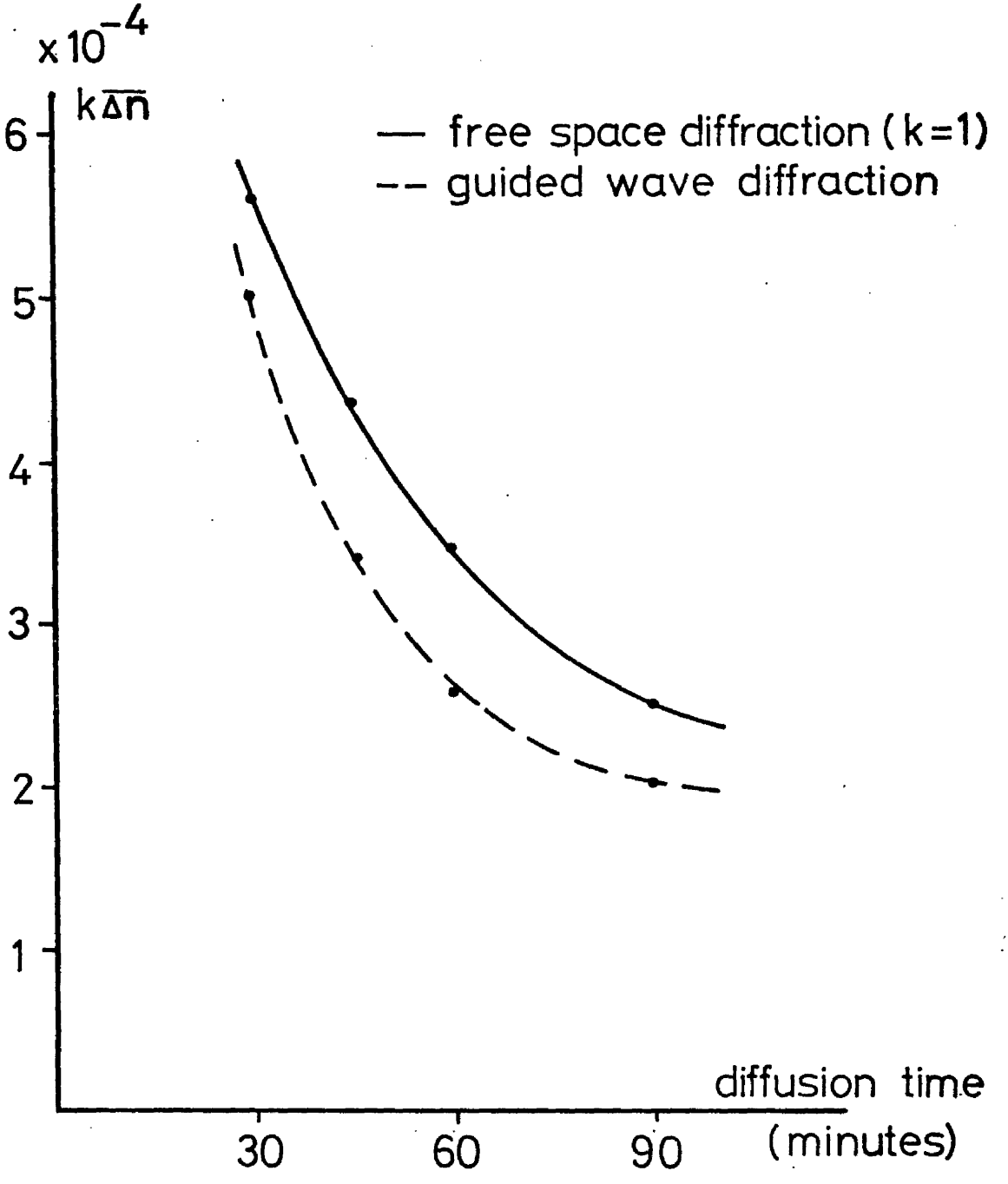

FIG 6.8 $k\overline{\Delta n}$ as a function of diffusion time

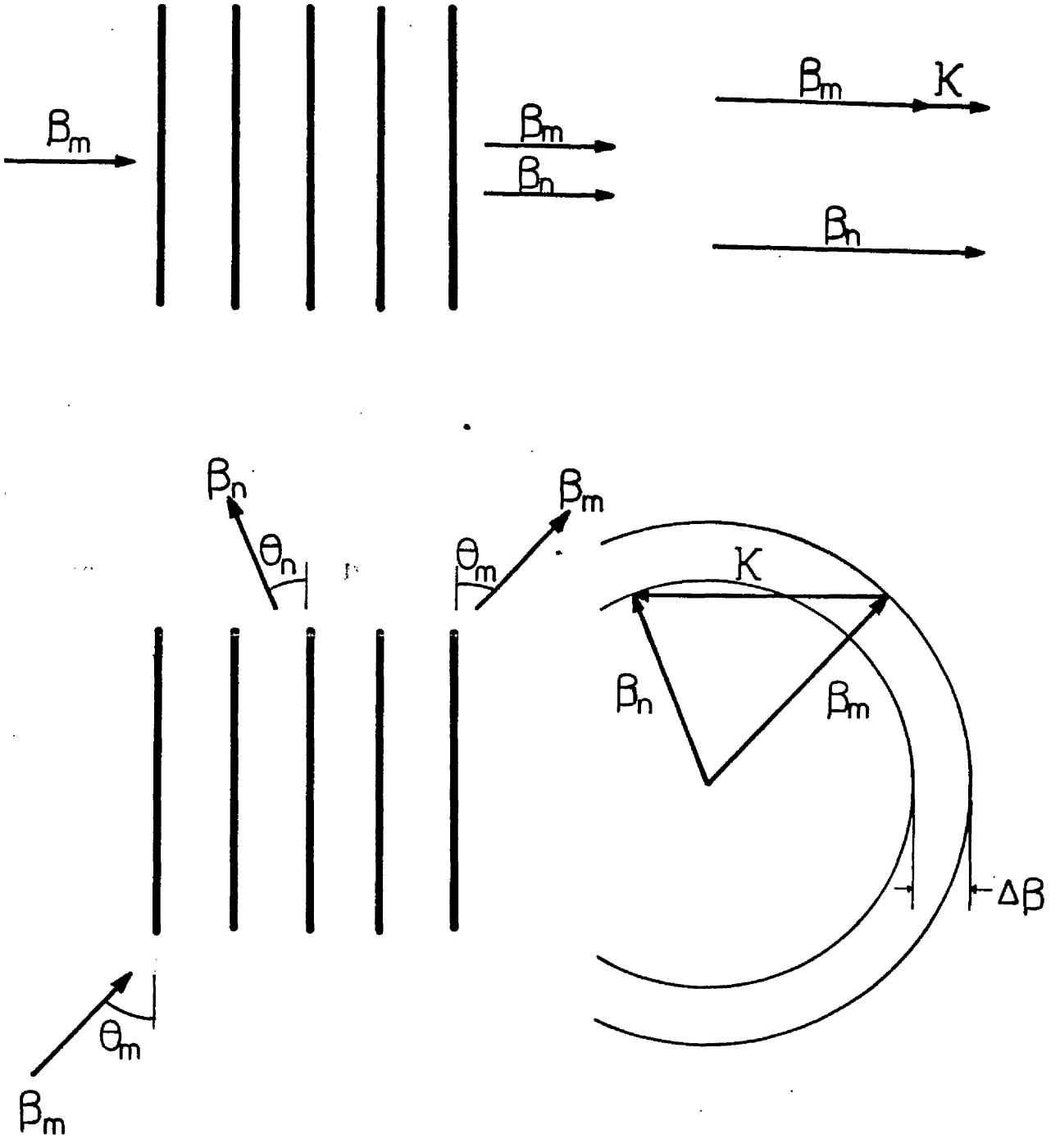

FIG 6.9 Phase matching diagram for (a) collinear and (b) non-collinear mode conversion of guided modes

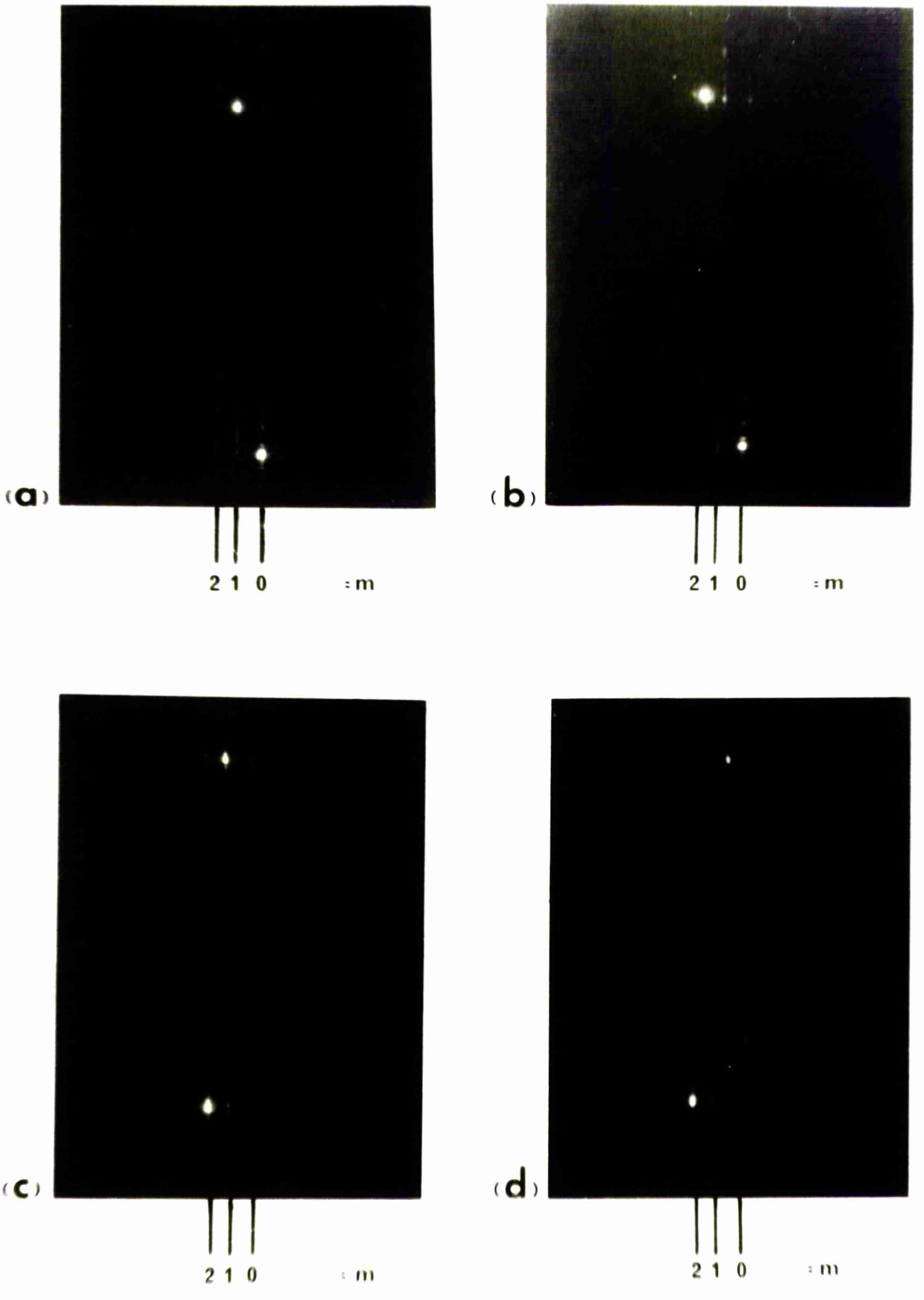

FIG 6.10 Photographs of diffraction patterns of output m-lines:
(a) $TE_0 \rightarrow TE_1$ (b) $TE_0 \rightarrow TE_2$ (c) $TE_2 \rightarrow TE_1$ and
(d) $TE_2 \rightarrow TE_0$

efficiencies were obtained in these periodic index waveguides (see Table 6.2). As is expected from the field distribution of the guided modes, the overlap integral of the field distribution E_{om} and E_{on} decreases with increasing film thickness when the modes are different (that is, m = n). This is in contrast to the case when $E_{om} = E_{on}$, which approaches unity as the film thickness increases. Bragg diffraction still decreases because the grating strength ($\alpha\overline{\Delta n}$) decreases with time (Fig. 6.8).

A two-step diffusion method was also tried. A first diffusion in diluted melt was carried out to form the waveguide, and a second diffusion in pure melt was used to form the periodic perturbation. Unfortunately the samples turned brown in the areas covered by the aluminium masks. Anodised aluminium and chromium masks had the same effect. It appeared that chemical reactions between the diffused silver and the ferrous impurities in the glass had taken place, aided by the presence of the masking material.

By polishing off the brown stain (typically 10^{-1} μm thick), light was coupled into the waveguide, and Bragg diffraction was observed. Hence the validity of such a technique was demonstrated, however, a detailed analysis of the 'brown staining' effect is required before working devices can be fabricated.

6.3.2 Periodic Index Waveguides by Proton Exchange in $LiNbO_3$

Single mode slab waveguide incorporating gratings were fabricated in a single diffusion process using the proton exchange process. Fig. 6.11 shows the output m-line for three cases : (a) well off Bragg angle, producing only a transmitted beam, (b) near Bragg angle incidence, giving approximately equal splitting between diffracted and transmitted beams, and (c) Bragg angle incidence giving maximum diffraction. No increase in random scattering was visible in the grating region, and the effective index of the TE_o mode was measured to be 2.259, while the maximum diffraction efficiency was 90%.

Since the index profile is a step change in index, a constant value Δn (=0.12) was assumed over the film thickness. It was noted that because of the high index change, the calculation depends strongly on the value of L, the interaction length, and several periodic exchanges between zero and first order beams had occured for L = 750 μm. The overlap field integral is estimated to be 0.89, hence the diffracted efficiency calculated is 94% ($\pm$5%). The measured value compares favourably with this value.

The measured angular half bandwidth $\Delta\Theta$ was 19' (in air). This measured value corresponds to an internal acceptance angle (in the waveguide) of 8', which is in good agreement with the theoretical calculation of 6'.

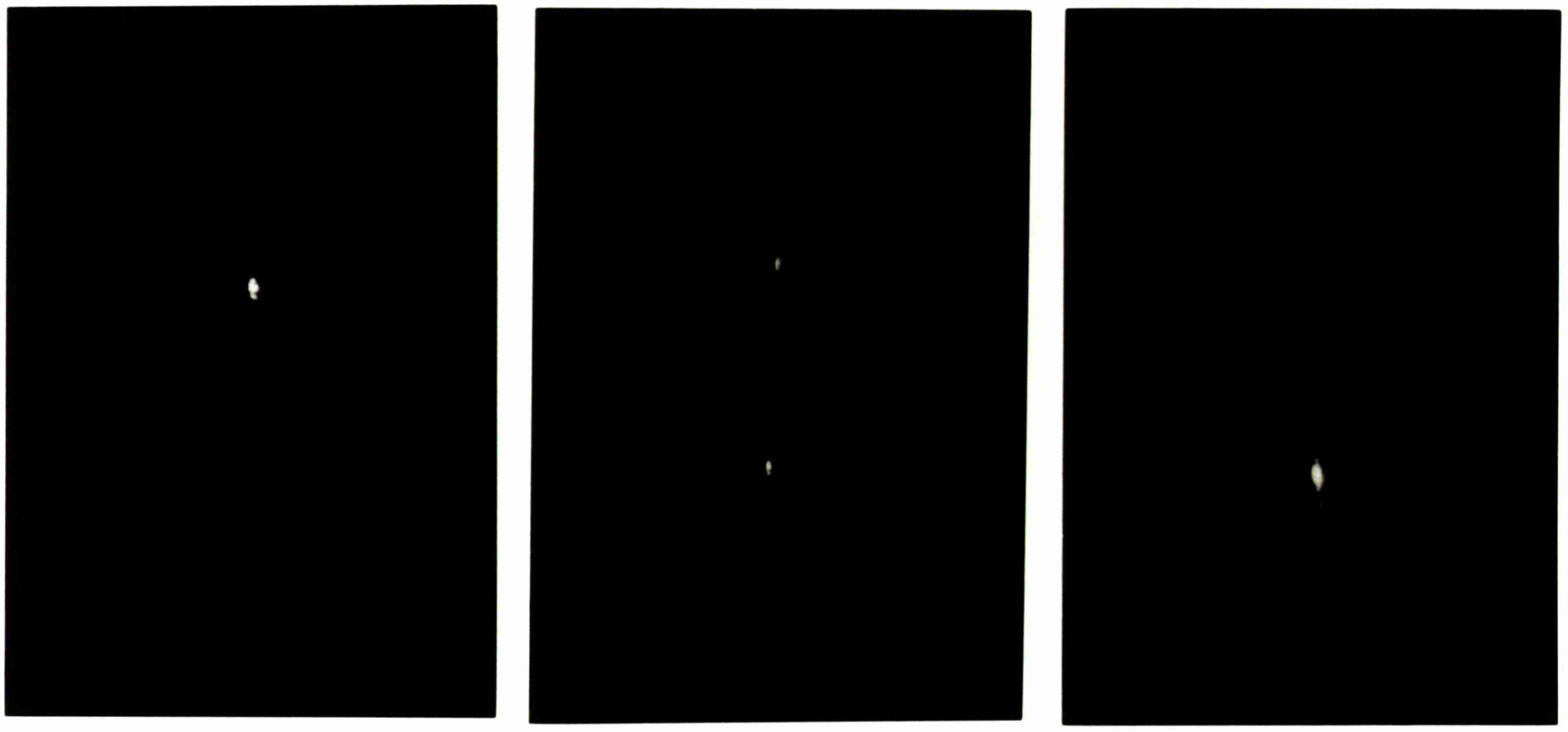

(a) (b) (c)

FIG 6.11 Output m-line of periodic index waveguide by proton exchange in $LiNbO_3$ for three cases : (a) $\theta \neq \theta_B$, (b) $\theta < \theta_B$, and (c) $\theta = \theta_B$

6.3.3 Periodic Index Waveguides by Ti indiffusion in $LiNbO_3$

Bragg deflectors using both one-step and two-step diffusion techniques were fabricated, and a common feature observed on all the samples was the presence of shallow corrugations. The modulation depths of these corrugations were measured to be typically between 250Å and 350Å, and they did not contribute to any coupling of beams (the waveguides were relatively deep, 1 to 1.5um for single mode propagation, and are slightly buried). Fig. 6.12 is a photograph of the polished edge of a sample showing the cross-section of the diffracted and transmitted beams. The angle between the two beams was typically $\sim 5.5^{o}$. The scattered light level along the path of the guided beam was monitored at $\theta \neq \theta_B$ using a photodetector, and no pronounced peak was observed in the grating region.

The results of the diffraction efficiency measurements are summarised in Fig. 6.13. For a single diffusion process ($t_1 = 0$), a maximum efficiency of 64% was obtained for a diffusion time of $t_2 = t_{min}$. As t_2 increases, the efficiency drops gradually to a few per cent at $t_2 = 10$ hrs. The situation is complicated by the fact that $\overline{\Delta n}$ decreases as diffusion time increases, while the overlap field integral c increases. By plotting the ratio of $\Delta n(0)_{theoretical}$ (equation 4.3.2) to $\Delta n_{measured}$ (from guided wave diffraction) (Fig. 6.14), $k\overline{\Delta n}$ can be expressed in terms of $\Delta n(0)_{theoretical}$ as

$$k\overline{\Delta n} = (4.375t + 25)\ n(0)_{theoretical} \qquad (6.3.3)$$

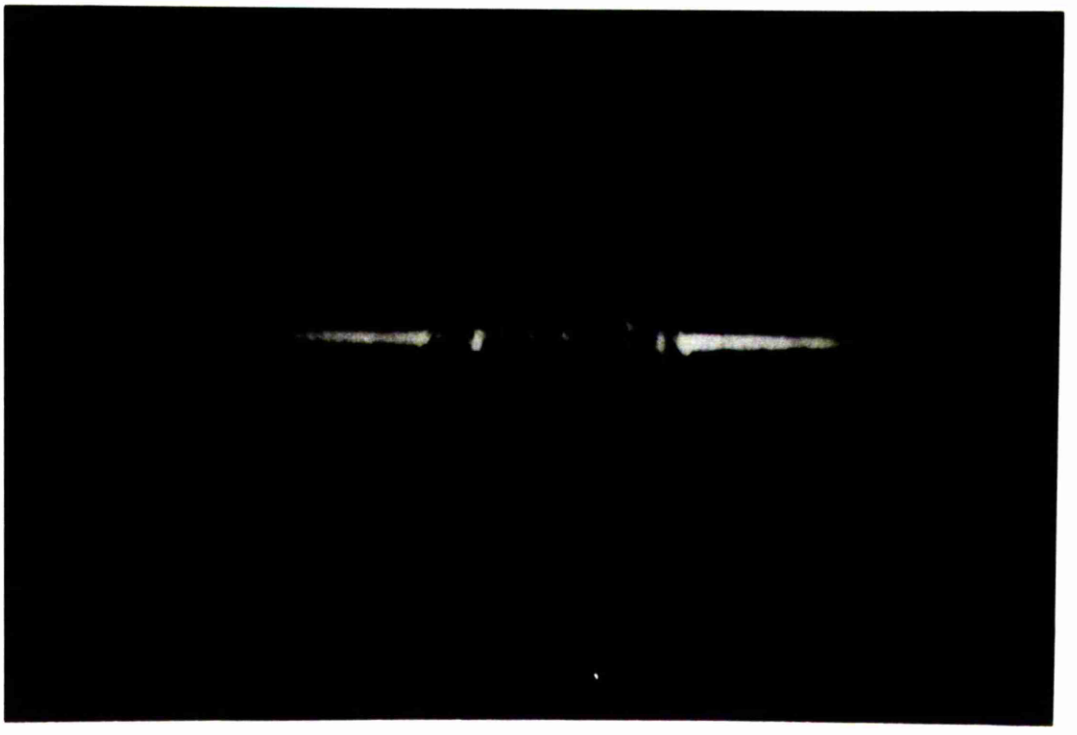

FIG 6.12 Photograph of the polished edge of a Bragg deflector by Ti:in-diffusion in $LiNbO_3$

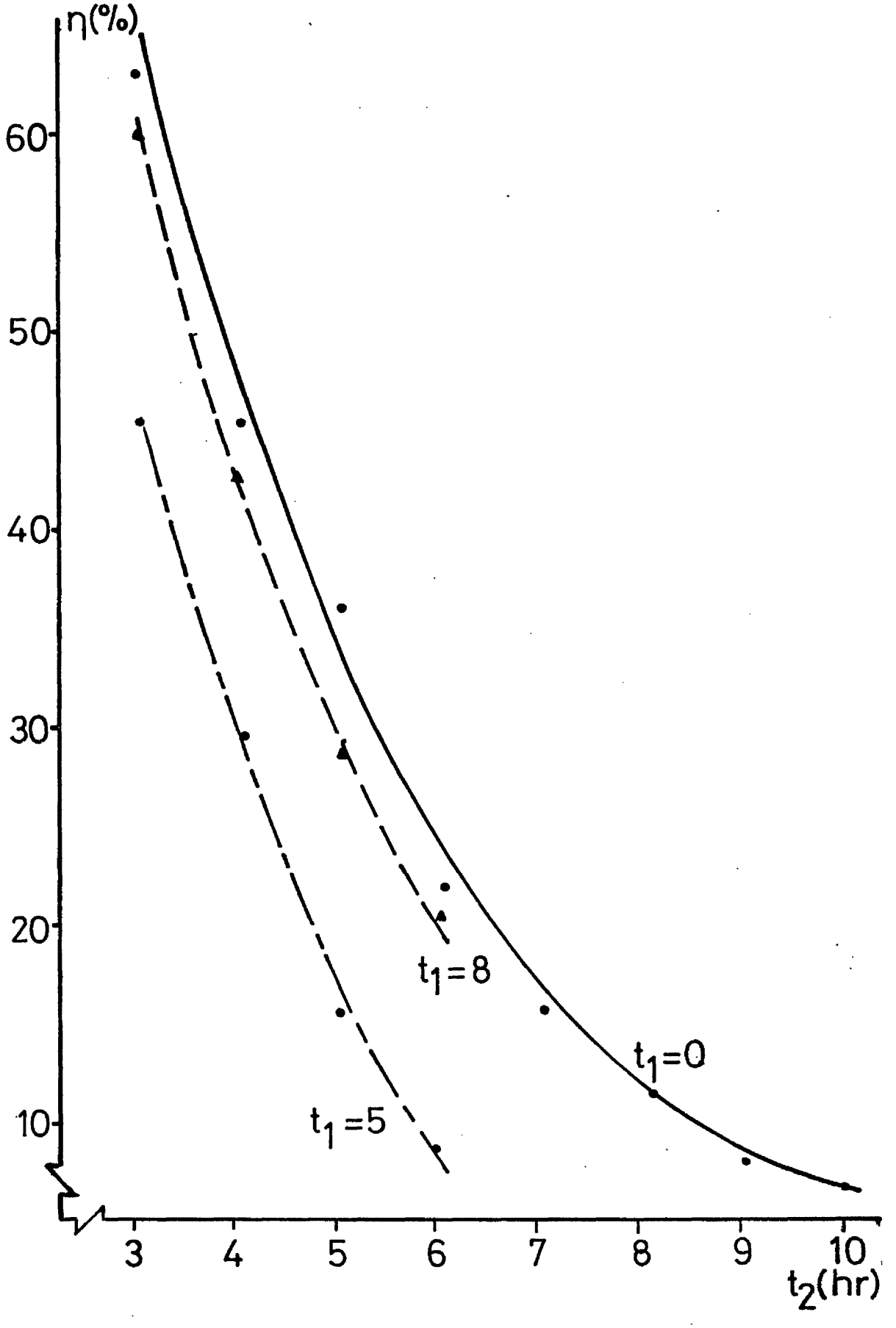

FIG 6.13 Diffraction efficiency as a function of diffusion time

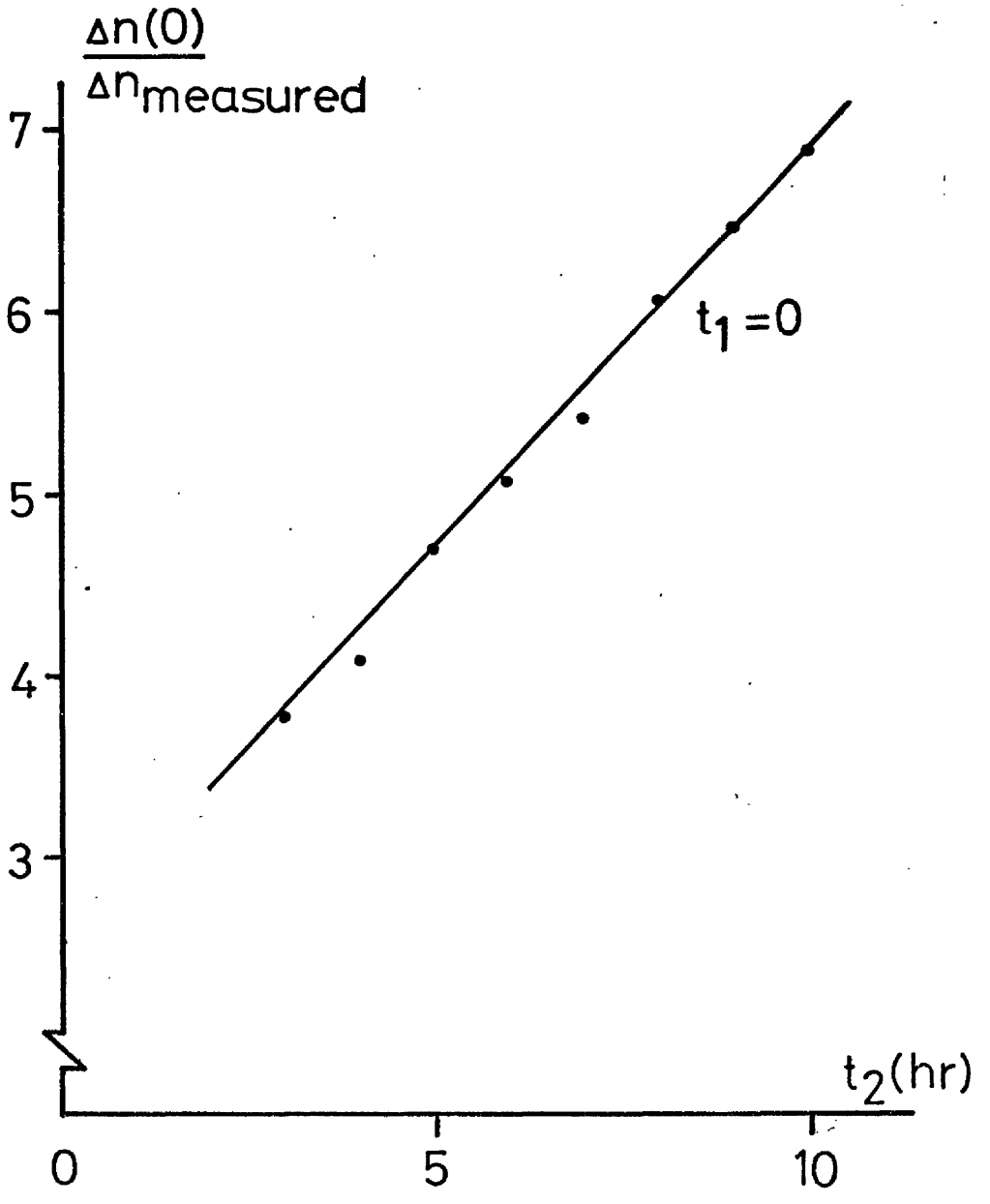

FIG 6.14 Fractional reduction of $\Delta n(0)$ against diffusion time

where t is the diffusion time, 3 hrs < t < 10 hrs, for one-step diffusion gratings.

For the two-step diffusion process, maximum efficiencies of 60% and 46% were measured for total diffusion times of 11 hours (t_1=8 hrs.) and 8 hours (t_1=5 hrs.) respectively. Hence a well-guided mode ($t_1 > t_{min}$) with high diffraction efficiency is possible using this technique.

The depth of the waveguide increases with diffusion time t, while the Ti concentration at the surface decreases proportionally to $1/\sqrt{t}$[6.5]. The addition of a Ti grating by a second diffusion leads to a periodic refractive index increase near the surface. The added concentration of Ti plus that already present in the guide contributes to the index difference ($\overline{\Delta n}$), and a large $\overline{\Delta n}$ can be obtained for a short diffusion time t_2 if t_1 is made sufficiently long. Further details are given by Bjorn[6.6]. The change in slope of the curve in Fig. 6.13 is due to the diffusion kinetics being modified by the initial presence of Ti in the guide. This modification is rather complex, and detailed study is required to characterize it.

6.3.4 Periodic Corrugated Waveguides By Holographic Technique

To confirm the presence of mode conversion[6.7-6.10] and multiple reflections within a grating region[6.10], four-layered corrugated waveguides were fabricated. The corrugated waveguides were uniform waveguide structures with photoresist

gratings on top. The grating pattern was recorded using the interferometer technique onto the resist film, with the grating lines oriented at Θ_B with respect to the long edge of the waveguide. The high index resist layer raises the modal field towards the surface, hence increasing the evanescent tail at the superstrate and consequently the grating interaction. Since our coupled wave theory is valid only for shallow gratings, we will not make a quantitative comparision of the theory with experiments, although the coupled-wave analysis has been applied to four-layered Bragg filters[6.11]. However, a qualitative study will be given here.

6.3.4.1 Four-layered Corrugated Bragg Deflectors

Deflectors with grating periods ranging from 0.25μm to 0.4μm were fabricated ($70^{\circ}<2\theta<120^{\circ}$), and photographs of two such devices are shown in Fig. 6.15. As can be observed, the intensity distribution of the (wide) diffracted beam (Fig 6.15a) tapers off from one edge to the other. Also, the existence of multiple reflections of the incident beam within the grating element is evident when comparing the much wider width of the diffracted (Fig. 6.15a) or transmitted (Fig. 6.15b) beams to the actual length of grating (rectangular patch in the photographs) traversed by the incident beam. In both cases shown, two polarisation states (TE and TM) existed within the beams, and mode conversion was confirmed as the outcoupled beams exhibited two closely spaced m-lines of different polarizations. There was strong scattering at the grating region (the whole

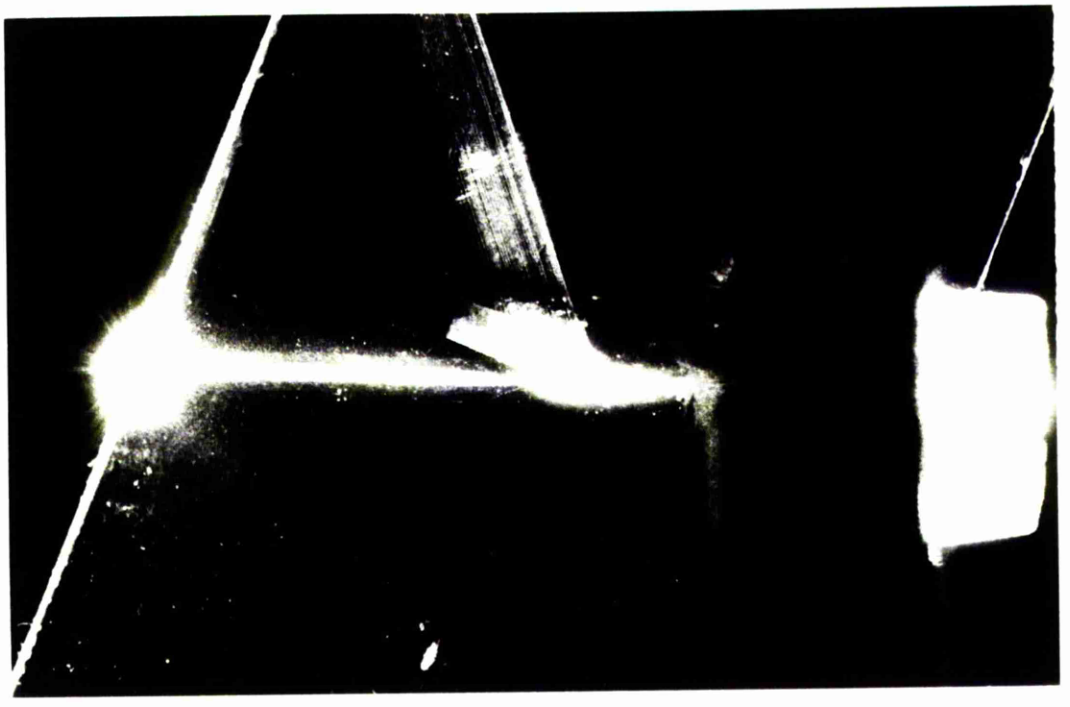

(a)

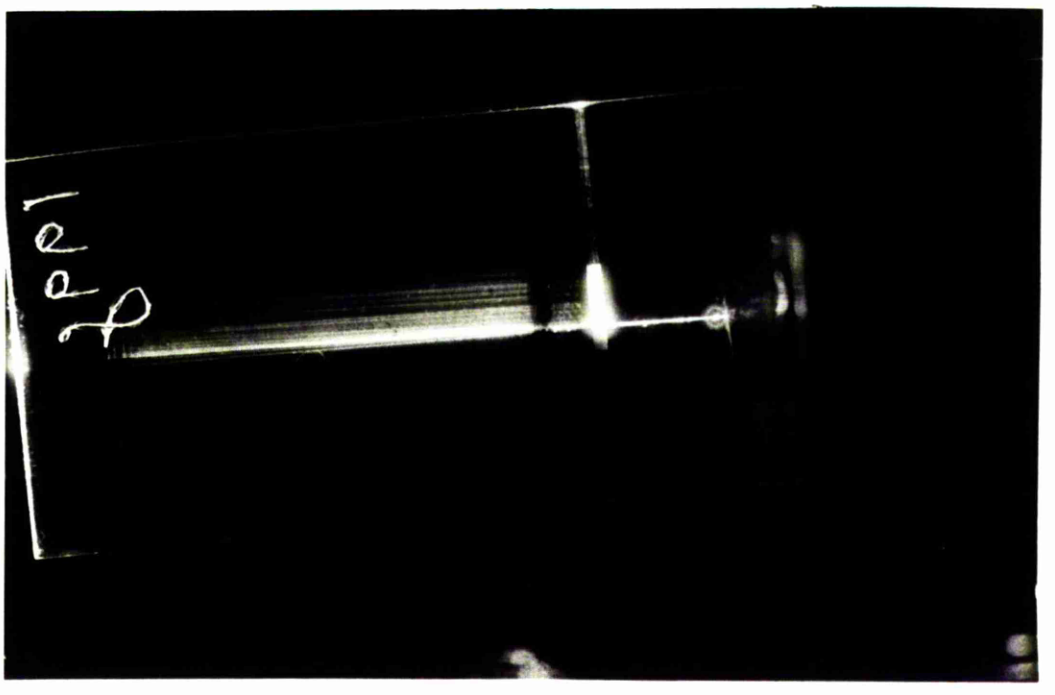

(b)

FIG 6.15 Photographs of the experimental four-layered corrugated Bragg deflectors

rectangular patch brightened up) because the critical angle at the film-cover interface (see chapter 2) was modified by the presence of the high index resist layer, and part of the guided light coupled into this layer and scattered out.

The variation of power across the width of the beam is caused by two major mechanisms. Firstly, the intensity of the diffracted beam tapers off across its width because the power of the incident beam is gradually diffracted off the grating as the beam traverses the corrugated region. Secondly, cumulative phase shifts due to multiple reflections in the grating region lead to 'breaking up' of the beam, similar to the 'interference effect' in conventional optics.

The overall diffraction efficiency was observed to be strongly dependent on θ[6.12], the incidence angle. For the same device shown in Fig. 6.15a, Fig. 6.16 shows expanded views of the diffracted beam for three cases : (a) $\theta<\theta_B$, (b) $\theta=\theta_B$ and (c) $\theta>\theta_B$. The additional phase shift can lead to almost total phase cancellation except at the two edges of the beam (Fig. 6.16a), or it can lead to a shifting of the (reduced) main lobe across its width (Fig. 6.16c). These experimental results are analogous to that of Bragg grating filters, with the appearance of sidelobes in their frequency responses being introduced by phase mismatch due to change in wavelength. In our case, detuning θ from θ_B has the effect of introducing an additional phase shift which changes the intensity pattern of the diffracted pattern, and these changes are displaced in space along the grating.

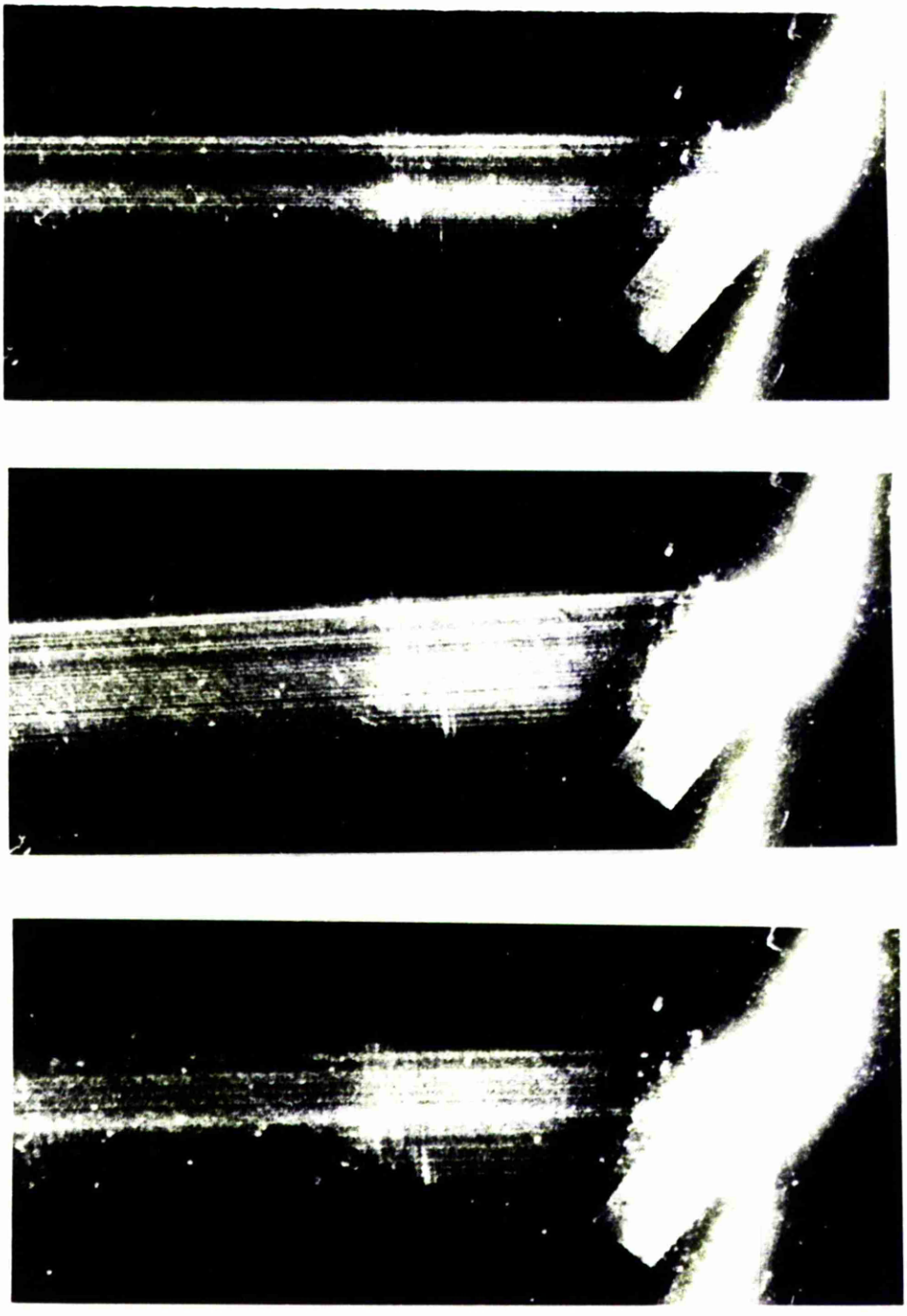

FIG 6.16 Photographs showing changes in the intensity pattern of the reflected beam: (a) $\theta < \theta_B$, (b) $\theta \simeq \theta_B$ and (c) $\theta > \theta_B$

In general, because of variation in the thickness of the guide and the resist, and the grating depths, there was variation in the response of the deflector along the length of the grating. This was not so for the periodic index grating.

6.3.4.2 Three-layered Corrugated Bragg Deflectors

To make further comparison between theory and experiment, three-layered corrugated waveguides were fabricated. Due to the problems encountered in the ion-milling step, only a few deflectors (eight altogether) of this type were successfully constructed.

Fig. 6.17 shows photographs of two such deflectors, the deflection angle (2 Θ) being approximately 45^{o} and 90^{o} respectively. The broadening of the transmitted beam (due to multiple reflections within the grating) is evident, and there is less scattering at the grating region compare to those of the four-layered devices. In order to minimise the broadening of the transmitted beam when making measurement, the incident beam was adjusted to traverse as near as possible to the top edge of the grating.

The deflector parameters and results are summarised in Table 6.3. The experimental results are compared with theoretical calculations using both one-dimensional and two-dimensional solutions. The incident beam was estimated to be 250μm $\pm$ 25μm wide, and the total percentage error in the calculation is $\pm$ 10%. In all cases, the measured responses agree better with the two-dimensional theory predictions,

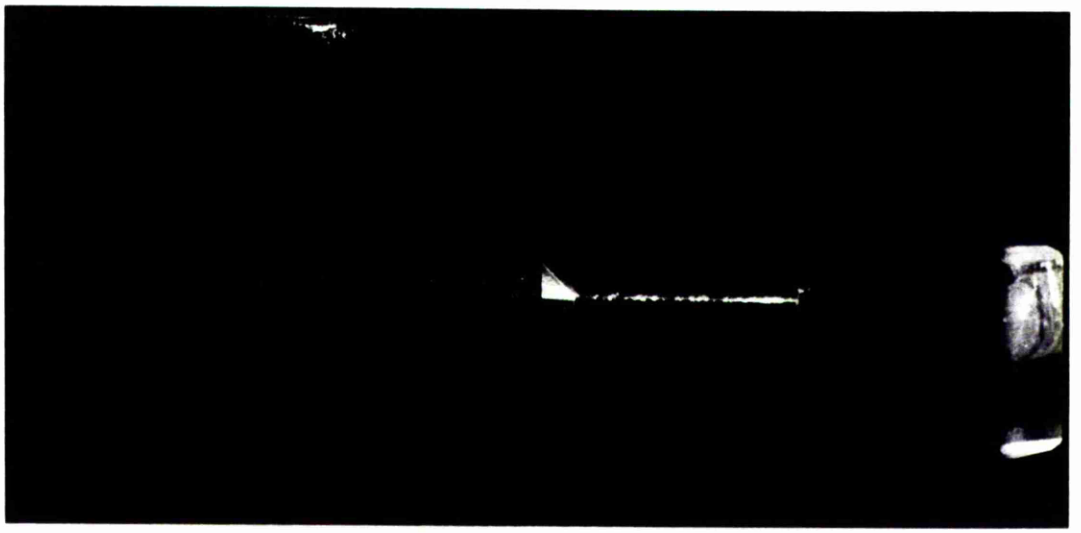

(a)

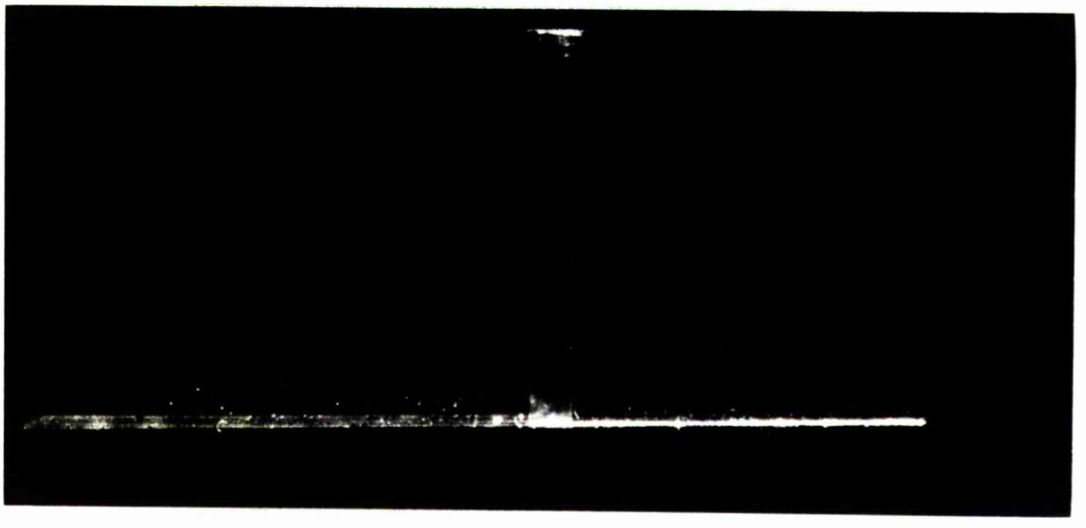

(b)

FIG 6.17 Photographs of the experimental three-layered corrugated Bragg deflectors

TABLE 6.3 EXPERIMENTALLY MEASURED 90° BRAGG DEFLECTORS

Device	T(μm)	N_E	N_M	L(μm)	Δh(nm)	Λ(μm)	$\Delta\theta_{mea}$(')	$\eta_{d\ mea}$(') (+5%)	$N_{d\ cal}$(1-D) (%) (+5%)	$N_{d\ cal}$(2-D) (%) (+5%)	$\Delta\theta_{cal}$ (1-D) (')
196f	0.9133	1.5471	1.545	606.5	15	0.2899	15	35	67.2	41.9	1
203d	0.9256	1.5474	1.5454	423.4	13.2	0.2886	7	20	36.5	25	1
210c	0.9642	1.5486	1.5467	502.6	11.8	0.2885	7	18	34.5	20	1

$$\eta_d \text{ (one-dimensional)} = \tanh^2 (\kappa L)$$

$$\eta_d \text{ (two-dimensional)} = 1 - J_o(\omega_o) - J_1(\omega_o)$$

$$n_f = 1.5673$$

$$n_s = 1.5125$$

especially at high efficiency, and there is no TE-TE diffraction for 2 θ_B=90°. The error in the one-dimensional theory increases as efficiency goes up. The bandwidths predicted are also very much less than the measured values, indicating that the one-dimensional solution is not applicable in this case.

6.3.4.3 Beam Profile Measurements

Sample tracing of the diffracted beam profiles are shown in Fig. 6.18. The tapering of the intensity across its width can be clearly seen (Fig. 6.18a). At phase mismatch condition ($\theta=\theta_B$), the diffracted beam intensity drops rapidly except at the edges of the grating. The phase-mismatch introduces a destructive interference which cancels out the diffracted field, as long as there is sufficient interaction distance. In the two-dimensional case this interaction distance depends on the incident beam width, and not on the grating length.

6.4 Conclusions

Experimental Bragg waveguide deflectors were constructed and their responses compared with theory. For the periodic index waveguide deflectors formed by diffusion techniques, the results are in good agreement with one-dimensional coupled wave predictions. For the corrugated waveguide deflectors formed by holographic technique, the results are in better agreement with two-dimensional coupled wave predictions. The existence of mode

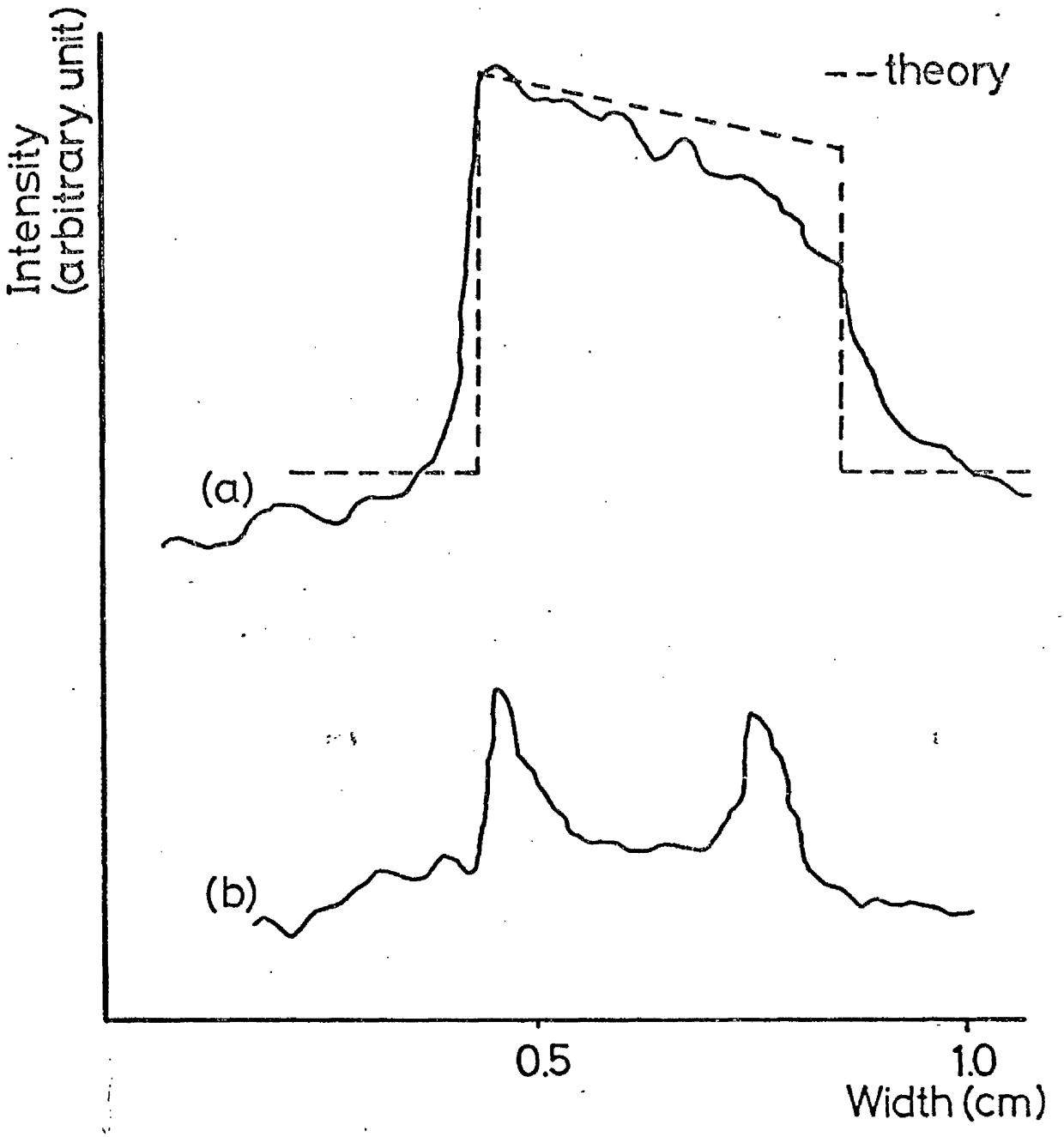

FIG 6.18 Beam profile of the diffracted beam (sample 203d) : (a) $\theta = \theta_B$ and (b) $\theta \neq \theta_B$

conversion (TE-TM) and variation in power across the widths of the transmitted and diffracted beams were observed, and there is no TE-TE coupling at $2\,\Theta_B = 90^o$.

References

6.1 P.K. Tien
Appl. Opt., 10 p.2395 (1971)

6.2 H. Kogelnik
'Proc. Symp. Modern Physics' (Polytechnic Press, Brooklyn, New York 1967)

6.3 W.J. Tomlinson and H.P. Weber
J. Opt. Soc. Am., 63 p.685 (1973)

6.4 D. Marcuse
Bell Syst. Tech. J., 51 p.1801 (1975)

6.5 A. McLachlan
Ph.D. Thesis, Faculty of Engineering, University of Glasgow (1981)

6.6 B. Bjortorp
Ph.D. Thesis, Faculty of Engineering, University of Glasgow (to be submitted)

6.7 K. Wagatsuma, H. Sasaki and S. Saito
IEEE J. Quan. Elect., QE-15 p.632 (1979)

6.8 T. Fukuzawa and M. Nakamura
Opt. Lett., 4 p.343 (1979)

6.9 J.K. Powers and D.A. Bryan
Opt. Lett., 5 p.513 (1980)

6.10 J. Van Roey and P.E. Lagasse
Appl. Opt., 20 p.423 (1981)

6.11 A. Yi Yan
Ph.D. Thesis, Faculty of Engineering, University of Glasgow (1978)

6.12 J. Marcou, N. Gremiller and G. Thomin
Opt. comm., 32 p.63 (1980)

Chapter 7

Dicussion and Conclusions

7.1 Discussion of Results

Periodic structures plays an important role in the field of integrated optics because of their unique properties. To investigate their usefulness, two types of single mode passive Bragg deflectors were fabricated and tested : periodic index waveguide formed by diffusion through a grating mask, resulting in a periodic variation of local refractive index in the waveguide, and periodic thickness (corrugated) waveguide incorporating a photoresist grating on top of the waveguide (four-layered devices), or with the pattern etched directly onto the surface of the guide (three-layered devices).

7.1.1 Periodic Index Waveguides

In general, periodic index waveguides are more efficient than corrugated waveguides because of stronger perturbation of the guided light.

Periodic waveguides have been realised in $LiNbO_3$ waveguides using surface corrugations[7.1] formed by ion-etching, or through a photorefractive process[7.2]. For $LiNbO_3$ waveguides, the evanescent tail at the superstrate decays rapidly due to the large refractive index difference. Hence a deep corrugation, which is difficult to fabricate, is required for strong interaction. Also random scattering at the grating

region exists because of the rough surfaces introduced by the ion-milling step. For the photorefractive grating, the $LiNbO_3$ crystal has to be specially doped, and the effect decays slowly with time. Annealing to make the grating more stable results in lower efficiency[7.3].

We have demonstrated in this work that periodic index gratings could be produced by the novel technique of diffusion. After the fabrication of periodic structure in glass by silver/sodium ion-exchange, we have further extended the technique to $LiNbO_3$ by Ti indiffusion and by proton-exchange in benzoic acid.

Distinct features of these devices include negligible random scattering and strong perturbation at the grating regions, and the devices are mechanically more rugged compared to corrugated waveguides, because the grating is embedded within the guiding layer, and hence is less prone to environmental disturbance.

The grating mask (periodicity = 3μm, interaction length L = 750μm) was delineated on top of the substrate by conventional photolithographic technique, followed by vacuum deposition and lift-off. Good quality stripe patterns were obtained, indicating the high resolution and faithful reproduction of the planar technology used.

7.1.1.1 Ion-exchanged Gratings in Glass

The fabrication tolerance was relaxed by using 0.1% diluted $AgNO_3/NaNO_3$ melt, and good quality single mode waveguides (losses < 0.5 dB/cm at 0.633 μm) incorporating gratings were formed simultaneously in a one-step diffusion process on the same substrate.

The measured diffraction efficiency and bandwidth for the first order Bragg diffraction are in excellent agreement with the one-dimensional coupled-wave solution, and the response follows closely the $\sin^2(\kappa L)$ dependence, where κ is the coupling constant. A maximum efficiency of 76% was measured, probably due to the finite Gaussian beam used.

To investigate the side-diffusion mechanism underneath the grating mask, multimode waveguides were fabricated. As is expected, the diffraction efficiency decreases with diffusion time, and could be modelled by a simple expression. Mode conversion (TE_m-TE_n) was also observed in these devices, and they are the most efficient of this type of passive periodic waveguides reported. Low insertion loss is expected from this type of devices, because they are extremely inefficient as output couplers[7.4], unlike surface corrugated waveguides.

In order to increase the flexibility of this fabrication technique, a two-step diffusion process was investigated, using the first diffusion to form the waveguide and a second diffusion to form the grating structure. This was not

successful because the samples turned brown in the areas covered by the masks, and light could not be coupled in. This 'brown staining' is probably due to the chemical reaction between the diffused Ag ions and the ferrous impurities in the glass, aided by the presence of the mask. However, working devices are envisaged by using purer glass substrates, or by using different diffusion ions.

7.1.1.2 Ti-indiffused Gratings in $LiNbO_3$

Ti indiffusion is the most common technique for fabricating optical waveguides in $LiNbO_3$, and we used this method to produce periodic index gratings in y-cut $LiNbO_3$. Periodic corrugations (modulation depth $\sim$250Å to 350Å) were also observed on the surfaces of these devices, but their contribution to the coupling between the zero and first order beam is negligible, because with such a large periodicity (3 μm) the corrugated grating would act as an output coupler (radiator) rather than the desired phase-matching element.

For a single diffusion process ($t_1 = 0$), a maximum efficiency of 64% was measured for a diffusion time of $t_2 = t_{min}$. However, a long diffusion time (1.5 to 2 times t_{min}) is usually chosen to improve the repeatability of the guides, because the effective index as well as its rate of change decreases with time. In this case the efficiency drops to a only few per cent for t_2 = 10 hrs., and the response could be modelled by a simple expression. Side diffusion is a problem in this diffusion technique. Z-cut $LiNbO_3$ could be used to ease the problem,

because z-cut material has less lateral diffusion, but to use the large r_{33} electro-optic coefficient (for active devices), more complicated electrode patterns are required.

To circumvent this low efficiency situation, the two-step diffusion process was employed. Deep waveguides were fabricated with a diffusion time of t_1 = 5 hrs. and 8 hrs. respectively, and with a second diffusion time of $t_2 = t_{min}$ (3 hrs. for 200Å) to form the grating region, efficiencies of 60% and 46% were measured respectively. We demonstrated that a well-guided mode ($t_1 > t_{min}$) with high diffraction efficiency is possible with a two-step diffusion process. Furthermore, the diffusion time and the Ti thickness for the first and second diffusion step can be chosen independently for optimised performance.

7.1.1.3 Proton-exchanged gratings in $LiNbO_3$

Proton exchange is a new method for fabricating waveguides in $LiNbO_3$ [7.5]. Although much work is required before the full mechanism can be understood, the method is attractive because of the high index change ($\Delta n_e \sim 0.12$) possible. High efficiency gratings (diffraction efficiency $\sim$ 90%) were obtained in x-cut $LiNbO_3$ substrates using the one-step diffusion process, and both the measured efficiency and bandwidth are in good agreement with the calculated values using the one-dimensional coupled-wave solution.

Only TE modes are suported in x- or y- cut

samples, and the waveguides are very shallow (< 1 μm) because of the high index change. This may pose a problem in coupling between fibre and film. To ease this problem, guides can be made which suport both TE and TM modes by combining the proton-exchange process with Ti indiffusion[7.6], and Δn_e can be varied from its maximum value (0.12) to 0.01 by either using lithium rich solution (e.g. benzoic acid with lithium benzoate) or annealing[7.7]. It is envisaged that two-step diffusion devices can also be fabricated using these techniques.

7.1.2 Periodic Thickness (Corrugated) Waveguides

Our theoretical studies showed that two distinct features are present in oblique incidence which are not present in normal incidence : Firstly, the presence of strong coupling between TE and TM modes, which is shown to be dependent on the angle of incidence. The TE-TM coupling vanishes at 0^o and the TE-TE coupling at 45^o (similar to the 'Brewster effect' in conventional optics). Secondly, the variation of power across the width of the transmitted and diffracted beams. At high efficiency, the beam 'breaks up'. These features were not observed in the periodic index waveguides produced because of the small Bragg angles ($\Theta_B < 4^o$). In order to demonstrate these two unique properties in oblique incidence (and specifically a right angle deflection), submicron corrugated gratings were produced by holographic technique.

7.1.2.1 Four-layered Corrugated Devices

Because of problems encountered in the ion-milling step, deep surface corrugations were not possible, and hence four-layered devices were fabricated to demonstrate the second property : variation of power across the width of the transmitted and diffracted beams. Sputtered 7059 homogeneous glass waveguides were used. The presence of the high index photoresist layer on top of the guide pulls the modal field towards the surface and increases the interaction, and our qualitative experimental results confirmed the two unique properties of oblique incidence.

7.1.2.2 Three-layered Corrugated Devices

Since our coupled-wave formalism is valid only for shallow gratings, three-layered devices were fabricated to allow further comparison between theories and experimental results.

There is less scattering at the grating regions compared to that of the four-layered devices, and the measured responses agree better with the two-dimensional theory predictions, especially at high efficiency. The error in the one-dimensional predictions increases as efficiency goes up, and the bandwidth is also very much less than the measured values, indicating that for large angle deflection the one-dimensional solutions are not applicable.

7.2 Applications

Wavelength selective devices are desirable for use in optical communication. Many wavelength multi/demultiplexers have been demonstrated[7.8-7.12] using a prism, interference filters, and diffraction gratings. Losses in these devices are important, and the grating type has a sharp wavelength selectivity and hence allows large numbers of channels. Grating demultiplexers in thin film waveguides have advantages such as high efficiency and small dimensions, and are suitable for monolithic integration with photodetectors to form an integrated optical wavelength demultiplexer (WDM) receiver terminal (Fig. 7.1). However, careful design is necessary to reduce crosstalk between different channels because of mode conversion.

The periodic index gratings fabricated by diffusion techniques seem promising for such an application, because low insertion loss and high efficiency are possible, and the technique is a planar technology. In conjunction with established micro-electronics technology, both the gratings and the detectors can be formed on the same semiconductor substrate by diffusion processes. Gratings in distributed feedback and distributed Bragg reflector lasers using semiconductor substrates can also be formed using this diffusion technique.

The production of submicron gratings using techniques such as electron-beam and x-ray lithography is envisaged, and the holographic technique can be used to generate low-distortion x-ray masks. If, however, side-diffusion renders the submicron gratings inefficient, the two-step diffusion technique developed

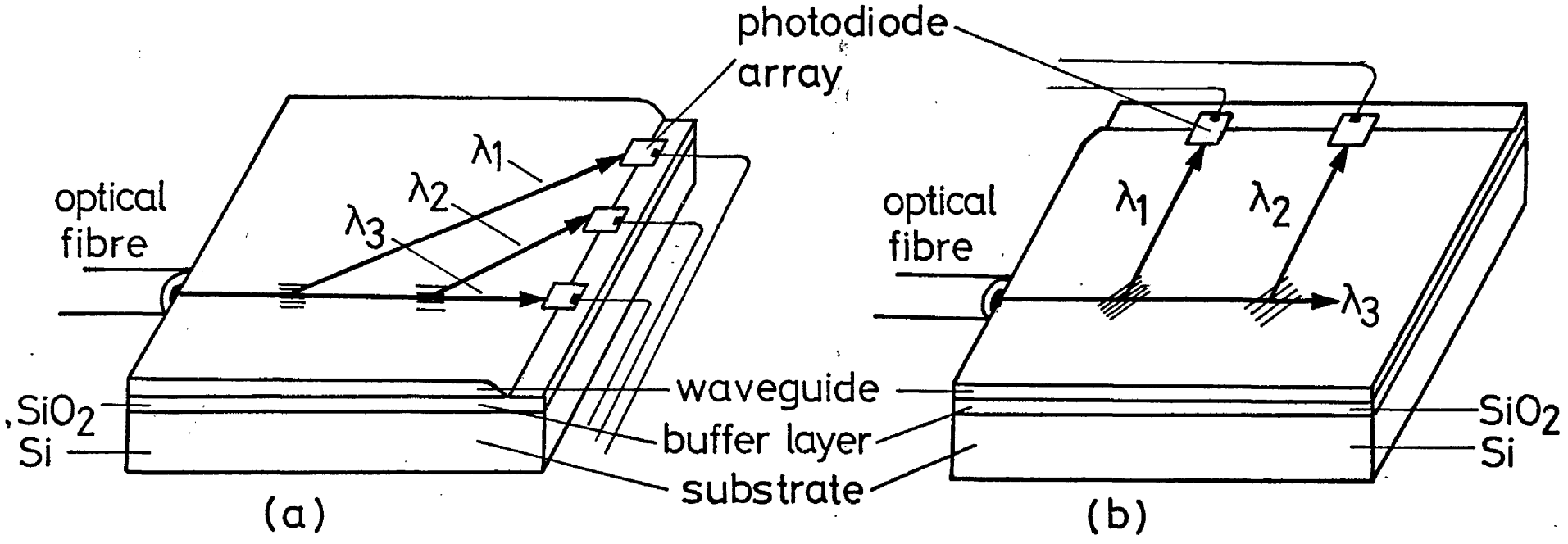

FIG 7.1 Integrated optical wavelength demultiplexer : (a) transmission grating type ; (b) reflection grating type

can circumvent this problem. Alternatively, ion-implantation can be used instead of diffusion.

The two unique properties of oblique incidence may limit the application of grating structures in specific functions, such as the lensless beam expander[7.13], where the 'breaking up' of the diffracted beam sets a limit to the maximum efficiency obtainable. However, devices such as the thin film polarizer can be made based on the zero TE-TE coupling at 45^{o}.

Future integrated optical circuits may also be interconnected by means of stripe waveguides. Denser packing of devices and lower cross-talk interference is possible by taking advantage of the lateral confinement of the guided light. A device that is of great interest is a stripe waveguide filter, or demultiplexer. A Y-junction stripe waveguide filter (Fig. 7.2) suffers from the follows limitations:

(a) scattering at the junction increases noise level;

(b) the interaction length of the grating is dictated by the geometry of the Y-junction, imposing a limitation on the bandwidth obtainable;

(c) in order to achieve a narrowband filter, a chirped grating is required to phase match the variation in mode index at the junction (due to change in width of the stripe waveguide). This is difficult because of the limited space available at the junction.

All these limitations can be overcome by the proposed directional coupler filter design (Fig. 7.3). This particular design has the following advantages:

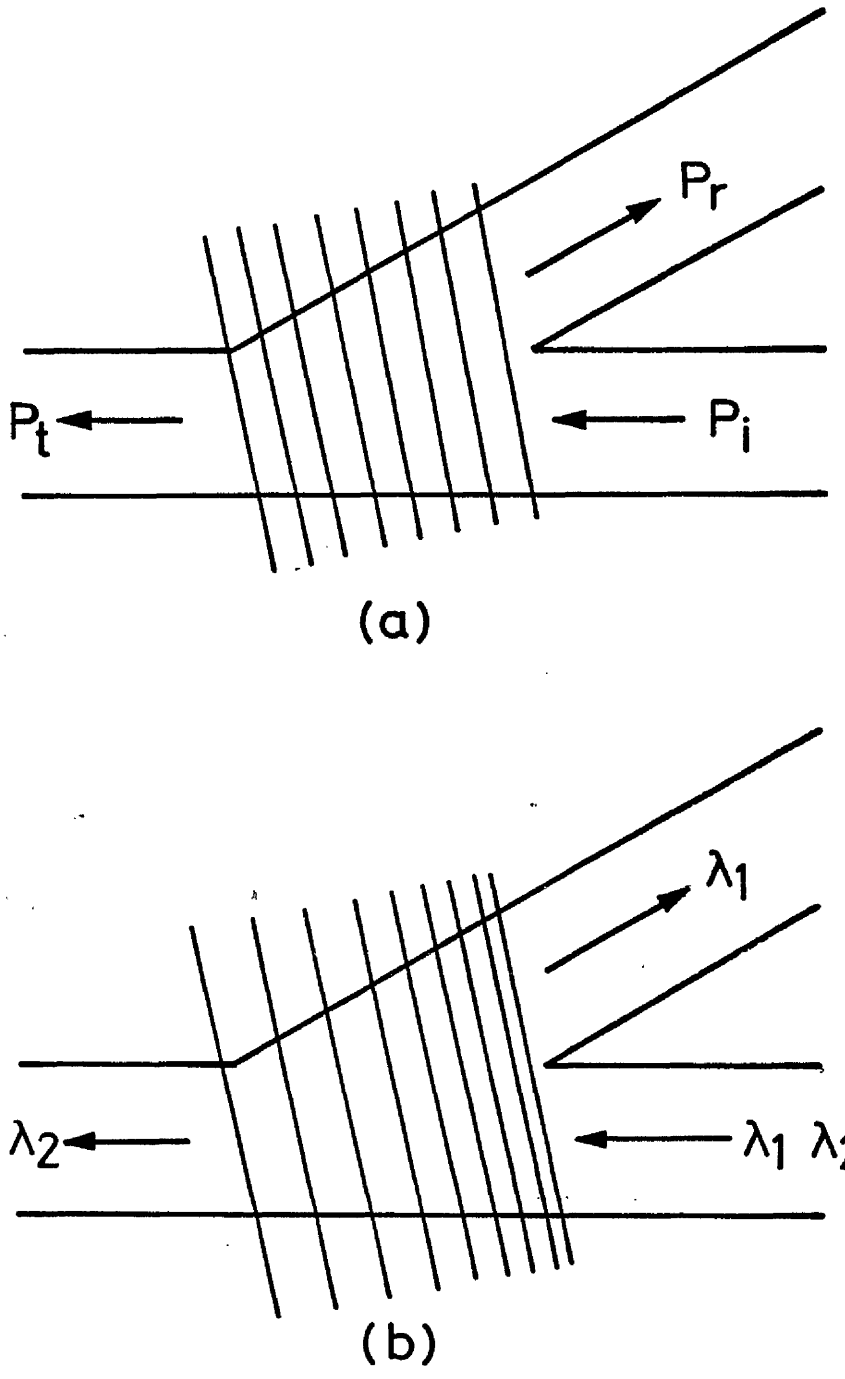

FIG 7.2 Y-junction stripe waveguide :
(a) power splitter; (b) Bragg filter

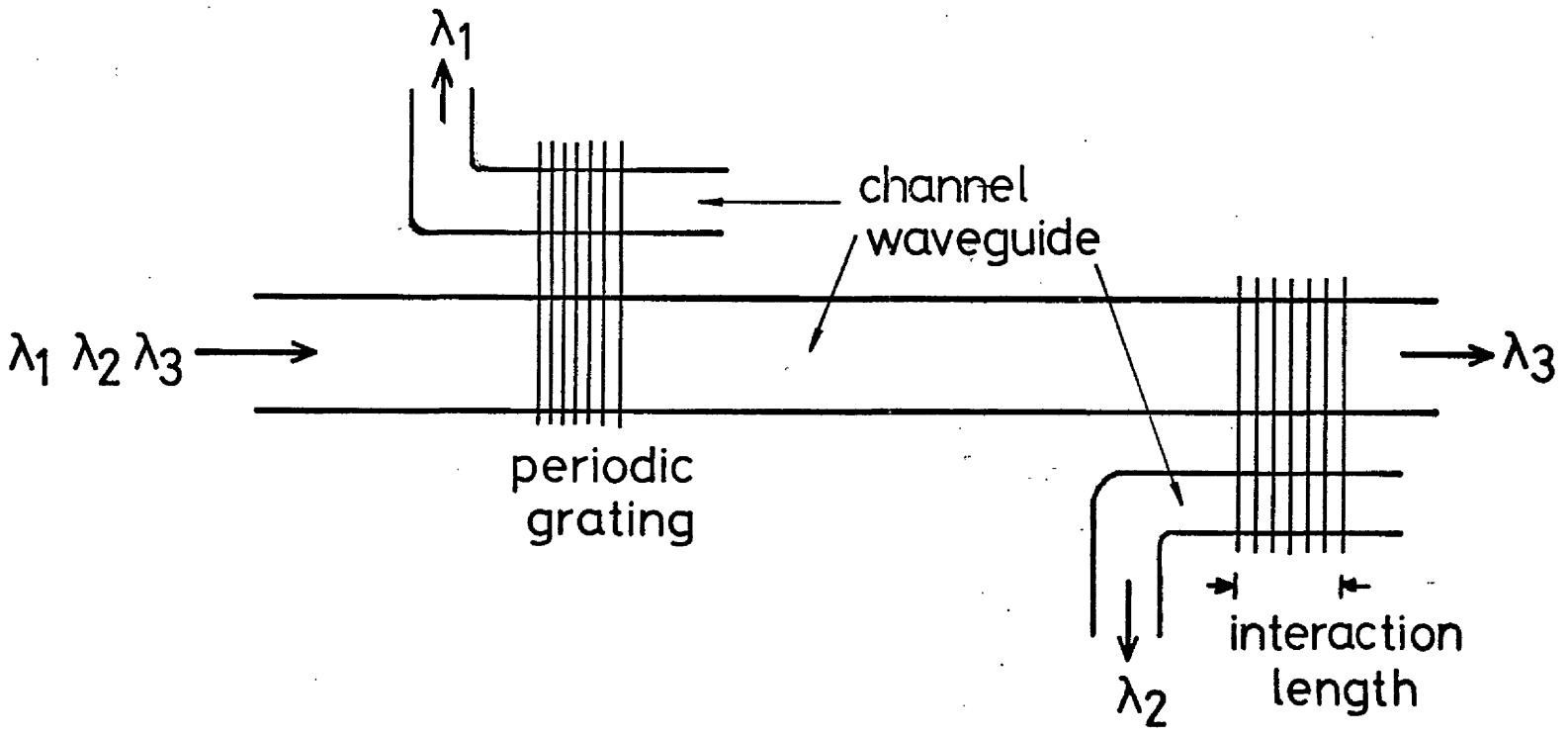

FIG 7.3 Proposal for a channel waveguide filter using periodic gratings

(a) low noise level, because the stripe waveguides are not identical, hence no coupling will occur without the phase-matching element;

(b) narrow bandwidth is achievable because the grating length is not limited. Also no chirped grating is required because there is no change in mode index, hence the fabrication step in the generation of the grating is simpler;

(c) the grating strength can be tapered to reduce the sidelobe response of the filter by a masking technique, giving lower crosstalk;

(d) by using normal incidence, the limitation set by the unique properties in oblique incidence is eliminated.

7.3 Conclusions

This thesis has been concerned with the experimental and theoretical studies of single mode passive Bragg deflectors for integrated optics.

The general properties of homogeneous and inhomogeneous dielectric slab waveguides are outlined in the thesis, using both 'geometrical optics' and 'electromagnetic field theory'. It is shown that the latter approach has to be used to obtain a complete description of the mode propagation. Beam coupling to these planar guides is also described, in particular employing the prism coupling technique, as used in our experiments.

Novel techniques of fabricating periodic index waveguides by diffusion through a grating mask were developed in

this work (see list of publications), resulting in a periodic variation of local refractive index in the waveguides. The planar geometry of this type of grating was found to be superior to that of surface corrugation gratings in terms of ease of fabrication, lower scattering losses , strong interaction and mechanical ruggedness, and the diffraction efficiency could be adjusted by parameters such as melt dilution, diffusion time and so on. The flexibility of this planar technique was further demonstrated by a two-step diffusion process, indicating that waveguide parameters could be designed individually for optimised performance.

At this stage the periodicity of the grating mask is limited by the conventional photolithographic technique. Submicron gratings are envisaged, made by using the diffusion technique in conjunction with electron beam or x-ray lithography.

Theoretical studies on oblique incidence, using one-dimensional and two-dimensional coupled wave formalism, indicates two distinct properties not found in normal incidence : the presence of mode conversion between TE-TM modes, depending on the angle of incidence, and variation of power across the width of the transmitted and diffracted beams. At high efficiency, the beam 'breaks up'. The diffraction efficiency has a character in between co-directional and contra-directional coupling, having horizontal tangents at the zeros of the first order Bessel functions.

Such properties were not observed in the periodic index waveguides fabricated because of the small Bragg angles ($\Theta_B < 4^o$),

and submicron gratings were fabricated using holographic technique to demonstrate the two effects. The two properties were confirmed by experiments, and the results indicates that in this case the one-dimensional coupled wave solutions are not applicable, and that the two-dimensional coupled wave solutions have to be used instead. Better agreement is expected if the model is further developed to take into account the Gaussian profile of the incident beam.

Periodic structures recur in many branches of physics. These structures are unique and important because of their special properties, and is expected to play an important role in the field of 'Integrated Optics'.

References

7.1 H.Kotani, M. Kubato, M. Kawabe, S. Namba and K. Masuda
Technical Digest of International Conference on Integrated Optics and Optical Fibre Communition, Tokyo, p.169 (1977)

7.2 V.E. Wood, N.F. Hartman, C.M. Verber and R.P. Kenan
J. Appl. Phys., 46 p.1214 (1975)

7.3 C.M. Verber, V.E. Wood, R.P. Kenan and N.F. Hartman
Ferroelectrics, 10 p.253 (1976)

7.4 D. Marcuse
I.E.E.E. J. Quant. Elect., QE-11 p.162 (1975)

7.5 J.L. Jackel and C.E. Rice
Appl. Phys. Lett., 41 p.508 (1982)

7.6 M. De. Macheli, J. Botineau, P.Sibillot, D.B. Ostrowsky, and M. Papuchon
Opt. Comm., 42 p.101 (1982)

7.7 M. De. Macheli, J. Botineau, S. Neveu, P. Sibillot, D.B. Ostrowsky, and M. Papuchon
Opt. Lett., 8 p.114 (1983)

7.8 W.J. Tomlinson
Appl. Opt., 16 p.2180 (1977)

7.9 W.J. Tomlinson and G.D. Aumiller
Appl. Phys. Lett., 31 p.169 (1978)

7.10 W.J. Tomlison and C. Lin
Electron. Lett., 14 p.345 (1978)

7.11 K. Aoyama and J. Minowa
Appl. Opt., 18 p.1253 (1979)

7.12 H.W. Yen, H.R. Friedrich, R.J. Morrison and G.L. Tangonan
Opt. Lett., 6 p.639 (1981)

7.13 H.M. Stoll
Appl. Opt., 17 p.2562 (1978)

'List of Publications'

Pun, E.Y.B. and Yi-Yan, A. :'Fabrication of periodic waveguides by ion exchange', Appl. Phys. Lett., 1981, **38**, pp673-674.

Pun, E.Y.B., Wong, K.K., Andonovic, I., Laybourn, P.J.R. and R.M. De La Rue :'Efficient waveguide Bragg deflection grating on $LiNbO_3$', Elect. Lett., 1982, **18**, pp740-742.

Yi-Yan, A., Andonovic, I., Pun, E.Y.B. and Bjortorp, B. : 'Passive beam splitter in $LiNbO_3$ by Ti indiffusion', to be published in Appl. Phys. Lett., July issue, 1983.

FIG 5.15 Blistering of the resist inside the ion beam etcher